Static field shimming in the human brain for ultra-high field MRI : conceptual limits and development of a novel hardware prototype

Bruno Pinho Meneses

université PARIS-SACLAY

Static Field Shimming in the Human Brain for Ultra-High Field MRI: Conceptual Limits and Development of a Novel Hardware Prototype

Homogénéisation du Champs Magnétique Statique dans le Cerveau Humain pour l'IRM à Ultra-Haut Champs : Limites Conceptuelles et Développement d'un Nouveau Prototype

Thèse de doctorat de l'université Paris-Saclay

École doctorale n° 575, Physique et ingénierie : électrons, photons et sciences du vivant (EOBE)
Spécialité de doctorat: Imagerie et Physique Médicale
Unité de recherche : Université Paris-Saclay, CEA, CNRS, BAOBAB, 91191 Gif-sur-Yvette, France
Référent : Faculté des sciences d'Orsay

Thèse présentée et soutenue à Paris-Saclay, le 29/04/2021, par

Bruno PINHO MENESES

Composition du Jury

Vincent LEBON Professeur de universités, Université Paris-Saclay	Président
Richard BOWTELL Professeur, University of Nottingham	Rapporteur & Examinateur
Andrew WEBB Professeur, Leiden University	Rapporteur & Examinateur
Jean-Christophe GINEFRI Directeur de Recherche, Université Paris-Saclay	Examinateur
Jason STOCKMANN Professeur Assistant, Massachusetts General Hospital	Examinateur
Direction de la thèse **Alexis AMADON** Directeur de Recherche CEA NeuroSpin, Université Paris-Saclay	Directeur de thèse
Guy AUBERT Professeur, Université de Poitiers	Invité

Thèse de doctorat

NNT : 2021UPAST045

THESIS

Static Field Shimming in the Human Brain for Ultra High Field MRI: Conceptual Limits and Development of a Novel Hardware Prototype

by

Bruno Pinho Meneses

Submitted in partial fulfilment of the requirements for the degree
of Doctor of Philosophy at Université Paris-Saclay,
under the supervision of

Dr Alexis Amadon
CEA NeuroSpin
Université Paris-Saclay

May 2021

Hic Rhodus, hic saltus

Aesop

Acknowledgements

THE single authorship in this thesis cover could erroneously lead one to believe that this was the work of a single person. It was certainly not. It was built upon discussions and collaboration with incredible researchers, to whom I'm grateful and would like express my sincere *thank you!*

First, I would like to thank my thesis supervisor, Alexis Amadon, for his guidance, never-ending patience and assistance throughout this work. He was always ready to answer and discuss my questions in MRI physics and give me a helping hand in experiments and hardware assembly, not to mention providing valuable input for helping me produce high quality abstracts, papers and this manuscript. All this certainly helped the good flow of this research work, and I'm very grateful for his mentoring.

I'd like to thank my colleagues from the Instrumentation team: Edouard Chazel, Michel Luong and Eric Giacomini for the rich discussions and for providing RF hardware essential to my work. Particularly, I'd like to express my deep appreciation for Edouard's incredible and highly professional work in the assembly of the AVANTI2 coil, a fundamental piece that allowed me to obtain high quality images for the validation of my work. Thanks to Michel's expertise in RF coil design and Edouard's seriousness and rigor, the resulting images were impeccable.

Speaking of essential hardware, another fundamental piece for the successful experiments in this thesis was the current driver electronics, provided by Jason Stockmann. I'd like to thank his help and expert advice on our shimming experiments. His willingness to share his expertise with different research teams, in a collaborative rather than competitive approach, for the benefit of science, should serve as example for all researchers.

To Nicolas Boulant, I'd like to say that I deeply appreciated our many discussions on electromagnetism, whether they were on the induced currents in the cryostat due to its vibration in a magnetic field, which was completely unrelated to my work, or on the intrinsic limitations to B_0 shimming in the human brain, which started as curious discussions and evolved into a whole chapter of this thesis. To this fellow electromagnetism and whisky appreciator, I have only one question: "Do Braziou?".

I also must thank Alexandre Vignaud for his many valuable input, always sharing his insightful views on the pertinence of my work and helping me ask and address the right

questions. I'm also thankful for his career advice, which helped me see a clear picture of the many possibilities in the life after thesis.

I'd also like to thank Guy Aubert. Although we only met on rare occasions, our discussions were always deeply interesting and enlightening.

I'd like to acknowledge the contributions of the other members of the METRIC team: Franck Mauconduit for his great help with sequence programming, Cécile Rabrait-Lerman for providing information on Iseult which helped us design our shim system accordingly, and Vincent Gras for his B_0 de-noising routine. Also, outside the METRIC team, I'd like to thank Michel Bottlaender and Josselin Houenou for providing access to their subjects for assembly of our fieldmap database, the radiographers for their help in ensuring smooth acquisitions, Luisa Ciobanu for lending us Skully, and Jeremy Bernard for helping us with 3D printings.

A successful PhD work doesn't consist only of scientific exchange, but also depends on a healthy and friendly environment. Therefore, I thank the many people which helped creating such an atmosphere. Raphaël Tomi-Tricot, initially a classmate in engineering school, coincidentally a PhD colleague many years later and now a workmate and friend. Caroline Le Ster, my desk-mate until we were both kicked out of our office. Renata Batista, my desk neighbor and fellow countrywoman, with whom I could take a break from speaking French and speak in Portuguese. Fawzi Boumezbeur, with whom I discussed philosophy on the bus. Paul-François Gapais, a fellow appreciator of fine writing. Loubna El Gueddari, an appreciator of terrible jokes. Chaithya Giliyar Radhakrishna, the life-saving streamer man. Redouane Jamil, a fellow movie aficionado. And several others: Lisa Leroi, Carole Lazarus, Gaël Saïb, Zo Raolison, Emilie Poirion, Mathilde Ripart, Guillaume Daval-Frerot and Pauline Agou.

Good times outside of work were also essential. Ensuring unforgettable moments inside a camper van in the middle of nowhere or simply virtually during pandemic times were my dear friends Vitor, Roda, Doug, Predo, Ana and Carol. To Rodolfo and Pedro I owe special thanks. To Rodolfo for yearly welcoming me in the land of the queen for the "colônia de férias do Rods". To Pedro for being the best roommate a PhD student in the final moments of his thesis could ever ask for, for the nice discussions on electromagnetism, and for reassuring me in moments of doubt. Also, when on vacation in Brazil, my longtime friends Augusto, Murilo, Elvis, Igor and Eliseu would be waiting for me and ready for any endeavor. I shall not forget my friend Rodrigo and our annual meetings at the beach.

A very warm thank you to my parents Irismar and Carlos, and to my sister Gabriela, who are always rooting for me and supporting my decisions, even when it means me being thousands of kilometers apart from them. I love you.

Finally, I thank my fiancee, Ianê, who has been with me since engineering graduation times, working together until late at night, who supports me even when it means spending years apart and seeing each other only a few times each year, and with whom I have the pleasure to share the most stunning views and the most amazing food.

* * *
* *
*

Contents

List of Figures

List of Tables

Symbols Used

Symbol	Constant name	Value
$\hbar$	Planck constant (reduced)	$1.055 \times 10^{-34}\,\mathrm{J \cdot s}$
k_B	Boltzmann constant	$1.381 \times 10^{-23}\,\mathrm{J \cdot K^{-1}}$
γ_{H}	^{1}H gyromagnetic ratio	$267.5 \times 10^{6}\,\mathrm{rad \cdot s^{-1} \cdot T^{-1}}$
$\frac{1}{2\pi}\gamma_{\mathrm{H}}$	^{1}H gyromagnetic ratio (reduced)	$42.57 \times 10^{6}\,\mathrm{Hz \cdot T^{-1}}$

Symbol	Description	Unit
B_0	static main field	$\mathrm{kg \cdot s^{-2} \cdot A^{-1}}$ (T)
B_1^+	coil transmission field	T
B_1^-	coil reception field	T
BW	radiofrequency bandwidth	$\mathrm{s^{-1}}$ (Hz)
E	electric field	$\mathrm{V \cdot m^{-1}}$
$\mathcal{E}$	energy	$\mathrm{kg \cdot m^2 \cdot s^{-2}}$ (J)
f	temporal frequency	$\mathrm{s^{-1}}$ (Hz)
f_0	Larmor temporal frequency	$\mathrm{s^{-1}}$ (Hz)
G	spatial static field gradients	$\mathrm{T \cdot m^{-1}}$
k	spatial frequency	$\mathrm{m^{-1}}$
M	macroscopic magnetisation	$\mathrm{A \cdot m^{-1}}$
$\mathrm{M_o}$	macroscopic equilibrium magnetisation	$\mathrm{A \cdot m^{-1}}$
$\mathcal{P}$	power	$\mathrm{J \cdot s^{-1}}$ (W)
T	temperature	K
T_1	spin-lattice relaxation time	s
T_2	spin-spin relaxation time	s
T_2^*	effective spin-spin relaxation time	s
α	magnetisation nutation angle (flip angle)	degree (°), rad
α_E	Ernst flip angle	degree (°), rad
γ	gyromagnetic ratio	$\mathrm{rad \cdot s^{-1} \cdot T^{-1}}$
$\delta\mathrm{B}_0$	static field inhomogeneity	T

Δf_0	offset from carrier frequency	s^{-1} (Hz)
$\Delta\omega$	offset from carrier angular frequency	$\mathrm{rad} \cdot \mathrm{s}^{-1}$
ω_0	Larmor angular frequency	$\mathrm{rad} \cdot \mathrm{s}^{-1}$
χ	magnetic susceptibility	—

Mathematical notations

The imaginary unit is expressed by $\imath$, such that $\imath^2 = -1$.
Italic bold letters denote vectors, *e.g.* $\boldsymbol{v}$.
Upper-case bold letters denote matrices, *e.g.* $\mathbf{M}$.
Vector or matrix transpose is represented by an exponent T following the object, *e.g.* $\boldsymbol{v}^{\mathrm{T}}$.
Vector dot product and cross product are denoted by $\cdot$ and $\times$, respectively.

General Introduction

SINCE its first demonstration for tomographic imaging of the human body in the late 1970s, Magnetic Resonance Imaging (MRI) has never ceased to gain momentum. It has become the gold-standard in medical imaging due to its versatility, provided not only by its multitude of natural contrasts (T_1,T_2, Proton-Density) but by the ingenious and rich set of pulse sequences that allow the observation of anatomy, flow, metabolic activity and more.

MRI relies on a strong main magnetic field B_0 to generate a net magnetization in body tissues, which is then manipulated to generate an image. This magnetization increases with the main magnetic field, and despite losses associated with thermal noise in the signal reception chain and physiological noise in the human body, image signal-to-noise ratio (SNR) increases supra-linearly with the main magnetic field. This is why significant effort has been made to increase the MRI main field from 0.35 T in its first in-vivo demonstration to 7 T available nowadays in clinical scanners. Even stronger scanners at 9.4 , 10.5 and 11.7 T, currently dedicated to research, may very well also find their place in clinical routine one day. These Ultra-High Field (UHF) scanners can indeed achieve submillimetre resolutions within viable acquisition time.

To benefit from SNR gains brought by UHF, the Iseult project was launched in 2007 with the Institute of Research of the Fundamental laws of the Universe (IRFU) at CEA to conceive a whole-body 11.7 T MRI scanner which is currently being installed at NeuroSpin.

With such a strong magnet, we expect to greatly enhance Contrast-to-Noise Ratio (CNR) in functional MRI (fMRI), a window to the intricate workings of the human brain. The intrinsic higher SNR will also be beneficial for X-nuclei (Sodium, Phosphorus, Lithium) imaging and spectroscopy. And of course, for most anatomical sequences. The increased SNR, CNR and resolution across a wide range of imaging sequences is also expected to shed light on clinical challenges such as early diagnosis of neuro-degenerative diseases.

The exploitation of such a powerful magnet, however, is accompanied by several engineering and methodological challenges. One of such challenges is related to inhomogeneity in the main magnetic field. MRI requires highly homogeneous magnetic field inside the useful scanning region. However, even when the main magnet is designed to provide excep-

tional homogeneity levels in air, when a patient is inserted in the magnetic field, magnetic susceptibility gradients between different tissues, and especially between tissues and air, will produce inhomogeneous magnetic fields close to these boundaries. These will degrade the previously homogeneous magnetic field and generate artifacts in images stemming from B_0-sensitive sequences. The susceptibility-induced inhomogeneity grows linearly with the main magnetic field, thus being problematic for imaging at UHF.

A notoriously B_0-sensitive sequence is Echo-Planar Imaging (EPI), the most commonly employed sequence in fMRI studies. It tends to present strong geometric distortion and signal loss around sinuses and ear-canals, regions of significant interest in a lot of neuroscience studies performed with fMRI. Such artifacts are already intense at 7 T, and are therefore expected to be worsened at 11.7 T.

Thesis Overview

Mitigation of B_0 related artifacts at UHF is therefore essential, and it is the main goal of this thesis project. As we will see, there are different paths that can be taken to attack this problem. In this work, we have decided to tackle the root of the problem, by trying to reduce the magnetic field excursions inside the human brain through the application of counteracting magnetic fields.

But beforehand, we have to understand its origin, its multifaceted character and which solutions are being employed. Therefore, this manuscript is divided into two main parts: the first one presents the fundamental equations describing the problem and the current state-of-the-art in the hardware used for susceptibility-induced B_0-inhomogeneity mitigation.

In chapter 1, we first remind the reader of some aspects of electromagnetic theory that will be employed in this work. Then, we show the mechanism behind the "apparition" of an inhomogeneous magnetic field in the human brain when the human head is immersed in a strong magnetic field. Finally, basic MRI theory is laid-out and, from the fundamental equations describing the MRI phenomenon, we evaluate how magnetic field excursions will produce image artifacts; we observe that artifacts are indeed worse as magnetic field excursions increase. We will notice that reducing magnetic field excursion is only one of the possible ways to reduce inhomogeneity related artifacts, but while each solution will carry a penalty, reducing the magnetic field excursion seems to be the one with less adverse effects.

Mitigation of these artifacts through the reduction of the magnetic field excursions is performed with the generation of counteracting magnetic fields. The different types of hardware employed for this and their evolution throughout the years are the topic of chapter 2. This process, known as shimming, is usually performed with coils correcting field Spherical Harmonics(SH) up to third degree in modern MRI scanners, but the correction provided by the SH-based shimming with this degree is expected to be insufficient at 11.7 T. Improvement of SH-based shimming is possible by increasing the degree of the

SH coil set, but this implies adding several space-consuming coils, building up to a heavy and eventually impractical system.

As a compact and versatile solution, shimming systems composed of small circular coils regularly placed over a cylindrical surface enclosing the patient's head, so-called matrix Multi-Coil Arrays (MCA), have been shown to provide comparable performance to that of high-degree SH-based systems, while being driven by relatively low currents. However, up to the moment when this thesis project started, there had been barely any attempt of optimizing the geometry and position of these coils to target a particular anatomy such as the human brain.

Since the magnetic field distribution inside the human brain presents similarities across subjects, we felt that current shimming solutions could be optimized to present high performances if their design considered the actual magnetic field excursion inside the human brain as target. We were not alone on this line of thought, and we have seen efforts from different research groups in similar directions within the last three and half years.

In the second part of the manuscript, therefore, we show our developed methodology for the design of brain-optimized shim systems.

In chapter 3, from the acquisition and treatment of a large database of B_0 fieldmaps in the human brain, a simplified coil design method is presented, the so-called Dipole Boundary Method, and employed in the computation of subject-optimal stream-functions (SF) on a cylindrical geometry. The similarity between the obtained coil wirepaths after discretization of the subject-optimal SF into windings called for the application of Singular Value Decomposition (SVD) to find a small set of coils to constitute a brain-dedicated shim system.

In chapter 4, we explore the limiting aspects of the B_0 shimming problem in the human brain. We describe the magnetic sources of inhomogeneous field and the correction structures as series of Solid Harmonics, which are found enlightening to understand the conditions for improved shimming. A numerical approach is applied on the large fieldmap database to explore the best possible homogeneity that could be attained inside the human brain. Finally, the potential benefits of localized shimming instead of whole brain shimming are studied.

At last, the most important results of this thesis are presented in chapter 5. Although the coils obtained with the method developed in chapter 3 will present quite complex winding patterns, they carry valuable information of where electric current is most demanded for correcting magnetic field inhomogeneity in the human brain. Therefore they serve as a guideline to place independent smaller loop-like coils to obtain a brain-optimized MCA. Thus a methodology for selecting coil geometry and position to design an MCA based on SF-SVD is presented. A so-called "SCOTCH" prototype is built with 36 channels, and tested for brain imaging at 7 T.

* * *
* *
*

Part I

Fundamentals and State of the Art

Chapter 1

Fundamentals

Chapter Outline

Physical principles laying the foundations of this thesis will be presented in this chapter. Essential electromagnetic theory for the understanding of this work is presented in section 1.1, mainly adapted from [Jackson 2007], together with the derivation of governing equations and properties of the magnetic fields studied herein.

Afterwards, we show the mechanism leading to the appearance of an inhomogeneous magnetic field in the human brain after patient's insertion in the scanner.

Finally, in section 1.2, magnetic resonance imaging (MRI) is presented. An overview on how anatomic images can be generated by manipulating abundant hydrogen (^{1}H) proton's $\frac{1}{2}$-spin through synchronized electromagnetic field pulses will be exposed, and we develop the basic MRI signal equations under the presence of magnetic field inhomogeneity to

describe its adverse effect in imaging. Further details on MRI physics and sequence design can be found in [Brown 2014, Bernstein 2010].

1.1 Electromagnetism

A distribution of electric charges in space, described by an electric charge density $\rho(\boldsymbol{x}, t)$, will produce an electric field $\boldsymbol{E}(\boldsymbol{x}, t)$. If the charges start moving, an electric current density $\boldsymbol{J}(\boldsymbol{x}, t)$ arises, and with it a magnetic field $\boldsymbol{B}(\boldsymbol{x}, t)$. Moreover, temporal variations in the magnetic induction will induce electric fields and, reciprocally, temporal variations in the electric field will produce a magnetic induction field. These intricate relations between fields and their sources are described by Maxwell's equations, first presented in 1861 as a set of twenty equations and further grouped into four elegant equations by Oliver Heaviside, presented here in their differential form:

$$\boldsymbol{\nabla} \cdot \boldsymbol{D}(\boldsymbol{x}, t) = \rho(\boldsymbol{x}, t) \tag{1.1}$$

$$\boldsymbol{\nabla} \cdot \boldsymbol{B}(\boldsymbol{x}, t) = 0 \tag{1.2}$$

$$\boldsymbol{\nabla} \times \boldsymbol{E}(\boldsymbol{x}, t) = -\frac{\partial \boldsymbol{B}(\boldsymbol{x}, t)}{\partial t} \tag{1.3}$$

$$\boldsymbol{\nabla} \times \boldsymbol{H}(\boldsymbol{x}, t) = \boldsymbol{J}(\boldsymbol{x}, t) + \frac{\partial \boldsymbol{D}(\boldsymbol{x}, t)}{\partial t} \tag{1.4}$$

Equations 1.1 through 1.4 are Gauss's Law, for electric fields and for magnetic fields, Faraday's Law and Ampère's Law, respectively. The electric displacement $\boldsymbol{D}(\boldsymbol{x}, t)$ and the auxiliary field $\boldsymbol{H}(\boldsymbol{x}, t)$ relate to the electric and magnetic fields by:

$$\boldsymbol{D}(\boldsymbol{x}, t) = \varepsilon_0 \boldsymbol{E}(\boldsymbol{x}, t) + \boldsymbol{P}(\boldsymbol{x}, t), \tag{1.5}$$

and

$$\boldsymbol{H}(\boldsymbol{x}, t) = \frac{\boldsymbol{B}(\boldsymbol{x}, t)}{\mu_0} - \boldsymbol{M}(\boldsymbol{x}, t) \tag{1.6}$$

with ε_0 the vacuum permitivity, μ_0 the vacuum permeability, $\boldsymbol{P}(\boldsymbol{x}, t)$ and $\boldsymbol{M}(\boldsymbol{x}, t)$ the medium polarization and magnetization, respectively. Particularly, for linear, isotropic media:

$$\boldsymbol{P}(\boldsymbol{x}, t) = \varepsilon_0 \chi_e \boldsymbol{E}(\boldsymbol{x}, t) \tag{1.7}$$

$$\boldsymbol{M}(\boldsymbol{x}, t) = \chi_m \boldsymbol{H}(\boldsymbol{x}, t) \tag{1.8}$$

with χ_e and χ_m the electric and magnetic susceptibilities, respectively. Both equal to zero for vacuum.

The fields store electric and magnetic energy, given by:

$$W_e = \frac{1}{2} \int_{\mathcal{V}} \boldsymbol{E} \cdot \boldsymbol{D} \, d^3x \tag{1.9}$$

and

$$W_m = \frac{1}{2} \int_{\mathcal{V}} \boldsymbol{H} \cdot \boldsymbol{B} \, d^3x \tag{1.10}$$

In conductive media, the electric field generates current flow as dictated by Ohm's Law:

$$\boldsymbol{J}(\boldsymbol{x},t) = \sigma \boldsymbol{E}(\boldsymbol{x},t) \tag{1.11}$$

with σ the electric conductivity of the medium. In turn, there is power dissipation:

$$\mathcal{P} = \int_{\mathcal{V}} \boldsymbol{J} \cdot \boldsymbol{E}\, d^3x \tag{1.12}$$

Finally, in *magnetostatic* analysis, employed for the design of shim coils, there is no temporal dependency on the fields, causing equations 1.3 and 1.4 to reduce to:

$$\boldsymbol{\nabla} \times \boldsymbol{E}(\boldsymbol{x}) = \boldsymbol{0} \tag{1.13}$$

$$\boldsymbol{\nabla} \times \boldsymbol{H}(\boldsymbol{x}) = \boldsymbol{J}(\boldsymbol{x}) \tag{1.14}$$

In addition, applying the divergence operator on both sides of equation 1.14, we obtain

$$\boldsymbol{\nabla} \cdot \boldsymbol{J}(\boldsymbol{x}) = 0. \tag{1.15}$$

This consequence of magnetostatics is what will allow us to associate to a current density, particularly a surface current density, a stream function (cf. section 1.1.5).

1.1.1 Poisson's and Laplace's Equations

As consequences of equations 1.13 and 1.2, electrostatic fields, being *irrotational*, can be derived from an electric scalar potential $V(\boldsymbol{x})$, while the *divergence-less* magnetic field can be derived from a magnetic vector potential $\boldsymbol{A}(\boldsymbol{x})$ as:

$$\boldsymbol{E}(\boldsymbol{x}) = -\boldsymbol{\nabla} V(\boldsymbol{x}) \tag{1.16}$$

$$\boldsymbol{B}(\boldsymbol{x}) = \boldsymbol{\nabla} \times \boldsymbol{A}(\boldsymbol{x}) \tag{1.17}$$

Inserting 1.16 and 1.17 into Gauss's and Ampère's laws, respectivelly, and considering non-magnetic and non-dielectric media, we obtain:

$$\nabla^2 V(\boldsymbol{x}) = -\frac{\rho(\boldsymbol{x})}{\varepsilon_0} \tag{1.18}$$

$$\boldsymbol{\nabla}(\boldsymbol{\nabla} \cdot \boldsymbol{A}(\boldsymbol{x})) - \nabla^2 \boldsymbol{A}(\boldsymbol{x}) = \mu_0 \boldsymbol{J}(\boldsymbol{x}) \tag{1.19}$$

Where equation 1.18 is the *Poisson equation* for the electric potential, and equation 1.19 will turn into Poisson's equation for the magnetic potential through a convenient *gauge transformation* where $\boldsymbol{A}(\boldsymbol{x})$ is chosen such that it has zero divergence (Coulomb gauge), resulting in:

$$\nabla^2 \boldsymbol{A}(\boldsymbol{x}) = -\mu_0 \boldsymbol{J}(\boldsymbol{x}) \tag{1.20}$$

Moreover, in a region free of magnetic or electric field sources ($\boldsymbol{J}(\boldsymbol{x}) = \boldsymbol{0}$ and $\rho(\boldsymbol{x}) = 0$) we obtain **Laplace's equations** for the potentials:

$$\nabla^2 V(\boldsymbol{x}) = 0 \tag{1.21}$$

$$\nabla^2 \boldsymbol{A}(\boldsymbol{x}) = \boldsymbol{0} \tag{1.22}$$

Alternatively, in the source-free scenario, applying the curl operator on Ampère's law yields Laplace's equation for the magnetic field:

$$\nabla^2 \boldsymbol{B}(\boldsymbol{x}) = \boldsymbol{0} \tag{1.23}$$

thus bypassing the need for a magnetic vector potential in this particular case. Moreover, in MR field homogeneity studies, only the magnetic field in the direction of the main B_0 field, usually chosen as the z direction, is of interest, and we can restrain our analysis to:

$$\nabla^2 B_z(\boldsymbol{x}) = 0 \tag{1.24}$$

Poisson's or Laplace's equation together with pertinent boundary conditions can be solved, numerically or analytically (if the geometry of the problem allows), to obtain the electric and magnetic fields of any distribution of sources in a particular environment.

Solutions which are pertinent to this work are discussed in the following sections.

1.1.2 Solution to Poisson's equation: Biot-Savart Law

The obtention of the electric current distribution necessary to generate a target magnetic field in space, the first step in coil design, is accomplished by solving an inverse problem that can be formulated by means of the Biot-Savart Law, developed through the works of Oersted, Biot, Savart and Ampère.

While a straightforward presentation of this law is sufficient for its subsequent use in coil design, we chose to present its derivation from Poisson's equation. Indeed the intermediate steps leading to it will be useful in the following sections for stating properties of the solutions of Poisson and Laplace's equations that can come in handy in the coil design process.

Green's Identities

Given any two scalar functions $\Psi(\boldsymbol{x})$ and $\Phi(\boldsymbol{x})$ in a domain $\mathcal{V} \in \mathbb{R}^3$ with boundary $\mathcal{S}$, the first and second Green's identities are, respectively:

$$\int_{\mathcal{V}} \left(\Phi \nabla^2 \Psi + \boldsymbol{\nabla}\Phi \cdot \boldsymbol{\nabla}\Psi \right) d^3x = \oint_{\mathcal{S}} (\Phi \boldsymbol{\nabla}\Psi) \cdot d\boldsymbol{a} \tag{1.25}$$

$$\int_{\mathcal{V}} \left(\Phi \nabla^2 \Psi - \Psi \nabla^2 \Phi \right) d^3x = \oint_{\mathcal{S}} (\Phi \boldsymbol{\nabla}\Psi - \Psi \boldsymbol{\nabla}\Phi) \cdot d\boldsymbol{a} \tag{1.26}$$

The second identity can be used to solve Poisson's equation. Let $\Phi(\boldsymbol{x}') = A_i(\boldsymbol{x}')$, with A_i any of the three orthogonal components of $\boldsymbol{A}$, and $\Psi(\boldsymbol{x}) = G(\boldsymbol{x}, \boldsymbol{x}')$ some arbitrary function, substitution into 1.26 yields:

$$\int_{\mathcal{V}} A_i \nabla'^2 G \, d^3x' = -\mu_0 \int_{\mathcal{V}} G(\boldsymbol{x}, \boldsymbol{x}') J_i d^3x' + \oint_{\mathcal{S}} (A_i \boldsymbol{\nabla}' G(\boldsymbol{x}, \boldsymbol{x}')) \cdot d\boldsymbol{a}' - \oint_{\mathcal{S}} (G(\boldsymbol{x}, \boldsymbol{x}') \boldsymbol{\nabla}' A_i) \cdot d\boldsymbol{a}'. \tag{1.27}$$

At this point, if we can construct a convenient function $G(\boldsymbol{x}, \boldsymbol{x}')$ such that

$$\nabla'^2 G(\boldsymbol{x}, \boldsymbol{x}') = \delta(\boldsymbol{x} - \boldsymbol{x}') \tag{1.28}$$

we obtain an expression for A_i of the form:

$$A_i(\boldsymbol{x}) = -\mu_0 \int_{\mathcal{V}} G(\boldsymbol{x}, \boldsymbol{x}') J_i d^3x' + \oint_{\mathcal{S}} \left(A_i \boldsymbol{\nabla}' G(\boldsymbol{x}, \boldsymbol{x}')\right) \cdot d\boldsymbol{a}' - \oint_{\mathcal{S}} \left(G(\boldsymbol{x}, \boldsymbol{x}') \boldsymbol{\nabla}' A_i\right) \cdot d\boldsymbol{a}' \tag{1.29}$$

Finding an analytical expression for $G(\boldsymbol{x}, \boldsymbol{x}')$ that can also effectively deal with the available boundary conditions – that is, zero-out the integral that demands a boundary information we do not possess – would solve Poisson's equation for $\boldsymbol{A}$, and the magnetic field $\boldsymbol{B}$ could be calculated thereafter.

Green's Functions

Functions $G(\boldsymbol{x}, \boldsymbol{x}')$ satisfying equation 1.28 compose the class of *Green Functions* for the Laplacian operator. One of such functions is

$$G(\boldsymbol{x}, \boldsymbol{x}') = -\frac{1}{4\pi \left|\boldsymbol{x} - \boldsymbol{x}'\right|} \tag{1.30}$$

Inserting this particular Green function into 1.29 and assuming that A_i decreases faster than r^{-1}, both surface integrals vanish and the expression for the magnetic vector potential becomes

$$A_i(\boldsymbol{x}) = \frac{\mu_0}{4\pi} \int_{\mathcal{V}} \frac{J_i(\boldsymbol{x}')}{\left|\boldsymbol{x} - \boldsymbol{x}'\right|} d^3x', \tag{1.31}$$

providing the solution for the Poisson's equation for the magnetic vector potential as a straight forward relation to the current density distribution.

Green's functions can be powerful tools providing integral solutions for a wide-range of differential equations presenting the most diverse boundary conditions. The construction of such functions, however, is not always a simple task. Fortunately, in this work, only simple Green functions of the form

$$G(\boldsymbol{x}, \boldsymbol{x}') = -\frac{1}{4\pi \left|\boldsymbol{x} - \boldsymbol{x}'\right|} + F(\boldsymbol{x}, \boldsymbol{x}') \tag{1.32}$$

will be called for, with $F(\boldsymbol{x}, \boldsymbol{x}')$ a function satisfying $\nabla^2 F = 0$ and chosen in a way to simplify the boundary condition surface integrals.

Biot-Savart Law

From 1.31, assembling all components of the magnetic vector potential we have:

$$\boldsymbol{A}(\boldsymbol{x}) = \frac{\mu_0}{4\pi} \int_{\mathcal{V}} \frac{\boldsymbol{J}(\boldsymbol{x}')}{\left|\boldsymbol{x} - \boldsymbol{x}'\right|} d^3x. \tag{1.33}$$

Finally, the magnetic field can be obtained applying the curl operator on both sides of the previous equation, leading to:

$$\boldsymbol{B}(\boldsymbol{x}) = \frac{\mu_0}{4\pi} \int_{\mathcal{V}} \frac{\boldsymbol{J}(\boldsymbol{x}') \times (\boldsymbol{x} - \boldsymbol{x}')}{\left|\boldsymbol{x} - \boldsymbol{x}'\right|^3} d^3x'. \tag{1.34}$$

This is the Biot-Savart law, relating a current distribution to the magnetic field it generates.

Uniqueness

Green's first identity can be used now to prove that, given a particular boundary condition (either the value of the function or of its normal derivative on the boundary), solution to Poisson's equation is uniquely determined.

Proof. Let $g_1(\boldsymbol{x})$ and $g_2(\boldsymbol{x})$ be two functions satisfying Poisson's equation $\nabla^2 g(\boldsymbol{x}) = -f(\boldsymbol{x})$ for given Dirichlet or Neumann boundary conditions. Defining a function $U = g_2 - g_1$ and applying 1.25:

$$\int_{\mathcal{V}} \left(U\nabla^2 U + \boldsymbol{\nabla} U \cdot \boldsymbol{\nabla} U \right) d^3x = \oint_{\mathcal{S}} (U \boldsymbol{\nabla} U) \cdot d\boldsymbol{a} \tag{1.35}$$

The integral on the surface vanishes, since either U or $\boldsymbol{\nabla} U$ is equal to zero on the boundary. The Laplacian of U is also zero, and we are left with

$$\int_{\mathcal{V}} |\boldsymbol{\nabla} U|^2 d^3x = 0. \tag{1.36}$$

The gradient of U must be zero, and U is a constant. For Dirichlet boundary conditions, $U = 0$ and $g_1 = g_2$. For Neumann boundary conditions, they could differ by a constant, but since the fields, given by derivatives of potentials, carry the physical meaning, the solution will still be unique. □

Uniqueness is important not only because it guarantees the consistency of a solution, but because it highlights the importance of the boundary in defining it. For a field satisfying Laplace's equation, its value on the boundary of the region of interest provides all the necessary information for knowing the field in the interior. This is of great practical utility, as measurements of the field could be restricted to a surface instead of a whole volume.

1.1.3 Magnetic Fields in Matter

Nuclear spin, electron spin and orbital motion engender the magnetic dipole moments intrinsic to matter. The "reaction" of such magnetic dipoles to an applied external field originates:

- the NMR phenomenon, making magnetic resonance imaging possible.
- the atomic magnetism of bulk matter which, on the other hand, is at the root of image distortions and signal losses this work aims to correct.

Therefore, concepts of magnetic dipole moment, how it generates magnetic field and interacts to an external field, are briefly reviewed.

Magnetic Dipole Moment

Given a localized electric current density $\boldsymbol{J}$ in space, the magnetic vector potential it generates is given by eq. 1.33. Let the origin of the coordinate system be somewhere

within the current distribution; then the calculation of the potential at a point $\boldsymbol{x}$ such that $|\boldsymbol{x}| \gg |\boldsymbol{x}'|$ allows a Taylor series approximation of $|\boldsymbol{x} - \boldsymbol{x}'|^{-1}$ in the form

$$\frac{1}{|\boldsymbol{x} - \boldsymbol{x}'|} \approx \frac{1}{|\boldsymbol{x}|} + \frac{\boldsymbol{x} \cdot \boldsymbol{x}'}{|\boldsymbol{x}|^3} \tag{1.37}$$

and substitution into the magnetic potential expression leads, after some algebra, to

$$\boldsymbol{A}(\boldsymbol{x}) = \frac{\mu_0}{4\pi} \frac{\boldsymbol{m} \times \boldsymbol{x}}{|\boldsymbol{x}|^3} \tag{1.38}$$

which in turn generates a magnetic field

$$\boldsymbol{B}(\boldsymbol{x}) = \frac{\mu_0}{4\pi|\boldsymbol{x}|^3} \left[\frac{3(\boldsymbol{m} \cdot \boldsymbol{x})\boldsymbol{x}}{|\boldsymbol{x}|^2} - \boldsymbol{m} \right] \tag{1.39}$$

where

$$\boldsymbol{m} = \frac{1}{2} \int \boldsymbol{x}' \times \boldsymbol{J}(\boldsymbol{x}')\, d^3x' \tag{1.40}$$

is the magnetic dipole moment or simply magnetic moment. A detailed derivation is available in [Jackson 2007]. Magnetic moments other than the dipolar one could be obtained through a different procedure [Gray 1978], but the dipole is usually the dominating term at long range, and is the one of interest in this work.

Taking a simpler current distribution, such as an electric current I running through an arbitrarily shaped thin loop $\mathcal{C}$, the magnetic moment becomes

$$\begin{aligned} \boldsymbol{m} =& \frac{I}{2} \oint_{\mathcal{C}} \boldsymbol{x}' \times d\boldsymbol{l} \\ =& I\boldsymbol{a} \end{aligned} \tag{1.41}$$

where $\boldsymbol{a}$ is the vector area of the loop.

When immersed in magnetic field, a dipole presents potential energy

$$U = -\boldsymbol{m} \cdot \boldsymbol{B} \tag{1.42}$$

and is submitted to a torque

$$\boldsymbol{N} = \boldsymbol{m} \times \boldsymbol{B} \tag{1.43}$$

These two expressions are a starting point for understanding MRI, where the bulk nuclear magnetic moment intensity will depend on the difference of potential energy between the different states of the nuclear spins, and applied torque on this magnetization will conduct its dynamics.

Magnetization

Interaction of the magnetic dipoles of the electron spin and orbital motion with an external applied magnetic field results in magnetization. The once arbitrarily oriented dipoles, averaging to a null magnetic moment macroscopically, will now be oriented in such a way that a bulk magnetization $\boldsymbol{M}$, already introduced in equation 1.6, arises. The substitution $\boldsymbol{m} \to d\boldsymbol{m} = \boldsymbol{M} dV$ into 1.38 and subsequent integration provides:

$$\boldsymbol{A}(\boldsymbol{x}) = \frac{\mu_0}{4\pi} \int_{\mathcal{V}} \frac{\boldsymbol{\nabla}' \times \boldsymbol{M}}{|\boldsymbol{x} - \boldsymbol{x}'|}\, d^3x' + \frac{\mu_0}{4\pi} \oint_{\mathcal{S}} \frac{\boldsymbol{M} \times d\boldsymbol{a}'}{|\boldsymbol{x} - \boldsymbol{x}'|} \tag{1.44}$$

Alternatively, we have:

$$\boldsymbol{\nabla} \times \boldsymbol{H} = 0, \tag{1.45}$$

which means a scalar potential Φ_M can be attributed to the the auxiliary field, relating by $\boldsymbol{H} = -\boldsymbol{\nabla}\Phi_M$. Applying the divergence operator on both sides of equation 1.6 and writing $\boldsymbol{H}$ as a function of the scalar potential:

$$\boldsymbol{\nabla} \cdot (-\boldsymbol{\nabla}\Phi_M) = \frac{\boldsymbol{\nabla} \cdot \boldsymbol{B}}{\mu_0} - \boldsymbol{\nabla} \cdot \boldsymbol{M}$$

$$\nabla^2 \Phi_M = \boldsymbol{\nabla} \cdot \boldsymbol{M} \tag{1.46}$$

This is once again Poisson's equation which has a solution given by

$$\Phi_M = -\frac{1}{4\pi} \int_V \frac{\boldsymbol{\nabla}' \cdot \boldsymbol{M}(\boldsymbol{x}')}{|\boldsymbol{x} - \boldsymbol{x}'|}\, d^3x', \tag{1.47}$$

or, to effectively deal with the magnetization drop to zero as we move outside the volume boundaries, the following surface integral term is added:

$$\Phi_M = -\frac{1}{4\pi} \int_V \frac{\boldsymbol{\nabla}' \cdot \boldsymbol{M}(\boldsymbol{x}')}{|\boldsymbol{x} - \boldsymbol{x}'|}\, d^3x' + \frac{1}{4\pi} \oint_S \frac{\boldsymbol{M}(\boldsymbol{x}') \cdot d\boldsymbol{a}'}{|\boldsymbol{x} - \boldsymbol{x}'|}. \tag{1.48}$$

For a localized magnetization, integration by parts in equation 1.47 leads to:

$$\Phi_M = -\frac{\boldsymbol{m}}{4\pi} \cdot \boldsymbol{\nabla} \left(\frac{1}{|\boldsymbol{x} - \boldsymbol{x}'|} \right) \tag{1.49}$$

which is a convenient expression for analyzing the magnetic field generated by ferromagnetic pieces placed around the MRI bore for magnetic field homogenization [Roméo 1984].

1.1.4 Solution to Laplace's Equation in Spherical Coordinates: Solid Harmonics

We now focus our attention to the case where no magnetic field sources are present in the domain of the field we wish to express. Should these domains be spheres or spherical shells, Laplace's equation for the magnetic field (1.24) in spherical coordinates is:

$$\frac{1}{r^2}\frac{\partial}{\partial r}\left(r^2 \frac{\partial B_z}{\partial r}\right) + \frac{1}{r^2 \sin\theta}\frac{\partial}{\partial \theta}\left(\sin\theta \frac{\partial B_z}{\partial \theta}\right) + \frac{1}{r^2 \sin^2\theta}\frac{\partial^2 B_z}{\partial \varphi^2} = 0 \tag{1.50}$$

which can be solved through separation of variables [Bayin 2006]. This equation unfolds into three separate ordinary differential equations: a second-order homogeneous differential equation in φ, a second-order Cauchy-Euler differential equation in r and the general Legendre equation in θ.

Associated Legendre Polynomials

The solution for the general Legendre equation

$$(1 - x^2)\frac{d^2 P_{nm}(x)}{dx^2} - 2x\frac{dP_{nm}(x)}{dx} + \left[n(n+1) - \frac{m^2}{1 - x^2}\right] P_{nm}(x) = 0 \tag{1.51}$$

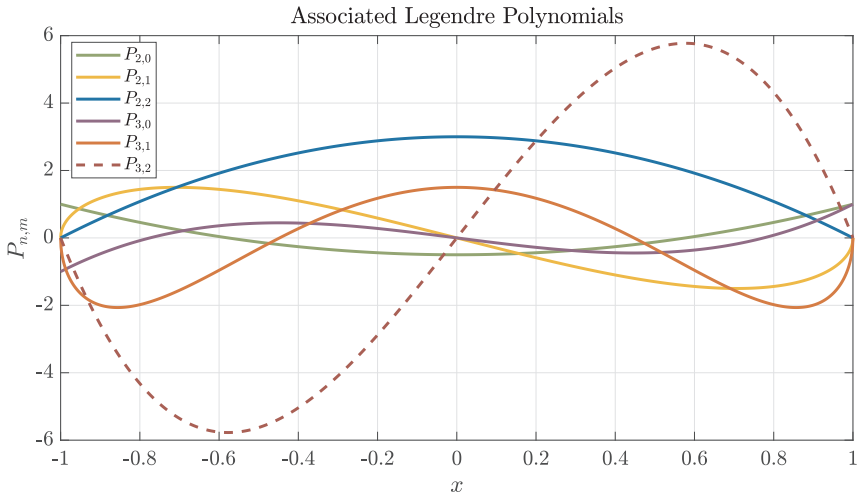

Figure 1.1 – Examples of Associated Legendre Polynomials of various degrees and orders.

consists in a family of polynomial functions $P_{nm} : [-1, 1] \to \mathbb{R}$, called Associated Legendre Polynomials, of degree n and order m ([MacRobert 1948, Abramowitz 2013] notation), with $n \geq 0$ and $m \in \mathbb{Z}$, given by the following formula:

$$P_{nm}(x) = \frac{(1-x^2)^{\frac{m}{2}}}{2^n n!} \frac{d^{n+m}}{dx^{n+m}} (x^2 - 1)^n \tag{1.52}$$

They obey the following orthogonality relation:

$$\int_{-1}^{1} P_{n'm}(x) P_{nm}(x) dx = \frac{2}{2n+1} \frac{(n-m)!}{(n+m)!} \delta_{n'n} \tag{1.53}$$

with $\delta_{n'n}$ the Kronecker delta function.

Some examples of associated Legendre polynomials are shown in Fig. 1.1.

Spherical Harmonics

The solutions of the aforementioned second-order homogeneous differential equation in φ, together with the associated Legendre $\cos\theta$-polynomials, form the Spherical Harmonic functions $Y_{n,m} : [0, \pi] \times [0, 2\pi] \to \mathbb{R}$, which are defined as:

$$Y_{nm}(\theta, \varphi) = \begin{cases} P_{nm}(\cos\theta) \cos m\varphi & m \geq 0 \\ P_{n|m|}(\cos\theta) \sin |m| \, \varphi & m < 0 \end{cases} \tag{1.54}$$

Spherical harmonics are presented here in their real valued, unnormalized form. They find the most diverse applications, from quantum mechanics to image processing. They are orthogonal and complete, therefore any function of (θ, φ) with domain $[0, \pi] \times [0, 2\pi]$ can be expanded into a series of spherical harmonics.

Solid Harmonics

Incorporating the solution to the Cauchy-Euler differential equation in r, Solid Harmonics

$$\mathcal{R}_{nm}(r, \theta, \varphi) = r^n Y_{nm}(\theta, \varphi) \tag{1.55}$$

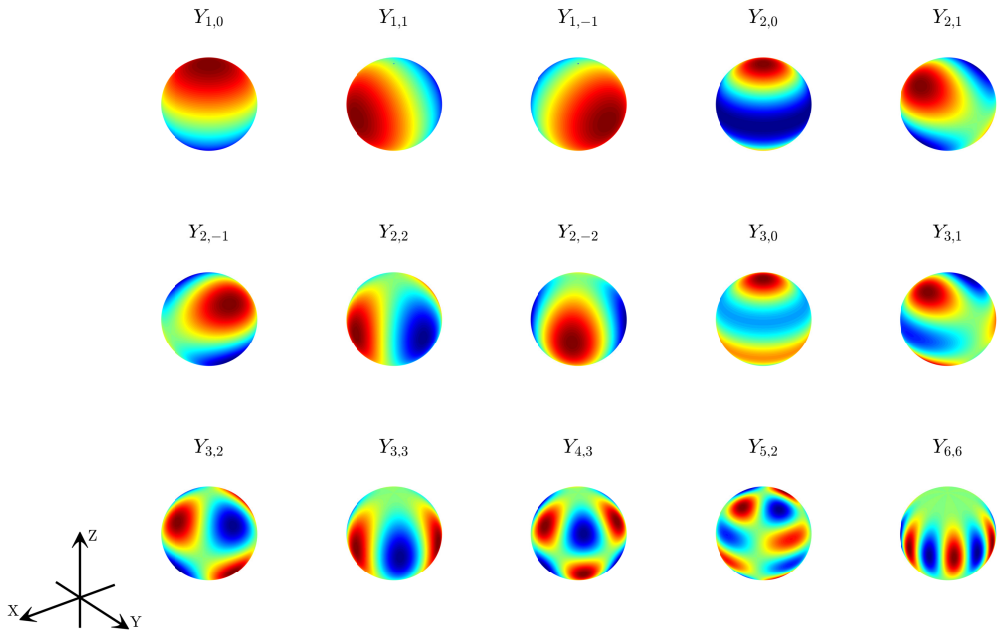

Figure 1.2 – Examples of Spherical Harmonic functions of varius degrees and orders.

and

$$\mathcal{I}_{nm}(r,\theta,\varphi) = \frac{1}{r^{n+1}} Y_{nm}(\theta,\varphi) \tag{1.56}$$

are obtained, where functions $\mathcal{R}_{nm}$ and $\mathcal{I}_{nm}$ are called Regular (RSH) and Irregular Solid Harmonics (ISH), respectively.

The solution to Laplace's equation is obtained by linear combination of Solid Harmonics of every degree and order, given by:

$$B_z(r,\theta,\varphi) = \sum_{n=0}^{+\infty} \sum_{m=-n}^{n} A_{nm}\mathcal{R}_{nm}(r,\theta,\varphi) + B_{nm}\mathcal{I}_{nm}(r,\theta,\varphi) \tag{1.57}$$

with coefficients A_{nm} and $B_{nm} \in \mathbb{R}$.

It is important to notice that, unlike Spherical Harmonics, Solid Harmonics are not orthogonal, neither complete. Contrarily to Spherical Harmonics, which can represent any function of θ and φ, Solid Harmonics can only represent the subspace of functions of (r,θ,φ) that obey Laplace's equation.

Particular Case: $r = 0 \in \mathcal{V}$

Naturally, within a spherical region $\mathcal{V}$, centered at $r = 0$, coefficients B_{nm} are zero for all degrees to account for the impossibility of a singularity. The magnetic field generated by the main magnet of an MRI scanner, for instance, in a spherical Region of Interest (ROI) encompassing the origin and with no magnetic source, obeys Laplace's equation and thus can be decomposed into RSH as:

$$B_z(r,\theta,\varphi) = \sum_{n=0}^{+\infty} \sum_{m=-n}^{n} A_{nm} r^n Y_{nm}(\theta,\varphi). \tag{1.58}$$

This expression contains the rationale behind magnetic field homogenization, particularly, spherical harmonics based shimming. It will be recalled in chapter 2, where detailed accounts on magnetic field shimming will be provided.

Under Dirichlet's boundary conditions, $B_z(r,\theta,\varphi)$ is known on the boundary $\mathcal{S}$, a sphere of radius R. With $r = R$, $B_z(R,\theta,\varphi)$ is a function of only θ and φ, therefore, orthogonality of spherical harmonics allows us to obtain the linear coefficients A_{nm} from the integrals:

$$A_{nm} = \begin{cases} \dfrac{2n+1}{2\pi R^n}\dfrac{(n-m)!}{(n+m)!}\displaystyle\int_0^{2\pi} d\varphi \int_0^{\pi} d\theta \sin\theta P_{nm}(\cos\theta)\cos(m\varphi)B_z(R,\theta,\varphi) & m>0 \\ \dfrac{2n+1}{4\pi R^n}\displaystyle\int_0^{2\pi} d\varphi \int_0^{\pi} d\theta \sin\theta P_{n0}(\cos\theta)B_z(R,\theta,\varphi) & m=0\,, \\ \dfrac{2n+1}{2\pi R^n}\dfrac{(n-|m|)!}{(n+|m|)!}\displaystyle\int_0^{2\pi} d\varphi \int_0^{\pi} d\theta \sin\theta P_{n|m|}(\cos\theta)\sin(|m|\varphi)B_z(R,\theta,\varphi) & m<0 \end{cases} \tag{1.59}$$

making each coefficient uniquely determined; Laplace's equation is therefore solved.

Mean Value Theorem

Applying Green's second identity (1.26) with $\Psi = B_z$ and $\Phi = G$, a Green function, we obtain:

$$B_z(\boldsymbol{x}) = \oint_{\mathcal{S}} \left(B_z \boldsymbol{\nabla}' G(\boldsymbol{x},\boldsymbol{x}')\right)\cdot d\boldsymbol{a}' - \oint_{\mathcal{S}} \left(G(\boldsymbol{x},\boldsymbol{x}')\boldsymbol{\nabla}' B_z\right)\cdot d\boldsymbol{a}'. \tag{1.60}$$

Choosing $\mathcal{S}$ to be any sphere centered at $\boldsymbol{x}$ with radius $R_{\mathcal{S}}$, and $G(\boldsymbol{x},\boldsymbol{x}') = -\frac{1}{4\pi|\boldsymbol{x}-\boldsymbol{x}'|} + \frac{1}{4\pi R_{\mathcal{S}}}$, the surface integral on the right vanishes, and the magnetic field in $\boldsymbol{x}$ is given by:

$$B_z(\boldsymbol{x}) = \frac{1}{4\pi R_{\mathcal{S}}^2}\oint_{\mathcal{S}} B_z(\boldsymbol{x}')\, da', \tag{1.61}$$

which is the average magnetic field on $\mathcal{S}$.

Our interest here is not on the theorem itself, but in a consequence: since the magnetic field at any point is equal to the average of the magnetic field around it, the extrema of any function satisfying Laplace's equation can only be located at the boundary of the domain. Thus, in the absence of magnetic field sources within some region of interest, the boundary not only holds the key for determining the spherical harmonics coefficients, but also directly hands the information on the worst field excursion within the region. If one wishes to improve field homogeneity of such a region, minimization of the peak-to-peak value on the surface guarantees lower excursions in the interior of the region. And contrarily to spherical harmonics coefficients, peak-to-peak information is readily available after field measurement.

Green's Function Expansion into Solid Harmonics

Having introduced the Solid Harmonics, a useful expansion for the Green function

$$G(\boldsymbol{x},\boldsymbol{x}') = \frac{1}{|\boldsymbol{x}-\boldsymbol{x}'|} \tag{1.62}$$

into this basis is (modified from [Jackson 2007]):

$$\begin{aligned}\frac{1}{|\boldsymbol{x}-\boldsymbol{x}'|} &= \sum_{n=0}^{+\infty}\sum_{m=-n}^{n}(2-\delta_{m0})\frac{(n-|m|)!}{(n+|m|)!}\frac{r_<^n}{r_>^{n+1}}Y_{nm}(\theta',\varphi')Y_{nm}(\theta,\varphi)\\ &= \sum_{n=0}^{+\infty}\sum_{m=0}^{n}(2-\delta_{m0})\frac{(n-m)!}{(n+m)!}\frac{r_<^n}{r_>^{n+1}}P_{nm}(\cos\theta')P_{nm}(\cos\theta)\cos m(\varphi-\varphi')\end{aligned} \tag{1.63}$$

with $r_>$ and $r_<$ being the greater or smaller of $|\boldsymbol{x}|$ and $|\boldsymbol{x}'|$. The expansion carries important information concerning spherical harmonic coefficients for this particular Green function, which is at the core of integral expressions for the magnetic field and potential. In chapter 4, this expression will be called to show that any magnetic field-generating structure located outside $\mathcal{V}$ can only generate RSH-based fields. Moreover, this expansion is a powerful tool, put to good use in the work of [Roméo 1984] on the analytical design of field-correcting structures.

1.1.5 Stream Functions

Perhaps first introduced by Lagrange [Lagrange 1869] in his study of uncompressible flow of matter, the concept of stream function (SF), represented by scalar functions which can describe divergence-less vector fields, is very convenient for analyzing electric current flow in magnetostatics. In particular, it is a useful tool in inverse problems aiming to obtain the optimal current density that generates a target field, and it will be called in chapters 3 and 5.

Although a less common topic in electromagnetism textbooks, Emile Durand describes these functions in detail throughout his book entitled *Magnétostatique* [Durand 1968]. It lays out the required conditions for defining a stream function (denominated current function in his book) and presents an analysis that is not limited to divergence-less current densities.

A more recent reference showing the use of stream functions for inverse problem solving in coil design is the work of [Peeren 2003], where a formal treatment of SF is presented.

We introduce here the essential characteristics of SF required for this work, and refer the reader to the two aforementioned references for further detail.

Divergence-Less Current Density and Associated Stream Function

As already stated, in magnetostatic, current densities are divergence-less. We will be particularly interested in current densities over arbitrary surfaces $\mathcal{S}\subset\mathbb{R}^3$. In this case, the definition of the divergence for the vector field $\boldsymbol{j}(\boldsymbol{x})$ on $\mathcal{S}$ is

$$\boldsymbol{\nabla}\cdot\boldsymbol{j}(\boldsymbol{x}) = \lim_{|A(\boldsymbol{x})|\to 0}\frac{1}{A(\boldsymbol{x})}\oint_C \boldsymbol{j}(\boldsymbol{x}')\cdot(d\boldsymbol{x}'\times\hat{\boldsymbol{n}}(\boldsymbol{x}')), \tag{1.64}$$

with C an arbitrary curve around $\boldsymbol{x}$ and $A(\boldsymbol{x})$ the area enclosed by the curve. With zero divergence

$$\lim_{|A(\boldsymbol{x})|\to 0}\frac{1}{A(\boldsymbol{x})}\oint_C \boldsymbol{j}(\boldsymbol{x}')\cdot(d\boldsymbol{x}'\times\hat{\boldsymbol{n}}(\boldsymbol{x}')) = 0, \tag{1.65}$$

or

$$\lim_{|A(\boldsymbol{x})|\to 0} \frac{1}{A(\boldsymbol{x})} \oint_C (\hat{\boldsymbol{n}}(\boldsymbol{x}') \times \boldsymbol{j}(\boldsymbol{x}')) \cdot d\boldsymbol{x}' = 0, \tag{1.66}$$

which can be satisfied if

$$\hat{\boldsymbol{n}}(\boldsymbol{x}) \times \boldsymbol{j}(\boldsymbol{x}) = \boldsymbol{\nabla}\psi(\boldsymbol{x}), \tag{1.67}$$

where $\psi(\boldsymbol{x})$ is some scalar function defined on $\mathcal{S}$, and denominated stream function (SF). This expression leads to the constitutive relation

$$\boldsymbol{j}(\boldsymbol{x}) = \boldsymbol{\nabla}\psi(\boldsymbol{x}) \times \hat{\boldsymbol{n}}(\boldsymbol{x}), \tag{1.68}$$

which links the vector field to its associated stream function.

Alternatively, we see that the SF can be computed from $\boldsymbol{j}(\boldsymbol{x})$ as

$$\psi(\boldsymbol{x}) = \int_{\boldsymbol{a}}^{\boldsymbol{x}} \boldsymbol{j}(\boldsymbol{x}') \cdot (d\boldsymbol{x}' \times \hat{\boldsymbol{n}}(\boldsymbol{x}')), \tag{1.69}$$

with $\boldsymbol{a} \in \mathcal{S}$ and $\psi(\boldsymbol{a}) = 0$, an arbitrary choice that won't alter the physical quantity of interest, which is $\boldsymbol{j}(\boldsymbol{x})$.

With current flow being confined within the boundaries of the surface $\mathcal{S}$, another condition can be imposed on the stream function. Let $\mathcal{S}$ be delimited by boundaries $\partial\mathcal{S}_i$, no electric current should flow through the boundaries, leading to

$$(\boldsymbol{\nabla}\psi \times \hat{\boldsymbol{n}}) \cdot \boldsymbol{\tau} = 0, \tag{1.70}$$

where $\boldsymbol{\tau}$ is an unitary vector perpendicular to the boundary and to $\hat{\boldsymbol{n}}$. This leads to

$$\boldsymbol{\nabla}\psi \cdot (\hat{\boldsymbol{n}} \times \boldsymbol{\tau}) = 0, \tag{1.71}$$

which is the directional derivative of ψ along the boundary. As such, $\psi(\partial\mathcal{S}_i) = C_i$, with C_i being a constant, for all boundaries of the surface $\mathcal{S}$.

Finally, we can show that the current flow through a line connecting any two points $\boldsymbol{x}_1$ and $\boldsymbol{x}_2$ in $\mathcal{S}$ is

$$I_{12} = \int_{\boldsymbol{x}_1}^{\boldsymbol{x}_2} \boldsymbol{j}(\boldsymbol{x}) \cdot (d\boldsymbol{x} \times \hat{\boldsymbol{n}}(\boldsymbol{x})) = \psi(\boldsymbol{x}_2) - \psi(\boldsymbol{x}_1). \tag{1.72}$$

Discretization into Windings

The interest in stream functions is twofold. First, it simplifies the inverse problem of finding an optimal current density vector into that of obtaining a scalar function. Second, as we will see, the stream function is a convenient tool for easily discretizing the current density $\boldsymbol{j}(\boldsymbol{x})$ into windings for building an actual coil that will best approximate the ideal current distribution $\boldsymbol{j}(\boldsymbol{x})$.

Given two SF isolevels (cf. Fig. 1.3), each with coordinates such that $\psi(\boldsymbol{x}) = \psi_1$ and $\psi(\boldsymbol{x}) = \psi_2$, the current flow $I = \psi_2 - \psi_1$ within those levels can be approximated by a current I flowing in the path defined by coordinates $\boldsymbol{x}$ such that $\psi(\boldsymbol{x}) = (\psi_1 + \psi_2)/2$ [Peeren 2003].

Obtaining all the stream function isolevels such that the difference between neighbor levels is the current I, all wirepaths can be defined and the surface current density is therefore discretized into windings and can be translated into a real coil.

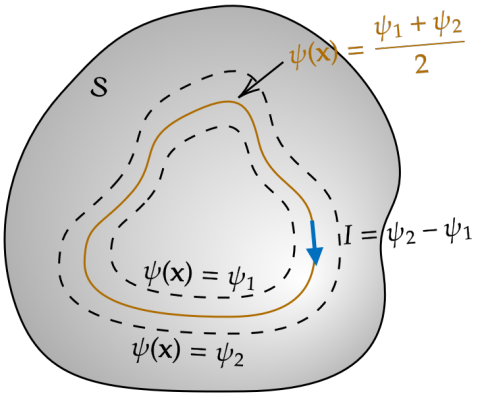

Figure 1.3 – Stream Function over an arbitrary surface.

1.2 The Main B0 Field in MRI and Susceptibility Induced Inhomogeneity

1.2.1 The Main B0 Field

As it will be shown shown in this section, MRI relies on highly uniform magnetic fields. However, a perfectly homogeneous magnetic field in the air, although theoretically possible, is practically impossible. Nevertheless, great effort is done to ensure highly homogeneous magnetic fields in a spherical or elliptical ROI of typically 20 cm (for head imaging).

MRI requires an intense main magnetic field, called the B_0 field. Most modern scanners employ fields of 1.5 T and 3.0 T, and higher intensity 7 T scanners, already employed for many years in research, are starting to find their place in clinical practice.

The Main Magnet

The generation of such strong magnetic fields is challenging, not only to achieve the high field intensity required, but also to provide sufficient homogeneity in a useful scanning region. These magnetic fields need to be generated by superconducting [Iwasa 2009] coils, usually presenting a design such as shown in Fig. 1.4. The gold standard metric for homogeneity provided by some magnet design is the peak-to-peak difference $((B_{\max} - B_{\min})/B_0)$, given in ppm, of the magnetic field over a spherical or elliptical surface. This can be seen as a consequence of the Mean Value Theorem, as it assures that worst field excursion within some region where the magnetic field respects Laplace's equation will be located on the boundary of the region.

Magnet design is carried out such that a large Diameter of Spherical Volume (DSV) of typically around 50 cm has inhomogeneity of a few ppm units [Wang 2013]. However, deviations in fabrication and interaction with the environment will cause the real magnetic field to be degraded in homogeneity. Correction fields will need to be applied to bring the magnet back within specification.

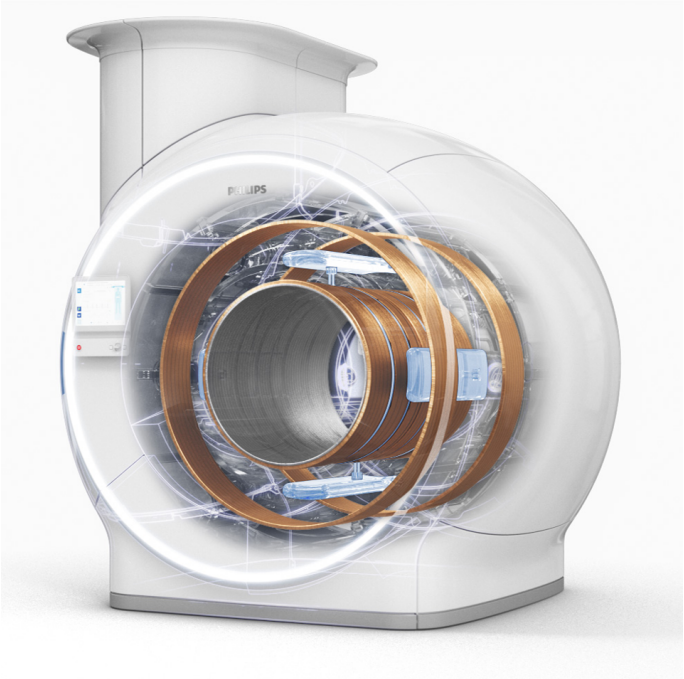

Figure 1.4 – Typical magnet design. From philips.com.

From a RSH expansion perspective (section 1.1.4), the magnetic field, designed to be dominated by the zeroth degree component, will now present non-zero RSH coefficients due to the aforementioned deviations.

Magnet Shimming

Correction of the inhomogeneous magnetic field is carried out through a process called *Shimming* [Chmurny 1990], which received its name from optimally positioning ferromagnetic pieces, known as shims, on the surface of early permanent magnets initially employed in NMR and MRI.

We will leave a more detailed discussion on shimming to the next chapter, with particular interest in shimming susceptibility-induced inhomogeneity (explained in the next subsection). Suffice to say for the time being that shimming is accomplished by the generation of magnetic fields that, when added up to the main field, will zero-out or greatly reduce RSH coefficients up to a certain degree. This is accomplished either by *active* shimming using coils generating RSH field shapes of various degrees and orders, or by *passive* shimming, judiciously placing ferromagnetic pieces around the cylindrical MRI bore such that, when magnetized by the main magnetic field, they will generate a magnetic field acting to zero-out the non-zero degree RSH coefficients. An interesting account of passively shimming a highly inhomogeneous magnet is provided in [Hoult 1998].

To give some figures, after the design and homogenization steps, the resulting inhomogeneity in a 3 T MRI scanner is expected to be less than 1.8 ppm in a 50 cm × 50 cm × 45 cm air-filled region [Webb 2016]. But as we will see, insertion of a patient inside this homogeneous magnetic field will be a source of inhomogeneity.

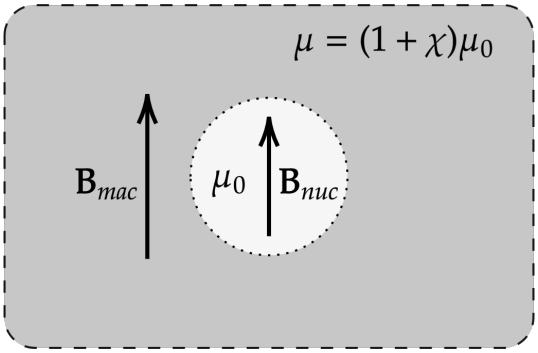

Figure 1.5 – Representation of the conceptual sphere of Lorentz, used to calculate the magnetic field experienced by the nucleus. The rationale consists in subtracting the contribution of the nucleus itself in the macroscopic field, such that we obtain the field inside the sphere that is imposed by sources external to it. It is calculated considering a sphere of magnetic permeability μ_0 surrounded by a medium of magnetic susceptibility χ. Such a configuration can be shown to present a nuclear field given by equation 1.73.

1.2.2 Susceptibility-Induced Inhomogeneity and Inhomogeneous Field Pattern in the Human Brain

When a subject, or sample, is placed in a magnetic field, the different materials composing it become magnetized (equation 1.8). The magnetized media, in turn, will produce a magnetic field of their own, as predicted by equations 1.44 or 1.47, adding up to the previously homogeneous (or almost homogeneous) MRI field. This phenomenon gives rise to the sample induced inhomogeneity, at the origin of the infamous B_0 related artifacts which we aim to mitigate in this work.

To calculate such inhomogeneous magnetic field, the macroscopic magnetization can be approximated by $\boldsymbol{M}(\boldsymbol{x}) \approx (\chi(\boldsymbol{x})/\mu_0)B_0\hat{\boldsymbol{z}}$; the magnetic potential and subsequent macroscopic magnetic field can then be computed. Maxwell's equations, however, provide bulk properties of the material, and to obtain the magnetic field experienced by the nuclei, the conceptual "sphere of Lorentz" (cf. Fig. 1.5) [Durrant 2003] must be employed, leading to a field

$$\boldsymbol{B}_{nuc}(\boldsymbol{x}) = \left(1 - \frac{2}{3}\chi(\boldsymbol{x})\right)\boldsymbol{B}_{mac}(\boldsymbol{x}) \tag{1.73}$$

"felt" by the nucleus. Where $\boldsymbol{B}_{mac}$ is the surrounding magnetic field supposedly constant in close vicinity of the point of interest.

As an alternative to the integral-based computation, which can be time consuming and inconvenient when dealing with susceptibility discontinuities on the boundaries between different media, several fast computation approaches have been proposed to estimate sample-induced magnetic fields. The works of [Salomir 2003] and [Marques 2005] proposed fast Fourier Transform (FT) based approaches, subsequently assessed in-vivo by [Koch 2006c]. Those methods are easy to implement and rely on FT of the magnetic

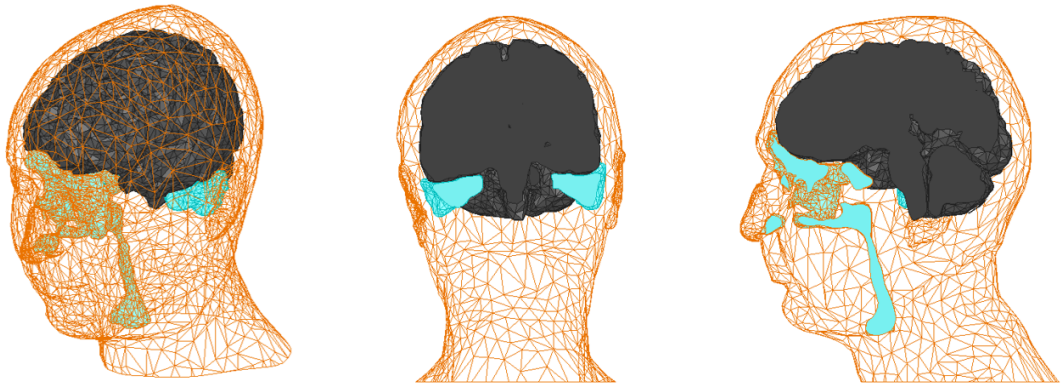

Figure 1.6 – Different views of a high resolution 3D model of a realistic human head. Air cavities in the head corresponding to ear canals and sinuses are shown in light blue, with the brain shown in dark gray.

susceptibility distribution in space, such that

$$\delta B_0(\boldsymbol{x}) = B_0 \, \mathcal{F}^{-1} \left\{ \left(\frac{1}{3} - \frac{k_z^2}{k^2} \right) \mathcal{F} \{\chi\} \right\}, \tag{1.74}$$

with $\boldsymbol{k} = (k_x, k_y, k_z)$ the coordinates in the transformed spatial-frequency space.

Brought back to the space domain, expression 1.74 becomes

$$\nabla^2 \delta B_0 = \left(\nabla^2 \chi - 3 \frac{\partial^2 \chi}{\partial z^2} \right) \frac{B_0}{3}. \tag{1.75}$$

It shows that the δB_0 intensity grows linearly with the applied magnetic field, and also that susceptibility gradients act as sources of field inhomogeneity. Since it is a Poisson's equation, we can also infer that inhomogeneity will be stronger closer to the regions were susceptibility gradients appear, and should decrease at greater distances.

Magnetic Field Distribution in the Human Brain at Ultra-High Field

To obtain the expected magnetic field distribution in the human brain, we apply the generalized Susceptibility Voxel Convolution (gSVC) method [Lee 2018], an improved FT-based δB_0 calculation method. This method improves accuracy by considering a cubic kernel (instead of spherical) for evaluating the magnetic field contribution from each voxel, leading to reduced aliasing issues intrinsic to the previously proposed methods, which would require oversampling or zero-padding for increased accuracy if compared to gSVC.

The gSVC method is applied to a realistic 3D model of the human head [Makris 2008] (cf. Figure 1.6) discretized into a rectangular grid of 1 mm isotropic resolution. The original 3D model presents detailed segmentation of different tissues in the head, but for the purposes of this simulation, the only distinction required will be between "tissue" and "air", as these present the more significant difference in terms of susceptibility. Air and tissue magnetic susceptibilities were set to $\chi_{\text{air}} = 0.36 \times 10^{-6}$ and $\chi_{\text{tis}} = -9.03 \times 10^{-6}$, respectively.

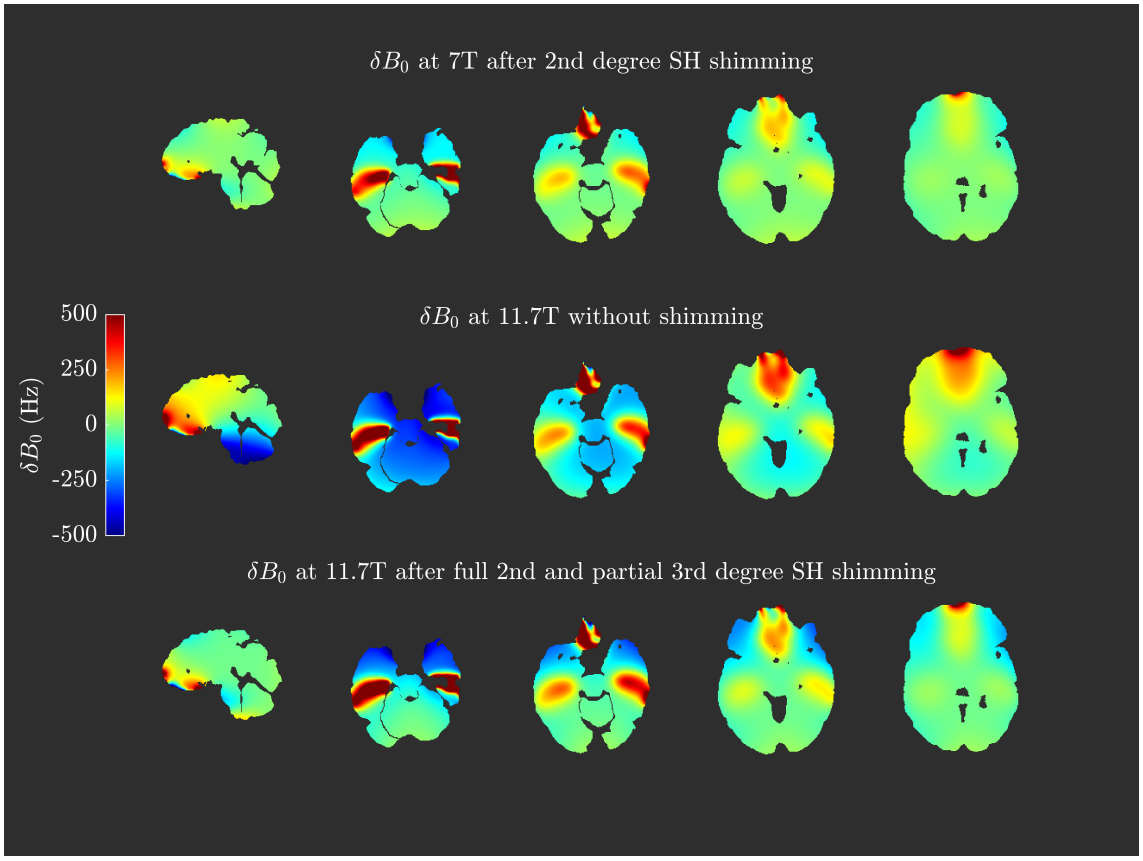

Figure 1.7 – δB_0 maps for different slices at different magnetic fields and SH shimming degrees. From left to right: sagittal slice in the middle of the brain, axial slices starting above the ear canals and moving in the dorsal direction spaced by 10 mm steps.

Simulations are performed considering magnetic fields of 7 T and 11.7 T. The magnetic field inhomogeneity obtained at 7 T is then shimmed with spherical harmonics up to 2^{nd} degree, which is commonly available in commercial UHF scanners. At 11.7 T, spherical harmonic shimming is performed considering full 2^{nd} degree and partial 3^{rd} degree, with a total of 4 third degree coils (of degree and orders [3,0],[3,-1],[3,1] and [3,2]), as will be available in the Iseult magnet. Thus, magnetic field inhomogeneity expected at the ultra-high fields of 7 T (commercially available MRI) and 11.7 T (Iseult magnet) can be compared.

The resulting fieldmaps at selected slices are shown in Fig.1.7. The highest intensity field excursions are observed in the ventral region of the brain, particularly in the prefrontal cortex (PFC) and temporal lobes (TL). Inhomogeneity then diminishes as we move to the dorsal region. The overall behavior is consistent to what would be expected from equation 1.75, higher field excursion is observed next to air/tissue interfaces.

It is also observed that, despite having four extra shim coils, expected field excursion "hotspots" will be more intense at 11.7 T.

In Fig.1.8, a histogram of the magnetic field excursion across voxels in the brain is provided for both magnetic fields. A greater spread is observed at 11.7 T, with a significant presence of high field excursion across voxels, as expected from observation of the

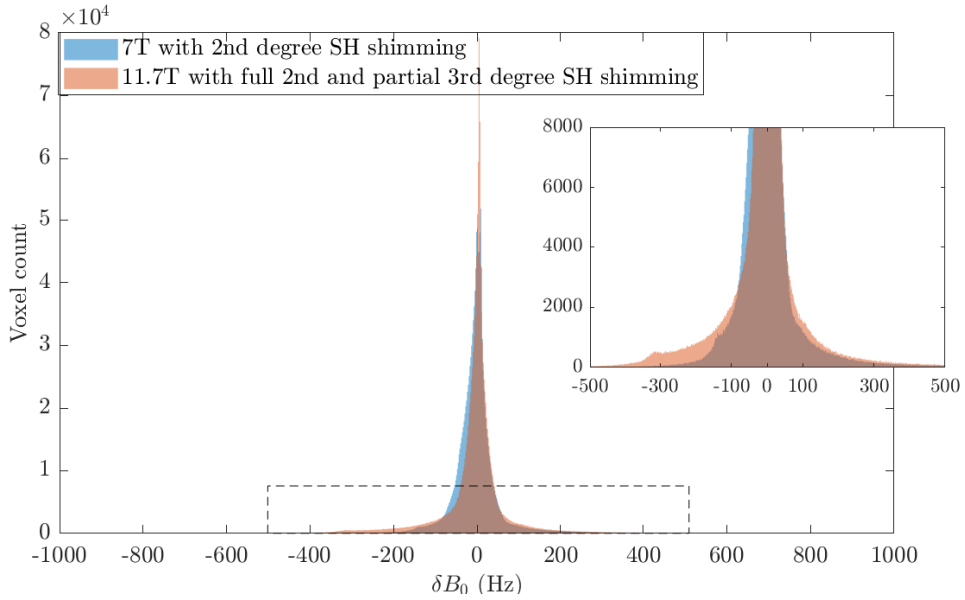

Figure 1.8 – Histogram of magnetic field excursion across voxels in the brain at 7 T and 11.7 T. A zoom within the dashed region is provided for detailed assessment.

fieldmaps.

Inhomogeneity Metrics

To properly quantify the inhomogeneity observed in those fieldmaps, or in any fieldmap, several metrics can be employed. The choice of which metric to use will depend on the application. The standard deviation of the field excursion across voxels in the ROI will be the most commonly employed metric in imaging applications, whereas the linewidth or Full Width at Half Maximum (FWHM) [Kreis 2020] is preferred to describe the shim quality in spectroscopic applications. No metric alone, however, can convey a full picture of the B_0 quality in a ROI; therefore we briefly review some of the most commonly used metrics and apply them to the fieldmaps at hand.

For a K-voxel ROI, the global inhomogeneity is given by

$$\sigma_{\delta B_0} = \sqrt{\frac{1}{K-1}\sum_{k=1}^{K}\left(\delta B_{0k} - \mu_{\delta B_0}\right)^2} \tag{1.76}$$

with

$$\mu_{\delta B_0} = \frac{1}{K}\sum_{k=1}^{K}\delta B_{0k}. \tag{1.77}$$

The lower the SD, the more homogeneous the magnetic field in the ROI is. This metric is preferred relatively to the L_2 norm. It provides an indication of the spread of δB_0 while being robust to eventual B_0 offsets that can be corrected by frequency adjustment of the MRI scanner. It is usually given in Hz, after multiplication by the gyromagnetic ratio γ_{H} for the ^{1}H proton, or in ppm. The choice of unity will depend on the message being conveyed. For instance, it is more convenient to use Hz when analyzing an artifact such

Table 1.1 – Compilation of inhomogeneity metrics, from simulated fieldmaps, for the magnetic field distribution in the human brain when under 7 T and 11.7 T main magnetic fields, and shimmed by different SH coil sets.

Fieldmap	σ Hz	p_{100} %	s_{80} Hz	s_{90} Hz	s_{95} Hz	s_{98} Hz
7 T with 2nd degree SH shimming	72.5	7.8	47.9	82.0	134.2	225.7
11.7 T with no shimming	197.1	50.7	191.9	336.5	450.9	523.3
11.7 T with partial 3rd degree SH shimming	118.6	14.5	66.8	143.8	242.7	370.6

as geometric distortion, whose intensity depends mainly on the field excursion absolute intensity (cf. section 1.3).

For the human brain, this metric can be applied either to the whole brain, or to a specific ROI, such as brain regions (PFC, TL) or specific slices. This would provide further information on where the employed shimming technique is more effective, or where inhomogeneity is more intense.

The field excursion distribution in the brain being non-Gaussian, $\sigma_{\delta B_0}$ alone doesn't provide all the information on the field distribution. Other metrics such as the frequency range containing some percentage of ROI voxels can also be employed [Juchem 2011, Stockmann 2018] to provide complementary information on the homogeneity quality. We then define the metric s_p as the lowest frequency value superior to the absolute field excursion of p percent of voxels in the ROI.

As it will be reviewed in section 1.3, each acquisition sequence is more or less sensitive to B_0 inhomogeneity. There can be field excursion values above which information will be lost, therefore it might also be useful to compute the percentage p_{f_c} of voxels whose absolute field excursion is superior to a critical frequency f_c in Hz.

Still under a range perspective, peak-to-peak range $\delta B_{0_{pp}}$ is yet another option, although not commonly employed in the analysis of sample-induced inhomogeneity.

Inhomogeneity at 7 T and 11.7 T

For the simulated magnetic fields in the above 3D model, we obtain $\sigma_{7\,\mathrm{T,SH_2}} = 72.5\,\mathrm{Hz}$, $\sigma_{11.7\,\mathrm{T}} = 197.1\,\mathrm{Hz}$ and $\sigma_{11.7\,\mathrm{T,SH_{2+}}} = 118.6\,\mathrm{Hz}$ in our brain model. These inhomogeneities confirm what was observed in the fieldmaps and field excursion histograms. Despite the presence of SH shim coils up to partial 3rd degree, and the significant inhomogeneity reduction from the unshimmed to shimmed field at 11.7 T, the final inhomogeneity is still vastly superior to that at 7 T. A compilation of metrics is shown in table 1.1.

All other metrics presented also point to much worse inhomogeneity at 11.7 T. Particularly, the p_{100} indicates almost double the amount of voxels over 100 Hz, which we will see can cause severe image distortion.

As we will see, in clinical routine, there is no need to estimate the magnetic field based on the head geometry, since a fieldmap can be reconstructed from a Gradient Recalled Echo (GRE) acquisition. These methods, however, can be very helpful when analyzing passive shimming approaches, as they can easily predict the behavior of some diamagnetic material (such as bismuth) placed close to the zones of high inhomogeneity.

1.3 Magnetic Resonance Imaging Under B0-Related Imperfections

In this section, we recall the theoretical basis for MRI, accompanied by mathematical descriptions of the degrading effects related to the main magnetic field inhomogeneity.

1.3.1 Nuclear Magnetic Resonance

The hydrogen proton possesses intrinsic $\frac{1}{2}$-spin. The spin is an observable in quantum mechanics described by the Pauli spin matrices [Griffiths 2017]. From these matrices, one observes two possible states for the spin, $S_\pm = \pm\hbar/2$. Associated to the spin state is a magnetic moment

$$\boldsymbol{\mu} = \gamma \boldsymbol{S}, \tag{1.78}$$

where γ is the gyromagnetic ratio. This ratio is a multiple of the nuclear magnetom ($\mu_N = e\hbar/2m_p$), with e the charge of the electron and m_p the proton mass. When immersed in the B_0 magnetic field, assumed to be oriented in the z-axis, the spins in a sample will be directed along the z-axis and two possible energy states

$$E_\pm = \pm\frac{\hbar\gamma B_0}{2} \tag{1.79}$$

appear (with energies calculated from 1.42). They correspond to parallel (negative energy) and anti-parallel (positive energy) spin states relative to the B_0 field. The states have an energy gap $\Delta E = \hbar\gamma B_0$.

Due to the energy gap, according to the Boltzmann distribution, the amount of spins in each state is not the same, and this will engender, for half-spin nuclei, a net nuclear magnetization [Abragam 2007]

$$M_0 \approx \rho\frac{\gamma^2\hbar^2}{4k_BT}B_0, \tag{1.80}$$

where ρ is the spin density, k_B is the Boltzmann constant and T the sample temperature in Kelvin.

As body tissues are mostly composed of water and fat molecules, ^{1}H protons are abundant in the human body. Therefore, their magnetization will be stronger than that of other nuclei, which makes ^{1}H the most commonly employed nucleus for MRI. Its gyromagnetic ratio is $\gamma_{\mathrm{H}} = 42.58\,\mathrm{MHz\,T^{-1}}$. Notice at this point that ppm variations in the magnetic field will barely affect the resulting equilibrium magnetization. Magnetization will vary mostly according to the water content in each tissue, leading to a spatial distribution of $\rho(\boldsymbol{x})$, which we will eventually transform into an image.

The bulk magnetization can be manipulated by the application of specifically tailored magnetic fields. Its dynamics is described by the Bloch equation [Bloch 1946]

$$\frac{d\boldsymbol{M}}{dt} = \gamma \boldsymbol{M} \times \left(\boldsymbol{B} - \frac{\Omega}{\gamma}\hat{\boldsymbol{z}} \right) - \frac{M_{x'}\hat{\boldsymbol{x}}' + M_{y'}\hat{\boldsymbol{y}}'}{\mathrm{T}_2} - \frac{M_z - M_0}{\mathrm{T}_1}\hat{\boldsymbol{z}}, \tag{1.81}$$

with $\boldsymbol{M}(\boldsymbol{x},t) = M_{x'}(\boldsymbol{x},t)\hat{\boldsymbol{x}}' + M_{y'}(\boldsymbol{x},t)\hat{\boldsymbol{y}}' + M_z(\boldsymbol{x},t)\hat{\boldsymbol{z}}$. The equation is presented here in a rotational frame $(\hat{\boldsymbol{x}}', \hat{\boldsymbol{y}}', \hat{\boldsymbol{z}})$, convenient for NMR and MRI analysis, with $\Omega\hat{\boldsymbol{z}}$ the vector about which the original laboratory frame $(\hat{\boldsymbol{x}}, \hat{\boldsymbol{y}}, \hat{\boldsymbol{z}})$ is made to rotate with angular velocity Ω. Constants T_1 and T_2 are the spin-lattice and spin-spin relaxation times, respectively. They are related to interactions of spins with their surroundings and will cause any magnetization component not in the main magnetic field direction to exponentially vanish with T_2 time constant, while the longitudinal magnetization grows to the equilibrium magnetization M_0 with T_1 time constant. Spatial dependency of the quantities were omitted in the equation for simplicity, but in a non-uniform sample, T_1, T_2 and $\boldsymbol{B}$ vary spatially.

In the presence of magnetic field inhomogeneity, the T_2 term actually needs to be changed to the T_2^* ($< \mathrm{T}_2$). The T_2^* is related to a faster decay of the transverse magnetization caused by loss of phase coherence induced by macroscopic and mesoscopic B_0 inhomogeneity. This loss of phase coherence can actually be recovered by the use of spin-echo sequences, thus obtaining a T_2-weighted signal, but as we will see in section 1.3.3, T_2^*-weighting due to mesoscopic magnetic changes in the environment is required in functional MRI (fMRI), thus the macroscopic inhomogeneity will need to be corrected to enhance the mesoscopic effects.

Excitation

The sample can be excited by sending a RF pulse with carrier wave tuned to some frequency ω_{RF} equal or close to the Larmor frequency. We can conveniently analyze what happens in the sample in the rotational frame with $\Omega = \omega_{RF}$. Thus, in addition to the main magnetic field $B_0\hat{\boldsymbol{z}}$ and non-uniform $\Delta B_0(\boldsymbol{x})\hat{\boldsymbol{z}}$ containing controlled gradient fields (section 1.3.2) and δB_0 inhomogeneity, we apply the RF magnetic field

$$\boldsymbol{B}_1^+(t) = B_1^+(t)(\cos\varphi_{RF}\hat{\boldsymbol{x}}' + \sin\varphi_{RF}\hat{\boldsymbol{y}}') \tag{1.82}$$

assumed to be symmetric in time, centered at $t = 0$, during a short period of time $\tau_{RF} \ll \mathrm{T}_1, \mathrm{T}_2$. Considering initial magnetization

$$\boldsymbol{M}\left(\boldsymbol{x}, -\frac{\tau_{RF}}{2}\right) = M_0(\boldsymbol{x})\hat{\boldsymbol{z}}, \tag{1.83}$$

and assuming that $M_z(t) \approx M_0$, the resulting transverse magnetization in the rotational frame can be shown to be (in phasor notation $M_+ = M'_x + \imath M'_y$)

$$M_+\left(\boldsymbol{x}, \frac{\tau_{RF}}{2}\right) = \imath\gamma M_0(\boldsymbol{x}) e^{\imath\left(\varphi_{RF} - \Delta\omega\frac{\tau_{RF}}{2}\right)} \int_{-\frac{\tau_{RF}}{2}}^{\frac{\tau_{RF}}{2}} B_1^+(t) e^{i\Delta\omega t}\, dt, \tag{1.84}$$

with $\Delta\omega$ defined as

$$\Delta\omega = \gamma B_0 + \gamma\Delta B_0 - \omega_{RF}. \tag{1.85}$$

Figure 1.9 – Failed inversion artifact in the inferior frontal cortex, a zone known to have strong B_0 inhomogeneity. Image from [Damme 2021].

The assumption of small variation in the longitudinal magnetization is called small tip angle approximation. The flip angle (FA) under this approximation is defined as

$$\alpha = \arcsin \frac{|M_+|}{|M_0|} \approx \gamma \left| \int_{-\frac{\tau_{RF}}{2}}^{\frac{\tau_{RF}}{2}} B_1^+(t) e^{i\Delta\omega t}\, dt \right| \tag{1.86}$$

which was actually shown to be a good approximation for a FA up to 90° [Boulant 2012].

The magnetization is therefore flipped by an angle α relatively to the main magnetic field. If we set $\omega_{RF} = \gamma B_0$ and $\Delta B_0 = 0$, a homogeneous excitation will be observed in the sample and the FA is seen to be proportional to the DC component of the RF pulse.

In the presence of magnetic field inhomogeneity δB_0, equation 1.86 states that the excitation profile will depend on the spectral content of B_1^+. An almost uniform FA could be imposed throughout the entire sample as long as the pulse is broadband or *non-selective*, such as a short-duration rectangular pulse. A rectangular pulse could very well provide small flip angles everywhere in the sample, but 180° pulses are sometimes needed to enhance contrast in Inversion Recovery sequences. If the rectangular pulse is kept short to guarantee non-selectivity, the B_1^+ intensity must rise, which would lead to intense power deposition in the sample, disrespecting Specific Absorption Rate (SAR) limits. If the rectangular pulse is stretched in time to reduce average power deposition, the profile becomes more and more *selective*, and regions with strong δB_0 excursion will suffer from failed inversion. This causes known hyper-signal image artifacts in T_1-weighted MP-RAGE (cf. Fig. 1.9), which occur even with adiabatic pulses presumably robust to B_0 field inhomogeneity but also prone to SAR limitation issues at UHF.

Precession

Once the magnetization flipped and the RF field turned off, magnetization evolution can once again be described by solving Bloch's equation, but this time taking relaxation effects into account and staying in the laboratory frame (i.e. $\Omega = 0$).

Let $M_+(\boldsymbol{x}, 0) = M_0(\boldsymbol{x}) \sin\alpha e^{\imath\varphi_0(\boldsymbol{x})}$ be the transverse and $M_z(\boldsymbol{x}, 0) = M_0(\boldsymbol{x}) \cos\alpha$ the longitudinal magnetization after excitation, with $\varphi_0(\boldsymbol{x})$ incorporating the initial phase distribution after excitation, their time evolution as obtained from Bloch's equation is

$$M_+(\boldsymbol{x}, t) = M_x(\boldsymbol{x}, t) + \imath M_y(\boldsymbol{x}, t) = M_+(\boldsymbol{x}, 0) e^{-\frac{t}{\mathrm{T}_2(\boldsymbol{x})}} e^{-\imath\gamma(B_0 + \Delta B_0(\boldsymbol{x}))t}, \tag{1.87}$$

$$M_z(\boldsymbol{x}, t) = M_z(\boldsymbol{x}, 0) e^{-\frac{t}{\mathrm{T}_1(\boldsymbol{x})}} + M_0(\boldsymbol{x}) \left(1 - e^{-\frac{t}{\mathrm{T}_1(\boldsymbol{x})}}\right). \tag{1.88}$$

This solution is a counter-clockwise precessing magnetization about the z-axis, with the transverse component decaying with the spin-spin relaxation rate, and the longitudinal component growing back to the equilibrium net magnetization M_0 with the spin-lattice relaxation rate.

In the absence of ΔB_0, we see that the precession will occur at the so-called Larmor frequency $\omega_0 = \gamma B_0$. Which is the natural, *resonant* frequency of the spins.

Reciprocity and the NMR Signal

As we know from equation 1.44, magnetization produces a magnetic field. A time-varying magnetization as the one obtained after solving Bloch's equation would produce a time-varying magnetic field, which can induce an electric voltage $\mathcal{E}$ in some arbitrary loop $\mathcal{C}$ as predicted by Faraday's law. Therefore

$$\begin{aligned}
\oint_{\mathcal{C}} \boldsymbol{E} \cdot d\boldsymbol{x} = \mathcal{E} &= -\frac{\partial}{\partial t} \int \boldsymbol{B} \cdot d\boldsymbol{a} \\
&= -\frac{\partial}{\partial t} \int \boldsymbol{\nabla} \times \boldsymbol{A} \cdot d\boldsymbol{a} \\
&= -\frac{\partial}{\partial t} \oint_{\mathcal{C}} \boldsymbol{A} \cdot d\boldsymbol{x} \\
&= -\frac{\partial}{\partial t} \oint_{\mathcal{C}} \left(\frac{\mu_0}{4\pi} \int_{\mathcal{V}_s} \frac{\boldsymbol{M}(\boldsymbol{x}') \times (\boldsymbol{x} - \boldsymbol{x}')}{|\boldsymbol{x} - \boldsymbol{x}'|^3} d^3x' \right) \cdot d\boldsymbol{x} \\
&= -\frac{\partial}{\partial t} \int_{\mathcal{V}_s} \boldsymbol{M}(\boldsymbol{x}') \cdot \left(\oint_{\mathcal{C}} \frac{\mu_0}{4\pi} \frac{d\boldsymbol{x} \times (\boldsymbol{x}' - \boldsymbol{x})}{|\boldsymbol{x}' - \boldsymbol{x}|^3} \right) d^3x' \\
&= -\frac{\partial}{\partial t} \int_{\mathcal{V}_s} \boldsymbol{M}(\boldsymbol{x}') \cdot \boldsymbol{\mathcal{B}}(\boldsymbol{x}')\, d^3x'
\end{aligned} \tag{1.89}$$

where $\boldsymbol{\mathcal{B}}$ is the magnetic field that would be produced by the receiving loop in the sample region $\mathcal{V}_s$ should a unit current circulate in that loop. This shows that the signal induced by the precessing magnetization in the loop $\mathcal{C}$ actually depends on the magnetic field that the loop would generate on the sample, thus the name Reciprocity Principle [Hoult 1976].

Let $\boldsymbol{\mathcal{B}}(\boldsymbol{x}) = \mathcal{B}(\boldsymbol{x}) \cos\theta_{\mathcal{B}}(\boldsymbol{x})\hat{\boldsymbol{x}} + \mathcal{B}(\boldsymbol{x}) \sin\theta_{\mathcal{B}}(\boldsymbol{x})\hat{\boldsymbol{y}}$ for some arbitrary receive coil; then the signal from a precessing magnetization as in equation 1.87, calculated from equation 1.89,

boils down to

$$s(t) \approx \omega_0 \int_{\mathcal{V}_s} e^{-\frac{t}{\mathrm{T}_2(\boldsymbol{x})}} |M_+(\boldsymbol{x},0)|\, \mathcal{B}(\boldsymbol{x}) \sin\left(\gamma(B_0 + \Delta B_0(\boldsymbol{x}))t + \theta_{\mathcal{B}}(\boldsymbol{x}) - \varphi_0(\boldsymbol{x})\right) d^3x, \quad (1.90)$$

which is the Free Induction Decay (FID) [Hahn 1950]. It is the response received from the sample after excitation, which ceases after total decay of the transverse magnetization.

Demodulation of the FID with a frequency Ω leads to

$$s(t) \approx \omega_0 \int_{\mathcal{V}_s} e^{-\frac{t}{\mathrm{T}_2(\boldsymbol{x})}} |M_+(\boldsymbol{x},0)| \mathcal{B}(\boldsymbol{x}) e^{\imath((\Omega - \gamma B_0 - \gamma \Delta B_0(\boldsymbol{x}))t + \varphi_0(\boldsymbol{x}) - \theta_{\mathcal{B}}(\boldsymbol{x}))} d^3x. \quad (1.91)$$

If $\Omega = \omega_0$, in a uniform sample with uniform $\mathcal{B}$ and $\Delta B_0(\boldsymbol{x}) = 0$, the signal becomes

$$s(t) \approx \omega_0 M_0 \mathcal{B} \sin\alpha V_s e^{-\frac{t}{\mathrm{T}_2}} = \frac{\rho V_s \gamma^3 \hbar^2 \sin\alpha}{4 k_B T} \mathcal{B} e^{-\frac{t}{\mathrm{T}_2}} B_0^2. \quad (1.92)$$

This expression shows the explicit increase in intrinsic signal with the increase of the main magnetic field. Although a quadratic relation is observed, it does not take into account the losses in the receive coil and receive chain, nor physiological noise, which will make the SNR still present a supralinear evolution with the magnetic field, but actually of $B_0^{1.65}$ [Pohmann 2016]. This highlights the interest in moving to higher magnetic fields.

This signal has power spectral density (PSD)

$$|S(\omega)|^2 \propto \frac{{\mathrm{T}_2}^2}{1 + {\mathrm{T}_2}^2 \omega^2}, \quad (1.93)$$

which is a Cauchy distribution. This expression can be used to estimate the T_2 value for a sample, given by

$$\mathrm{T}_2 = \frac{1}{\pi \mathrm{FWHM}}. \quad (1.94)$$

Where in this case, the FWHM is for a perfectly shimmed sample.

If the precessing magnetization has natural frequency other than ω_0, say shifted by $\sigma\omega_0$, with σ in ppm, its spectrum is shifted and its PSD becomes $|S(\omega - \sigma\omega_0)|^2$.

In a heterogeneous sample, ^{1}H proton spins of different molecules will experience slightly different magnetic fields due to a shielding effect caused by its surrounding molecular structure, such that the natural precession frequency is shifted relatively to γ by the aforementioned σ factor. For instance, fat is shifted from water by 3.5 ppm. This effect is known as chemical shift, and it is the basis for NMR spectroscopy.

If a sample is composed of different molecules, a broadband excitation will flip the magnetization of ^{1}H proton spins in the different molecules, which will precess at different frequencies. The frequency spectrum of the acquired signal will be composed of a sum of Cauchy distributions centered at different frequencies, one for each molecule, and with peak intensity roughly varying according to the concentration of the molecule in the sample and the T_2 relaxation rate.

Homogeneity levels used for magnet design are actually defined such that differentiation of different molecules becomes possible, thus, to differentiate properly fat from water, a magnet should have homogeneity better than 3.5 ppm in its useful region.

1.3.2 Magnetic Resonance Imaging and Selected Pulse Sequences

As already stated, magnetization in a non-uniform sample will depend on the spin density $\rho(\boldsymbol{x})$ across space. Excitation and signal reception as described so far were such that spatial localization of the sources of signal was not possible. This "issue" was ingeniously overcome by Paul Lauterbur [Lauterbur 1973] and Peter Mansfield [Mansfield 1977b] by the addition of spatial encoding gradient fields, making it possible to reconstruct an image through inverse Fourier Transform of the acquired data.

The omitted information in $\Delta B_0(\boldsymbol{x})$ in the previous expression is now made explicit as

$$\Delta B_0(\boldsymbol{x}) = \boldsymbol{G}(t) \cdot \boldsymbol{x} + \delta B_0(\boldsymbol{x}), \tag{1.95}$$

with $\boldsymbol{G}(t) = G_x(t)\hat{\boldsymbol{x}} + G_y(t)\hat{\boldsymbol{y}} + G_z(t)\hat{\boldsymbol{z}}$ the encoding gradient fields.

By introducing this additional magnetic field in equation 1.91, we obtain

$$s(t) = \Lambda \int_{\mathcal{V}_s} e^{-\frac{t}{\mathrm{T}_2(\boldsymbol{x})}} \rho(\boldsymbol{x}) e^{\imath\varphi_0(\boldsymbol{x})} e^{-\imath 2\pi \left(\boldsymbol{k}(t)\cdot\boldsymbol{x} + \gamma\delta B_0(\boldsymbol{x})\right)} d^3x, \tag{1.96}$$

with

$$\boldsymbol{k}(t) = \gamma \int_0^t \boldsymbol{G}(u)\, du. \tag{1.97}$$

where uniform FA and $\mathcal{B}(\boldsymbol{x})$ sensitivity profile were assumed, and Λ is simply a proportionality constant comprising those.

Considering that the signal is acquired within a short time interval centered at some instant TE (the echo-time), such that there is almost no relaxation during this acquisition window, and with $\delta B_0(\boldsymbol{x}) = 0$, we have

$$s(\boldsymbol{k}(t)) = \Lambda \int_{\mathcal{V}_s} e^{-\frac{\mathrm{TE}}{\mathrm{T}_2(\boldsymbol{x})}} \rho(\boldsymbol{x}) e^{\imath\varphi_0(\boldsymbol{x})} e^{-\imath 2\pi \boldsymbol{k}(t)\cdot\boldsymbol{x}}\, d^3x. \tag{1.98}$$

This expression is a Fourier Transform of $\rho(\boldsymbol{x})e^{-\imath\varphi_0(\boldsymbol{x})}e^{-\frac{\mathrm{TE}}{\mathrm{T}_2(\boldsymbol{x})}}$ into reciprocal *k-space*. Therefore, by inverse Fourier Transform, an image with accurate delineation of different tissues can be reconstructed due to the diverse ^{1}H proton content in each tissue, leading to the Proton Density contrast. Moreover, different T_2 values across tissues contribute to yet another contrast mechanism, the T_2-contrast.

Thus, k-space data need to be judiciously sampled in order to reconstruct an image. To do so, gradients are driven in sequence while data sampling is performed such that a significant region of the k-space is swept, providing the discretized data $s(n\Delta k_x, m\Delta k_y, p\Delta k_z)$ for $-N/2 \leq n \leq N/2$, $-M/2 \leq m \leq M/2$ and $-P/2 \leq n \leq P/2$, where N, M and P are the amount of points sampled for each direction in k-space. Then, an inverse *Discrete* Fourier Transform (DFT) is applied on the k-space data and a discrete image $\hat{\rho}(n\Delta x, m\Delta y, p\Delta z)$ can be reconstructed.

The question of "which" data should be acquired from k-space is dictated by properties of the DFT. Some basic relations are:

$$\mathrm{FOV}_{x,y,z} = \frac{1}{\Delta k_{x,y,z}}, \tag{1.99}$$

$$\Delta\{x, y, z\} = \frac{1}{2k_{\{x,y,z\},max}}, \tag{1.100}$$

and

$$\Delta k = \gamma G \Delta t. \tag{1.101}$$

Therefore, depending on the size of the object being imaged and the desired resolution, the number of data points, sampling times and gradient intensity are set.

Several sequences exist for acquiring k-space data. We will describe here the two sequences that will be employed in this work: the Gradient Recalled Echo (GRE) [Markl 2012] and the Echo Planar [Mansfield 1977a]. We will initially present them in the absence of δB_0 field excursion.

Gradient Recalled Echo

The pulse chronogram for the 3D GRE sequence is shown in Fig.1.10.

GRE is one of the most widely used sequences and one of the first introduced for MRI. In its 3D application, it starts with a non-selective excitation of flip-angle α.

Subsequently, two of the three available gradients, say G_y and G_z, are employed for phase and partition encoding. Each one is driven with trapezoidal pulses with varying intensities during a fixed period of time, such that k_y and k_z are set to $m\Delta k_y$ and $p\Delta k_z$.

Then the readout gradient G_x is initially driven with negative intensity until we reach $k_{x,\min}$ (or $-N\Delta k_x/2$) in k-space; at which point the gradient is switched to positive intensity and the echo starts to be measured at sampling period τ_s, leading to a k-space sampling

$$\boldsymbol{k}(TE + n\tau_s) = n\Delta k_x \hat{\boldsymbol{x}} + m\Delta k_y \hat{\boldsymbol{y}} + p\Delta k_z \hat{\boldsymbol{z}} \tag{1.102}$$

with

$$\Delta k_x = \gamma G_x \tau_s \tag{1.103}$$

$$m\Delta k_y = \gamma G_y^m \tau_{PE} \tag{1.104}$$

$$p\Delta k_z = \gamma G_z^p \tau_P \tag{1.105}$$

$$G_y^m = \frac{m}{\gamma FOV_y \tau_{PE}} \tag{1.106}$$

Thus, k_y and k_z are kept fixed in k-space while k_x is swept from $-N\Delta k_x/2$ to $N\Delta k_x/2$ within the $N\tau_s$ interval. This acquires one line in k-space, out of a total of $M \times P$ lines required. Thus the process is repeated after a repetition time TR, but with phase and partition encoding gradients set to different amplitudes.

The repetition time TR might not be long enough for the longitudinal magnetization to return to equilibrium; this causes the magnetization before excitation to be different from the equilibrium magnetization M_0, providing a reconstructed signal with weighting [Ernst 1966]

$$S_{\mathrm{GRE}} = \rho(\boldsymbol{x}) \sin\alpha \frac{1 - e^{-\frac{\mathrm{TR}}{\mathrm{T_1}}}}{1 - \cos\alpha e^{-\frac{\mathrm{TR}}{\mathrm{T_1}}}} e^{-\frac{\mathrm{TE}}{\mathrm{T_2^*}}}, \tag{1.107}$$

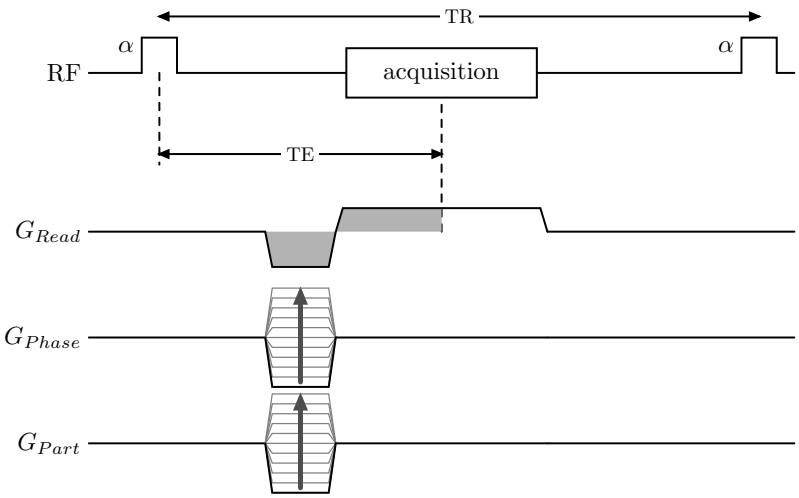

Figure 1.10 – The 3D-GRE Sequence Diagram is shown. It starts with a non-selective excitation of FA α. We then proceed with phase and partition encoding, and employ a negative readout gradient bringing us to the "edge" of the k-space zone we want to cover. Polarity of the readout gradient is reversed and the echo sampling is started. After a time TR from the excitation, the process is repeated with phase and partition encoding gradients driven with different amplitudes to acquired different points in the k-space.

which, for fixed TR, has maximum intensity at the Ernst angle

$$\alpha_E = \arccos e^{-\frac{\mathrm{TR}}{\mathrm{T_1}}}. \tag{1.108}$$

Echo Planar Imaging

The Echo Planar Imaging (EPI) [Mansfield 1977a, Rzedzian 1983] is a fast acquisition technique where, instead of acquiring a single k-space line after each excitation, an entire k-space plane is acquired. If τ_{ES} is the echo spacing, i.e. the delay between the acquisition of two consecutive lines of the k-space plane, then:

$$\boldsymbol{k}(TE + n\tau_s + m\tau_{ES}) = n\Delta k_x \hat{\boldsymbol{x}} + m\Delta k_y \hat{\boldsymbol{y}} + p\Delta k_z \hat{\boldsymbol{z}} \tag{1.109}$$

EPI high speed makes it capable of acquiring a temporal series of images of the entire brain within a short enough interval to capture variations in the T_2^* relaxation time related to the changes of the blood oxygenation levels caused by brain activity. It produces the Blood Oxygenation Level-Dependent (BOLD) contrast [Ogawa 1990] which allows functional MRI (fMRI) studies.

At the same time, it requires fast gradient switching with high intensity in order to be robust against T_2^*-decay blurring [Haacke 1999] effects and long-TE signal-loss (cf. below).

1.3.3 B0-Related Artifacts

All the required tools to understand the mechanism behind B_0-related artifacts are now in our hands.

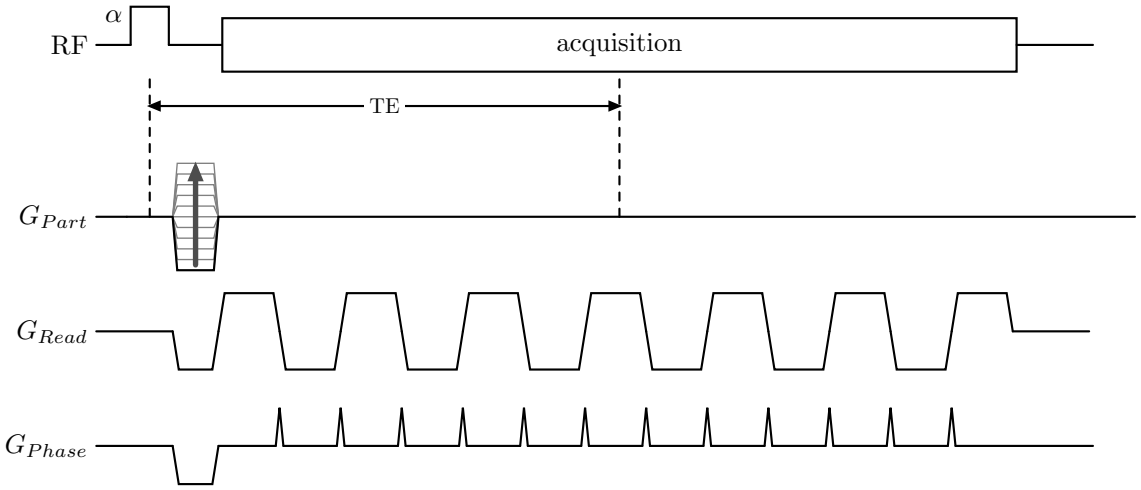

Figure 1.11 – The 3D-EPI Sequence Diagram is shown. Readout and phase encoding gradients are rapidly switched to acquire an entire k-space plane after the excitation, instead of a single line, as opposed to GRE. The process is repeated with a TR period using different partition encoding amplitudes.

By looking at the signal equation in the presence of δB_0, we will be able to better understand and quantify its impact on the reconstructed image. In addition, we will observe that B_0-related artifacts are not dependent on δB_0 alone, and that the problem could be attacked from many different perspectives.

Similar analyses on the mechanisms behind B_0 related artifacts, serving as inspiration for this subsection, are available in [Zhao 2005, Koch 2009, Mullen 2020].

Geometric Distortion

In the presence of $\delta B_0(\boldsymbol{x})$ inhomogeneity, the signal equation for EPI is

$$
\begin{aligned}
&s(\mathrm{TE}+n\tau_s+m\tau_{ES}) = \\
&= \Lambda \int_{\mathcal{V}_s} e^{-\frac{\mathrm{TE}}{\mathrm{T}_2^*(\boldsymbol{x})}} \rho(\boldsymbol{x}) e^{\imath\varphi_0(\boldsymbol{x})} e^{-\imath 2\pi\left(n\Delta k_x x + m\Delta k_y y + p\Delta k_z z + \gamma\delta B_0(\boldsymbol{x})(\mathrm{TE}+n\tau_s+m\tau_{PE})\right)} d^3x \\
&= \Lambda \int_{\mathcal{V}_s} e^{-\frac{\mathrm{TE}}{\mathrm{T}_2^*(\boldsymbol{x})}} \rho(\boldsymbol{x}) e^{\imath(\varphi_0(\boldsymbol{x})-\gamma\delta B_0(\boldsymbol{x})\mathrm{TE})} e^{-\imath 2\pi\left(n\Delta k_x\left(x+\frac{\gamma\delta B_0(\boldsymbol{x})\tau_s}{\Delta k_x}\right)+m\Delta k_y\left(y+\frac{\gamma\delta B_0(\boldsymbol{x})\tau_{PE}}{\Delta k_y}\right)+p\Delta k_z z\right)} d^3x \\
&= \Lambda \int_{\mathcal{V}_s} e^{-\frac{\mathrm{TE}}{\mathrm{T}_2^*(\boldsymbol{x})}} \rho(\boldsymbol{x}) e^{\imath(\varphi_0(\boldsymbol{x})-\gamma\delta B_0(\boldsymbol{x})\mathrm{TE})} e^{-\imath 2\pi\left(k_x\left(x+\frac{\delta B_0(\boldsymbol{x})}{G_x}\right)+k_y\left(y+\gamma\delta B_0(\boldsymbol{x})\tau_{ES}FOV_y\right)+k_z z\right)} d^3x
\end{aligned}
\tag{1.110}
$$

The change of variables

$$
\begin{aligned}
x' &= x + \frac{\delta B_0(\boldsymbol{x})}{G_x} \\
y' &= y + \gamma\delta B_0(\boldsymbol{x})\tau_{ES}FOV_y
\end{aligned}
\tag{1.111}
$$

in equation 1.110 shows that, as iFFT reconstruction is applied to the acquired signal, the actual reconstructed image $\hat{\rho}(\boldsymbol{x}')$ will be an image with voxel shifts

$$\begin{aligned}\frac{\delta x(\boldsymbol{x})}{\Delta x} &= \frac{\gamma \delta B_0(\boldsymbol{x})}{\gamma G_x \Delta x} \\ \frac{\delta y(\boldsymbol{x})}{\Delta y} &= \frac{\gamma \delta B_0(\boldsymbol{x}) \tau_{ES} M}{R_{PE}}\end{aligned} \tag{1.112}$$

in the readout and phase-encoding directions, respectively, relatively to the real object $\rho(\boldsymbol{x})$ being scanned.

In the phase-encoding direction distortion we have added a new term R_{PE} which was not yet presented. It is the *acceleration factor* in the phase-encoding direction. Acquisition acceleration is possible through the use of parallel-imaging techniques such as GeneRalized Autocalibrating Partially Parallel Acquisitions (GRAPPA) [Griswold 2002], reducing acquisition time by seemingly skipping k-space lines in the phase-encoding and partition-encoding directions. This reduces the effective echo-spacing time τ_{ES} by a factor R_{PE}.

It is now possible to provide some figures. Conventional clinical scanners can achieve gradient fields of $30\,\mathrm{mT\,m^{-1}}$ to $80\,\mathrm{mT\,m^{-1}}$ [Webb 2016, Winkler 2018]. Considering 1 mm resolution in the readout direction and a $40\,\mathrm{mT\,m^{-1}}$ gradient we obtain a $0.6\,\mathrm{px\,kHz^{-1}}$ geometric distortion in the readout direction. This is quite small, and even under the harsh 11.7 T conditions, 98 % of voxels are under 370 Hz (cf. simulation in subsection 1.2.2), which would lead to a maximum voxel shift of only 0.2 px for these voxels. Even when considering the maximum magnetic field excursion of 2.1 kHz, the voxel is shifted by 1.2 px, which starts to be significant, but still very small compared to what we will observe in the phase-encoding direction.

For brain imaging, the phase encoding direction is usually set to be in the patient's Anterior-Posterior (AP) axis. A FOV of around 220 mm is required for imaging the entire brain, and if a resolution of 1 mm is required, this leads to $M = 220$. Typical echo-spacing times for EPI are within 0.5 ms to 0.7 ms. Assuming $\tau_{ES} = 0.7\,\mathrm{ms}$ and a non-accelerated acquisition ($R_{PE} = 1$), voxel shift is $0.15\,\mathrm{px\,Hz^{-1}}$. This is approximately 256 times greater than the geometric distortion in the readout direction for a same magnetic field excursion. Taking once again our example at 11.7 T, 14.5 % of voxels will present magnetic field excursion superior to 100 Hz, which would lead to at least 15.4 px shift, or 15.4 mm, in this group of voxels. At this point, acceleration would help improve the situation, but even with $R_{PE} = 3$, the geometric distortion would still be 5.1 mm. If increased to 4, the highest acceleration value usually employed, at least 3.9 mm geometric distortion would be observed in 14.5 % of brain voxels.

We are therefore starting to get an idea of how image can be affected. Also, at 11.7 T, we see that without acceleration, much of the acquired image would be useless due to these intense artifacts.

Yet another important factor is the echo-spacing. Being able to reduce it would help mitigate geometric distortion. Reducing its value requires covering a k-space line faster,

thus, having stronger gradients. At the same time, if the gradient can reach higher values but the slew-rate is not high enough, it will act as a bottleneck, and the total echo-spacing will actually increase instead of decrease due to the ramp-up time. Increasing the slew-rate, on the other hand, increases the probability of Peripheral Nerve Stimulation (PNS), causing discomfort and even being harmful to the patient. Nevertheless, recent advances in PNS-constrained gradient coil design [Davids 2021] might be very helpful to achieve lower echo-spacing, thus helping mitigate geometric distortion artifacts, although more intense gradients will bring an SNR penalty due to increased acquisition bandwidth.

Signal Loss Due to Intra-Voxel Dephasing

Yet another problematic artifact for imaging is signal loss. It is caused by the action of gradients of δB_0 inside a voxel, making the spins inside it lose phase coherence, therefore causing a drop in signal intensity.

Consider the signal inside a voxel located at $\boldsymbol{x}_0$ with $\boldsymbol{k} = \mathbf{0}$, and the magnetic field inside that voxel given by $\delta B_0(\boldsymbol{x}) = \delta B_0(\boldsymbol{x}_0) + \boldsymbol{\nabla}\delta B_0(\boldsymbol{x})\big|_{\boldsymbol{x}=\boldsymbol{x}_0} \cdot (\boldsymbol{x} - \boldsymbol{x}_0)$:

$$S = \Lambda\rho(\boldsymbol{x}_0)e^{\imath\varphi_0'} \int_{x_0-\frac{\Delta x}{2}}^{x_0+\frac{\Delta x}{2}} \int_{y_0-\frac{\Delta y}{2}}^{y_0+\frac{\Delta y}{2}} \int_{z_0-\frac{\Delta z}{2}}^{z_0+\frac{\Delta z}{2}} e^{-\imath 2\pi \mathrm{TE}\gamma\boldsymbol{\nabla}\delta B_0(\boldsymbol{x})|_{\boldsymbol{x}=\boldsymbol{x}_0}\cdot(\boldsymbol{x}-\boldsymbol{x}_0)} dx\, dy\, dz \tag{1.113}$$

leading to signal magnitude

$$|S| = \Lambda\rho(\boldsymbol{x}_0)\Delta x\Delta y\Delta z \left|\operatorname{sinc}\left(\pi\gamma\mathrm{TE}\frac{\partial\delta B_0}{\partial x}\Delta x\right)\operatorname{sinc}\left(\pi\gamma\mathrm{TE}\frac{\partial\delta B_0}{\partial y}\Delta y\right)\operatorname{sinc}\left(\pi\gamma\mathrm{TE}\frac{\partial\delta B_0}{\partial z}\Delta z\right)\right| \tag{1.114}$$

exhibiting the effect of intra-voxel dephasing in the image signal. The effect of the mean voxel field $\delta B_0(\boldsymbol{x}_0)$ will be a phase offset which was incorporated in φ_0'.

There are some useful takeaways from this expression since, first of all, it shows that not only the magnetic field excursion is important in resulting image quality but also its gradients. Second, once again there are multiple factors at play, such as the resolution and the echo-time TE.

One could, therefore, envision reducing TE or the resolution to avoid signal-loss, but once again there will be drawbacks. In GRE sequences TE can be made quite short, one or two milliseconds, and while this is useful to provide high signal not only by avoiding intra-voxel dephasing but also to be less affected by T_2 or T_2^* decays, T_2^* contrast will be lost. The T_2^* contrast is essential for BOLD fMRI, where the Contrast-to-Noise Ratio (CNR) is given by [Wald 2012]

$$CNR = -tSNR\ \mathrm{TE}\frac{\mathrm{T}_{2\mathrm{act.}}^* - \mathrm{T}_{2\mathrm{rest}}^*}{\mathrm{T}_{2\mathrm{act.}}^*\mathrm{T}_{2\mathrm{rest}}^*}, \tag{1.115}$$

where $tSNR$ is the temporal SNR, and $\mathrm{T}_{2\mathrm{rest}}^*$ and $\mathrm{T}_{2\mathrm{act.}}^*$ are the T_2^* decays during the resting state and during cerebral activation induced by a certain task. We explicitly see the importance of a longer TE, which will usually be between 20 ms to 30 ms in fMRI.

Moreover, even if reducing TE was allowed from the application perspective, significantly reducing it in EPI requires a much shorter echo-train, and gradients are once again

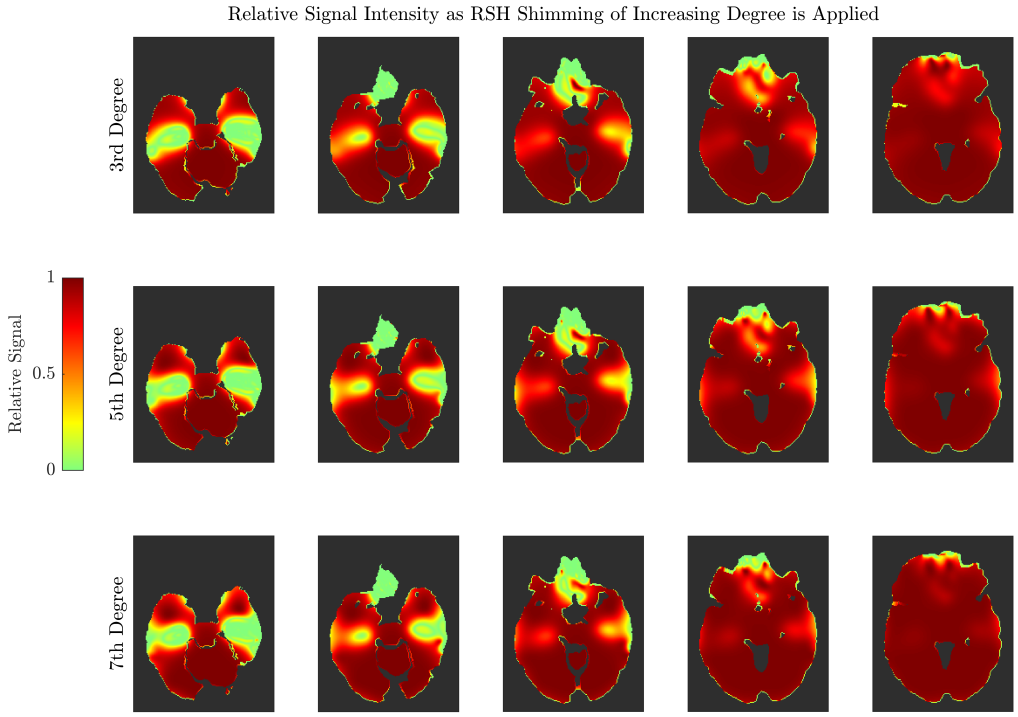

Figure 1.12 – Relative Signal Intensity: losses (in green) are due to intra-voxel dephasing close to head cavities - Results of simulations on our 3D model at 11.7 T, with TE = 25 ms and voxel size = 1 mm.

needed to be driven at higher intensity, stumbling once again into the issues previously discussed.

As a consequence, we will attack the δB_0 inhomogeneity issue with the intention of also reducing the gradients of δB_0. Let us see if this holds with our 3D model.

A simulation of whole-brain RSH shimming with increasing degrees with δB_0 as target for minimization at 11.7 T shows that strong signal-loss is expected over the ear canals and sinus (cf. Fig. 1.12), as calculated from equation 1.114 with TE = 25 ms and 1 mm resolution. This is not surprising given the δB_0 distribution which we are already familiarized with.

Evaluating the relative signal improvement $S/S_0 - 1$ as the SH degree is increased, we obtain the maps shown in Fig. 1.13. Overall, by reducing the δB_0 inhomogeneity there will be both improvement and degradation of the signal. When moving from 3^{rd} to 5^{th} degree, it is not clear if we improve more than we degrade. On the other hand, when moving from 3^{rd} to 7^{th} degree, although degradation is still seen, zones of improvement in signal are more predominant.

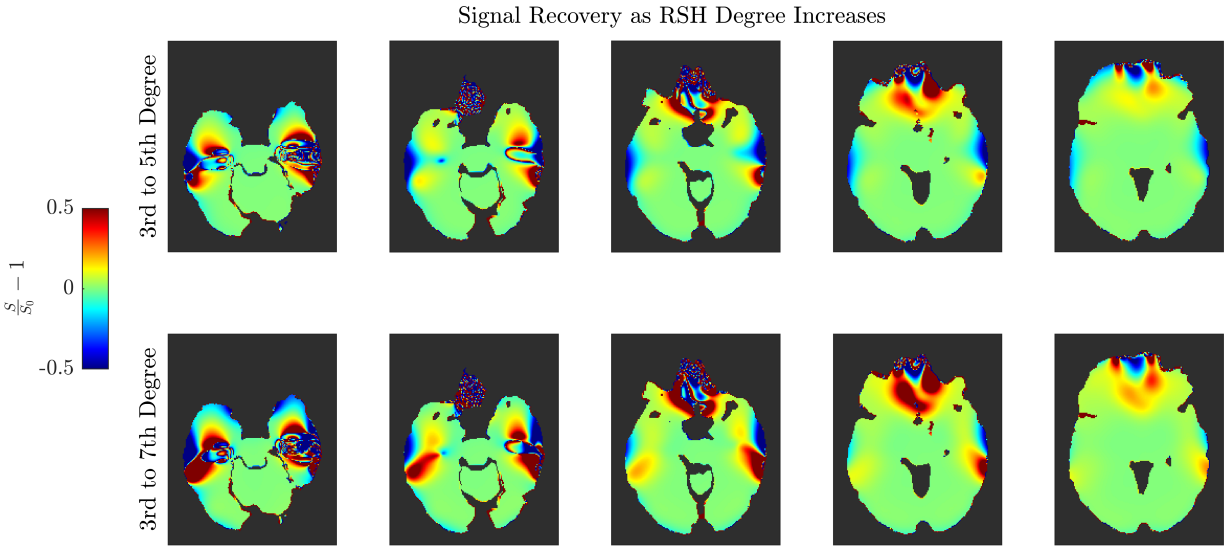

Figure 1.13 – Relative signal improvement after shimming.

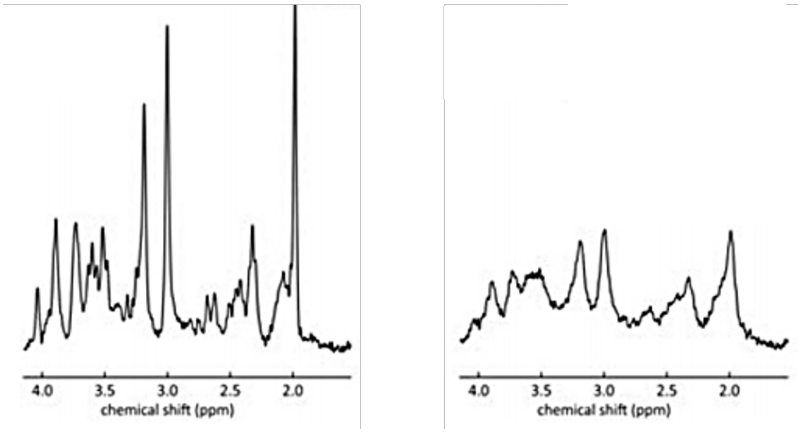

Figure 1.14 – Line broadening in spectroscopy due to poor homogeneity. With a good shimming shown at the left and poor shim on the right. We can clearly see both loss of signal and broader peaks, which would make harder, albeit impossible, to recognize different molecules. Image adapted from [Juchem 2020a].

Other Artifacts

The two artifacts previously described are the most commonly encountered in conventional EPI sequences.

Other fast sequences such as balanced Steady-State Free Precession (bSSFP) [Bieri 2013] present banding artifacts due to B_0 inhomogeneity; Compressed Sensing MRI sequences [Lustig 2007] such as T_2^*-weighted Sparkling [Lazarus 2019], presenting moderate echo train lengths, will surfer from intra-voxel dephasing.

In spectroscopy, there will be line broadening (cf. Fig. 1.14) in the presence of magnetic field gradients inside the sample. Then, there is also the already discussed failed-inversion in MP-RAGE.

As we will see in some examples in the following chapter, image artifacts at 7 T are already intense. The need for improved methods for correcting sample-induced inhomogeneity is pressing, and while optimized shimming hardware would be beneficial for improving image quality at 7 T, it might very well be essential for obtaining exploitable EPI images at 11.7 T.

* * *
* *
*

Chapter 2

B0 Shimming in the Human Brain: Methodology and Hardware

Chapter Outline

Main hardware solutions employed for sample-specific B_0 shimming will be discussed in this chapter. Active and passive approaches will be outlined, with active devices in the spotlight since they are much simpler to adjust to provide subject-tailored corrections. These are accomplished by setting electric current intensities in each coil composing the system, in a process that, for the user, can potentially be as simple as pressing a button.

An overview on shim coil design will be provided. Nevertheless we suggest the reader to refer to [Poole 2007a] for a rich exploration of coil designs.

Then a brief historical review of subject-specific shimming methods, particularly with Multi Coil Arrays, will be provided. We suggest [Stockmann 2018] for further reading.

2.1 Introduction

It will be shown in this chapter that a multi-echo GRE acquisition provide a temporal phase evolution isochromats associated to $\delta B_0(\boldsymbol{x})$ excursion, therefore containing a fieldmap information. This information is post-processed to estimate the magnetic field distribution in space, $\boldsymbol{b} \in \mathbb{R}^K$ with $b_k = \delta B_0(\boldsymbol{x}_k)$ across a series of K voxels at coordinates $\boldsymbol{x}_k \in \mathbb{R}^3$ $(k = 1, \ldots, K)$ composing the ROI. It will present an inhomogeneity $\sigma(\boldsymbol{b})$, which is now our task to mitigate.

Inhomogeneity mitigation, through subject-specific shimming, can be either active or passive. In any case, the problem will usually consist in obtaining a linear relation $\mathbf{B} \in \mathbb{R}^{K\times N}$ between a set of adjustable characteristics $\boldsymbol{q} \in \mathbb{R}^N$ of field-generating entities and the magnetic field each entity generates in the target ROI. Addition of the correction fields on $\boldsymbol{b}$ would result in

$$\boldsymbol{b}_r = \boldsymbol{b} + \mathbf{B}\boldsymbol{q}. \tag{2.1}$$

The quantities $\boldsymbol{q}$ should then be optimized such that residual inhomogeneity $\sigma(\boldsymbol{b}_r)$ is minimized.

In active shimming, $\boldsymbol{q}$ will be a set of electric currents driving independent coils; in passive shimming, $\boldsymbol{q}$ could be the volume of some magnetic material to be positioned inside predetermined slots.

There will usually be constraints associated with the inverse problem of finding the optimal $\boldsymbol{q}$. Current drivers, employed for active shimming, are limited to some maximum current value and/or to a maximum total power it can deliver. In the case of passive shimming, the problem might have an integer constraint, thus $\boldsymbol{q} \in \mathbb{Z}^N$.

2.2 Field Mapping

The first step in shimming consists in measuring the $\delta B_0(\boldsymbol{x})$ distribution in the anatomy of interest. We can easily adapt the signal equation 1.110 presented for EPI to the GRE acquisition scheme, where we will observe some convenient properties:

$$s(\mathrm{TE} + n\tau_s) = \Lambda \int_{\mathcal{V}_s} e^{-\frac{\mathrm{TE}}{\mathrm{T}_2^*(\boldsymbol{x})}} \rho(\boldsymbol{x}) e^{\imath(\varphi_0(\boldsymbol{x}) - \gamma\delta B_0(\boldsymbol{x})\mathrm{TE})} e^{-\imath 2\pi\left(k_x\left(x + \frac{\delta B_0(\boldsymbol{x})}{G_x}\right) + k_y y + k_z z\right)} d^3x \tag{2.2}$$

We can see that δB_0 related information will be present in the phase of the reconstructed signal. The phase in each voxel in the reconstructed data evolves with the echo-time TE proportionally to the field excursion at that point. However, the total phase also depends on the initial phase of the magnetization after excitation. Therefore, by acquiring multiple echoes at different echo times, the difference in echo times ΔTE results in a difference in phase

$$\Delta\varphi(\boldsymbol{x}) = -2\pi\gamma\Delta\mathrm{TE}\delta B_0(\boldsymbol{x}) \tag{2.3}$$

By employing multi-echo GRE sequences, the phase maps can be used to estimate the δB_0 maps.

There are some practical considerations:

- In the MRI scanner reference frame, the phase evolution will be positive.

- Acquiring more echoes for fieldmap estimation will provide robustness to noise, as long as the echo times are not too large; otherwise associated phase maps will have low SNR and degrade the δB_0 estimation rather than improve it.

- The phase reconstructed in the MRI system is limited to a $[-\pi, \pi]$ range, therefore phase unwrapping, either temporal [Robinson 2014] or spatial [Karsa 2019], must be implemented.

- If temporal phase unwrapping is implemented, it is necessary that the time difference between at least two echoes respect the Nyquist criteria: $\Delta\text{TE} \leq 1/(2\gamma \max(\delta B_0))$.

From the above equation, we note that the reconstructed information is geometrically displaced by an increment $\delta B_0(\boldsymbol{x})/G_x$ in the readout direction; but if G_x is large enough, the induced distortion can be made negligible. For instance, a 100 Hz excursion would cause a 0.1 mm distortion under a $20\,\text{mT}\,\text{m}^{-1}$ readout gradient. High gradient strengths can be obtained by increasing the readout bandwidth of the GRE sequence according to: $\gamma \times G \times FOV_r = BW$. However, increased readout bandwidth will increase the level of noise, reducing SNR.

2.2.1 Field Mapping Methodology Employed in This Work

As it will be shown in the following chapters, for the purpose of this study, a database of fieldmaps in the human brain was acquired at 3 T. Estimation of the fieldmaps was performed using the DICOM phase images as reconstructed by the scanner in adaptive combine [Walsh 2000] mode. Temporal phase unwrapping was performed due to the easiness of implementation. To guarantee no wrapping in the phase difference between the first and second echoes, two consecutive GRE acquisitions were employed to allow the TEs to be sufficiently close. Further details on acquisition parameters are available in subsection 5.1.4.

In-vivo experiments, on the other hand, were conducted in a 7 T scanner. Once again, DICOM phase images reconstructed by the scanner were used for fieldmap estimation. Reconstruction mode, however, was sum-of-squares [Larsson 2003]. These in-vivo experiments were performed under strict SAR constraints, in a so-called restricted-SAR mode (more information in subsection 5.1.7). This mode required long TR, which considerably increased acquisition time, making the use of two consecutive GRE acquisitions (as employed at 3 T) for temporal unwrapping very time consuming. It was therefore decided to use a single GRE sequence with three echoes and perform spatial unwrapping, which, contrarily to temporal unwrapping, does not require close echo times. More details on sequence parameters and fieldmap estimation pipeline is available in subsection 5.1.7.

2.3 Spherical Harmonics Based Shimming: Overview of Coil Design and Application

Spherical-harmonics-based shimming is the standard solution in the MRI industry, with every commercial scanner being equipped with at least first-degree SH shimming capabilities (through the gradient coils), and optionally as much as a third degree SH coil set.

This solution is employed for human brain shimming despite the fact that the magnetic field distribution inside the brain cannot be decomposed into a set of SH coefficients [Hillenbrand 2005]. This is because the magnetic field inside the human head cannot satisfy Laplace's equation [Pan 2012, Webb 2016], as observed from the build-up of magnetic field sources at air/tissue interfaces (cf. equation 1.75). The implications of this characteristic will be discussed in chapter 4.

Despite this "incompatibility", any field correction coil would generate a magnetic field satisfying Laplace's equation; therefore a set of coils each generating a unique SH pattern is a logical choice to address shimming in any sample, organ or ROI. Moreover, from simulations shown in chapter 1, at 11.7 T, inhomogeneity drops from 197.1 Hz, when unshimmed, to 118.6 Hz with the use of SH-based coils of up to partial third degree (a 39.8 % drop).

With SH patterns of different degrees and orders being orthogonal, no interaction between coils is expected, making it easier to adjust the currents in each coil, specially at the time when this technology was proposed in [Golay 1958], with NMR shimming performed in samples by observing the resulting FID [Chmurny 1990].

2.3.1 Shim Coil Design

A clear mathematical framework for designing shim coils capable of generating accurate SH fields of a given degree and order was first laid-out in [Roméo 1984]. From the SH decomposition of the magnetic field generated by a current filament positioned on a cylindrical surface, ingenious insights led to the definition of optimal wire disposition to generate such SH-generating coils, as shown in Fig. 2.1a.

If Roméo and Hoult claimed that literature on shim coil design was scarce by the time of their work, the situation surely has changed, and nowadays there is no shortage of information addressing gradient and shim coil design. The most widespread methods employed are either based on Turner's Target Field Method (TFM) [Turner 1986, Turner 1988, Turner 1993], or the Inverse Boundary Element Method (IBEM), developed upon the work of Pissanetzky [Pissanetzky 1992].

Turner transferred the ill-posed coil design problem [Adamiak 1981, Poole 2010] from the space domain to a reciprocal domain by means of a Fourier-Bessel transform. Together with the definition and transform of a target $B_z(\boldsymbol{x})$ field along an infinite cylindrical surface, the optimal current density on a cylindrical coil former of larger radius can be obtained to generate the target field in the reciprocal space, with subsequent unique inverse

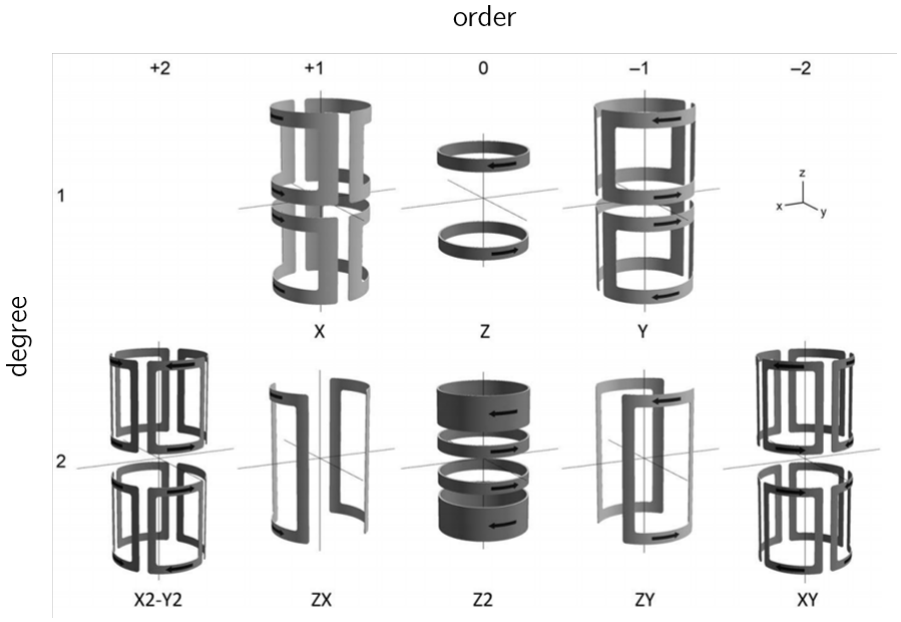

(a)

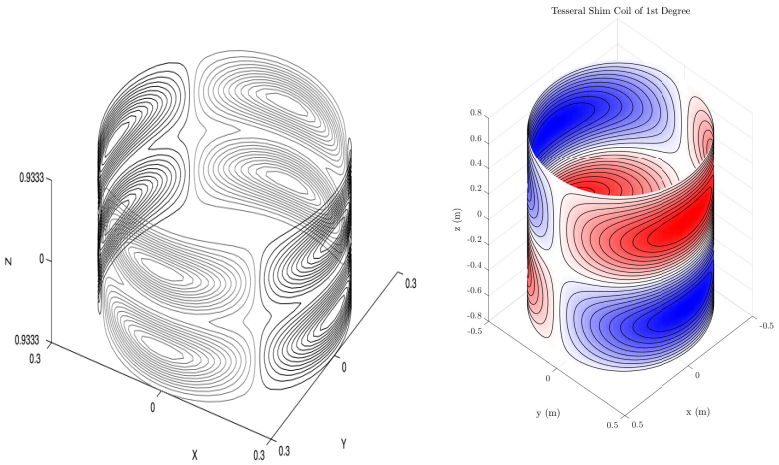

(b) (c)

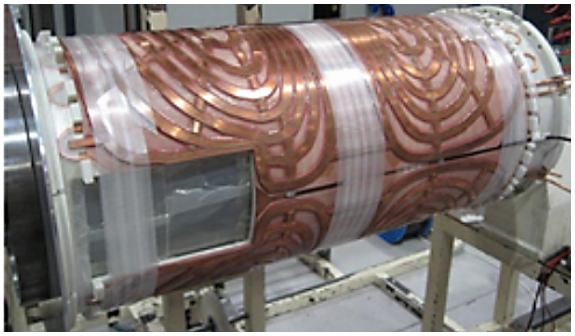

(d)

Figure 2.1 – Examples of gradient and shim coils obtained from various design methodologies: (a) discrete coil design from [Roméo 1984]; (b) the TFM–SF approach was used to compute a 2nd degree, 2nd order tesseral shim coil (from [Brideson 2002]); (c) the original Dipole Boundary Method introduced in chapter 3 led to this unshielded y-gradient design; (d) a shoulder-slotted gradient insert designed with the IBEM (from [Poole 2007a]).

transform. If a limited number of control points for the target magnetic field is employed, regularization can be achieved by assembling a functional containing the coil's magnetic energy and target field constraints. Alternatively, power dissipation can also be used for regularization [Engelsberg 1992].

Novel TFM was developed to consider finite length coil formers [Forbes 2001, Forbes 2002, Forbes 2003]. In [Brideson 2002], analytical expressions for stream functions on cylindrical surfaces generating SH-based coils of general order and degrees were provided with a combined target-field & stream-function approach.

Although the TFM is a powerful method for gradient and shim coil design, the IBEM presents itself as a more versatile technique, capable of being employed in the most diverse kinds of coil former geometries due to its discretization of the domain into a triangular mesh. It solves the inverse problem of finding optimal current flow on a surface by means of a stream function with regularization based on power dissipation and/or magnetic field energy. Despite its initial formulation in 1992 by Pissanetzky, only in 2003 a first rigorous mathematical treatment of IBEM appeared [Peeren 2003], and a subsequent practical implementation of a gradient coil designed with IBEM was shown in [Lemdiasov 2005]. The method was then applied for the design of various novel coils in [Poole 2007a], and has not ceased to gain interest since. The numerical problem formulation can take several design aspects into account, including resulting forces, torque, shielding. Different norms were studied as cost functions in [Poole 2010, Poole 2014]. Adaptations of the method led to the Equivalent Magnetization Current method [Lopez 2009a, Lopez 2009b], where, exploiting the association between magnetization and bounded currents, a magnetization is attributed to nodes in a triangular mesh and the inverse problem is set to compute the optimal magnetization generating some arbitrary target field. This magnetization can then be used to calculate the current density over the coil former or directly perform discretization into winding as it is also equivalent to a stream function.

Some examples of coil design obtained from those methods are shown in Fig. 2.1.

The set of mentioned references is far from exhaustive, but we hope they'll provide a starting point if the reader wishes to dive into greater details.

2.3.2 Characterization

SH-based coil design is performed such that each coil addresses a $\mathcal{R}_{nm}(r, \theta, \varphi)$ RSH function of particular degree and order as target field, but power dissipation or magnetic energy limits in the coil design process will already cause the resulting magnetic field to not be pure, that is, it will generate SH fields of degrees and orders other than what was intended, but with much lower intensity. Moreover, deviations from the ideal design will inevitably occur in the fabrication process, causing further deviation of the produced magnetic field from the calculated field. Therefore, the resulting shim coil needs to be characterized, i.e. its magnetic field spatial distribution generated per unit current must be measured.

For characterization, a baseline fieldmap at zero electric current and at least one fieldmap generated by the coil when driven by some fixed current should be acquired,

providing the magnetic field of a coil per unit current $\mathcal{B}_c(\boldsymbol{x}_p)$ across voxels $p = 1, ..., P$ in a phantom large enough to cover the desired scanning region. When employed for shimming of some target field at voxels $\boldsymbol{x}_k$, linear interpolation of the coil fieldmap $\mathcal{B}_c$ can be performed to obtain its value on the voxels of interest; alternatively, a SH fit of $\mathcal{B}_c$ could be employed, providing a set of SH coefficients A_{nm} which can be used to compute the magnetic field at points $\boldsymbol{x}_k$ with equation 1.58. When decomposing into SH coefficients, it should be fitted by SH functions up to at least the same degree the coil was designed to produce. In [Chang 2018], it is recommended that the SH fit is performed with increasing degree until the residual from the fit shows no significant reduction. This allows the characterization of higher-order cross-terms generated by the actual coil.

To filter noise and account for potential non-linearity, multiple fieldmap acquisitions could be performed at different electric currents [Juchem 2010c,Chang 2018,Juchem 2020a], with a resulting normalized fieldmap or SH coefficients estimated from a linear regression. At least six current settings per coil are recommended by [Juchem 2020a]. Further recommendations include having a phantom with a single dominant resonance, to avoid the influence of satellite peaks in the phase evolution. In addition, to avoid geometric misregistration due to B_0-induced geometric distortions in the image, the acquisition bandwidth should be as high as possible while maintaining SNR at acceptable levels.

After characterization of a set of C coils with SH-fitting to some degree N, the estimated magnetic field produced by a coil c with current i_c in the voxels of the target region is:

$$\boldsymbol{b}_c = \begin{bmatrix} \mathcal{R}_{0,0}(\boldsymbol{x}_1) & \mathcal{R}_{1,-1}(\boldsymbol{x}_1) & \mathcal{R}_{1,0}(\boldsymbol{x}_1) & \dots & \mathcal{R}_{N,N}(\boldsymbol{x}_1) \\ \mathcal{R}_{0,0}(\boldsymbol{x}_2) & \mathcal{R}_{1,-1}(\boldsymbol{x}_2) & \mathcal{R}_{1,0}(\boldsymbol{x}_2) & \dots & \mathcal{R}_{N,N}(\boldsymbol{x}_2) \\ \vdots & \vdots & \vdots & \ddots & \vdots \\ \mathcal{R}_{0,0}(\boldsymbol{x}_K) & \mathcal{R}_{1,-1}(\boldsymbol{x}_K) & \mathcal{R}_{1,0}(\boldsymbol{x}_K) & \dots & \mathcal{R}_{N,N}(\boldsymbol{x}_K) \end{bmatrix} \begin{bmatrix} A^c_{0,0} \\ A^c_{1,-1} \\ A^c_{1,0} \\ \vdots \\ A^c_{N,N} \end{bmatrix} i_c, \tag{2.4}$$

with $A^c_{n,m}$ the characteristic RSH coefficient of degree n and order m of channel c.

Considering the contribution of all channels, the problem becomes

$$\begin{aligned} \boldsymbol{i} &= \underset{\boldsymbol{i}\in\mathbb{R}^C}{\operatorname{argmin}}\ \sigma(\boldsymbol{b} + \mathbf{R}\mathbf{A}\boldsymbol{i}), \\ &\text{s.t. } |i_c| \le I_{\max}, \quad 1 \le c \le C, \\ &\sum_{c=1}^{C} |i_c| \le I^{\text{total}}_{\max}, \\ &\sum_{c=1}^{C} r_c i_c^2 \le \mathcal{P}_{\max}. \end{aligned} \tag{2.5}$$

with potential constraints related to the maximum current per channel $I_{\max}$, maximum sum of currents $I^{\text{total}}_{\max}$ and maximum power $\mathcal{P}_{\max}$, calculated from coils' resistances r_c.

2.3.3 Static and Dynamic Shimming

In clinical routine, the so-called static global shimming is normally performed. In this modality of fieldmap-based shimming, $\boldsymbol{b}$ will be composed of voxels within a cuboid, that can be defined by the user, closely enclosing the anatomy of interest. The system will then estimate the ideal electric currents that need to be input into the SH coil set to reduce inhomogeneity in this ROI. Alternatively, the user may prefer to accurately segment the ROI, producing a brain mask, for instance, with software such as FSL's Brain Extraction Tool [Smith 2009] or 3D Slicer [Kikinis 2014], and compute the ideal shim currents or coefficients to improve homogeneity inside the ROI, which might provide slightly better results than the cuboid-region shimming. For B_0-sensitive sequences such as EPI, global shimming even at 3^{rd} degree is still insufficient for geometric distortion mitigation at UHF (cf. Fig. 2.2a).

Significant improvement in B_0-inhomogeneity correction using the same set of SH coils can be achieved by slice-by-slice shimming with Dynamic Shim Updating (DSU) [Blamire 1996, Morrell 1997, Graaf 2003, Koch 2006b]. In the DSU technique, each slice in a 2D acquisition is used as ROI, and electric currents are optimized to correct inhomogeneity in it. Then the optimized set of currents is switched in real-time for the slice to be acquired in the slice series. Managing DSU, however, can be cumbersome. Shim coils are usually not shielded, causing the fast switching required for DSU to generate eddy-currents in the MRI cryostat, inducing a long time constant for the shim field to settle. This needs to be compensated with pre-emphasis [Van Vaals 1990, Juchem 2010a, Fillmer 2016] in order for scanning with DSU not to last too long; preemphasis may in turn demand dedicated high power current amplifiers. Comparisons of images and inhomogeneities obtained under global and DSU techniques are shown in Fig. 2.2b&c.

2.3.4 High-Degree Spherical-Harmonic Shimming

Improving SH-based shimming performance implies increasing the SH degree, therefore adding more SH-based coils to the shim system. Very High Order Shimming (VHOS) systems are commercially available and equipped with SH-based coils up to partial 5^{th} and even 6^{th} degree. Such VHOS arrays have been employed for both global and dynamic shimming [Pan 2012, Chang 2018, Schwerter 2019, Hetherington 2021] (cf. Fig.2.3). An innovative interslice current updating technique is employed in [Schwerter 2019] to reduce eddy-currents. And in [Hetherington 2021], shim degeneracy is shown to cause slice-by-slice and simultaneous 2-slice (also known as multiband MB = 2) shimming to provide the same inhomogeneity reduction performance.

Although high quality images can be obtained using VHOS systems, with substantial improvement compared to a 2^{nd} degree SH baseline, this kind of system can be quite heavy ($> 60\,\text{kg}$), and is not a very compact solution.

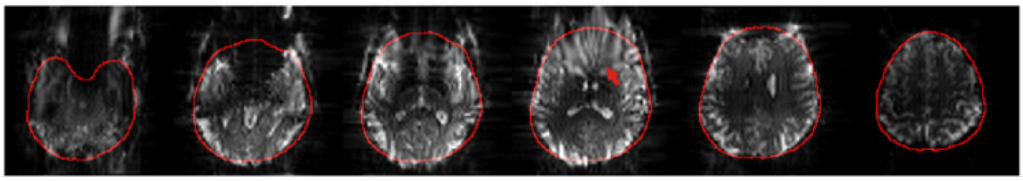

(a)

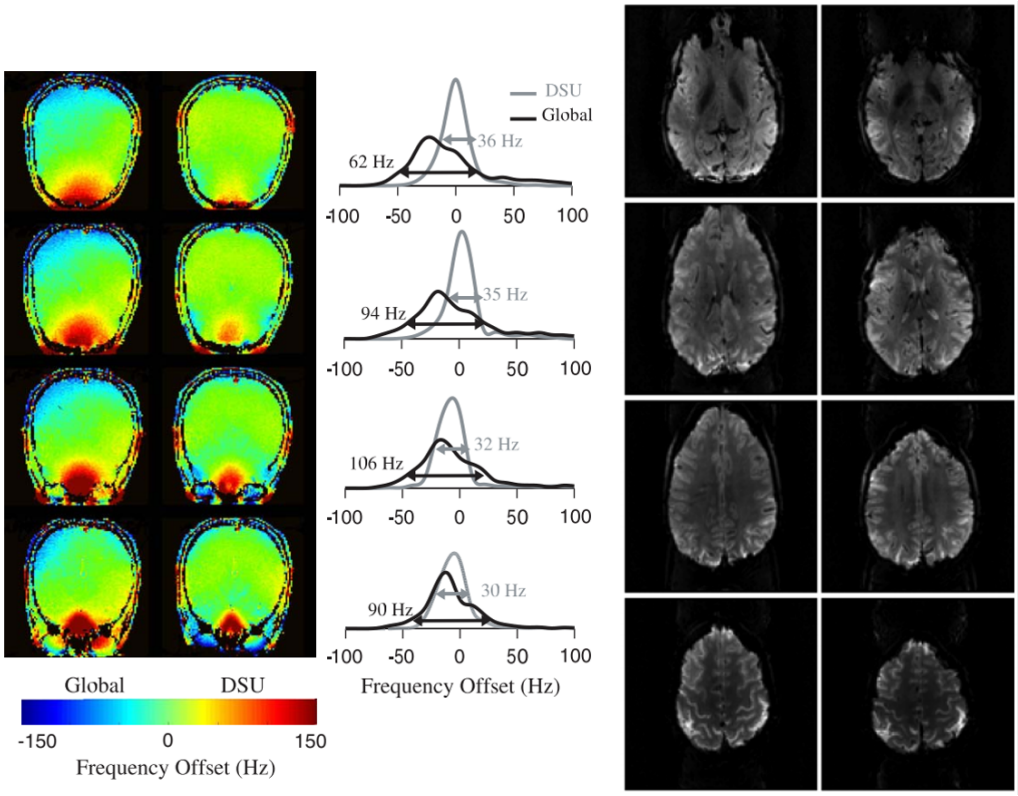

(b) (c)

Figure 2.2 – (a) Spherical harmonic global shimming up to 3rd degree at 7 T is shown to leave considerable geometric distortion in EPI across different slices in the human brain, acquired without PE acceleration and 0.7 ms echo-spacing (adapted from [Juchem 2015]). (b) B_0-fieldmap comparison between global and DSU shimming techniques (from [Koch 2006b]) shows reduction of magnetic field excursion at 4 T with 2nd degree SH coils. (c) EPI image comparison between no shim (left) and 3rd degree DSU shim (right) at 7 T, with DSU showing greater image quality (adapted from [Fillmer 2016]).

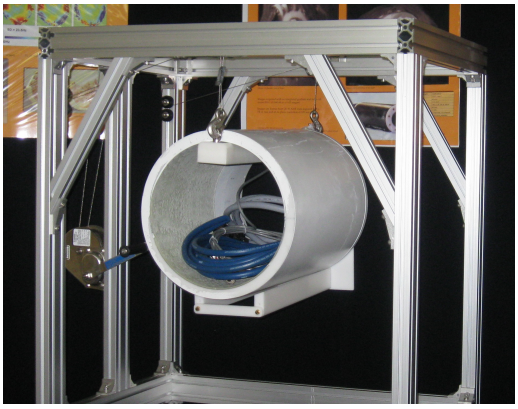

(a)

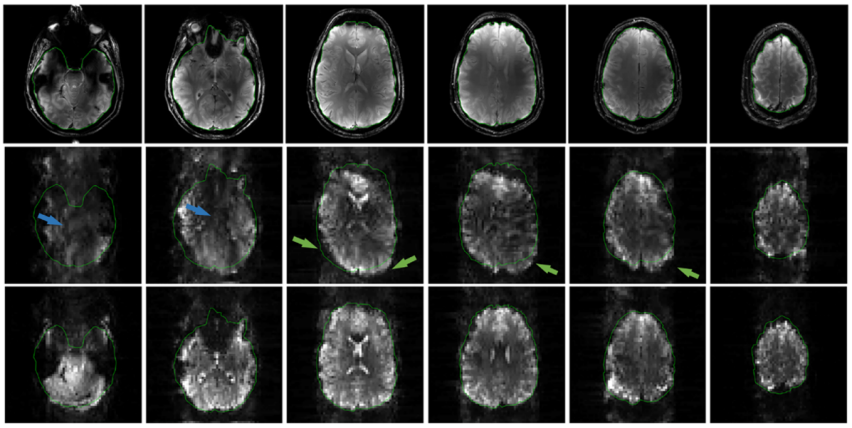

(b)

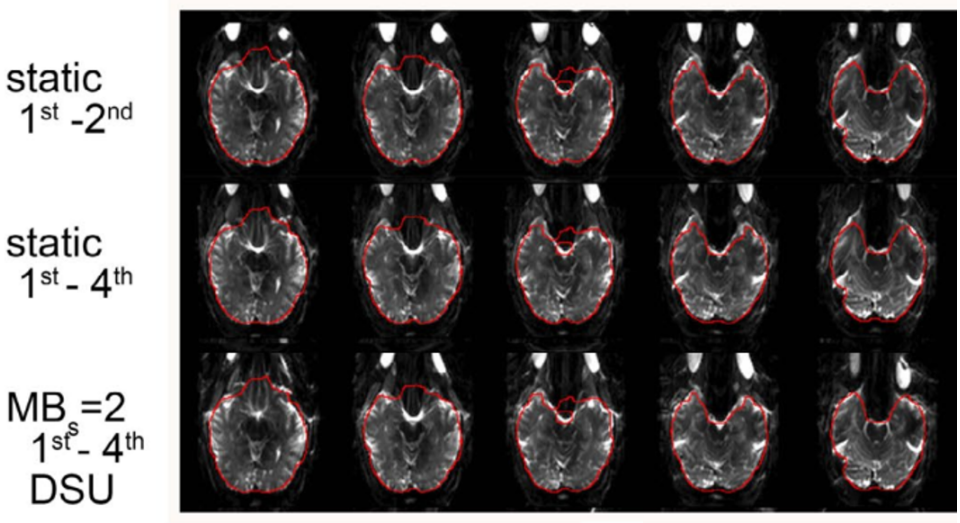

(c)

Figure 2.3 – (a) A VHOS system from Resonance Research, Inc, Billerica, MA, United States (rricorp.com). (b) from top to bottom row: anatomical reference (from GRE acquisition), EPI with 2^{nd} degree global shimming, EPI with 4^{th} and partial 5^{th} & 6^{th} degree global shimming. EPI acquisitions performed with GRAPPA = 2 and 0.58 ms echo spacing. Adapted from [Chang 2018]. (c) EPI acquisitions with MB = 2 under different SH degrees (up to 4^{th} degree and partial 5^{th} degree) and shimming techniques (global and DSU). In-plane acceleration factor of 3 and 0.9 ms echo spacing. Adapted from [Hetherington 2021].

2.4 Passive Shimming

In parallel with the developments around active SH-based shimming, subject-specific passive shimming was also explored. By strategically positioning magnetic materials around the subject's head, inhomogeneity in the brain can be compensated. These materials create magnetic fields as predicted by equation 1.44, and by judiciously choosing a magnetic material, its volume and its location, a magnetic field correction can be implemented.

Based on the conventional passive shimming used to shim the main magnet, a subject-specific approach using copy-toner magnetic ink was proposed in [Jesmanowicz 2001b, Jesmanowicz 2001a]. Ferroshim pieces were to be printed on specific positions in a matrix grid on a Mylar foil, which would be bent into a cylinder and placed around an RF coil. The optimization in this particular case consisted in minimizing the total volume of ferroshim under constraints on the SH coefficients resulting from the superposition of the inhomogeneous brain field with the ferroshim system field. This approach does not seem to have been widely adopted. Both the optimization computation and printing were time-consuming.

A somewhat intrusive approach was proposed in [Wilson 2002, Wilson 2003], where pyrolytic graphite, a strongly diamagnetic material was molded into an intra-oral shim (cf. fig. 2.4). Shims were also placed close to the ear canals. Mouth and ear passive shims led to inhomogeneity reduction in the inferior frontal cortex (IFC) and temporal lobes.

Koch *et al.* [Koch 2006a] showed the advantage of using both paramagnetic and diamagnetic materials for passive shimming, which increased the versatility of the correction magnetic fields that could be generated, improving homogeneity in the mouse brain at 9.4 T. Different stacking configurations of the materials (zinc and bismuth) were possible and placed inside pre-determined slots in a cylindrical former.

Further developments in passive shimming of the human brain were presented in [Yang 2011]. A small number of shim pieces were placed in an apparatus designed such that the position of the pieces could be optimally adjusted to match the subject's brain inhomogeneity.

Although some of the works on passive shimming provided good mitigation of δB_0 excursion, developments seem to have come to a halt in the early 2010's, coinciding with the development of Multi-Coil Arrays for B_0 shimming, the topic of the next section. The main disadvantage of any passive shimming method is the necessity of manually adjusting the position, form and quantity of shimming pieces, leading to a non-optimized workflow, hardly suitable for clinical practice.

2.5 Multi Coil Arrays

With passive shimming it was observed that localized magnetic field generation would be beneficial for susceptibility-induced inhomogeneity mitigation. Changing the magnetic field generated by a passive shim to address inter-subject variability, however, implies changing its volume, which is not practical. On the other hand, electric current passing

(a)

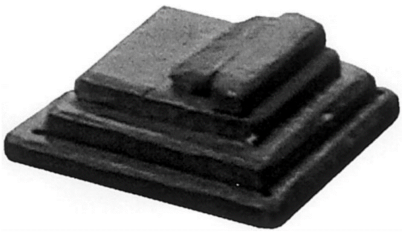

(b)

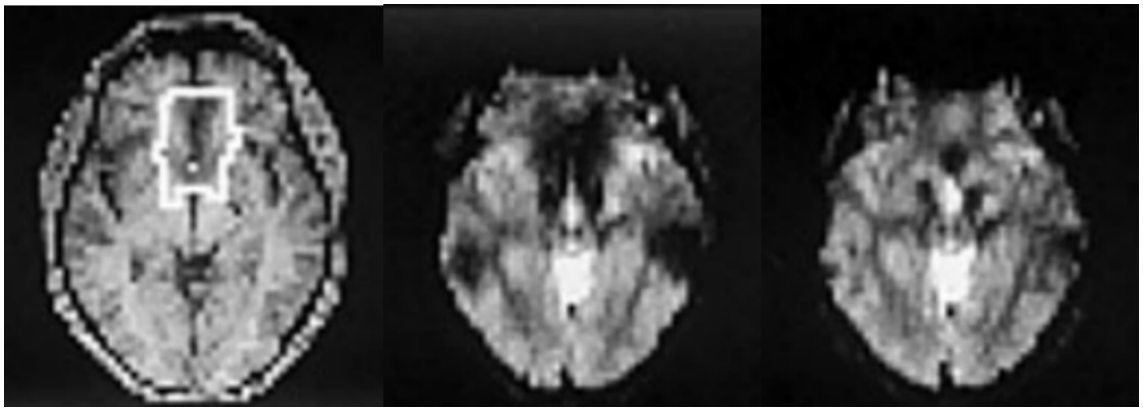

(c)

Figure 2.4 – (a) Printed ferroshims proposed in [Jesmanowicz 2001b] (from ismrm.org). (b) Intra-oral shim of pyrolytic graphite used in [Wilson 2002]. (c) Acquisitions at 3 T illustrating the use of oral and ear passive shims, with GRE anatomic reference, non-shimmed and passive-shimmed EPI from left to right (adapted from [Wilson 2002]).

through coils close to the shimming target could provide sufficient magnetic field for B_0 inhomogeneity mitigation and enough "malleability" for the field intensity, achieved by changing the electric current.

2.5.1 Localized Coils

One of the first such approaches, similar to the work of [Wilson 2002], was the use of a set of intra-oral coils for correcting IFC inhomogeneity [Hsu 2005]. This method provided a pattern of signal recovery similar to the intra-oral passive approach. However, this is a highly intrusive method, increasing patient discomfort in an already long and tedious examination. Also, despite adding the electric current intensity as a degree of freedom for addressing inter-subject variability, the magnetic field shape in the human IFC is too complex to be corrected by a single degree of freedom system.

2.5.2 Matrix Multi-Coil Arrays

Moving the coils out of the patient's head, the starting point of the MCA approach, was shown in [Juchem 2010b]. Six independently driven coils were placed adjacent to the frontal cortex. Currents were adjusted to reduce the inhomogeneity in the whole brain for

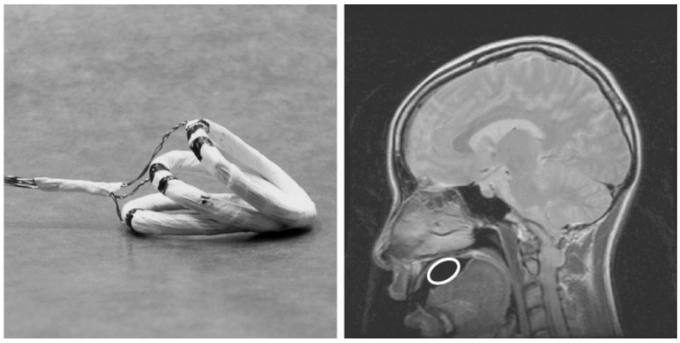

(a)

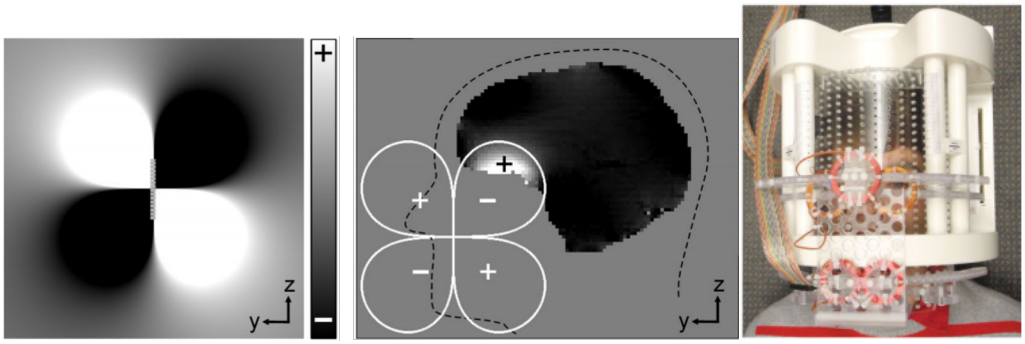

(b) (c)

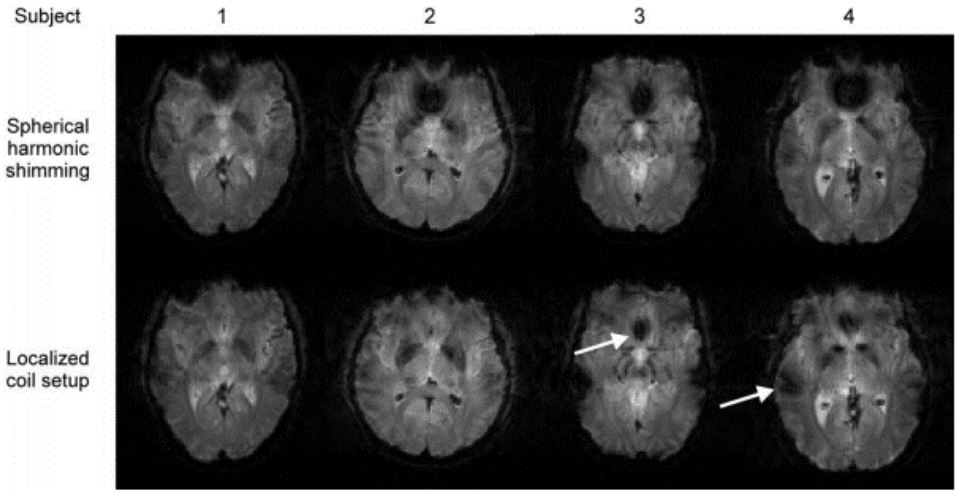

(d)

Figure 2.5 – First localized shim coil approaches for PFC shimming. (a) Intra-oral set implemented in [Hsu 2005]. (b) The dipolar field pattern produced by a circular coil is compared to the frontal cortex inhomogeneity, (c) PFC shim coils used in [Juchem 2010b], leading to the signal recovery in GE FLASH acquisitions shown in (d). Adapted from [Juchem 2010b].

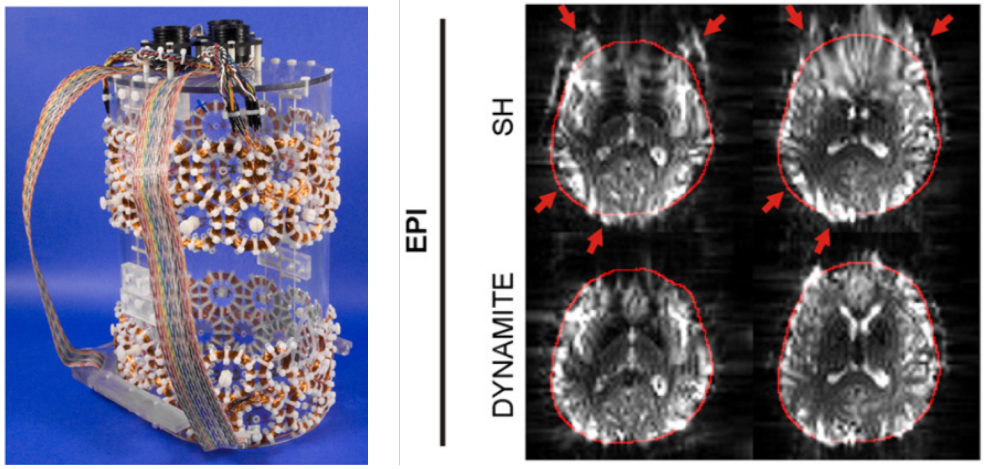

(a) (b)

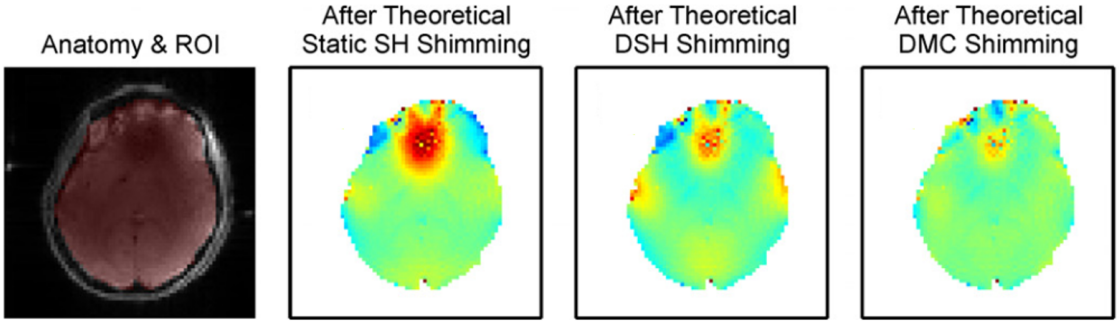

(c)

Figure 2.6 – (a) 48-channel matrix MCA used for static and dynamic shimming of the human brain (DYNAMITE). (b) Static 3rd degree SH shimming and DYNAMITE shimming are compared in EPI acquisitions at 7 T with no acceleration and 0.7 ms echo-spacing (as estimated from the 1.42 kHz phase-encoding BW). (c) Simulated fieldmaps from static and dynamic SH and DYNAMITE shimming are compared. Images adapted from [Juchem 2011] and [Juchem 2015].

each subject. The signal-loss artifact was, in some cases, fully eliminated in the Pre-Frontal Cortex (PFC), but mild signal-loss then appeared above the ear canals (cf. Fig. 2.5d). Nevertheless, great progress is seen comparatively to passive shimming approaches, since once the coil positions are established after the design process, only the electric currents will change, which can be performed in a time-efficient manner with the use of dedicated electronics.

By regularly placing several circular coils around a cylindrical former close to the human head, Juchem *et al.* [Juchem 2011] designed the first 48-channel matrix MCA (mMCA) applied for shimming of the human brain (cf. Fig. 2.6). In addition, these coils were employed in dynamic shimming, providing improved homogeneity when compared to static and dynamic SH shimming. The technique proposed by Juchem *et al.* was further denominated DYNAmic Multi-CoIl TEchnique (DYNAMITE). This mMCA arrangement was shown to be capable of modeling SH field shapes to good accuracy [Juchem 2013]; its

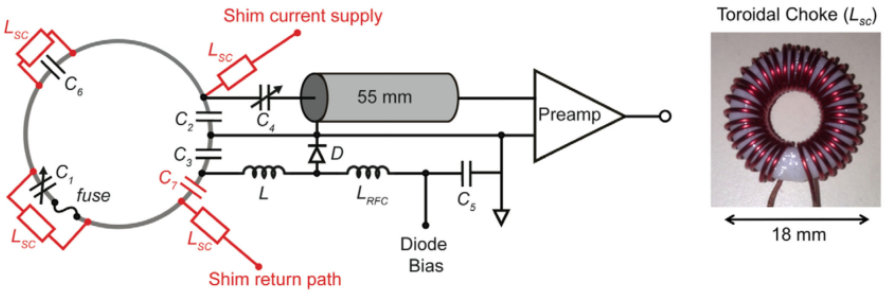

(a)

(b)

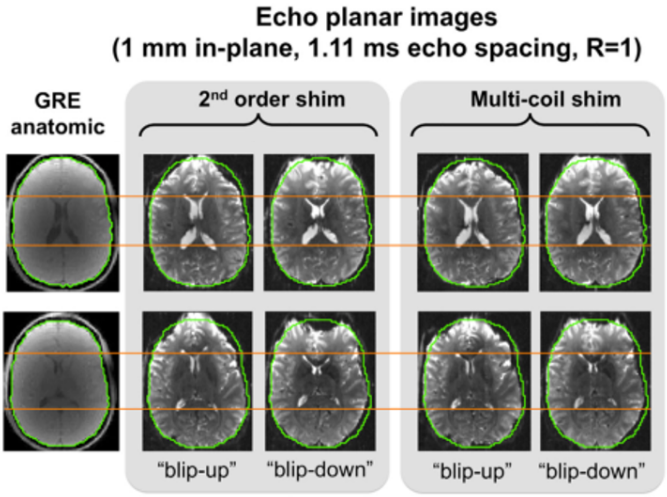

(c)

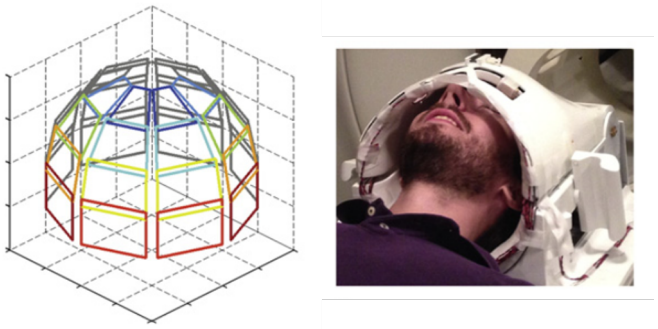

(d)

Figure 2.7 – The extra circuitry (in red) required to adapt an RF loop into a combined RF-B_0 shim loop is shown in (a). In (b), a before and after of the RF array converted into the combined RF-B_0 coil system is shown, and resulting EPI acquisitions at 3 T for two different volunteers (top and bottom rows) is shown in (c), with brain outline highlighted in green. Images adapted from [Stockmann 2016]. Another combined RF-B_0 array employed in [Truong 2014] is shown in (d).

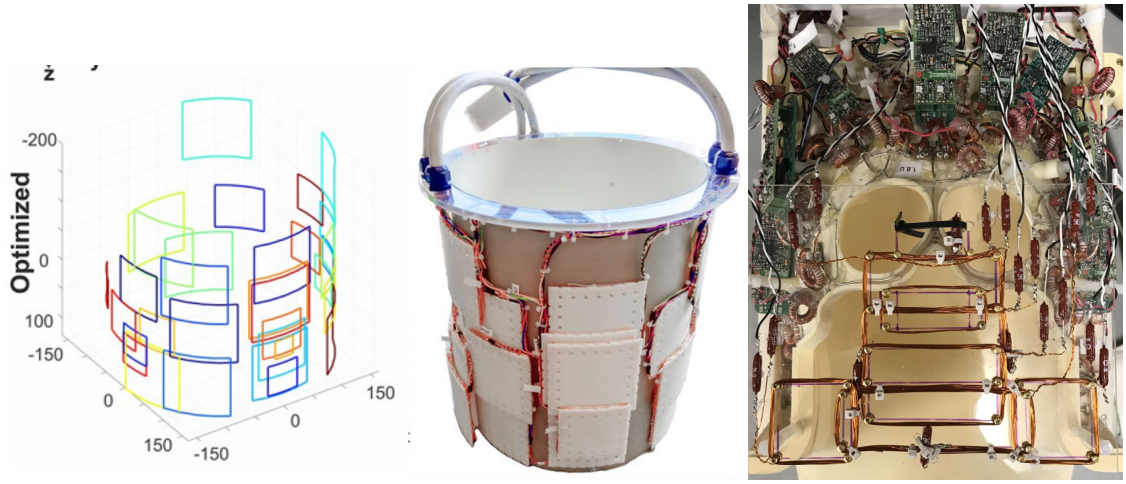

(a) (b)

Figure 2.8 – Optimized MCA developed in the works of [Aghaeifar 2020] (a); and optimized coils on a face-plate to address PFC inhomogeneity (b). From [Arango 2020].

benefits on EPI and spectroscopy were explored in [Juchem 2015, Juchem 2017b], where 48-channel DYNAMITE shimming was shown to outperform static 5^{th} degree and dynamic 4^{th} degree SH shimming.

To no surprise, this MCA technique started to be adopted by different research groups. Notable improvements in the hardware were done in the works of [Stockmann 2013, Han 2013, Truong 2014, Stockmann 2016], where the RF receive loops were adapted to run DC currents, boosting the capabilities of conventional RF arrays into the generation of B_0 shim fields, with minor degradation in SNR. This approach is rather economical in terms of space, with the only space requirement coming from inductive chokes used to connect the RF receive loops to the DC current driver while isolating the current driver from the RF signal.

In addition to high B_0 shimming performances in both static and dynamic techniques, the MCA approach doesn't suffer from the same drawback as dynamic SH shimming in terms of eddy-current generation, since the MCA coils are small and far from the cryostat.

The MCA approach has continued to be developed in recent works [Aghaeifar 2018, Zhou 2020, Esmaeili 2020], with some implementations addressing anatomies other than the brain [Topfer 2016, Darnell 2017, Darnell 2018]. It has also become available as a commercial solution provided by MR Shim, GmbH.

One important aspect of MCA design is its current driver. It should provide a stable current of at least 1 A (used in [Juchem 2011]), must be able to switch rapidly from one current configuration to the next for dynamic shimming, and finally be robust to gradient-induced voltages. The design of one such current driver is available through the Open Source Imaging initiative (https://www.opensourceimaging.org/project/current-driver-for-local-bo-shim-coils/). That driver has been implemented and employed in this work. Further details on the system topology are available in its original publication [Arango 2016].

2.5.3 MCA Optimization

The first matrix MCA and subsequent implementations were built either by regularly distributing circular coils around some cylindrical former, or took advantage of pre-existing RF loops. No optimization of the channels' positions and geometry had been performed.

With the perspective of brain imaging at 11.7 T with the Iseult MRI scanner [Quettier 2020], pushing the boundaries of MCA shimming capabilities is required, as B_0 inhomogeneity will be stronger. We expect that judicious placement and geometry of each coil will help boost performance for static whole-brain shimming. Therefore, we developed an optimized MCA design methodology for human brain shimming, based on Stream Functions Singular Value Decomposition from a large database of δB_0 fieldmaps. This method will be explained in chapters 3 and 5.

During the same time, Aghaeifar *et al.* also started to work on the optimization of MCA coil position and geometry, although their work is still limited to rectangular coil geometries [Aghaeifar 2020]. Interest in MCA optimization is rising, with novel optimization methodologies presented recently in [Arango 2020, Oh 2020, Cai 2020].

2.5.4 MCA Beyond B0 Shimming

The versatility of MCAs is not limited to their capacity of performing high performance static and dynamic shimming. Rudraptna *et al.* showed the use of an MCA for flip-angle homogenization through the application of a tailored $\delta B_0(\boldsymbol{x})$ shape between two RF excitation pulses [Rudrapatna 2016] with a single channel transmit RF coil. This idea has been extended with Integrated Shimming and Tip Angle Normalization (INSTANT), where joint optimization of RF, gradient and MCA waveforms has been performed to improve FA homogenization in single channel RF coils [Guerin 2020].

Furthermore, the proven ability of MCA to synthesize SH shaped fields such as linear gradients has allowed its use for image encoding: recent works show the possibility of producing concomitant gradient and shim fields with MCA's for MRI acquisition [Rudrapatna 2019, Juchem 2020b].

* * *
* *
*

Part II

Methodological Developments

Chapter 3

Dipole Boundary Method and Stream-Function SVD-Based Coil Design

Chapter Outline

This chapter was accepted for publication as:

B. Pinho Meneses and A. Amadon. *A fieldmap-driven few-channel shim coil design for MRI of the human brain.* Physics in Medicine & Biology, vol. 66, no. 1, 2020.

The methods presented in this chapter were object of the following patent:

B. Pinho Meneses and A. Amadon. *Static-magnetic-field shimming coil system for magnetic resonance imaging*, no. WO2020212463A1, October 2020.

The methods and principles contained in this chapter were also presented at international conferences as:

B. P. Meneses and A. Amadon. *The Dipole Boundary Method : a simple approach to compute stream functions for shim coil design.* In Proceedings of the 27th Annual Meeting of ISMRM, page 1476, Montreal, Canada, 2019.

B. P. Meneses and A. Amadon. *A novel few-channel coil design for human brain shimming based on stream function Singular Value Decomposition.* In Proceedings of the 27th Annual Meeting of ISMRM, page 1483, Montreal, Canada, 2019.

We exploit the inter-subject similarity of inhomogeneous static magnetic field patterns arising in the human brain under MRI examination to design a small set of shim coils providing performance equivalent to numerous coils based on high-order[1] Spherical Harmonics corrections. A hundred brain B_0-maps were first collected at 3 T. Ideal subject-specific electric current density stream functions are then computed with low power constraints, on a cylindrical surface. This step is repeated over tens of brain maps so that a Principal Component Analysis can be applied to the stream functions; the main components result in the small set of coils. Both 50-subject *hold-out* and 10-fold cross-validation are employed to evaluate consistency of the proposed system performance over *a posteriori* subjects. Simulations show that only 3 cylindrical coils manage to capture the principal magnetic field profiles in the human brain, thus providing a better static field inhomogeneity mitigation than that obtained from 16 unlimited-power high-order Spherical Harmonics coils, with inhomogeneity greatly reduced in the pre-frontal cortex compared to 2^{nd}-order shimmed baseline field acquisitions. The approach provides a very reduced channel count system for mitigating complex B_0-inhomogeneity patterns. Thus, a compact, cost-effective system could be conceived and driven by relatively low-budget electronics. The method should therefore have a strong impact in both Ultra-High and portable low-field MRI/MRS. Moreover, this technique can be applied to the design of shim coils addressing anatomies other than the brain.

[1]The terms order and degree are interchanged in this chapter relatively to the rest of this manuscript.

3.1 Introduction

As commercial and research MRI equipment move towards Ultra-High Field (UHF) of 7 T, 9.4 T, 10.5 T, 11.7 T and higher to benefit from increased SNR [Duyn 2012, Ladd 2018], therefore richness of information, we are faced with increased B_0 field inhomogeneity [Juchem 2017a], causing, if not properly mitigated, severe image artifacts, notably geometric distortion in Echo Planar Imaging (EPI) sequences [Jezzard 1995]. Spectroscopy is also largely impacted since inhomogeneous B_0 within a voxel translates into loss in spectral resolution.

The magnetic field distribution $\Delta B_0(\boldsymbol{x})$[2] generated on top of the main B_0 field due to non-homogeneous media (considering non-ferromagnetic media), of magnetic susceptibility $\chi(\boldsymbol{x})$, can be expressed as (adapted from [Salomir 2003]):

$$\nabla^2(\Delta B_0(\boldsymbol{x})) = \left(\nabla^2\chi(\boldsymbol{x}) - 3\frac{\partial^2\chi(\boldsymbol{x})}{\partial z^2}\right)\frac{B_0}{3} \tag{3.1}$$

Hence, the magnetic field inhomogeneity inside the human brain, apart from main field's intrinsic inhomogeneity, appears mainly due to magnetic susceptibility gradients between organic tissues and air cavities in the head. The intense B_0 field applied at their interface engenders non-uniform magnetization $\boldsymbol{M}(\boldsymbol{x})$ close to the brain, which in turn acts as a source of magnetic field characterized by a bounded current $\boldsymbol{J}_b(\boldsymbol{x}) = \boldsymbol{\nabla} \times \boldsymbol{M}(\boldsymbol{x})$ generating the inhomogeneous field distribution.

Global inhomogeneity in a specific anatomy is commonly measured as the standard deviation $\sigma(\gamma\Delta B_0)$ (with γ the gyro-magnetic ratio for the ^{1}H proton in Hz T^{-1}) computed from the sampled magnetic field excursion over all K voxels of interest, namely those in the human brain in this study.

From [Wald 2012], the geometric distortion in the Phase Encoding direction of an EPI sequence for a voxel with excursion ΔB_0 is

$$d_{PE} = \gamma\Delta B_0 \tau_{ES} FOV_{PE} \tag{3.2}$$

where, τ_{ES} is the echo-spacing time and FOV_{PE} the Field of View in the phase encoding direction. At $\tau_{ES} = 0.5$ ms, $FOV_{PE} = 200$ mm and $\gamma\Delta B_0 = 100$ Hz, geometric distortion computed from (3.2) would be 1.0 cm, which is quite large for high resolution images. Moreover, voxels with excursions higher than 100 Hz are predominant at 7 T specially in the frontal and temporal lobes, thus making the use of homogenizing systems necessary.

The efforts to homogenize, or shim, the B_0 field occurs in steps spanning from magnet design to patient specific corrections using dedicated coils driven by electric currents calculated for each patient.

Since any magnetic field within a spherical region free of magnetic field sources can be fully described by Solid Spherical Harmonics (SH) [Roméo 1984, Chmurny 1990], MRI systems are equipped with a set of so called SH shim coils to generate SH shaped fields and counteract $\Delta B_0(\boldsymbol{x})$ harmonic orders greater than zero. Then a calibration step just

[2] In this chapter, Δ is employed instead of δ.

before MRI scanning is performed, where a fieldmap of the anatomy of interest is acquired, SH coefficients are computed, and electric currents are injected into the coils to generate the adequate counteracting fields. Gradient coils perform the role of 1st order shim concomitantly with their dynamic space-encoding task. In addition, most UHF MRI systems present SH shim coils at 2nd and sometimes even 3rd order, totaling 5 to 12 coils dedicated to SH shimming.

For shimming of the human brain at UHF, built-in shim coils present in most MRI systems are insufficient to eliminate B_0-related artifacts [Pan 2012]. Hence, there is a need for improving the shim system.

While the straightforward approach would be to increase SH orders by building dedicated high-order shim inserts, as proposed in [Pan 2012], [Punchard 2013] and [Kim 2017], the amount of coils needed as a function of the desired SH order l is $N(l) = l^2 + 2l$. As more coils are needed, manufacturing complexity of both the shim insert and the associated electronics increases.

As a somewhat simpler alternative to SH based shimming, Multi-Coil Arrays (MCA) have been proposed for human brain shimming. They are composed of an array of independently-driven circular coils positioned around the subject's head [Juchem 2011, Aghaeifar 2018]. The concomitant use of RF receive loops to signal reception and B_0 shimming has also been employed, taking advantage of the existing loops in the RF coil for this new task [Han 2013,Stockmann 2013,Stockmann 2016]. Due to the many channels composing an MCA (up to 48 channels in reported experiments), the system is intrinsically versatile, i.e. used for global brain shimming but most useful for dynamic slice-by-slice shimming. The MCAs composed of 30 to 48 channels presented great performance when used in dynamic shimming and overall good performance in global shimming, comparable to 5th and 6th order SH inserts [Stockmann 2018].

So far, none of the systems described herein captured in their conception the specific magnetic field patterns in the human brain. As significant similarity among human brain fieldmaps can be observed, it could be argued that the generality of SH fields (as they form a basis for magnetic fields will null laplacian) is unnecessary when analyzing only one anatomy, and a smaller basis of field patterns could be obtained. Likewise, for MCAs, the location of the coils in most systems presented in the literature is likely non-optimal, with some recent exceptions in [Aghaeifar 2020] and [Meneses 2019c].

Principal Component Analysis (PCA) has been proved useful to extract a small set of field patterns that can represent the most common field distributions in the human brain fieldmaps [Adalsteinsson 1999]. Shim coils could then be designed based on those field patterns.

Inspired by such a possibility, we developed a novel approach [Meneses 2019b,Pinho Meneses 2020d] allowing improved performance on global shimming while keeping a small amount of total channels. In the hereby-presented approach, instead of applying PCA over 3D ΔB_0 fieldmaps, requiring creation of a common mask that may be bigger than some brains, causing unknown specification on the borders of the brain mask, PCA, by means of Singular Value Decomposition (SVD), is applied over more tractable 2D subject-

optimized current density Stream Functions [Peeren 2003] on a cylindrical geometry. The application of SVD on a representative collection of subject-optimized (SO) stream functions (SF) leads to a smaller set of SFs that are discretized into coils for composing a shim system.

We remark that similar approaches have been presented recently [Jia 2020,Arango 2019, Can 2019]. In [Jia 2020], fieldmaps are shimmed by unconstrained SH of some order (5^{th} or 6^{th}), then SO-SFs are computed under power dissipation constraints, tuned to achieve a residual field equivalent to that obtained by the SH shimming. Therefore, an indirect minimization of power dissipation is performed. While it is a sound approach, the resulting SVD based shim system presents relatively high channel count: 12 and 24 reported for achieving performances comparable to 5^{th} and 6^{th} order SH system, respectively, and although it is argued that these channel counts are lower than that of competing multi-coil array systems, manufacturing of SVD based coils is likely to be more complex, and therefore keeping the channel count to an even lesser amount should be favoured. Alternatively, a single channel SVD based shim system was presented in [Can 2019], providing relatively high inhomogeneity reduction that could be improved if more degrees of freedom were added.

In this paper, we give a detailed account of our SVD based coil design approach, and apply it on a database composed of 100 fieldmaps. It will be shown that a very reduced channel count system can be obtained by allowing power increase up to an optimal point.

3.2 Methods

The generation of a set of shim coils based on the actual magnetic field in the anatomy of interest consists mainly in three steps: (1) the acquisition of a representative database of fieldmaps $\Delta B_0^s(\boldsymbol{x})$ with $s = 1, ..., S$, S being the total number of subjects; (2) the computation of a SO-SF for each subject; and (3) the application of Singular Value Decomposition across the SO-SFs to obtain a reduced subset of SFs, subsequently discretized into windings at increasing cylinder radii.

3.2.1 Dipole Boundary Method for Field-map Based Coil Design

For SF computation, inspired by Inverse Boundary Element Methods (IBEM) [Pissanetzky 1992, Peeren 2003, Poole 2007b, Bringout 2015] and considering cylindrical geometry usually adopted for shim coil design, a simple inverse method is proposed to compute the SO-SFs. In this approach, a cylindrical surface is discretized into square loop elements, which may be considered as elementary magnetic dipoles, and the dipole current loop distribution is identified as the SF, providing a straightforward relation between magnetic field and SF.

We start by defining a conductive surface denoted $\mathcal{S} \subset \mathbb{R}^3$, a non-conductive region $\mathcal{V} \subset \mathbb{R}^3$ and a target magnetic field in the z direction inside $\mathcal{V}$ through an application $B_z : \mathcal{V} \to \mathbb{R}$.

For a target field $B_z(\boldsymbol{x})$, either a current density $\boldsymbol{j} : \mathcal{S} \to \mathbb{R}^3$ or its associated SF $\psi : \mathcal{S} \to \mathbb{R}$ needs to be computed in order to extract the wire patterns upon which a nominal current $\mathcal{I}$ must flow to generate B_z. From [Peeren 2003], those quantities relate by:

$$\boldsymbol{j}(\boldsymbol{x}) = \boldsymbol{\nabla}\psi(\boldsymbol{x}) \times \hat{\boldsymbol{n}}(\boldsymbol{x}) \tag{3.3}$$

with $\hat{\boldsymbol{n}}(\boldsymbol{x})$ the unitary vector normal to the surface $\mathcal{S}$ at point $\boldsymbol{x}$. Among several methods for coil design, the computation of the SF is preferred, since the inverse problem is simplified from estimating a vector field $\boldsymbol{j}$ into the estimation of a scalar function ψ. To address this inverse problem, we developed the Dipole Boundary Method (DBM) [Meneses 2019a], presented in detail herein.

In magneto-statics, the continuity equation for the current density is $\boldsymbol{\nabla} \cdot \boldsymbol{j}(\boldsymbol{x}) = 0$. Since $\boldsymbol{j}(\boldsymbol{x})$ is divergence-less, it can be broken up into a network of small current loops [Jackson 2007].

Naturally, this property remains valid for a surface. Therefore, any surface current density $\boldsymbol{j}(\boldsymbol{x})$ over a conductive surface $\mathcal{S}$ can be represented by an equivalent distribution of infinitesimal square loops with currents $I(\boldsymbol{x})$ over $\mathcal{S}$ (cf. Fig. 3.1a). It can be shown that the I-loop current network is equivalent to the $\boldsymbol{j}$-surface current density when it satisfies:

$$\boldsymbol{j}(\boldsymbol{x}) = \boldsymbol{\nabla} I(\boldsymbol{x}) \times \hat{\boldsymbol{n}}(\boldsymbol{x}). \tag{3.4}$$

Proof. To prove it, we compare the expression for the magnetic vector potential $\boldsymbol{A}(\boldsymbol{x})$ produced by a surface current density $\boldsymbol{j}(\boldsymbol{x})$ over a surface $\mathcal{S}$ with the potential produced by the equivalent system constituted by a network of infinitesimal square dipoles filling $\mathcal{S}$.

The surface current density $\boldsymbol{j}(\boldsymbol{x})$ produces a magnetic vector potential given by the following surface integral over $\mathcal{S}$

$$\boldsymbol{A}(\boldsymbol{x}) = \frac{\mu_0}{4\pi} \int_{\mathcal{S}} \frac{\boldsymbol{j}(\boldsymbol{x}')}{|\boldsymbol{x} - \boldsymbol{x}'|}\, ds'. \tag{3.5}$$

Let us now consider the configuration in which the same linear current density is represented by a network of square dipoles. The magnetic vector potential produced by a single dipole moment $\boldsymbol{m}$ located at $\boldsymbol{x}_m$ is given by

$$\boldsymbol{A}(\boldsymbol{x}) = \frac{\mu_0}{4\pi} \frac{\boldsymbol{m} \times (\boldsymbol{x} - \boldsymbol{x}_m)}{|\boldsymbol{x} - \boldsymbol{x}_m|^3}. \tag{3.6}$$

The vector field produced by a dipole network for the same domain $\mathcal{S}$ will be given by

$$\boldsymbol{A}(\boldsymbol{x}) = \frac{\mu_0}{4\pi} \int_{\mathcal{S}^{\mathrm{o}}} \frac{[I(\boldsymbol{x}')\hat{\boldsymbol{n}}(\boldsymbol{x}')] \times (\boldsymbol{x} - \boldsymbol{x}')}{|\boldsymbol{x} - \boldsymbol{x}'|^3}\, ds', \tag{3.7}$$

where $\mathcal{S}^{\mathrm{o}}$ is the interior of the set $\mathcal{S}$, with $\mathcal{S} = \mathcal{S}^{\mathrm{o}} + \partial\mathcal{S}$ and $\partial\mathcal{S}$ representing the boundary of $\mathcal{S}$.

Equation (3.7) can be further developed by applying particular vector identities. From

$$\nabla' \left(\frac{1}{|\boldsymbol{x} - \boldsymbol{x}'|} \right) = \frac{\boldsymbol{x} - \boldsymbol{x}'}{|\boldsymbol{x} - \boldsymbol{x}'|^3}, \tag{3.8}$$

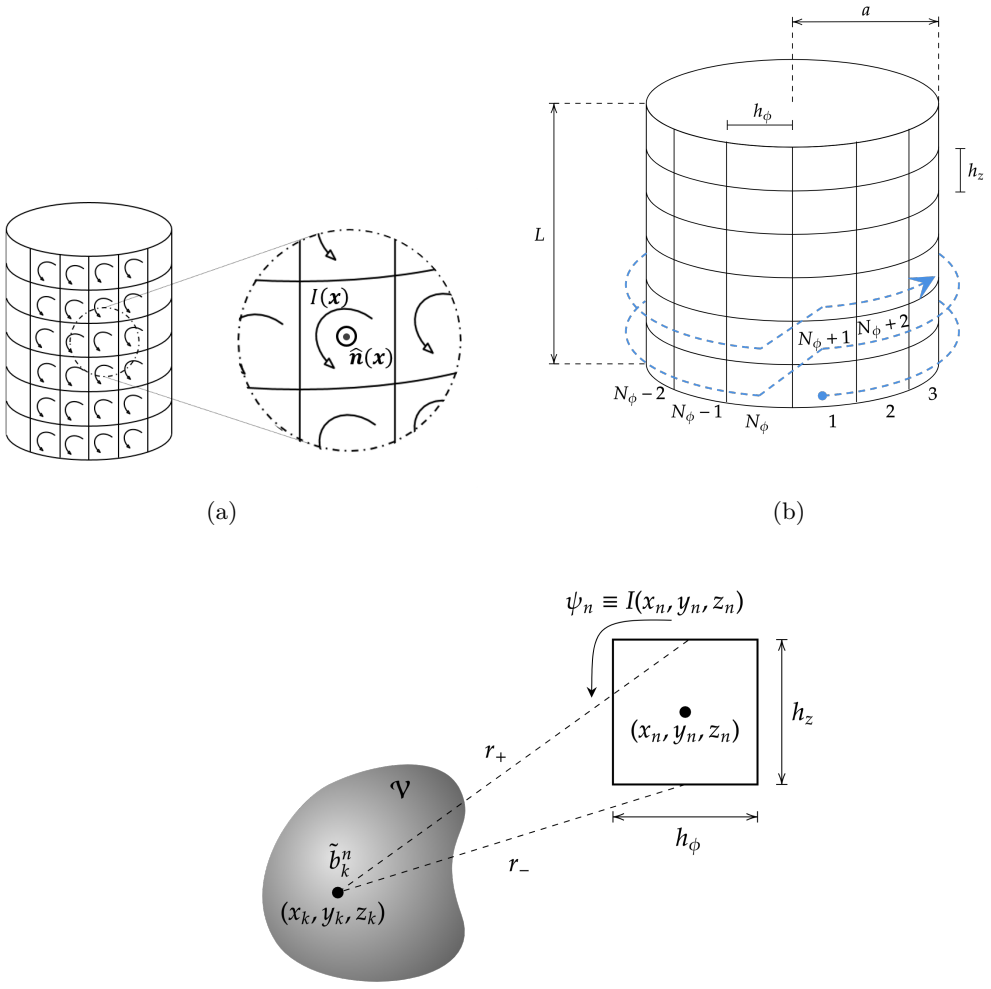

Figure 3.1 – (a) Surface current density $\boldsymbol{j}(\boldsymbol{x})$ represented by a distribution of dipoles of current $I(\boldsymbol{x})$ over the cylindrical surface. $\hat{\boldsymbol{n}}(\boldsymbol{x})$ is the unitary normal vector at each point over the surface, (b) subsequent rectangular elements enumeration and (c) dipole with current ψ_n generating a magnetic field $\tilde{b}_k^n$ in a control point of $\mathcal{V}$.

where ∇' is the gradient over the variable $\boldsymbol{x}'$, the vector potential produced by the dipole network can be expressed as

$$\boldsymbol{A}(\boldsymbol{x}) = \frac{\mu_0}{4\pi} \int_{\mathcal{S}^{\mathrm{o}}} [I(\boldsymbol{x}')\hat{\boldsymbol{n}}(\boldsymbol{x}')] \times \nabla' \left(\frac{1}{|\boldsymbol{x} - \boldsymbol{x}'|} \right) ds'. \tag{3.9}$$

For any scalar function $\psi(\boldsymbol{x})$ and vector field $\boldsymbol{u}(\boldsymbol{x})$, the following identity holds

$$\nabla \times (\psi \boldsymbol{u}) = \psi(\nabla \times \boldsymbol{u}) + \nabla\psi \times \boldsymbol{u}, \tag{3.10}$$

therefore

$$[I(\boldsymbol{x}')\hat{\boldsymbol{n}}(\boldsymbol{x}')] \times \nabla' \left(\frac{1}{|\boldsymbol{x} - \boldsymbol{x}'|} \right) = \frac{1}{|\boldsymbol{x} - \boldsymbol{x}'|} \nabla' \times [I(\boldsymbol{x}')\hat{\boldsymbol{n}}(\boldsymbol{x}')] - \nabla' \times \left[\frac{I(\boldsymbol{x}')\hat{\boldsymbol{n}}(\boldsymbol{x}')}{|\boldsymbol{x} - \boldsymbol{x}'|} \right], \tag{3.11}$$

and the expression for the magnetic potential vector becomes

$$\boldsymbol{A}(\boldsymbol{x}) = \frac{\mu_0}{4\pi} \left\{ \int_{\mathcal{S}^{\mathrm{o}}} \frac{1}{|\boldsymbol{x} - \boldsymbol{x}'|} \nabla' \times [I(\boldsymbol{x}')\hat{\boldsymbol{n}}(\boldsymbol{x}')] \, ds' - \int_{\mathcal{S}^{\mathrm{o}}} \nabla' \times \left[\frac{I(\boldsymbol{x}')\hat{\boldsymbol{n}}(\boldsymbol{x}')}{|\boldsymbol{x} - \boldsymbol{x}'|} \right] ds' \right\}. \tag{3.12}$$

We can show that

$$\nabla' \times [I(\boldsymbol{x}')\hat{\boldsymbol{n}}(\boldsymbol{x}')] = \nabla' I(\boldsymbol{x}') \times \hat{\boldsymbol{n}}(\boldsymbol{x}') \tag{3.13}$$

and

$$\nabla' \times \left[\frac{I(\boldsymbol{x}')}{|\boldsymbol{x} - \boldsymbol{x}'|} \hat{\boldsymbol{n}}(\boldsymbol{x}') \right] = \nabla' \left(\frac{I(\boldsymbol{x}')}{|\boldsymbol{x} - \boldsymbol{x}'|} \right) \times \hat{\boldsymbol{n}}(\boldsymbol{x}'), \tag{3.14}$$

then, the integral of the second term on the right side of (3.12) becomes

$$\int_{\mathcal{S}^{\mathrm{o}}} \nabla' \times \left[\frac{I(\boldsymbol{x}')\hat{\boldsymbol{n}}(\boldsymbol{x}')}{|\boldsymbol{x} - \boldsymbol{x}'|} \right] ds' = \int_{\mathcal{S}^{\mathrm{o}}} \nabla' \left(\frac{I(\boldsymbol{x}')}{|\boldsymbol{x} - \boldsymbol{x}'|} \right) \times \hat{\boldsymbol{n}}(\boldsymbol{x}') \, ds'. \tag{3.15}$$

We can apply the following identity on the right side of (3.15)

$$\int \nabla\psi(\boldsymbol{x}) \times \hat{\boldsymbol{n}}(\boldsymbol{x}) ds = -\oint \psi(\boldsymbol{x}) \, d\boldsymbol{l}, \tag{3.16}$$

leading to

$$\int_{\mathcal{S}^{\mathrm{o}}} \nabla' \left(\frac{I(\boldsymbol{x}')}{|\boldsymbol{x} - \boldsymbol{x}'|} \right) \times \hat{\boldsymbol{n}}(\boldsymbol{x}') \, ds' = -\oint_{\partial\mathcal{S}} \frac{I(\boldsymbol{x}')}{|\boldsymbol{x} - \boldsymbol{x}'|} \tag{3.17}$$

Finally,(3.12) becomes

$$\boldsymbol{A}(\boldsymbol{x}) = \frac{\mu_0}{4\pi} \left[\int_{\mathcal{S}^{\mathrm{o}}} \frac{\nabla' I(\boldsymbol{x}') \times \hat{\boldsymbol{n}}(\boldsymbol{x}')}{|\boldsymbol{x} - \boldsymbol{x}'|} \, ds' + \oint_{\partial\mathcal{S}} \frac{I(\boldsymbol{x}')}{|\boldsymbol{x} - \boldsymbol{x}'|} \, d\boldsymbol{l}' \right]. \tag{3.18}$$

To be able to compare the magnetic vector potential as expressed in (3.18) with the one in (3.5), the integral over $\mathcal{S}$ in the latter needs to be decoupled into two integrals over $\mathcal{S}^{\mathrm{o}}$ and $\partial\mathcal{S}$, thus obtaining

$$\boldsymbol{A}(\boldsymbol{x}) = \frac{\mu_0}{4\pi} \left[\int_{\mathcal{S}^{\mathrm{o}}} \frac{\boldsymbol{j}(\boldsymbol{x}')}{|\boldsymbol{x} - \boldsymbol{x}'|} \, ds' + \oint_{\partial\mathcal{S}} \frac{I(\boldsymbol{x}')}{|\boldsymbol{x} - \boldsymbol{x}'|} \, d\boldsymbol{l}' \right]. \tag{3.19}$$

Equations (3.19) and (3.18) are simply two different forms of expressing the magnetic vector potential produced by the same current distribution. Comparing the two expressions it is clear that, for $\boldsymbol{A}(\boldsymbol{x})$ to be the same in both cases,

$$\boldsymbol{j}(\boldsymbol{x}) = \nabla I(\boldsymbol{x}) \times \hat{\boldsymbol{n}}(\boldsymbol{x}), \tag{3.20}$$

concluding the proof.

□

Identifying (3.3) and (3.4), $I(\boldsymbol{x})$ is a SF for $\boldsymbol{j}(\boldsymbol{x})$. The SF takes on a physical meaning as the current carried by each square loop in the network, therefore it can be directly related to the magnetic field. By defining a finite grid with a limited number of elementary loops, a piece-wise constant basis function is chosen for the SF estimation. The $I(\boldsymbol{x})$-current loop distribution constitutes a stream function for the current density $\boldsymbol{j}$; i.e. the isoheight contours of $I(\boldsymbol{x})$ provide the current paths needed to approximate $\boldsymbol{j}$ [Peeren 2003]. There is no need to impose connectivity between the elementary current loop weightings, although power regularization will help obtain a smoother stream function, therefore less wire packing and less tortuous pathways.

From Biot-Savart law, the relation between the magnetic field $B_z(\boldsymbol{x})$ and the SF $\psi(\boldsymbol{x}) \equiv I(\boldsymbol{x})$ is easily obtained. The total magnetic field generated by the dipole network is simply the sum of the contributions of each dipole.

The coil former upon which the wires will be placed is defined as a cylinder of radius a and length L.

$$\mathcal{S} = \left\{(x, y, z) | x^2 + y^2 = a^2, -\frac{L}{2} \leq z \leq \frac{L}{2}\right\} \tag{3.21}$$

As the cylindrical surface is then discretized into square elements, let h be the desired discretization step in φ and z; the number of elements in the azimuthal direction is $N_\varphi = \lfloor 2\pi a/h \rceil$ and $N_z = \lfloor L/h \rceil$ in the z direction. As a consequence, effective discretization steps are $h_\varphi = 2\pi a/N_\varphi$ and $h_z = L/N_z$, generating rectangular elements which tend to squares as h is reduced. Center coordinates $\boldsymbol{x}_n$ of dipole n such as defined in Fig. 3.1b are:

$$\boldsymbol{x}_n = \left(a\cos\left(\alpha\frac{h_\varphi}{a}\right), a\sin\left(\alpha\frac{h_\varphi}{a}\right), -\frac{L}{2} + \frac{2\beta - 1}{2}h_z\right) \tag{3.22}$$

with $\alpha \equiv (n-1) \bmod N_\varphi$, $\beta = (n - \alpha - 1)/N_\varphi + 1$ and $n = 1, ..., N$, with $N = N_\varphi \times N_z$

Let the volume $\mathcal{V}$ be the anatomy of interest, the magnetic field excursion can be mapped over the K voxels composing the discretized anatomy. The mapping is used as target field $\boldsymbol{b} \in \mathbb{R}^K$, of elements $b_k = \Delta B_0(x_k, y_k, z_k)$ where $k = 1, ..., K$. Biot-Savart law is then applied to compute the contribution $\tilde{b}_k^n$ of dipole n with current $\psi_n \equiv I(x_n, y_n, z_n)$ to the total magnetic field in z at point (x_k, y_k, z_k). In the limit where $h \ll r_\pm$ the magnitude of the magnetic field is approximated by:

$$\tilde{b}_k^n = c_{k,n}\psi_n \tag{3.23}$$

with

$$c_{k,n} = \left[\frac{\mu_0}{4\pi a}(x_n x_k + y_n y_k - a^2)\left(\frac{1}{r_-^3} - \frac{1}{r_+^3}\right)\right] h_\varphi \tag{3.24}$$

and

$$r_{\pm} = \sqrt{(x_k - x_n)^2 + (y_k - y_n)^2 + \left[z_k - \left(z_n \pm \frac{h_z}{2}\right)\right]^2} \tag{3.25}$$

The total magnetic field in $\boldsymbol{x}_k$ generated by the current distribution is

$$\tilde{b}_k = \sum_{n=1}^{N} c_{k,n}\psi_n \tag{3.26}$$

Finally, in a matrix/vector form:

$$\tilde{\boldsymbol{b}} = \mathbf{C}\boldsymbol{\psi}, \tag{3.27}$$

with $\mathbf{C} = (c_{k,n}) \in \mathbb{R}^{K,N}$, $\boldsymbol{\psi} \in \mathbb{R}^N$ and $\tilde{\boldsymbol{b}} \in \mathbb{R}^K$. The quadratic error between the target field and the coil field

$$\varepsilon^2 = |\boldsymbol{b} - \tilde{\boldsymbol{b}}|^2 = |\boldsymbol{b} - \mathbf{C}\boldsymbol{\psi}|^2 \tag{3.28}$$

needs to be minimized by an appropriate choice of $\boldsymbol{\psi}$.

In addition to the quadratic error between target and produced magnetic field, power dissipation minimization needs to be taken into account for obtaining a feasible coil design. Mathematically, consideration of physical parameters of the coil such as power dissipation and stored magnetic energy acts as regularization for an otherwise ill-posed problem.

Inside any conducting region $\mathcal{V}_c$ with current density $\boldsymbol{J}(\boldsymbol{x})$ and electric conductivity κ, power dissipation can be calculated by:

$$P = \int\limits_{\mathcal{V}_c} \frac{|\boldsymbol{J}(\boldsymbol{x})|^2}{\kappa}\, dv. \tag{3.29}$$

If the region is a homogeneous thin sheet of thickness t,

$$P = \frac{1}{t\kappa} \int\limits_{\mathcal{S}} |\nabla\psi(\boldsymbol{x}) \times \hat{\boldsymbol{n}}(\boldsymbol{x})|^2\, ds. \tag{3.30}$$

For a cylindrical coil, the integral becomes:

$$P = \frac{1}{t\kappa} \int\limits_{\mathcal{S}} \left[\left(\frac{1}{a}\frac{\partial\psi}{\partial\varphi}\right)^2 + \left(\frac{\partial\psi}{\partial z}\right)^2\right] ds, \tag{3.31}$$

which is discretized into:

$$P \approx \frac{h_\varphi h_z}{t\kappa} \sum_{n=1}^{N} \left[\left(\frac{\psi_{n+1} - \psi_n}{h_\varphi}\right)^2 + \left(\frac{\psi_{n+N_\varphi} - \psi_n}{h_z}\right)^2\right]. \tag{3.32}$$

With a discretization performed to make the elements as close as possible to squares ($h_z \approx h_\varphi$):

$$P \approx \frac{1}{t\kappa} \sum_{n=1}^{N} \left[(\psi_{n+1} - \psi_n)^2 + (\psi_{n+N_\varphi} - \psi_n)^2\right] \tag{3.33}$$

or

$$P \approx \boldsymbol{\psi}^T \mathbf{R} \boldsymbol{\psi} \tag{3.34}$$

where $\mathbf{R} \in \mathbb{R}^{N\times N}$ is a block Toeplitz matrix

$$\mathbf{R} = \frac{2}{\kappa t}\begin{bmatrix} \mathbf{W} & -\mathbf{I} & \mathbf{0} & \dots & \mathbf{0} \\ -\mathbf{I} & \mathbf{W} & -\mathbf{I} & \dots & \mathbf{0} \\ \mathbf{0} & -\mathbf{I} & \mathbf{W} & \dots & \mathbf{0} \\ \vdots & \vdots & \vdots & \ddots & \vdots \\ \mathbf{0} & \mathbf{0} & \mathbf{0} & \dots & \mathbf{W} \end{bmatrix} \tag{3.35}$$

with $\mathbf{W} \in \mathbb{R}^{N_\varphi\times N_\varphi}$ a circulant matrix of first column $\boldsymbol{w} = \begin{bmatrix} 4 & -1 & 0 & \dots & 0 & -1 \end{bmatrix}^T$, $\mathbf{I} \in \mathbb{R}^{N_\varphi\times N_\varphi}$ an identity matrix and $\mathbf{0} \in \mathbb{R}^{N_\varphi\times N_\varphi}$ a null matrix.

To impose that no current flows outwards or inwards of the cylinder from its top or bottom, the SF value on each of these boundaries must be constant [Pissanetzky 1992, Peeren 2003, Poole 2007b, Bringout 2015]. This forces the first N_φ elements in $\boldsymbol{\psi}$ to be of equal unknown value $\boldsymbol{\psi}'_1$; and also forces the last N_φ elements of $\boldsymbol{\psi}$ to have equal unknown values $\boldsymbol{\psi}'_{N'}$. This imposition is expressed by the computation of a reduced SF $\boldsymbol{\psi}'$ with $N' = N - 2(N_\varphi - 1)$ elements such that $\psi'_i = \psi_{i+N_\varphi-1}$. The boundary-conditioned SF $\boldsymbol{\psi}'$ relates to $\boldsymbol{\psi}$ through the matrix formulation: $\boldsymbol{\psi} = \boldsymbol{\Gamma}\boldsymbol{\psi}'$ with $\boldsymbol{\Gamma} \in \mathbb{R}^{N\times N'}$ of form:

$$\boldsymbol{\Gamma} = \Big[\underbrace{\boldsymbol{e}_1 \quad \dots \quad \boldsymbol{e}_1}_{N_\varphi \text{ times}} \quad \boldsymbol{e}_2 \quad \dots \quad \boldsymbol{e}_{N'-1} \quad \underbrace{\boldsymbol{e}_{N'} \quad \dots \quad \boldsymbol{e}_{N'}}_{N_\varphi \text{ times}}\Big]^T \tag{3.36}$$

where $\{\boldsymbol{e}_i\}$ is the standard basis for $\mathbb{R}^{N'}$, e.g. $\boldsymbol{e}_1 = \begin{bmatrix} 1 & 0 & \dots & 0 \end{bmatrix}^T$.

Assembling power consumption and quadratic field error, optimal $\boldsymbol{\psi}$ is

$$\boldsymbol{\psi}(\lambda) = \boldsymbol{\Gamma} \underset{\boldsymbol{\psi}'\in\mathbb{R}^{N'}}{\operatorname{argmin}} \lambda \boldsymbol{\psi}'^T \boldsymbol{\Gamma}^T \mathbf{R} \boldsymbol{\Gamma} \boldsymbol{\psi}' + ||\boldsymbol{b} - \mathbf{C}\boldsymbol{\Gamma}\boldsymbol{\psi}'||_2^2 \tag{3.37}$$

where λ is a regularization parameter that can be tuned to balance the solution in terms of reducing power dissipation or increasing magnetic field fidelity.

The functional is then minimized by:

$$\boldsymbol{\psi}(\lambda) = \boldsymbol{\Gamma}\mathbf{D}\boldsymbol{\Gamma}^T\mathbf{C}^T\boldsymbol{b} \tag{3.38}$$

with

$$\mathbf{D} = [\boldsymbol{\Gamma}^T(\lambda\mathbf{R} + \mathbf{C}^T\mathbf{C})\boldsymbol{\Gamma}]^{-1}. \tag{3.39}$$

We note that any coil design method could be used in this step. Nevertheless, the method presented herein does not require a third-party triangular mesher, contrarily to conventional IBEM, and the adoption of a piecewise constant basis function for the SF avoids the computation of derivatives of the SF within each element and subsequent integration over the elemental surface. The contribution of each element to the magnetic field is restricted to the edges of the squares and is easily calculated. On the other hand, accuracy of this approximation will depend on mesh resolution, and very high resolution may be a computational burden. Appropriate choice of h will depend on the coil radius, and on the extent of the target field domain.

The SF is then used to obtain the geometric center of the wires that must be placed over the coil former so that a magnetic field of high fidelity to the target is generated.

The process of discretization into windings is performed by fixing a minimum allowed distance δ_w between any two wire's geometric centers. This distance bounds the maximum section w_s of circular wire that can be employed on the actual manufacturing of the coil and will also dictate the current $\mathcal{I}$ that needs to flow in the wires to generate the magnetic field that would be generated by $\boldsymbol{j}(\boldsymbol{x}) = \boldsymbol{\nabla}\psi(\boldsymbol{x}) \times \hat{\boldsymbol{n}}(\boldsymbol{x})$. Smaller δ_w provides higher magnetic field fidelity with the field that would be generated by the continuous current distribution $\boldsymbol{j}(\boldsymbol{x})$. On the other hand, for the relatively complex patterns that will be presented, low δ_w might make manufacturing difficult. In addition, power dissipation would increase.

From a nominal current $\mathcal{I}$, a family of isoheight curves of ψ representing the geometric centers of the coil wires can be obtained as detailed in [Peeren 2003]. Since δ_w is imposed, the nominal current needs to be calculated such that the resulting discretization into windings does not violate this supremum, a condition satisfied by:

$$\begin{aligned} \mathcal{I} &= \max_{\boldsymbol{x}\in\mathcal{S}} |\boldsymbol{j}(\boldsymbol{x})|\delta_w \\ &= \max_{\boldsymbol{x}\in\mathcal{S}} |\boldsymbol{\nabla}\psi(\boldsymbol{x})|\delta_w. \end{aligned} \tag{3.40}$$

Having obtained the family of loops that compose the coil for a given δ_w, let L_c with $c = 1, \ldots, C$ be the length of each of a total of C loops; the resistance of the coil can be calculated by:

$$r = \frac{1}{\sigma w_s} \sum_{c=1}^{C} L_c \tag{3.41}$$

which in turn is used to calculate the coil's power dissipation:

$$\mathcal{P} = r\mathcal{I}^2 \tag{3.42}$$

At nominal current, the inhomogeneity of the shimmed fieldmap is the standard deviation of the residual field: $\sigma\left(\boldsymbol{b} - \mathbf{C}\boldsymbol{\psi}\right)$. For purposes of performance evaluation, we define a metric η for inhomogeneity reduction (percentage rate):

$$\eta = 100 \times \left(1 - \frac{\sigma(\boldsymbol{b} - \mathbf{C}\boldsymbol{\psi})}{\sigma(\boldsymbol{b})}\right) \tag{3.43}$$

Finally, different values of λ will provide different values of $\mathcal{P}$ and η. Decreasing λ allows inhomogeneity reduction to increase (by reducing the quadratic error ε^2), at the cost of power dissipation increase. Hence λ needs to be tuned to obtain an appropriate trade-off. In the subsequent group analysis, for each subject in the database, the regularization parameter is tuned such that the resulting subject-optimal coil dissipates some desired target power $\mathcal{P}_T$; this process is equivalent to solving the inhomogeneity minimization under power constraints.

3.2.2 Singular Value Decomposition of Optimal SFs

For a fixed coil former geometry and individual regularization parameter λ_s, each subject's offset map $\boldsymbol{b}_s = \begin{bmatrix}\Delta B_0^s(\boldsymbol{x}_1) & \Delta B_0^s(\boldsymbol{x}_2) & \dots & \Delta B_0^s(\boldsymbol{x}_{K_s})\end{bmatrix}^T$ is input as target field in the DBM algorithm, outputting a SO-SF $\boldsymbol{\psi}_s$.

From the resulting set of S SO-SFs $\boldsymbol{\psi}_s$ calculated from a representative database of S subjects, the goal is to obtain a reduced set of M ($< S$) new SFs that could approximate the effects of each SO-SF, within a certain error, by adjusting the coefficients of their linear combination. To do so, Singular Value Decomposition is applied.

The SFs calculated for each target field in the database are assembled into a matrix $\boldsymbol{\Psi}_{\mathrm{DB}} = \begin{bmatrix}\boldsymbol{\psi}_1 & \boldsymbol{\psi}_2 & \dots & \boldsymbol{\psi}_S\end{bmatrix} \in \mathbb{R}^{N\times S}$. The matrix $\boldsymbol{\Psi}_{\mathrm{DB}}$ possesses an SVD, expressed as:

$$\boldsymbol{\Psi}_{\mathrm{DB}} = \mathbf{U}\boldsymbol{\Sigma}\mathbf{V}^T \tag{3·44}$$

where $\mathbf{U} \in \mathbb{R}^{N\times N}$ and $\mathbf{V} \in \mathbb{R}^{S\times S}$ are orthogonal matrices whose columns are eigenvectors of $\boldsymbol{\Psi}_{\mathrm{DB}}\boldsymbol{\Psi}_{\mathrm{DB}}^T$ and $\boldsymbol{\Psi}_{\mathrm{DB}}^T\boldsymbol{\Psi}_{\mathrm{DB}}$ respectively, and $\boldsymbol{\Sigma} \in \mathbb{R}^{N\times S}$ is a diagonal matrix of singular values of $\boldsymbol{\Psi}_{\mathrm{DB}}$.

From the SVD, we define the matrix $\boldsymbol{\Psi}_{\mathrm{SVD}}$ as:

$$\boldsymbol{\Psi}_{\mathrm{SVD}} = \mathbf{U}\boldsymbol{\Sigma} \tag{3·45}$$

where $\boldsymbol{\Psi}_{\mathrm{SVD}} = \begin{bmatrix}\boldsymbol{\psi}_1^{\mathrm{SVD}} & \boldsymbol{\psi}_2^{\mathrm{SVD}} & \dots & \boldsymbol{\psi}_S^{\mathrm{SVD}}\end{bmatrix} \in \mathbb{R}^{N\times S}$ is a matrix whose columns are a new set of SFs that by appropriate choice of linear coefficients, can be combined to reconstruct $\boldsymbol{\Psi}_{\mathrm{DB}}$.

The SVD modes represented by the columns of $\boldsymbol{\Psi}_{\mathrm{SVD}}$ are ordered in the matrix such that the first column is the mode that presents the highest correlation to the whole set of SO SFs, the second column is the second most correlated and so on. The elements in the diagonal of $\boldsymbol{\Sigma}$ are then the $\boldsymbol{\Psi}_{\mathrm{DB}}$ singular values in decreasing order; they are a measure of pertinence of each SVD mode in the reconstitution of $\boldsymbol{\Psi}_{\mathrm{DB}}$.

If all SVD modes are used for the reconstruction of $\boldsymbol{\Psi}_{\mathrm{DB}}$ the linear coefficients for the reconstruction of each column are in the columns of $\mathbf{V}^T$, such that:

$$\boldsymbol{\Psi}_{\mathrm{DB}} = \boldsymbol{\Psi}_{\mathrm{SVD}}\mathbf{V}^T \tag{3·46}$$

Since we intend to obtain a reduced dimension subset of SFs, only the first few columns of $\boldsymbol{\Psi}_{\mathrm{SVD}}$ are retained to constitute the shim system.

Retaining the M first columns of $\boldsymbol{\Psi}_{\mathrm{SVD}}$, the computation of performance and power consumption of a physical realization of the shim system starts with the discretization into windings of $\boldsymbol{\psi}_m^{\mathrm{SVD}}$ for $m = 1, \dots, M$. From this discretization, the resistance r_m and nominal current $\mathcal{I}_m$ of each SF-SVD coil is calculated.

For a fieldmap $\boldsymbol{b}$ being shimmed by the SF-SVD system, the optimal currents $\boldsymbol{i} = \begin{bmatrix}i_1 & i_2 & \dots & i_M\end{bmatrix}$ to be injected in each coil are calculated such that their application minimizes the quadratic error between target field and coil generated field:

$$\boldsymbol{i} = \underset{\boldsymbol{i}\in\mathbb{R}^M}{\operatorname{argmin}} \left|\left|\boldsymbol{b} - \mathbf{C}\sum_{m=1}^{M} i_m \frac{\boldsymbol{\psi}_m^{\mathrm{SVD}}}{\mathcal{I}_m}\right|\right|_2^2. \tag{3·47}$$

Total power dissipation and performance in inhomogeneity reduction for a shimmed subject are then calculated as:

$$\mathcal{P}_{\mathrm{SVD}} = \sum_{m=1}^{M} r_m i_m^2 \tag{3.48}$$

and

$$\eta_{\mathrm{SVD}} = 100 \times \left(1 - \frac{\sigma\left(\boldsymbol{b} - \mathbf{C} \sum\limits_{m=1}^{M} i_m \dfrac{\boldsymbol{\psi}_m^{\mathrm{SVD}}}{\mathcal{I}_m} \right)}{\sigma(\boldsymbol{b})} \right). \tag{3.49}$$

3.2.3 SVD Coil Calculation over Multiple Radii

The SF-SVD coil generation method described so far produces a number of different coils over the exact same cylindrical surface for all modes. This is not possible for a real system fabrication, thus the passage of SVD modes $m > 1$ to cylinders of larger radii $a_m > a$ is necessary. These new radii are defined according to the space necessary to accommodate the wires, together with the supporting structure upon where the wires will be placed.

Departing from $\boldsymbol{\psi}_m^{\mathrm{SVD}}$ over a cylindrical surface of radius a, a new SF $\boldsymbol{\psi}_{m,a_m}^{\mathrm{SVD}}$ over a cylinder of radius a_m such that both coils produce the same magnetic field in a region of interest $\mathcal{V}$ needs to be calculated.

The region of interest $\mathcal{V}$ should enclose all brains in the fieldmap database. The simplest region for the task is a sphere centered at the isocenter. Let $\mathcal{X}_s$ be the set of coordinates $\boldsymbol{x}_k$ of the K_s voxels of subject s, the radius of the smallest sphere enclosing all brains is $R_{\mathrm{sph}} = \sup \mathcal{R}$, where $\mathcal{R} = \{ \|\boldsymbol{x}\|_2 \,|\, \boldsymbol{x} \in \cup_{s=1}^{S} \mathcal{X}_s \}$.

Since the magnetic field generated by any external coil obeys Laplace's equation inside $\mathcal{V}$, the magnetic field over the boundary $\partial\mathcal{V}$ of $\mathcal{V}$, a spherical surface, is sufficient as target field for the computation of the new SF. Performing a regular discretization of the spherical surface into K_{sph} points, the matrices $\mathbf{C}_{\mathrm{sph}}$ and $\mathbf{C}_{\mathrm{sph},a_m}$ associating, respectively, $\boldsymbol{\psi}_m^{\mathrm{SVD}}$ and $\boldsymbol{\psi}_{m,a_m}^{\mathrm{SVD}}$ to the magnetic field they generate over $\partial\mathcal{V}$ can be computed and the new equivalent SF on the greater radius is:

$$\boldsymbol{\psi}_{m,a_m}^{\mathrm{SVD}} = \boldsymbol{\Gamma}_{a_m} \mathbf{D}_{\mathrm{sph},a_m} \boldsymbol{\Gamma}_{a_m}^T \mathbf{C}_{\mathrm{sph},a_m}^T \mathbf{C}_{\mathrm{sph}} \frac{\boldsymbol{\psi}_m^{\mathrm{SVD}}}{\mathcal{I}_m}. \tag{3.50}$$

with

$$\mathbf{D}_{\mathrm{sph},a_m} = [\boldsymbol{\Gamma}_{a_m}^T (\lambda \mathbf{R}_{a_m} + \mathbf{C}_{\mathrm{sph},a_m}^T \mathbf{C}_{\mathrm{sph},a_m}) \boldsymbol{\Gamma}_{a_m}]^{-1}. \tag{3.51}$$

The regularization parameter λ must be tuned to guarantee that the newly generated SF will produce a magnetic field to maintain the same shim system performance with minor or no increase in total power consumption.

Finally, after adequate "projections" of the SF-SVD coils onto larger cylindrical surfaces, a physically realizable set of shim coils is obtained.

3.2.4 Constitution of a Brain Fieldmap Database

A database of brain fieldmaps was assembled from MRI acquisitions of 100 consenting and healthy adult subjects, consisting of a 53/47 male to female ratio, of average 60 years (SD: 10) and 70 kg (SD: 15). The ΔB_0 brain maps were obtained at 3 T from a Prisma scanner (Siemens Healthcare, Erlangen) equipped with a 20-channel RF head coil and full 2^{nd} order SH shim coils.

For accurate ΔB_0 estimation, we based our ΔB_0 mapping on 3 echoes rather than 2. Yet to avoid sometimes tedious spatial phase unwrapping, we opted for temporal phase unwrapping of the third echo, based on the assumption that no phase excursion occurs between the first and second echoes beyond $\pm\pi$. This means that the first 2 echoes must be placed extremely close to one-another (0.7 ms to catch B_0 excursions within $\pm$ 714 Hz), which cannot be reached in a single sequence. Therefore after 2^{nd} order SH shimming, a 3D gradient echo sequence was played twice, one with 2 distant echoes $TE_1 = 1.88$ ms and $TE_3 = 4.9$ ms, and one with a single echo at $TE_2 = TE_1 + 0.7$ ms. Then a triple-point linear fit of the phase evolution was performed by gathering all three echoes, with correction of the potential temporal phase-unwrapping of the third echo based on the slope given by the first two echoes. The other sequence parameters were: sagittal orientation, isotropic voxel resolution = 1.7 mm, TR = 10 ms, Flip Angle = 8°, 2D Caipirinha acceleration factors = 2×2, TA = 44 s. The resulting ΔB_0 maps were cleaned with an outlier filter to avoid singularities, especially at the edge of the brain; the filter marked a brain voxel as outlier by comparing its excursion from the median to the variance, both statistics estimated from its neighbors; such outlier values were then replaced with their neighboring median. A mask of the brain was extracted from the magnitude image using FSL's Brain Extraction Tool. The quality of the brain masks and fieldmaps was checked visually in at least the three orthogonal central slices for each subject. Since the magnetization $\boldsymbol{M}$ of tissues generating the inhomogeneous magnetic field is $\boldsymbol{M} = (\chi/\mu_0)B_0\hat{\boldsymbol{z}}$, the ΔB_0 fieldmaps were linearly re-scaled to represent the inhomogeneity corresponding to a 7 T main field with no loss of accuracy. The acquisition at lower fields is advantageous as field inhomogeneity is lower, thus reducing geometric distortion and signal loss compared to what would be obtained at 7 T. The average and standard deviation of the inhomogeneity of the entire fieldmap database is $\bar{\sigma}_{base} = 65.7$ Hz (11.4) after re-scaling to 7 T.

3.2.5 Choice of Design and Validation Parameters

Our goal is to achieve optimal shimming with a low power budget. Limiting power dissipation helps reduce costs related to both electronics and heat management. By guaranteeing low power dissipation, dedicated cooling systems can be avoided, as the forced air flow in the MRI tunnel may be sufficient to maintain a low, safe temperature. The most obvious way to limit the required power is to make the cylindrical shim set as close as possible to the human head. Thus, the cylindrical coil former dimensions were set to $a = 140$ mm (so that it could be placed at the exterior of our in-house RF head coil) and $L = 300$ mm. Mesh resolution for SF computation is set to $h = 4$ mm. To assess accuracy of the piece-

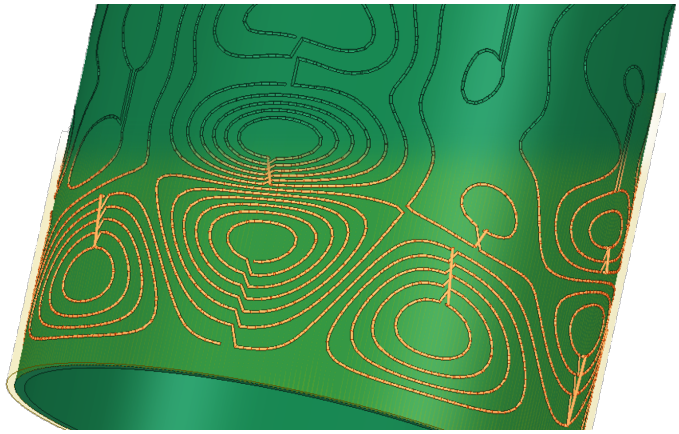

Figure 3.2 – 3D model of a realistic system setup for a single layer (channel) of an SF-SVD shim system; depicting groove paths for wire accommodation (top) and realistic wiring of an SVD coil layer (bottom). Note the wire bridges in the dimension orthogonal to the cylindrical surface to connect concentric loops.

wise constant basis function under this particular discretization, different values of h were tested for one random fieldmap in the database, with insignificant changes in performance and power consumption for h inferior to 4 mm.

Discretization into windings for SO and SVD coils is performed with $\delta_w = 2.4\,\text{mm}$ and with copper wire of $1.54\,\text{mm}^2$ circular section (1.4 mm diameter) and electric conductivity $\kappa = 5.96 \times 10^7\,\text{S}\,\text{m}^{-1}$. Under this discretization, characteristic power dissipation of each coil and performance over its associated map are calculated from (3.42) and (3.43).

This particular choice of discretization parameters allows the use of relatively large copper wire gauge, resulting in lower power dissipation at high current. Large wire gauges tend to preserve their form once bent, a convenient characteristic for manufacturing. Moreover, the 2.4 mm inter-wire spacing leaves enough room for a manufacturing based on accommodating the wires into grooves milled onto a support structure, as depicted in Fig. 3.2.

For analysis of system performance at different power dissipation values, 8 power targets were chosen for SO-SF generation: 1 W, 3 W, 7 W, 15 W, 25 W, 50 W, 75 W and 100 W. The regularization parameter for each subject is tuned to reach each power target. Hence, eight sets of SFs $\boldsymbol{\Psi}_{\text{DB}}^{1\,W}$, $\boldsymbol{\Psi}_{\text{DB}}^{3\,W}$, ..., $\boldsymbol{\Psi}_{\text{DB}}^{100\,W}$ are obtained and subsequently decomposed into the SVD SFs $\boldsymbol{\Psi}_{\text{SVD}}^{1\,W}$, $\boldsymbol{\Psi}_{\text{SVD}}^{3\,W}$, ..., $\boldsymbol{\Psi}_{\text{SVD}}^{100\,W}$. Note that in this step, average power across the SO coils is forced to be very close to the power target and with low standard deviation, but there is no guarantee that the resulting SF-SVD coils will present the same power dissipation characteristics. The superscript on $\boldsymbol{\Psi}_{\text{SVD}}^{\mathcal{P}_T}$ serves only to associate the SVD SF to its generating SO-SFs.

The shimming capabilities of the SF-SVD system over "new" fieldmaps is assessed by generating the SF-SVD coils from 50 randomly selected maps forming a design set $\mathcal{D}$ and simulating the system's performance over $\mathcal{D}$ and the set of remaining 50 fieldmaps $\mathcal{T}$, called test set. This is known as the hold-out method for validation. The sets $\mathcal{D}$ and $\mathcal{T}$ are kept the same for the eight power targets so as to provide comparable systems. Unless specified otherwise, the performance and power estimations will be reported for $\mathcal{T}$.

It will be observed that $\mathcal{P}_T = 15\,\mathrm{W}$ provides a good compromise between inhomogeneity reduction and power dissipation. Therefore, the resulting $\mathbf{\Psi}_{\mathrm{SVD}}^{15\,W}$ SF-SVD shim system will be retained for subsequent analysis on robustness of the method and comparison to SH shimming.

3.2.6 Cross-validation

For a more statistically significant evaluation of the SF-SVD method's robustness to new fieldmaps, 10-fold cross-validation is performed for 15 W target power SO-SFs. In this analysis, the fieldmap database is divided into 10 disjoint clusters $\mathcal{K}_j$, $j = 1, ..., 10$, composed by 10 fieldmaps each. Each cluster is then used once as test set $\mathcal{T}_j = \mathcal{K}_j$, with the remaining clusters used as design set $\mathcal{D}_j = \cup_{i \neq j} \mathcal{K}_i$. For each generation, average performance of the resulting SF-SVD shim system is evaluated over $\mathcal{D}_j$ and $\mathcal{T}_j$ and the resulting ratios $\bar{\eta}(\mathcal{T}_j)/\bar{\eta}(\mathcal{D}_j)$ are used as a metric to evaluate how well the SF-SVD system behaved over the new subjects. Only the first 3 SVD modes for each generation are retained to compose the SF-SVD system.

3.2.7 Performance Assessment and Realistic Design Evaluation

Comparison of the $\mathbf{\Psi}_{\mathrm{SVD}}^{15\,W}$ SF-SVD shim system performance against unlimited power high-order SH shimming is then carried-out.

To avoid computational burden, the simulations described so far are performed assuming the SVD coils are at the same cylindrical radius and magnetic fields over the ROIs are computed directly from the ideal stream functions. Nevertheless, to validate this approximation, we explore a feasible system design, whereby the projection of the 2^{nd} and 3^{rd} $\mathbf{\Psi}_{\mathrm{SVD}}^{15\,W}$ modes is performed upon radii a_2 and a_3, chosen to be 144.8 mm and 149.6 mm respectively. This choice leaves a 4.8 mm-distance between successive channel wiring centers, providing enough space for the return wires, resin coating for fixation and the associated supporting structure of each coil. The first SF-SVD coil is maintained unchanged over radius $a = 140\,\mathrm{mm}$. The spherical surface considered for target field calculation has 12 cm radius and is discretized such that the amount of control points is in the order of the number of voxels in the ROIs of our database (roughly 300,000 voxels in the brain). The behavior of this new, feasible system is then evaluated. Afterwards, discretization into windings is performed on the projected stream functions and the magnetic field generated in the ROIs is now computed from the current flow in the actual current paths using Biot-Savart law. The eventual loss of performance of the realistic winding system is assessed.

Overall, the dimensions of a 3-layer shim insert would be the following: considering 5 mm thickness for inner and outer cylindrical formers including burried wires, a total thickness of about 2 cm would be expected, with 27 cm internal diameter and 30 cm length.

3.3 Simulation Results and Discussion

3.3.1 Subject Optimal SF Computation

After tuning of the regularization parameter and SF computation for the eight power targets, resulting mean and standard deviation of power dissipation across the 100 SO coils are: 1.0 W (0.04), 3.1 W (0.1), 7.2 W (0.4), 15.4 W (0.9), 25.7 W (1.5), 51.9 W (3.3), 77.7 W (5.7) and 104.1 W (11.8), which are sufficiently close to the desired power dissipation targets for the purposes of this analysis.

Performance and final inhomogeneity obtained from SO-SF shimming are reported as functions of mean power dissipation in Fig. 3.3.

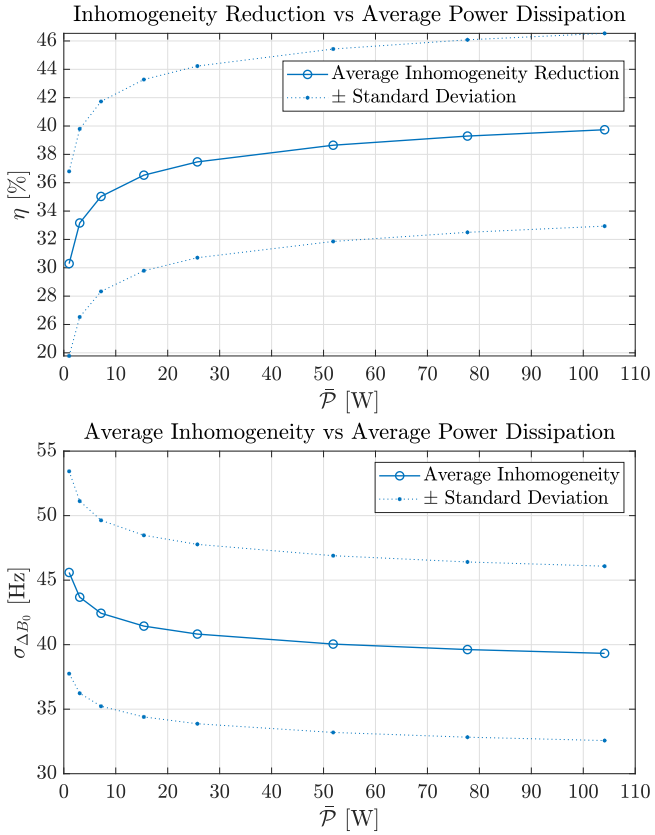

Figure 3.3 – Inhomogeneity reduction and final inhomogeneity at 7T over a 100-subject database after SO coil shimming for increasing power dissipation designs.

As expected from the functional in (3.37), it can be observed that a steady reduction of B0 inhomogeneity requires more than an exponential power increase. Improvement in average performance from $\bar{\eta} = 37.5\,\%$ to 39.7 % (from $\bar{\sigma}_{\Delta B_0} = 40.8\,\text{Hz}$ to 39.3 Hz) demands 78.4 W average power increase. For a system close to the patient's head, such growth in power dissipation, initially at 25.7 W, to obtain an absolute 2.2 % gain in performance, does not seem justifiable. On the other hand, the lowest performance shown in Fig. 3.3, 30.3 % ($\bar{\sigma}_{\Delta B_0} = 45.6\,\text{Hz}$), is already superior to a full 5^{th} order SH shimming (cf. Fig. 3.8), and the associated average power dissipation is merely 1.0 W. A raise in power dissipation from 1.0 W to 25.7 W provides an absolute increase of 7.2 % in average performance, showing

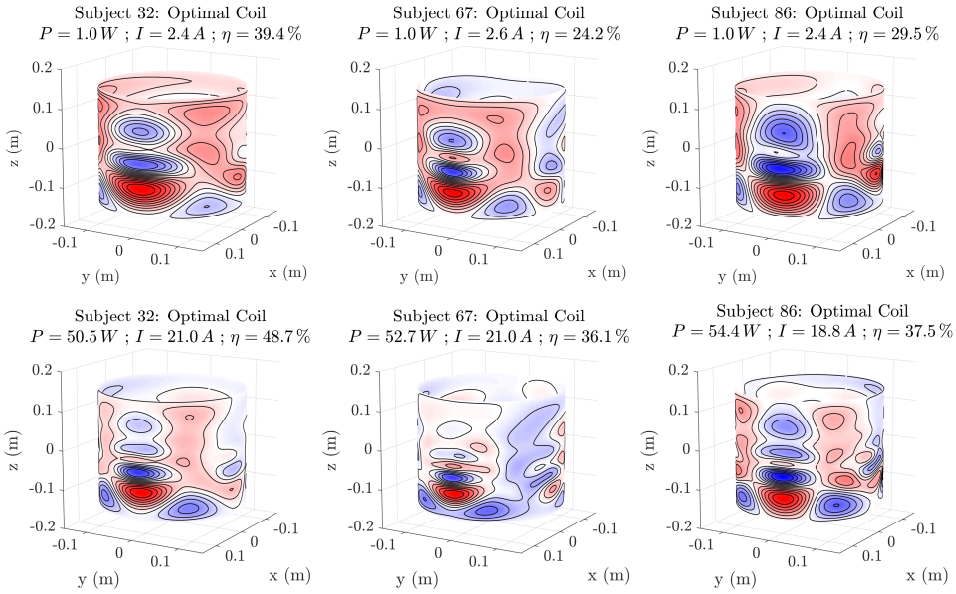

Figure 3.4 – Wire geometric centers of subject-optimal coils for 3 subjects at two different performances and power dissipation for each subject. The colormap represent the SF intensity around the cylindrical surface (red is positive, blue is negative, which gives the sign of the current flow in the depicted windings).

a better performance increase to power increase ratio, and keeping the system under acceptable power dissipation levels. The greater improvement in performance within the lower power ranges is clearly marked, where it seems that power dissipation ranging from 15 W to 25 W should be privileged. Indeed, low power dissipation designs can be driven by low budget electronics and need not specific heat dissipation management.

Regarding the SO coils' wiring patterns in Fig 3.4, improvement of the brain magnetic field homogeneity requires the shape of the coil wirings to change and their nominal current and power to increase. In particular, the SF presents more rapid variations, leading to a more complex current flow needed to better address high magnetic field intensity and variations without degrading initially small magnetic field values. The circumference of current loops tends to decrease in this process, demanding higher current for generating a same magnetic field intensity.

The similarity between the wire patterns shown for these three subjects, also observed among all SO coils, is remarkable. There are concentrations of current flow in the front of the coil, to address the intense inhomogeneity in the orbito-frontal cortex. High current flow can also be observed in the regions close to the ears, which also present intense inhomogeneity caused by the interfaces with the ear canals. This similarity among coil patterns is an indicator that a small and effective shim coil system for the brain could be obtained through Singular Value Decomposition.

3.3.2 SF-SVD Coil Generation and Evaluation

Singular value decomposition is applied on each of the eight subject-optimal SF sets. The SF-SVD coil designs are shown in Fig. 3.5, where a tendency for symmetry can be observed, especially on the first mode. These wiring patterns are consistent with the overall brain symmetry. As the power consumption of the shim system is allowed to increase to provide better performance, it is once again observed that the loops associated to the current paths become shorter in length.

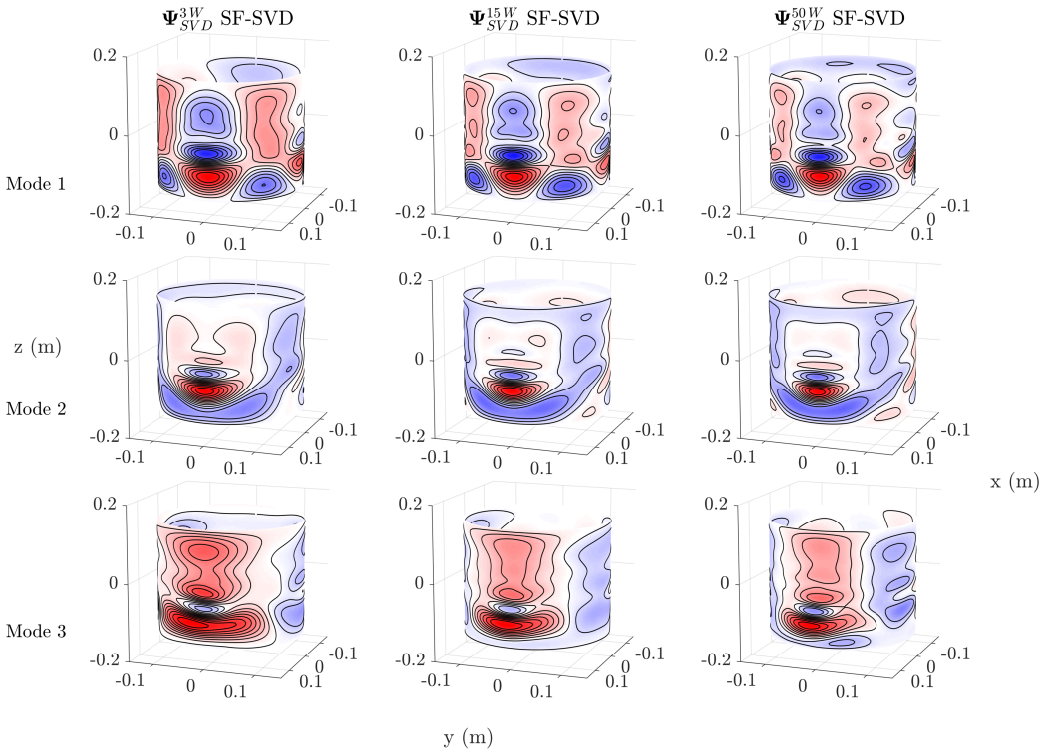

Figure 3.5 – Geometric centers of the windings obtained from the first three SF-SVD modes with increasing power dissipation. The colormap indicates the intensity of the SFs.

Performance increase as a function of power consumption and number of SVD modes (or channels) is shown in Fig. 3.6. It can be noticed that SF-SVD coils present a considerable drop in average performance relatively to their generating SO coils: an almost 15 % drop from $\mathbf{\Psi}^{1\,W}_{\mathrm{DB}}$ to $\mathbf{\Psi}^{1\,W,M=1}_{\mathrm{SVD}}$, and more than 20 % drop from $\mathbf{\Psi}^{100\,W}_{\mathrm{DB}}$ to $\mathbf{\Psi}^{100\,W,M=1}_{\mathrm{SVD}}$. Nevertheless, using a single coil for shimming, average inhomogeneity reduction ranging from 15.8 % to 18.0 % for $\mathcal{T}$ is remarkable. The drop in performance is an expected behavior, as the SF-SVD coils with a small number of modes M can only approximate the actual subject-optimal SFs that originated them.

As more SVD modes are added, further growth in performance is observed. For SF-SVD systems originated from higher target power SO SFs, addition up to the 4^{th} mode shows the most significant increase, which afterwards continues to grow slower but steadily as higher order modes are added. For all systems, the addition of the second mode provides

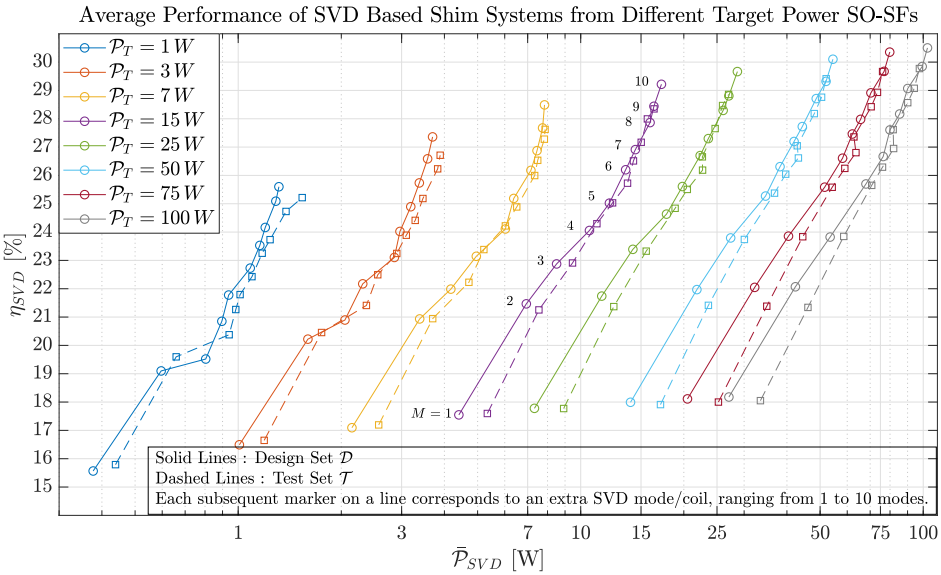

Figure 3.6 – Average performance and power dissipation of different SF-SVD shim systems. Each curve shows the evolution of average performance and average power dissipation of an SVD shim system, generated from SO-SFs targeting a specific power, with each marker (circle or square) representing a different number of SVD modes used to constitute the shim system (as exemplified on the $\mathcal{P}_T = 15\,W$ curve). Performances over $\mathcal{D}$ and $\mathcal{T}$ are shown separately on solid and dashed curves, respectively.

the most significant increase in average performance, between 3.3 % and 4.0 %. It can be asserted from the curves, and supported by the mathematical properties of SVD, that the few first modes generate field patterns that are common to most brains, thus having significant effect in reducing the inhomogeneity over the entire database. From the 5^{th} mode onward, the increase in performance as modes are added tends to be lower than 1 %, meaning that the coil being added is likely to address very particular field patterns on specific subjects, eventually related to a tilt or rotation of the patient's head, thus correlating much less to the whole database. As more modes are added, the increase in performance over the entire database will tend to be each time smaller, as they are more likely to be addressing particularities of single subjects.

It is observed that, for all designs, performances over $\mathcal{D}$ and $\mathcal{T}$ tend to grow together as more modes are added and present very close values. For the lower power consuming systems, average inhomogeneity reduction on $\mathcal{T}$ is slightly greater than on $\mathcal{D}$, when a low number of modes is used. The difference in performance over unknown maps observed for all systems is sufficiently small to conclude that the SF-SVD method manages to provide coils that adapt to the universe of different subjects. Difference in SF-SVD shimming performance over $\mathcal{D}$ and $\mathcal{T}$ starts to diminish in all cases as the first few modes are added but then rises again, favoring $\mathcal{D}$. This can be explained by the fact that higher order SVD modes tend to address precise characteristics of field patterns of smaller groups of subjects, which are not in $\mathcal{T}$, thus causing greater improvement over $\mathcal{D}$ than over $\mathcal{T}$. In addition, performance on $\mathcal{D}$ at higher target power systems tends to be greater than on $\mathcal{T}$ also for

the first few modes, which is caused by the greater field fidelity of the subject-optimal coils at higher power; these are more efficient in attenuating specific details of each subject's fieldmap in $\mathcal{D}$, thus introducing stronger bias on the SF-SVD coils.

For all simulated SF-SVD shim systems, slightly greater power dissipation is observed in $\mathcal{T}$. Careful analysis of the power dissipation in $\mathcal{D}$ and test set shows that average power dissipation was biased by an outlier in $\mathcal{T}$, as can be observed in Fig 3.7 for the 15 W system. Average power dissipation for $\mathbf{\Psi}_{SVD}^{15W,M=3}$ for instance is 8.5 W(SD:7.6) on $\mathcal{D}$ and 9.5 W(SD:9.5) on $\mathcal{T}$, but an outlier with 57.9 W is present in $\mathcal{T}$, biasing the average and standard deviation, which, without the outlier subject, are 8.5 W(SD:6.6), evidencing that the SF-SVD system shows equivalent power dissipation behavior whether shimming on $\mathcal{D}$ or $\mathcal{T}$. This outlier was present throughout all eight SF-SVD systems, accounting for the observed deviation in average power dissipation on $\mathcal{T}$.

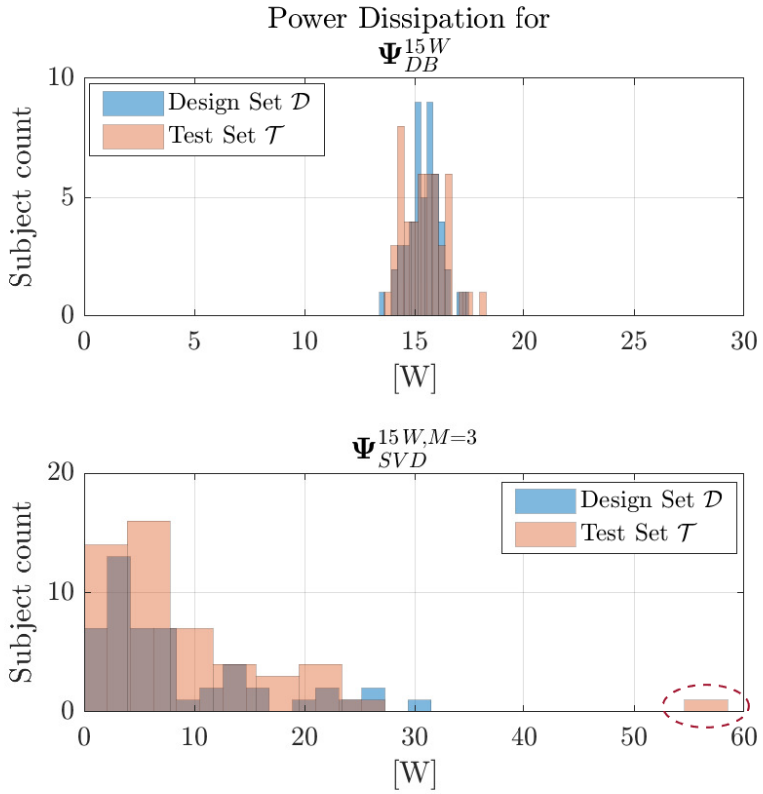

Figure 3.7 – Histogram of power dissipation across subjects for subject-optimal stream functions and SF-SVDs for a 15 W target system. Outlier subject identified by red ellipse.

It can also be noticed, from Fig. 3.7, that while the SO coils' power dissipation is very close to the target power set for their design, subsequent SVD application on the SO SF leads to new systems that show a large spread of power dissipation values. Nevertheless, for a fixed number of modes, Fig. 3.6 shows that the SVD system generated from SO SFs of larger target power will present proportionally larger average power dissipation.

If a low channel count is an important design criterion, SF-SVD systems obtained from SO-SFs of larger target power should be preferred. Although the low power $\mathbf{\Psi}_{SVD}^{1W,M=10}$

shim system would provide 25.2 % average inhomogeneity reduction at a low average power dissipation of 1.5 W, the total amount of 10 channels necessary to achieve such performance implies greater hardware complexity and size. On the opposite, the 4-channel $\mathbf{\Psi}_{SVD}^{100W,M=4}$ SF-SVD shim system would provide practically the same level of average inhomogeneity reduction, 25.6 %, with less than half the amount of channels. However, power consumption becomes considerably higher, 70.7 W, increasing thermal management complexity of the shim system.

A SF-SVD shim system based on the $\mathbf{\Psi}_{SVD}^{15W}$ SFs seems to provide an appropriate trade-off between performance and power dissipation, since, from this point onwards, SF-SVD systems based on higher power SO SFs will provide marginal performance improvement for a same number of channels.

Cross-validation statistics across the 10 different generations showed 0.97 average performance ratio between $\mathcal{T}$ and $\mathcal{D}$, 0.99 median ratio, 0.09 standard deviation and ranged within 0.80 and 1.09. Results show that independently of the random choice of subjects composing $\mathcal{D}_j$, the average inhomogeneity reduction of the SF-SVD shim system over $\mathcal{T}_j$ is maintained very close to that over $\mathcal{D}_j$, confirming robustness to new subjects.

3.3.3 Comparison between SF-SVD and unconstrained SH shimming

The performance of SF-SVD systems can be compared to what would be achieved when using Spherical Harmonics coils to shim the same database of subjects. For this simulation, the coefficients of each spherical harmonic order (from 0 to the desired SH shim system order) and degree were computed considering ideal coils and no power constraint was imposed on these coils. They were compared to a SF-SVD shim system based on the $\mathbf{\Psi}_{SVD}^{15W}$ SFs, as shown in Fig. 3.8.

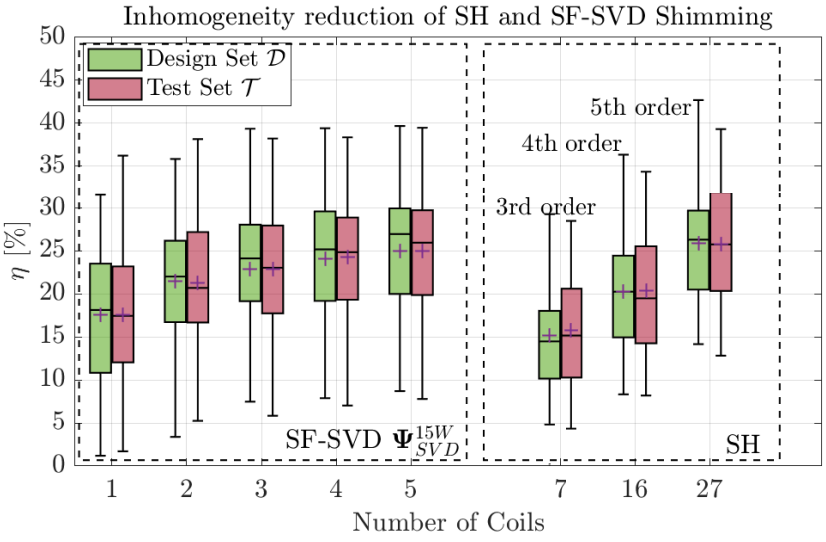

Figure 3.8 – Inhomogeneity reduction comparison between an unlimited power Spherical Harmonics shim system and a 15-W SF-SVD shim system.

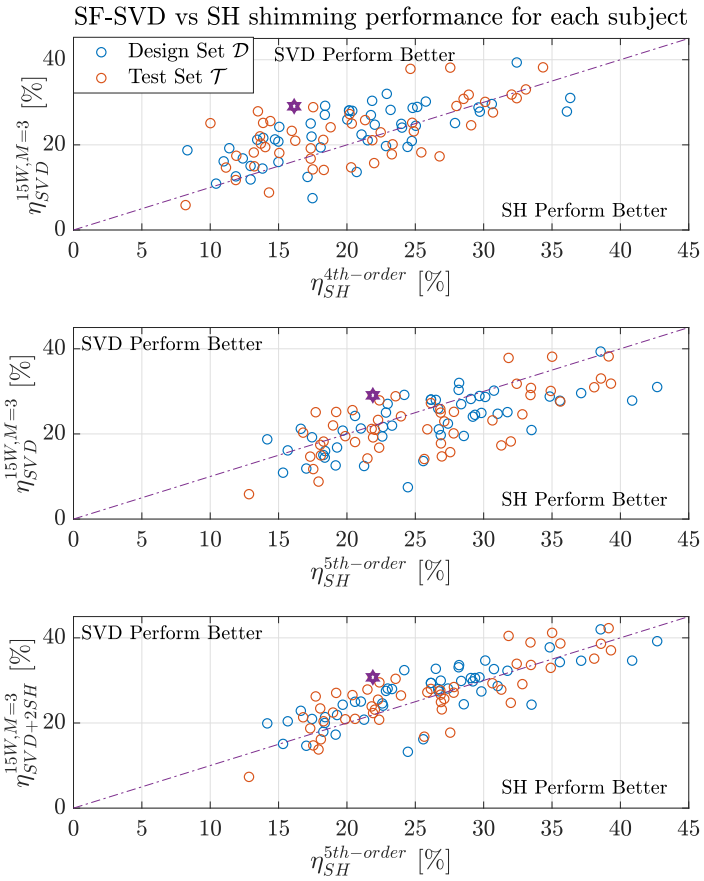

Figure 3.9 – Performance of a 15-W 3-channel SF-SVD shim system vs SH shim systems of different orders for each subject. The SF-SVD system is compared to 4^{th} (top plot) and 5^{th} (middle) order systems. The bottom plot shows its performance against 5^{th} (middle) order when combined with 2^{nd}-order refined shimming. The dash-dot line represents equal performance and is present to ease visualization. The purple star indicates the subject shown in the fieldmaps comparison of Fig. 3.10.

Focusing on $\mathcal{T}$, the single channel SF-SVD shimming shows better average performance (17.6 %) than a 7-channel full 3^{rd} order Spherical Harmonic based shim system (15.8 %). The 1-channel SF-SVD system's performance between the 25^{th} and 75^{th} percentiles ranges from 12.1 % to 23.2 %, while the 3^{rd} order SH system shows performances from 10.3 % to 20.6 % within the same percentiles. This shows a statistically superior performance for a single SVD channel system against a 7-channel SH system. Nevertheless, the 1-channel SF-SVD shim system presents very low performance on some subjects, as shown by the whiskers of its box plots. This situation can be improved by adding extra SVD modes (or channels) to the SF-SVD shim system. The 3-channel SF-SVD shim system's average performance of 22.9 % is superior to the 20.4 % performance presented by the 16-channel full 4^{th} order SH shimming system. In addition, 60 % of subjects in $\mathcal{T}$ present greater inhomogeneity reduction when shimmed by the 3-channel SF-SVD system. This is a remarkable achievement, as a 3-channel system is capable of outperforming a conventional

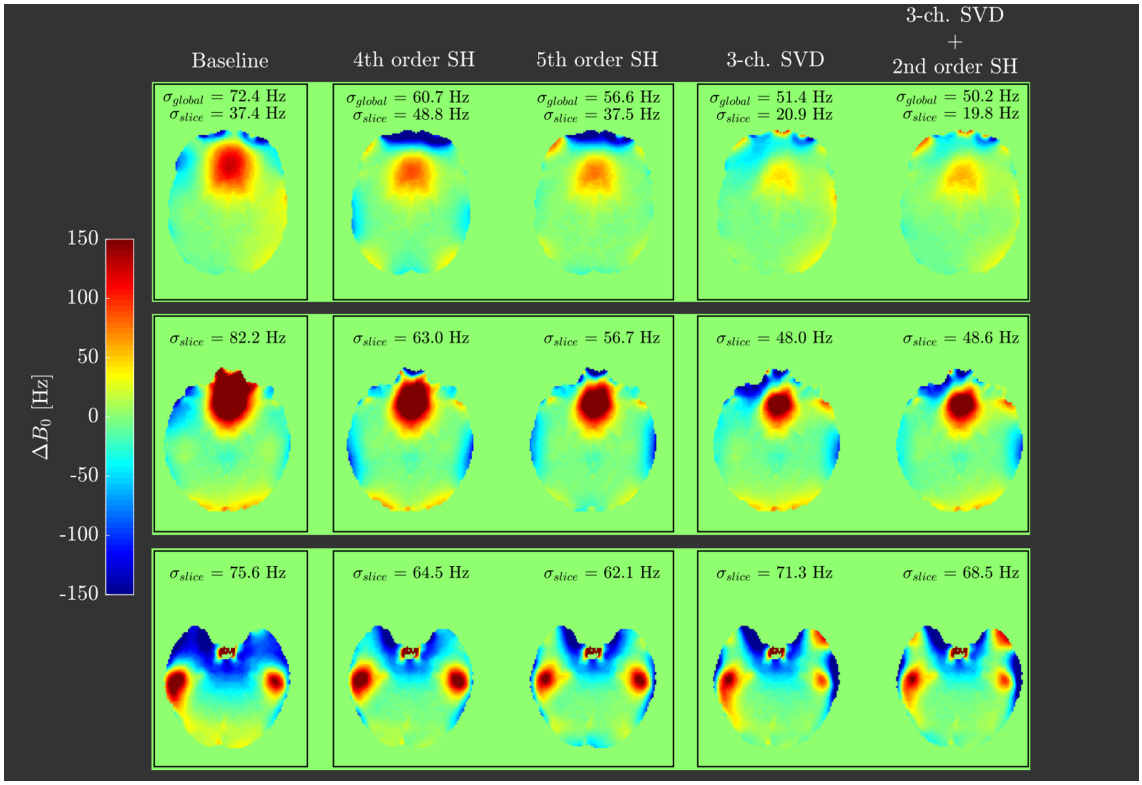

Figure 3.10 – Fieldmap comparison between Baseline, 4^{th}-order SH, 5^{th}-order SH, 3-ch. SF-SVD and mixed 3-ch. SF-SVD + 2^{nd}-order SH shims at different axial slices.

SH system composed by 16-channels, and establishes SF-SVD shim systems as an advantageous alternative to high-order shim inserts. The 27-channel 5^{th} order SH system, however, is harder to outperform, and even the 5-channel SF-SVD shim system does not achieve the same average performance. Nevertheless, SF-SVD performance simulations so far considered SF-SVD shimming over the 2^{nd} order SH shimmed fieldmaps, which implies a shimming pipeline composed by SH shimming with the scanner's built-in coils and subsequent application of the SF-SVD coil shimming on the resulting map. It would be possible to combine the built-in 2^{nd} order SH system with the 3-channel SF-SVD system in order to compute SH coefficients and channel currents at the same time, which is shown to improve performances (cf. Fig. 3.9).

Most subjects in $\mathcal{D}$ and $\mathcal{T}$ present greater inhomogeneity reduction when shimmed by the 3-channel SF-SVD shim system in comparison to the 4^{th} order SH system. As already noted, the 5^{th} order SH shim system outperforms the 3-channel SF-SVD system, with average performances of 25.9 % and 25.8 %, for $\mathcal{D}$ and $\mathcal{T}$ respectively. However, by combining the built-in 2^{nd} order shim coils with the 3-channel SF-SVD system, it can be observed that most subjects present higher inhomogeneity reduction when shimmed by the combined system, with average inhomogeneity reduction of 27.0 % and 26.8 % on $\mathcal{D}$ and $\mathcal{T}$, respectively, with 70 % and 62 % presenting performance when shimmed by the combined SF-SVD+SH system. This mixed system, which would only require a step of characterization of the scanner's shim coils to be implemented, provides better results than

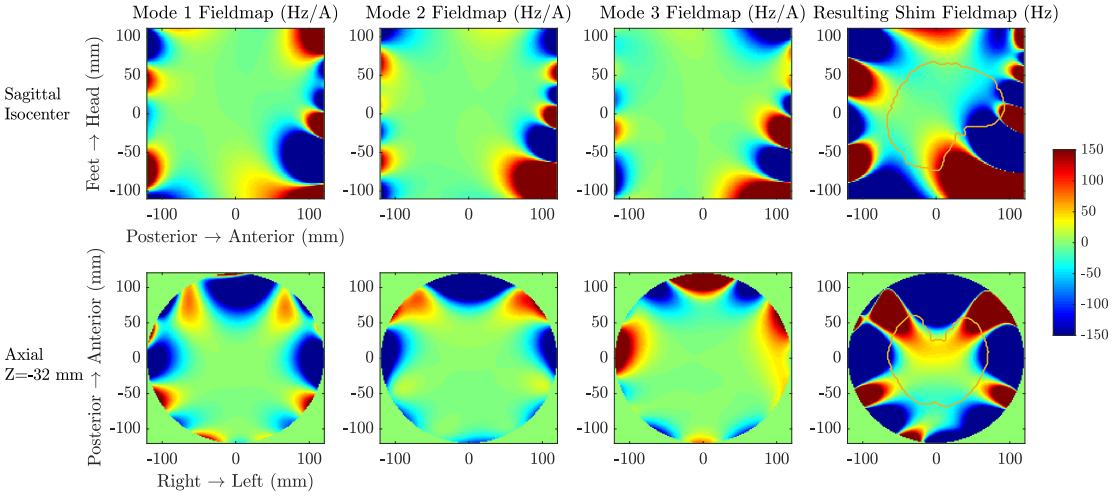

Figure 3.11 – Fieldmap per unit current for SF-SVD modes 1, 2 and 3; and resulting magnetic field pattern used for shimming a randomly picked subject using these 3 coils. The brain outline of the particular subject is shown in yellow.

a 27-channel high-order shim insert. Improved performances obtained with the combined SF-SVD+SH system come from scanner's shimming software inability to reach optimal shimming of the brain as it takes a larger region (Field of View) into account when computing built-in coil coefficients. Alternatively, a 2^{nd}-order re-shim could have been performed on the database before SO-SF computation, but if this improved 2^{nd}-order SH shimming is not implemented by the user, the SF-SVD system obtained from the re-shimmed database would under-perform. Thus, by not re-shimming, the designer is free to use the SF-SVD system with its full capacity and eventually improve performance by characterizing the scanner's coils and implementing the combined approach.

A comparison of shimmed fieldmaps is shown in Fig. 3.10 for a subject in $\mathcal{T}$. The 2^{nd} order shimmed baseline, 4^{th} and 5^{th} order SH shims, 3-ch. SF-SVD and mixed SF-SVD+2^{nd} order SH shimmed fieldmaps are shown at a few selected slices where intense inhomogeneity is present and the changes on the field patterns can be easily visualized. The areas of stronger inhomogeneity are mainly the frontal and temporal lobes, due to the air cavities located near those regions (sinus, ear canals). The values of global and slice inhomogeneity assert the superior performance of SF-SVD. After either SH or SF-SVD shimming, there are still wide regions containing magnetic field offsets of high intensity (superior to 100 Hz), but those regions are reduced in 3-ch. SF-SVD shimming compared to the 16-ch. and 27-ch. SH shimming.

In Fig. 3.11, the magnetic field distribution generated by each individual SF-SVD mode is shown on selected slices. The greater intensity of the magnetic field is observed in the frontal and temporal lobes, as expected. A high degree of symmetry is also remarkable on the 2 first modes, also consistent with the field patterns inside the human brain.

Although MCA shim systems were not simulated in this work for comparison with SF-SVD shim systems, how these systems perform relatively to SH systems can be used as a

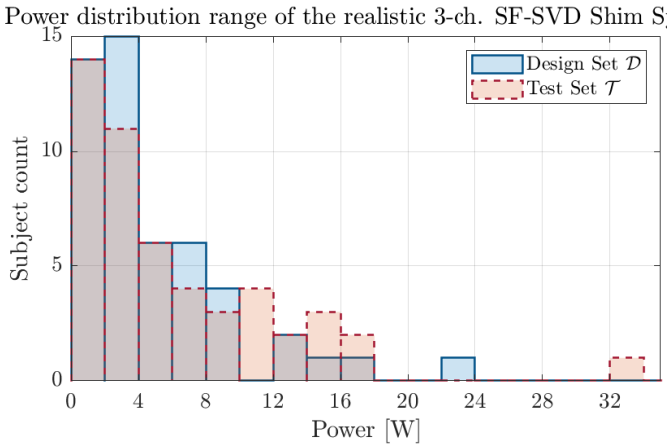

(a) Total power dissipation histogram.

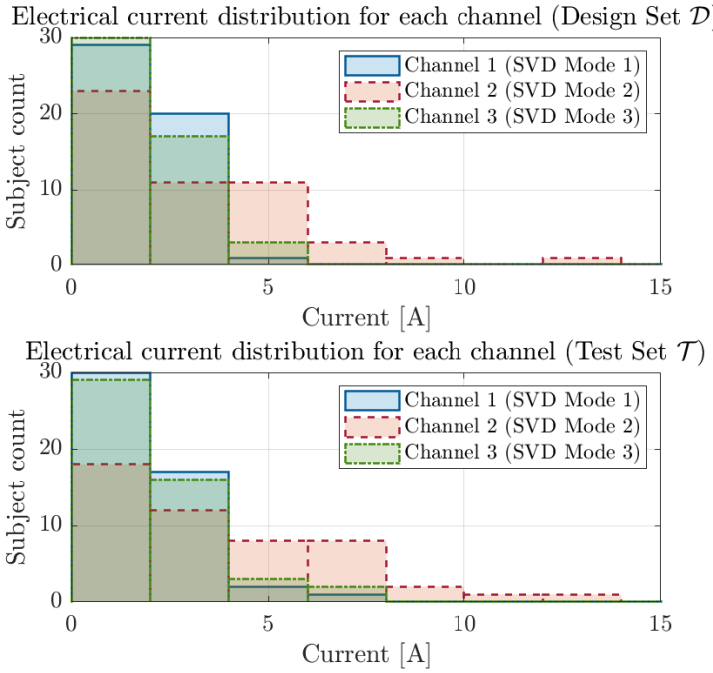

(b) Histogram of current for each of the 3 channels composing the SF-SVD shim system.

Figure 3.12 – Simulated electrical ratings of a realistic 3-ch. SF-SVD shim system applied on the design and test sets.

metric for assessing this feature. As reported in [Aghaeifar 2020], non-optimized 48-ch. and 65-ch. regular MCAs show inhomogeneity reduction values gravitating around those obtained by 4^{th} order SH shimming systems. Those are therefore equivalent performances to that of the proposed 3-ch. SF-SVD shim system. Optimized MCAs, a current trend in shim system design, however, can show equivalent performances to 5^{th} order SH systems with 32 channels [Aghaeifar 2020], thus surpassing the system proposed herein. Nonetheless, the very low amount of channels of the SF-SVD system is advantageous for building a compact, easy to control and efficient shim system for the whole human brain at UHF.

3.3.4 SF-SVD projection onto multiple radii and discretization into windings

The $\mathbf{\Psi}_{\mathrm{SVD}}^{15W}$ SF-SVD coil projections of second and third layers to higher radii were performed. Projected 3-coil shim system provided practically the same performances as before: 22.8 % vs 22.9 %. An increase in power dissipation is nevertheless observed, which is natural as practically the same field intensities are being generated from farther windings, leading to an average power dissipation of 12.3 W vs 9.5 W before coil projection to outer radii, with 98 % of subjects in $\mathcal{T}$ under 40 W. At this point we notice that performances of projected SF to outer radii can be maintained the same as long as power dissipation is free to increase.

On the other hand, the discretization into realistic windings can be costly in terms of performance. Using $\delta_w = 2.4$ mm, the magnetic fields obtained from the actual windings deviate from SF ideal fields, leading to 16.0 % inhomogeneity reduction for the 3-coil system on both design and test sets, a significant drop compared to the theoretically achievable performances of 22.8 % and 22.9 %. This is a drawback of high δ_w and it suggests a need for improving the quality of the discretization into windings. Therefore, the use of smaller wire gauges is required. A lower limit for the wire-gauge would depend on winding technology capabilities and power dissipation rise due to higher resistance of the windings. By decreasing the inter-wire spacing for the first layer to $\delta_w^{15W,M=1} = 1.2$ mm (allowing the use of 1 mm diameter wire), while keeping the 2.4 mm inter-wire spacing for second and third layers, the gap in performance is reduced, as inhomogeneity reduction for design and test sets are 20.5 % and 20.4 %, respectively. This realistic 3-channel SF-SVD design is comparable to the unconstrained 16-channel 4^{th} order SH system. Simulations showed no improvement when reducing δ_w for the second and third layers, thus the configuration with 1.2 mm inter-wire spacing for the first layer and 2.4 mm for both second and third layers should be preferred, as smaller values for δ_w will increase complexity of the windings.

Currents and power dissipation for this realistic SF-SVD insert are shown in Fig. 3.12. Its average power dissipation is 5.6 W and maximum power dissipation is 32.5 W, with 98 % of subjects requiring less than 18 W for shimming. Average currents for each channel are 1.8 A, 3.1 A and 1.9 A for modes 1, 2 and 3, respectively, on $\mathcal{D}$; and 2.0 A, 3.7 A and 2.0 A on $\mathcal{T}$. This range of currents could be easily driven by a low-cost, compact, open-source current drive [Arango 2019] (https://www.opensourceimaging.org/project/current-driver-for-local-bo-shim-coils/), which can deliver 8 A per output channel and whose channels could be connected in parallel to eventually supply the max current of 12 A observed in channel 2 of the SF-SVD shim system.

As a final remark, the 275 mm outer diameter of the in-house RF coil considered in this study is relatively small compared to most commercial RF coils, which have outer diameters as large as 380 mm. Preliminary simulations of the presented SF-SVD method applied to larger radius coil former (380 mm) have shown that for keeping performances of a 3-ch. SF-SVD system superior to that of a 4^{th} order SH shim system, average power dissipation grows to 360 W, i.e. 38 times higher than the power dissipation of the small radius system proposed herein. Such high power would require water cooling

for heat management, thus increasing complexity of the system despite the low channel count. Alternatively, as shown in Fig. 3.6, a high performance, low power system could be built if the number of channels is allowed to increase. Indeed, a 20 W average power SF-SVD shim system with equivalent performances to a 4^{th} order SH system can be designed if the number of channels is allowed to increase to at least 8. This highlights the importance of keeping a small radius coil former to achieve high-performance with low power consumption and low channel count.

3.4 Conclusion

From the presented results it can be established that the use of SF Singular Value Decomposition for obtaining a high performance few-channel shim system dedicated to a specific anatomy is promising. Inhomogeneity reduction produced by a 3-channel SF-SVD-coil insert with 15-20 W nominal power is equivalent to that achieved by a 4^{th}-order SH shim insert composed by 16 coils with unlimited power. Moreover, concomitant computation of 2^{nd} SH shim coefficients and SVD currents can improve performance, superior to 5^{th} order SH.

The SF-SVD method applied to 50 brain fieldmaps showed consistence in performance over a test set of subjects of equivalent size, thus confirming that the system can be used for shimming new brain fieldmaps. This was further confirmed by 10-fold cross-validation on the entire 100-brain database.

Provided enough space, the number of coils composing the SF-SVD could be increased, although simulations showed improvements to be small.

To further improve the performance of whole-brain shimming, dedicated shim systems could be designed for populations with specific anatomies, such as large vs small heads, or Asian vs Caucasian head shapes. Alternatively, SF-SVD shim systems could be designed for local shimming in specific areas of the brain, which, for a same power target, might boost performances in the selected region.

However, a drawback is the complexity of the wire patterns for SF-SVD coils, making the fabrication process more laborious, while for SH coils, several patents depicting relatively simple designs for SH insert fabrication have been proposed, e.g. [Punchard 2013]. Nevertheless, a 3D model of a possible implementation of a single channel SF-SVD shim system was shown in Fig. 3.2 for a groove-based design. Alternatively, the system could also be manufactured by cutting the paths through bulk copper.

Although the context of this study is neurological Ultra-High Field MRI, the presented method could easily be applied for anatomies other than the brain.

* * *
* *
*

Chapter 4

Physical Limits to Human Brain B0 Shimming, and Engineering Implications

Chapter Outline

A preliminary version of this study was presented at an international conference as:

B. Pinho Meneses and A. Amadon. *Analysis of Bo Field Shimming Limitations in the Human Brain at Ultra-High-Field.* In Proceedings of the 28th Annual Meeting of ISMRM, volume 28, page 4223, Virtual, 2020.

DESIGN of optimized shimming equipment is under way for UHF MRI of the human brain. Here shimming theoretical limits are explored. With a simple model, proof is given that, depending on field source distribution around a zone of interest, no shimming hardware external to such a zone can fully mitigate the inhomogeneous field. A simulation is performed on a 100-subject database to establish hard shim limits on the whole brain. On the other hand, 3D region-specific shimming is shown to be a very effective way to improve homogeneity in critical zones such as the pre-frontal cortex and around ear canals.

4.1 Introduction

When immersed in the uniform magnetic field B_0 of the MRI scanner, the media composing the human head (biological tissue, air) become magnetized, in turn generating a non-uniform magnetic field distribution $\delta B_0(\boldsymbol{x})$ obeying

$$\nabla^2 \delta B_0 = \left(\nabla^2 \chi - 3 \frac{\partial^2 \chi}{\partial z^2} \right) \frac{B_0}{3}, \tag{4.1}$$

(adapted from [Salomir 2003]) where $\chi(\boldsymbol{x})$ is the media's magnetic susceptibility.

Such inhomogeneous magnetic field distribution is at the origin of several kinds of image artifacts in human brain imaging, with geometric distortion in Echo Planar acquisitions being a notorious example [Lüdeke 1985, Jezzard 1995, Zhao 2005, Smith 2010, Mullen 2020].

As an example, in non-accelerated EPI single-shot acquisitions, under 0.5 ms inter-echo spacing and 200 mm Field-of-View (FOV) in the phase encoding direction, a 100 Hz excursion in the magnetic field leads to 10 mm geometric distortion in the reconstructed image [Jezzard 1995, Wald 2012]. It is therefore not surprising that much effort was directed to the design of shimming systems for the human brain, but as we will see, these are still very far from achieving the minimal inhomogeneity.

Other B_0 related complications are signal loss in T_2^*-weighting imaging, banding artefacts in SSFP sequences, failed inversion-recovery pulse, inhomogeneous flip angle distribution, and line broadening in spectroscopy.

With the current trend of increasing magnetic field intensity of clinical and research MRI scanners (7 T Siemens Terra, 10.5 T CMRR [Sadeghi-Tarakameh 2020], 11.7 T Iseult project [Quettier 2020]) to achieve higher Signal-to-Noise Ratio (SNR) and Constrast-to-Noise Ratio (CNR), susceptibility-induced inhomogeneity rises proportionally to the main field. High performance static field shimming becomes crucial for these scanners to deliver their full potential in applications such as functional MRI (fMRI) [Bandettini 2012].

Correction of inhomogeneous fields is either active, generated by electric current flow in conductors located around the patient, or passive, by the placement of ferromagnetic pieces in optimal positions [Jesmanowicz 2001a, Juchem 2006].

Subject specific shimming is performed with Spherical Harmonics based systems, usually integrated to the MRI scanner up to 3rd degree, but higher-degree SH-based systems have also been employed [Pan 2012]. Moreover non-SH-based Multi-Coil Array (MCA) systems [Juchem 2011, Stockmann 2013, Han 2013, Aghaeifar 2018] have gained traction in the last years. These have been shown to provide adequate homogeneity for numerous applications at Ultra High Field (UHF), but strong field excursion persists around the ear canals and in the pre-frontal cortex despite shimming, even when employing brain-optimized MCAs [Meneses 2019c, Aghaeifar 2020, Pinho Meneses 2020e].

Moreover, by analyzing the Solid Spherical Harmonics expansion of fundamental building-blocks for the perturbation and correction fields, the impossibility of a perfect shim for the human brain will be demonstrated in this work.

Aware of these unmet needs and of the impossibility of full mitigation of δB_0 by means of any external hardware, as shown in this work, we explore the limits to B_0 shimming of the human brain through unconstrained SH shimming simulations on a large database of 3D fieldmaps. Furthermore, assessment of realistic shim systems is performed through power constrained coil design, where homogeneity levels attained by such systems will be compared to the lowest achievable homogeneity. Knowledge of the attainable levels of homogeneity for diverse shimming strategies (whole-brain, region-specific, slice-wise) can provide meaningful insight for future shim system design, since for limited resources (channel count, maximum current and power), a region-specific shimming strategy could provide homogeneity levels unattainable when applying global (whole-brain) shimming.

4.2 Theory: physical Limits to B0 Shimming

B_0 homogeneity in the human brain is mainly disturbed by the presence of susceptibility gradients between paramagnetic air cavities and diamagnetic tissues, as exposed in equation 4.1. This perturbation can be seen as caused by a distribution of magnetic dipoles oriented in the B_0 field direction and located on air-tissue interfaces. For the human head, a distribution of dipole moments disturbing the once uniform magnetic field appears, located around the ear canals, sinus, mouth and any other interface with non-negligible susceptibility difference. Susceptibility differences also exist between white matter, gray matter and cerebrospinal fluid, but are less significant in comparison to that between air and tissues, and are considered negligible in this work.

Although there are mentions in the literature to the impossibility of perfectly shimming the magnetic field inside the brain [Hillenbrand 2005], no detailed account on the reason for such limitation has been provided.

In the subsequent analysis, the reference coordinate frame is defined such that axes x, y and z are oriented in the subject's PA, RL and FH directions, respectively, assuming the patient lies on his back. The main B_0 field is oriented in the positive z direction.

4.2.1 Laplace's Equation and Solid Harmonics

Any magnetic field in a source-free region obeys Laplace's equation. In the z direction one obtains:

$$\nabla^2 B_z(r,\theta,\varphi) = 0. \tag{4.2}$$

This equation has general solution given by

$$B_z(r,\theta,\varphi) = \sum_{n=0}^{+\infty}\sum_{m=-n}^{n} A_n^m \mathcal{R}_n^m(r,\theta,\varphi) + B_n^m \mathcal{I}_n^m(r,\theta,\varphi) \tag{4.3}$$

with

$$\mathcal{R}_n^m(r,\theta,\varphi) = r^n Y_n^m(\theta,\varphi), \tag{4.4}$$

$$\mathcal{I}_n^m(r,\theta,\varphi) = \frac{1}{r^{n+1}} Y_n^m(\theta,\varphi) \tag{4.5}$$

and

$$Y_n^m(\theta,\varphi) = \begin{cases} P_n^m(\cos\theta)\cos m\varphi & m \geq 0 \\ P_n^{|m|}(\cos\theta)\sin|m|\,\varphi & m < 0 \end{cases}, \tag{4.6}$$

where $\mathcal{R}_n^m$, $\mathcal{I}_n^m$ and Y_n^m are denominated Regular Solid Harmonic (RSH), Irregular Solid Harmonic (ISH) and Spherical (or Surface) Harmonic (SH), respectively, of degree n and order m; and function $P_n^m : [-1,1] \to \mathbb{R}$ is the Associated Legendre Polynomial given by

$$P_n^m(x) = \frac{(1-x^2)^{\frac{m}{2}}}{2^n n!}\frac{d^{n+m}}{dx^{n+m}}(x^2-1)^n. \tag{4.7}$$

Using the above definitions for RSH and ISH, the particular Green function for the Laplacian, $1/|\boldsymbol{x}-\boldsymbol{x}'|$, present in the formulas of scalar and vector magnetic potentials in magneto-statics, can be expanded into (adapted from [Jackson 2007]):

$$\frac{1}{|\boldsymbol{x}-\boldsymbol{x}'|} = \sum_{n=0}^{+\infty}\sum_{m=0}^{n}(2-\delta_{m0})\frac{(n-m)!}{(n+m)!}\frac{r_<^n}{r_>^{n+1}}P_n^m(\cos\theta)P_n^m(\cos\theta')\cos m(\varphi-\varphi') \tag{4.8}$$

with $r_>$ ($r_<$) the larger (smaller) between $|\boldsymbol{x}|$ and $|\boldsymbol{x}'|$.

4.2.2 Mathematical Analysis of Magnetic Field Sources Around the Brain

From equation 4.1, the inhomogeneous magnetic field appearing once the patient is immersed in the main B_0 field is caused by a distribution of magnetic dipoles located on air-tissue interfaces. As such, an infinitesimal magnetic dipole can be considered as a fundamental building-block to analyze the sample-induced B_0 inhomogeneity, defined as the B_0 standard deviation to mean ratio across the Region-Of-Interest (ROI).

To counteract the inhomogeneous magnetic field, active shimming systems are commonly employed, and an infinitesimal current filament can be used as another fundamental building block to describe the magnetic field of such systems.

Both fundamental pieces are depicted in fig.4.1. The perturbation is produced by a magnetic dipole of moment $\boldsymbol{m}_p = m_p\hat{\boldsymbol{z}}$, located at some arbitrary location $\boldsymbol{x}_p$ with

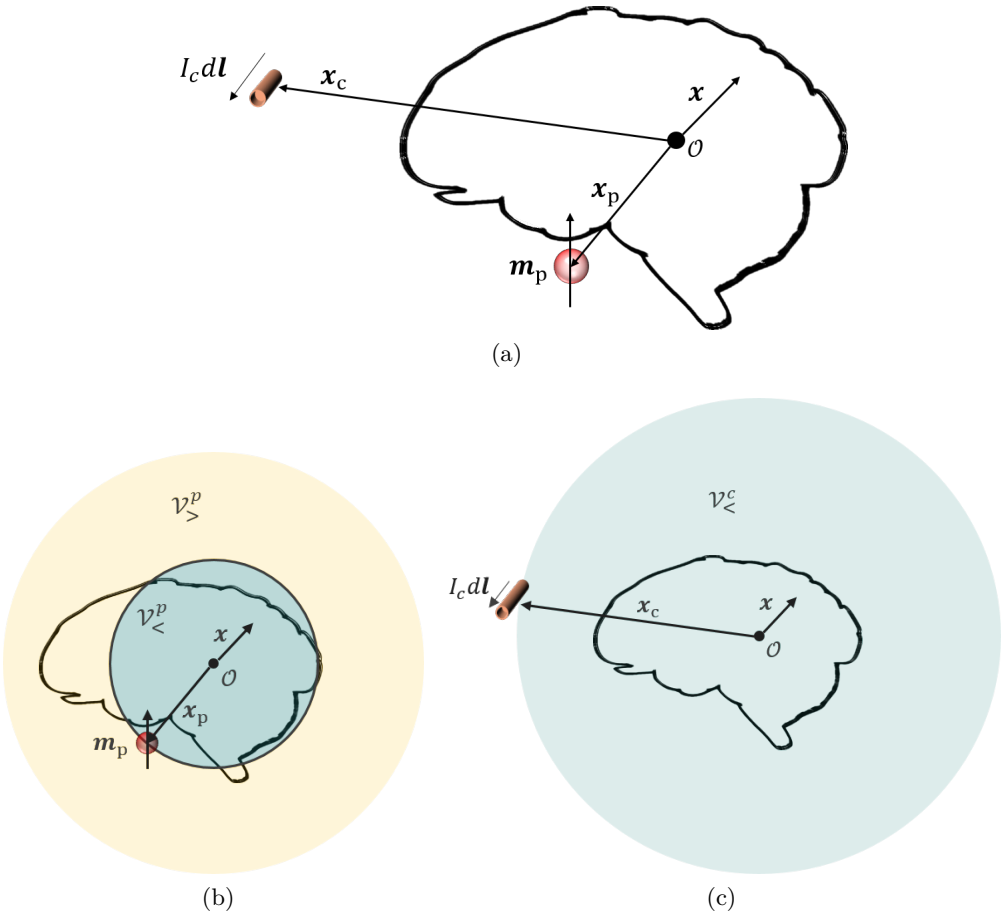

Figure 4.1 – (a) Disposition of fundamental building blocks for sample-induced magnetic perturbation ($\boldsymbol{m}_p$) and field correction ($I_c d\boldsymbol{l}$) around the brain. The MR magnet isocenter at $\mathcal{O}$ corresponds to the origin of the B_0 SH-decomposition. $\boldsymbol{x} \in \mathbb{R}^3$ points to an arbitrary brain voxel to be shimmed. (b) A representation of the regions where the magnetic field generated by a punctual sample-induced perturbation is described by RSH ($\mathcal{V}^p_<$) and ISH ($\mathcal{V}^p_>$). (c) The region $\mathcal{V}^c_<$ where the correction magnetic field is decomposed into RSH.

spherical coordinates $(r_p, \theta_p, \varphi_p)$; and the correction field is produced by a wire filament carrying current I_c, with length $d\boldsymbol{l}$, located at $\boldsymbol{x}_c$ with spherical coordinates $(r_c, \theta_c, \varphi_c)$ relative to SH isocenter $\mathcal{O}$.

Solid Harmonic Expansion of Sample Induced Perturbation

To analyze the magnetic field generated by $\boldsymbol{m}_p$ inside the brain, it is convenient to employ the magnetic scalar potential, given by:

$$\Phi_p(\boldsymbol{x}) = -\frac{\boldsymbol{m}_p}{4\pi} \cdot \nabla \frac{1}{|\boldsymbol{x} - \boldsymbol{x}_p|}. \tag{4.9}$$

From $\boldsymbol{B} = -\mu_0 \boldsymbol{\nabla} \Phi$, the magnetic field in the z direction is

$$B^p_z(\boldsymbol{x}) = \frac{\mu_0 m_p}{4\pi} \frac{\partial^2}{\partial z^2} \frac{1}{|\boldsymbol{x} - \boldsymbol{x}_p|}. \tag{4.10}$$

Substituting 4.8 into 4.10, according to the position of the point of interest $\boldsymbol{x}$ relatively to $\boldsymbol{x}_p$, one obtains two possible expressions for the magnetic field. Those are:

$$B_z^p(\boldsymbol{x}) = \frac{\mu_0 m_p}{4\pi r_p^3} \sum_{n=0}^{+\infty} \sum_{m=0}^{n} (2-\delta_{m0}) \frac{(n-m+2)!}{(n+m)!} \frac{P_{n+2}^m(\cos\theta_p)}{r_p^n} r^n P_n^m(\cos\theta) \cos m(\varphi-\varphi_p), \tag{4.11}$$

in $\mathcal{V}_<^p = \{\boldsymbol{x} \in \mathbb{R}^3 : |\boldsymbol{x}| < r_p\}$, and

$$B_z^p(\boldsymbol{x}) = \frac{\mu_0 m_p}{4\pi} \sum_{n=2}^{+\infty} \sum_{m=0}^{n-2} \frac{(2-\delta_{m0})(n-m)!}{(n+m-2)!} P_{n-2}^m(\cos\theta_p) \frac{r_p^{n-2}}{r^{n+1}} P_n^m(\cos\theta) \cos m(\varphi-\varphi_p) \tag{4.12}$$

in $\mathcal{V}_>^p = \{\boldsymbol{x} \in \mathbb{R}^3 : |\boldsymbol{x}| > r_p\}$. Equation 4.11 was adapted from [Roméo 1984], and equation 4.12 can be derived in a similar fashion.

We notice, therefore, that in $\mathcal{V}_<^p$ the magnetic field is composed exclusively of RSH, while ISH describe the magnetic field in $\mathcal{V}_>^p$. Moreover, let $\mathcal{V}_b$ be the brain region, the sample induced perturbations can produce both RSH and ISH fields in its interior as long as the intersection of $\mathcal{V}_b$ with sets $V_<^p$ and $V_>^p$ is non-null.

Solid Harmonic Expansion of Correction Fields

With the inhomogeneous field described, we move our attention to the correction fields. The filament chosen as building-block for correction devices has magnetic vector potential given by

$$d\boldsymbol{A}_c(\boldsymbol{x}) = \frac{\mu_0 I_c d\boldsymbol{l}}{4\pi} \frac{1}{|\boldsymbol{x}-\boldsymbol{x}_c|} \tag{4.13}$$

producing

$$dB_z^c(\boldsymbol{x}) = \hat{\boldsymbol{z}} \cdot (\nabla \times d\boldsymbol{A}_c(\boldsymbol{x})) \tag{4.14}$$

as magnetic field in the z direction.

Substitution of 4.8 into 4.13 and subsequent calculation of 4.14 leads to (adapted from [Roméo 1984])

$$dB_z^c(r,\theta,\varphi) = \frac{\mu_0 I_c \sin\theta_c d\varphi}{4\pi} \sum_{n=0}^{+\infty} \sum_{m=0}^{n+1} \left[\frac{(n-m)!}{(n+m)!} \frac{P_{n+1}^{m+1}(\cos\theta_c)}{r_c^{n+1}} - \frac{(n-m+2)!}{(n+m)!} \frac{P_{n+1}^{m-1}(\cos\theta_c)}{r_c^{n+1}} \right] \times r^n P_n^m(\cos\theta) \cos m(\varphi-\varphi_c). \tag{4.15}$$

in $\mathcal{V}_<^c = \{\boldsymbol{x} \in \mathbb{R}^3 : |\boldsymbol{x}| < r_c\}$.

As the shimming system is positioned around the patient's body or head, we have $\mathcal{V}_b \subset \mathcal{V}_<^c$; therefore, equation 4.15 is sufficient for describing the magnetic field in the subject's brain generated by shimming structures, and it is observed that this magnetic field only generates RSH.

Condition for Perfect B_0 Shimming

RSH and ISH functions are linearly independent. Therefore, any shimming apparatus placed around the head can only zero-out the sample-induced inhomogeneity in the brain

if $\mathcal{V}_{>}^{p} \cap \mathcal{V}_b = \emptyset$, i.e. there is no ISH term describing the magnetic field inside the brain. Or, stated in a simpler and generalized form, a region within an anatomy can only be shimmed to a perfectly homogeneous magnetic field by an external shimming apparatus if, and only if, the smallest sphere enclosing the said region does not contain any source of magnetic field.

4.3 Methods

We start by showing that the human brain does not satisfy the condition for perfect B_0 homogenization. Then, by performing RSH shimming in a large database of δB_0 fieldmaps, the minimal inhomogeneity theoretically achievable $\sigma_{\min}$ is estimated. In addition, we discuss how state-of-the-art shimming systems compare to the best achievable inhomogeneity. Different regions of interest are explored in this phase to compare global, slice-by-slice and slab-specific shimming.

Finally, the estimated ultimate inhomogeneity is compared to what could be achieved by optimal shim coils under power constraints.

4.3.1 Source Localization in a 3D Head Model

Using a 3D model of the human head [Makris 2008], with magnetic susceptibilities of air and tissues set to $\chi_a = 0.36 \times 10^{-6}$ and $\chi_t = -9.03 \times 10^{-6}$, respectively, the magnetic field source distribution around it is computed from the right side of equation 4.1:

$$\rho_m(\boldsymbol{x}) = \left(\nabla^2\chi - 3\frac{\partial^2\chi}{\partial z^2}\right)\frac{B_0}{3}. \tag{4.16}$$

A set $\mathcal{X}$ of all values of $|\boldsymbol{x}_s|$ such that $\rho_m(\boldsymbol{x_s}) \neq 0$ is obtained. Defining a ball[1] $\mathcal{B}(\inf \mathcal{X}, \mathcal{O})$, if $\mathcal{B} \cap \mathcal{V}_b \neq \mathcal{V}_b$, the brain cannot be perfectly shimmed by RSH. Nevertheless, $\mathcal{B}(\inf \mathcal{X}, \mathcal{O})$ or any other ball inside the brain (not necessarily centered at $\mathcal{O}$), not enclosing magnetic field sources, could still be perfectly shimmed.

4.3.2 Ultra-High-Degree Simulation of RSH Shimming

To determine the best achievable homogeneity given the theoretical limits, unconstrained RSH shimming simulations with increasing degree were performed on a 100-subject database of three dimensional δB_0 maps in the brain.

The database was built from fieldmaps acquired on a MAGNETOM Prisma 3 T imager (Siemens Healthcare GmbH, Erlangen, Germany) with 1.7 mm isotropic resolution, after 2^{nd} degree shimming. FSL's brain extraction tool [Smith 2002] was used for masking and restrict our analysis to the human brain. Fieldmap acquisitions were performed with two 3D gradient echo sequences, one with 2 distant echoes $\text{TE}_1 = 1.88$ ms and $\text{TE}_3 = 4.9$ ms, and one with a single echo at $\text{TE}_2 = \text{TE}_1 + 0.7$ ms. TE_1 and TE_2 are supposed to be close enough in time so that no phase excursion occurs in the brain beyond $\pm\pi$ during that

[1] A ball $\mathcal{B}(R, \boldsymbol{c})$ of radius R centered at $\boldsymbol{c} \in \mathbb{R}^3$ is defined as the set of $\boldsymbol{x} \in \mathbb{R}^3$ such that $|\boldsymbol{x} - \boldsymbol{c}| < R$.

0.7 ms interval (assumption: δB_0 does not exceed ± 714 Hz in the brain at 3 T). Then a double-point linear fit of the phase evolution between TE_1 and TE_2 is initially performed for phase unwrapping of the last echo; then a triple-point linear fit of the phase evolution is performed for δB_0 estimation. The resulting δB_0 maps were cleaned with an outlier filter to avoid singularities, especially at the edge of the brain. It was then scaled up by 7/3 for investigation at 7 T.

For the shimming simulations, given a target magnetic field $\boldsymbol{b} \in \mathbb{R}^K$ across K voxels, the set $\boldsymbol{a}$ of solid harmonic coefficients A_n^m for each degree $n = 1, ..., N$, with N the RSH degree employed in the simulation, is computed such that

$$\boldsymbol{a} = \underset{\boldsymbol{a} \in \mathbb{R}^{N^2+2N+1}}{\operatorname{argmin}} \; ||\boldsymbol{b} - \mathbf{R}\boldsymbol{a}||_2^2 , \tag{4.17}$$

with $\mathbf{R} \in \mathbb{R}^{K, N^2+2N+1}$ of the form

$$\mathbf{R} = \begin{bmatrix} \mathcal{R}_0^0(\boldsymbol{x}_1) & \mathcal{R}_1^{-1}(\boldsymbol{x}_1) & \mathcal{R}_1^0(\boldsymbol{x}_1) & \dots & \mathcal{R}_n^m(\boldsymbol{x}_1) & \dots & \mathcal{R}_N^N(\boldsymbol{x}_1) \\ \mathcal{R}_0^0(\boldsymbol{x}_2) & \mathcal{R}_1^{-1}(\boldsymbol{x}_2) & \mathcal{R}_1^0(\boldsymbol{x}_2) & \dots & \mathcal{R}_n^m(\boldsymbol{x}_2) & \dots & \mathcal{R}_N^N(\boldsymbol{x}_2) \\ \vdots & \vdots & \vdots & \ddots & \vdots & \ddots & \vdots \\ \mathcal{R}_0^0(\boldsymbol{x}_K) & \mathcal{R}_1^{-1}(\boldsymbol{x}_K) & \mathcal{R}_1^0(\boldsymbol{x}_K) & \dots & \mathcal{R}_n^m(\boldsymbol{x}_K) & \dots & \mathcal{R}_N^N(\boldsymbol{x}_K) \end{bmatrix} . \tag{4.18}$$

The inverse problem is solved using MATLAB's (The Mathworks, Natick, MA, USA) *lsqminnorm*.

For each subject, RSH shimming was performed targeting different types of brain regions: global, slice-by-slice and slab-specific. Slice-by-slice implies dynamic shimming of 1.7 mm transverse slices covering the whole-brain. Slab-specific shimming was performed considering three different slabs containing notoriously challenging regions to shim, namely the prefrontal cortex (PFC) and the temporal lobes (TLs). Temporal lobe shimming was further subdivided into two slab types: bilateral and unilateral. The choice of using slabs rather than employing precise segmentation of the regions of interest was made to account for common research and clinical practices. Slab masks were created manually for each subject with approximate thickness of 55 mm. Shimming is performed on the voxels in the intersection of the slab with the brain mask. The targeted slab characteristics are shown in fig.4.2.

4.3.3 Verification of the conditions for ultimate shimming

Considering a single, randomly selected subject from the database, validation of the condition for perfect shimming is performed by defining a spherical region enclosing critical inhomogeneity zones located in the ventral area of the prefrontal cortex, but not enclosing any obvious magnetic field sources (air cavities). RSH shimming of increasing degree is performed inside this ROI and it is compared to the achieved inhomogeneity for the same subject under global shimming. The spherical ROI is then shifted downward along the Head-Feet direction, and RSH shimming is applied on the voxels in the intersection of the brain mask with the ROI ($\rightarrow$ truncated sphere). If the proposed condition for ultimate shimming is consistent, the sphere entirely located inside the brain should provide better

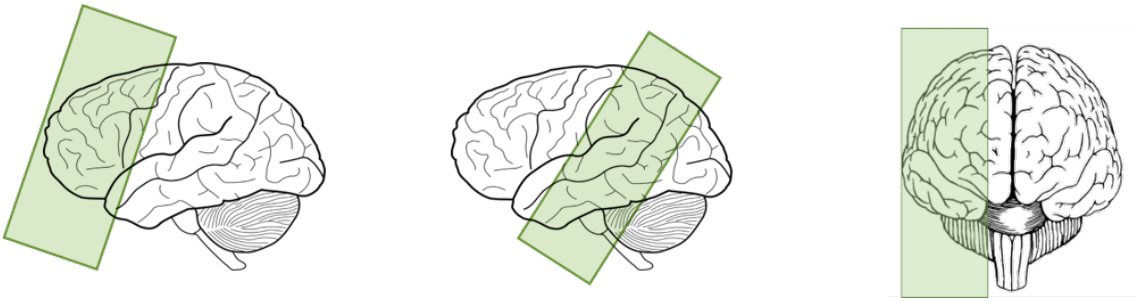

Figure 4.2 – Slab positioning for localized shimming simulations with RSH and SO coil design. Targets from left to right: prefrontal cortex, temporal lobes (bilateral) and temporal lobe (unilateral).

homogeneity than the subsequent truncated spheres. The spherical ROI has 38 mm radius and is shown in fig.4.9.

4.3.4 Comparison to optimal shim coil design

In order to explore practical aspects of coil design, and how realistic cylindrical systems could perform relatively to the best achievable inhomogeneity, the Dipole Boundary Method (DBM) [Pinho Meneses 2020b] is applied to compute subject-optimal stream-functions (SO-SFs) for each subject in the database under global and slab-specific shimming techniques.

SO-SFs are computed under different power dissipation targets to assess how performances relative to the best achievable homogeneity estimated from RSH shimming simulations are impacted by engineering limitations.

The SO-SFs are calculated over a cylindrical coil former of 140 mm radius, 300 mm length, with a 4 mm discretization step. Discretization into windings is performed with 2.4 mm minimum inter-wire spacing and copper wire of 1.54 mm^2 circular section. Power dissipation for each coil is then calculated for the obtained winding pattern. Target power for the designs are 3 W, 7 W, 15 W, 25 W, 50 W, 75 W and 100 W.

Inhomogeneity levels resulting from subject optimal designs are assessed and compared to very high-degree RSH shimming limits.

4.4 Results and Discussion

4.4.1 Magnetic Field Perturbation Sources in the Human Head

The disposition of points $\boldsymbol{x}_s$ satisfying $\rho_m(\boldsymbol{x}_s) \neq 0$ is shown in fig.4.3. A build-up of susceptibility-induced field sources is observed on the interface between the head and the surrounding air. Closer to the brain are the susceptibility-induced sources caused by susceptibility gradients between air cavities in the head (sinus and ear canals) and biological tissues. It is also apparent that, under the displayed configuration, the condition for perfect shimming cannot be fulfilled as it is impossible to obtain any brain-enclosing sphere that does not enclose perturbation sources.

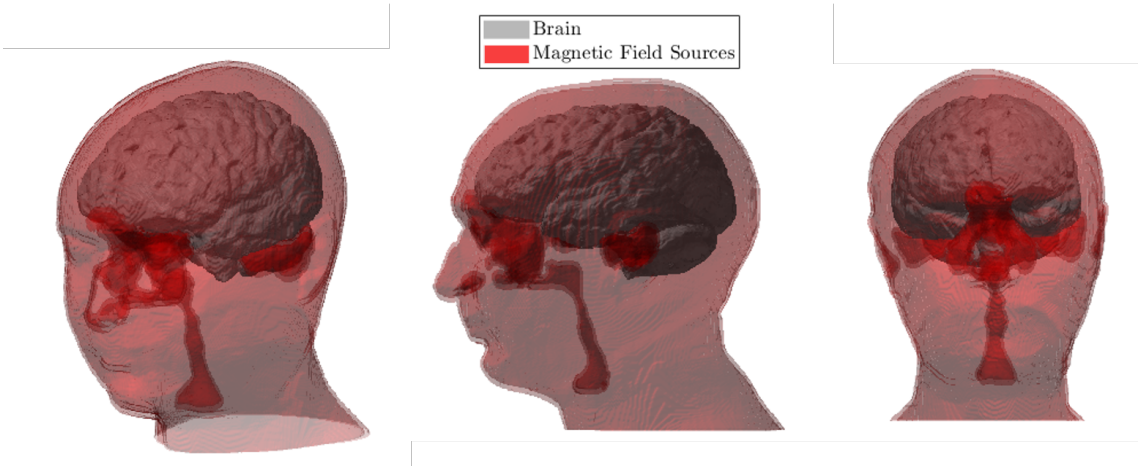

Figure 4.3 – Magnetic field source disposition around the human brain as computed from equation 4.16.

The distribution of perturbation sources estimated from 4.16 is compatible with the strong inhomogeneous magnetic field commonly observed in the temporal lobes and frontal lobe. These inhomogeneity hotspots are discussed throughout a vast literature, from simulated [Li 1995,Hillenbrand 2005,Kochan 2015] to measured data [Li 1996,Collins 2002]. Due to the proximity of the sources to the brain, intense magnetic field values appear in the brain cortex, reaching values as high as 800 Hz at 7 T, as gathered from the database.

4.4.2 Whole-brain B0 Homogeneity Limits

The results for human brain shimming with very high RSH degree are shown in fig.4.4. Baseline inhomogeneity across the database is 65.7 Hz (SD: 11.4 Hz). As RSH degree increases, a steep inhomogeneity drop is observed up to 20^{th} degree, with the rate of improvement of 1.5 Hz per degree when around 10^{th} degree and a contrasting slower improvement afterwards, with only 0.07 Hz per degree around 70^{th} degree. Due to limited computational resources and time, the maximum RSH degree was increased up to 90, presenting inhomogeneity of 15.9 Hz (SD: 3.4 Hz) in the brain, or an improvement of 75.8 % relative to baseline.

Consistent with theoretical developments, an asymptotic behavior, tending to non-zero inhomogeneity, can be inferred from the inhomogeneity evolution. The minimum inhomogeneity achievable in the database could be extrapolated using MATLAB's *Curve Fitting Tool*, providing an average 12.3 Hz (95 % Confidence Bounds: 10.9 Hz–13.7 Hz) for the database. This value represents an 81.3 % improvement in homogeneity in the human brain. In theory, this result indicates that inhomogeneity at UHF of 7 T and 11.7 T could be reduced to the equivalent of 1.4 T and 2.4 T MRI systems, respectively, although the practical implementation of such a system is very unlikely.

Regarding the voxels presenting absolute field excursion superior to 100 Hz, which would account for stronger B_0 related artifacts, it follows a similar trend to that of the inhomogeneity, reaching a virtually artifact-free configuration, as an average of less than

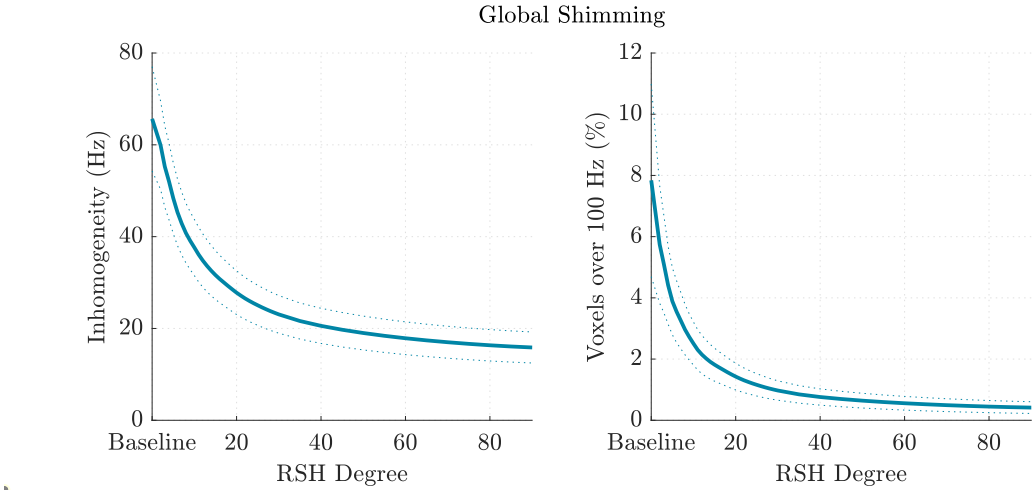

Figure 4.4 – Average inhomogeneity and proportion of voxels over 100 Hz across subjects in the database as RSH degree increases (reference field at 7 T). Metrics for each subject are computed considering all voxels in the brain mask after application of (a) global and (b) slice by slice shimming. Dotted lines indicate standard deviation of the metric across subjects in the database.

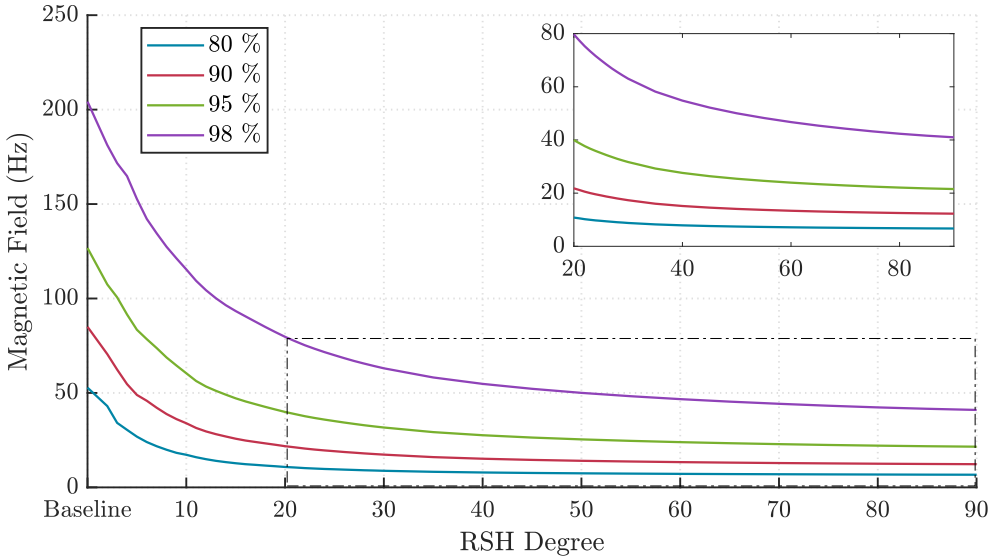

Figure 4.5 – Average on the 100-subject database of the absolute frequency range containing 80 , 90 , 95 and 98 % of voxels in the brain after global shimming as RSH degree increases.

0.5 % of voxels over 100 Hz is achieved. This reduction is dramatic relatively to the initial proportion of 7.8 %, which may cause information in a non-negligible portion of the brain to be lost in an EPI scan, for instance.

A more detailed visualization of how increasing RSH degrees act to reduce global inhomogeneity is provided in fig.4.5, where the evolution of the maximum $|\delta B_0|$ for the 80 , 90 , 95 and 98 % lowest absolute excursion voxels is shown. At relatively lower degrees, RSH functions act over all frequency ranges. As degree increases, RSH action seems to be localized, as significant changes are mostly observed in the 95 and 98 % ranges, thus on a smaller amount of voxels.

Fig.4.6 shows that strong inhomogeneity regions still remain even after global shimming at very high degree. And although inhomogeneity values at very high degree present a significant drop from baseline inhomogeneity, most shim systems presented in the literature have shown performances at most equivalent to 6^{th} degree RSH despite optimization of MCA loops placement and geometry in some studies [Zhou 2020, Pinho Meneses 2020e, Aghaeifar 2020].

In slice-by-slice shimming (cf fig.4.4b), inhomogeneity reduction as RSH degree increases is much greater. Inhomogeneity at 17^{th} degree is 12.6 Hz (SD: 3.4 Hz), and already inferior to the inhomogeneity at 90^{th} degree in global shimming. Voxels over 100 Hz are reduced to 0.2 % (SD: 0.1 %). The greater effectiveness of dynamic slice-by-slice shimming in mitigating B_0 inhomogeneity when compared to global shimming is known [Koch 2006b, Juchem 2011], and it is what makes it appealing for 2D acquisition schemes. From the results, we see that such a feature is linked to the lower RSH degree required, which indicates that less rapid spatial field variation is needed. From a shim system design

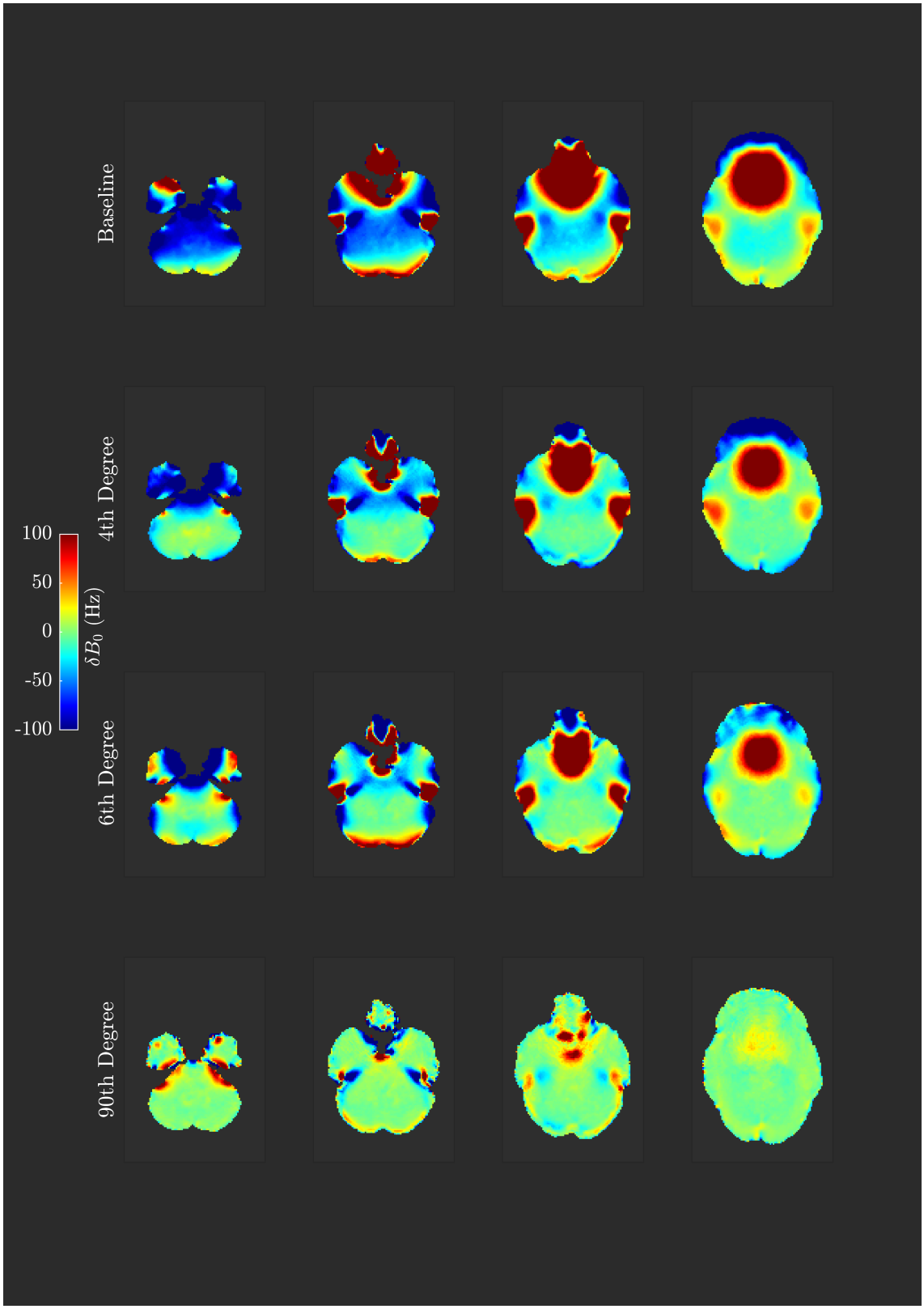

Figure 4.6 – Selected axial slices of brain fieldmap after RSH global shimming of different degrees. The slices show zones of high inhomogeneity. 4^{th} and 6^{th} degree fieldmaps are shown as examples of the maximum mitigation levels achieved by shimming systems so far as reported in the literature when performing global shimming. The best inhomogeneity obtained (90^{th} degree shimming) in our unconstrained simulations is also shown.

perspective, given some surface upon which wire patterns will be placed, being able to generate rapidly spatially varying fields means putting as many loops as possible covering the whole surface. These RSH simulations indicate that the same spatial distribution of coils in a Multi-Coil Array will be able to perform better in slice-by-slice shimming compared to global shimming due to the need of lower degree RSH. While an efficient technique for reducing inhomogeneity, if isotropic submillimeter resolution is desired, 2D acquisition of very thin slices might not provide sufficient SNR. Three-dimensional acquisitions become necessary, and global shimming could be required.

4.4.3 Slab Shimming Limits

While slice-by-slice shimming might be unsuited for submillimeter resolution, slab-specific acquisition can be a viable alternative if only a specific region of the brain is of interest. Figs. 4.7 and 4.8 show that this shimming modality could also improve homogeneity given a fixed degree of RSH components when compared to what would be achieved in the same ROI under global shimming. Fig.4.8 shows that at 3^{rd} degree (which is available to limited order in some UHF scanners), localized shimming in specific slabs could provide significant inhomogeneity reduction, with average drops of 7.7 Hz, 9.0 Hz and 8.0 Hz in the PFC and TLs (bilateral and unilateral), respectively. Moreover, considering the TL bilateral slab, when applying global shimming, a 6^{th} degree RSH shim system would be required to provide the same homogeneity as a 3^{rd} degree system if localized shimming was employed. From a hardware perspective, going from 3^{rd} to 6^{th} degree implies adding 33 coils. Therefore, great economy of resources is possible by changing the shimming strategy, provided whole-brain shimming is not an issue. It can also be noticed from the localized shimming simulations that global shimming seems to naturally concentrate efforts in mitigating inhomogeneity in the PFC, as there is a smaller gap in performance and coil number when switching from global to localized shimming. Such smaller relative improvements in the temporal lobes homogeneity has been noticed in several works [Stockmann 2018, Aghaeifar 2018, Aghaeifar 2020], but as can be seen, could be overcome if localized shimming was employed.

None of the shimming schemes presented so far satisfies the condition for ultimate shimming. In average, the residual inhomogeneity observed in the shimmed ROIs is still superior to 10 Hz.

4.4.4 Towards Perfect Shimming in Spherical ROIs

To further study the validity and consequences of the perfect shimming condition, RSH shimming simulations were performed in the four distinct ROIs shown in fig.4.9. We notice how RSH shimming in ROIs 3 and 4, which presumably satisfy the perfect shimming condition, converge faster to lower inhomogeneity values (8.0 Hz and 4.5 Hz, respectively) as RSH degree is increased, and present a more localized residual inhomogeneity compared to ROIs 1 and 2 (with final inhomogeneity of 32.7 Hz and 23.0 Hz, respectively). Nevertheless, residual inhomogeneity in ROIs 3 and 4 still remains. These are caused

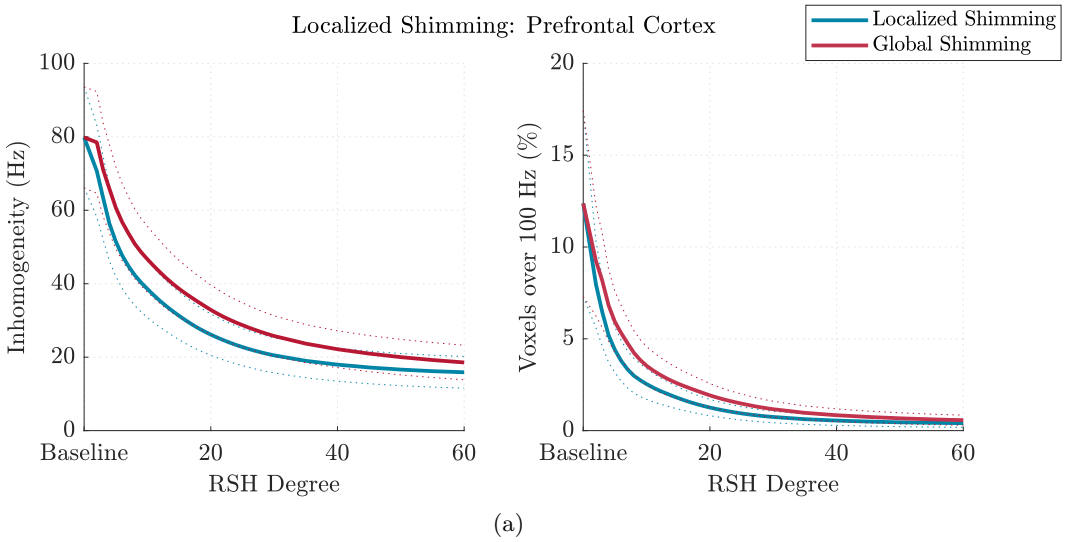

(a)

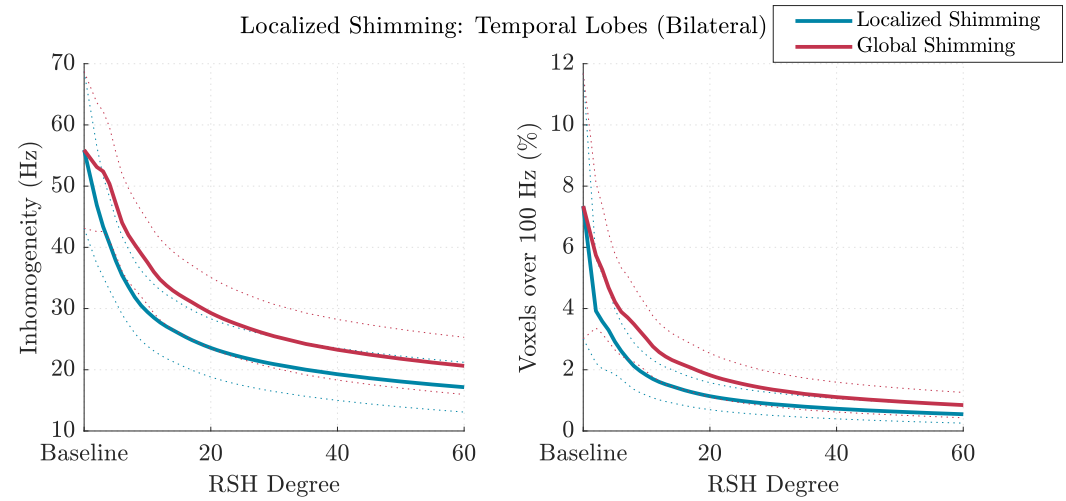

(b)

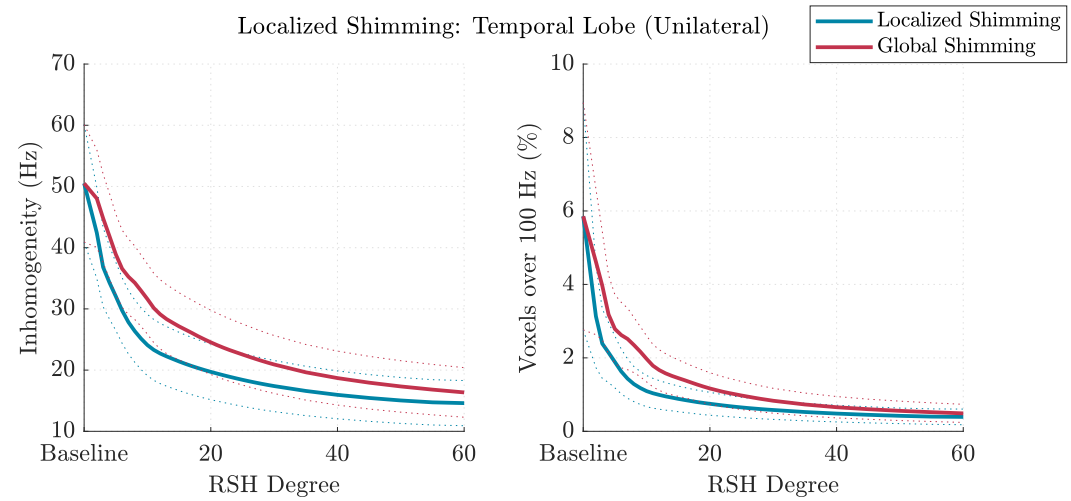

(c)

Figure 4.7 – Average inhomogeneity and proportion of voxels over 100 Hz across subjects in the database after global and localized RSH shimming of increasing degree. Metrics for each subject are computed considering the voxels inside target slabs enclosing the: (a) prefrontal cortex, (b) both temporal lobes and (c) a single temporal lobe. Dotted lines indicate standard deviation of the metric across subjects in the database.

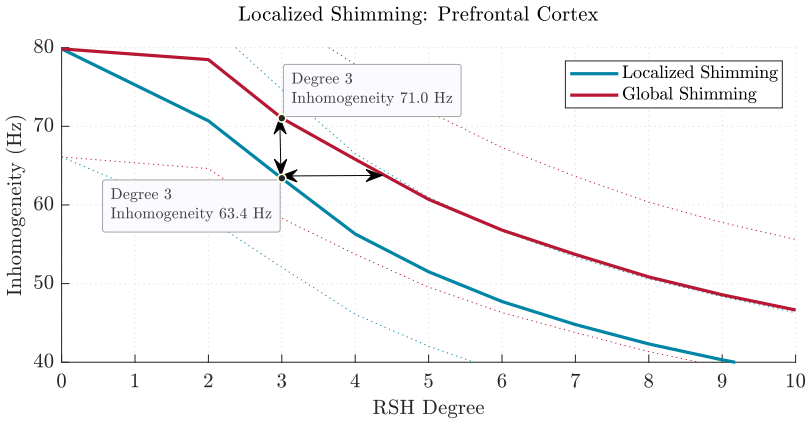

(a)

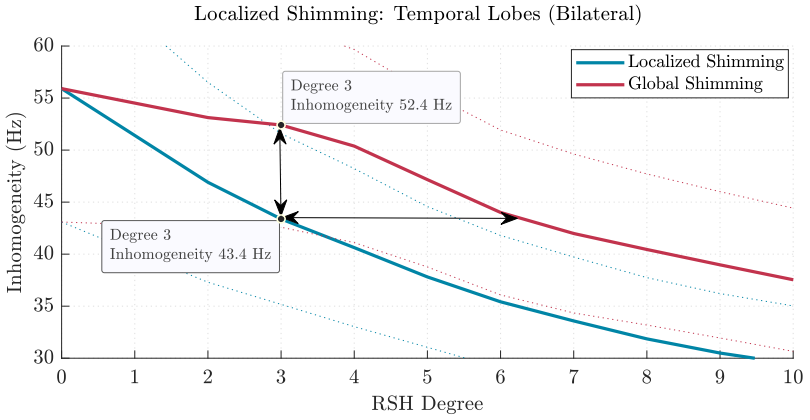

(b)

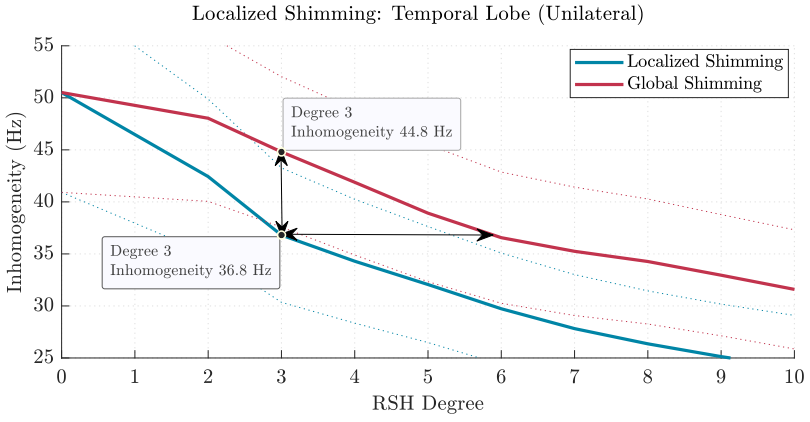

(c)

Figure 4.8 – Zoomed depiction of average inhomogeneity across the database in selected slabs for performance comparison between global and localized shimming techniques.

by susceptibility gradients between brain tissues and cannot be zeroed-out. We are also limited by numerical precision to compute infinitely higher-degree coefficients required to shim the excursion hotspots close to the sphere boundaries in ROIs 3 and 4. Moreover, contrarily to intuition, these results also show that fitting the same number of degrees of freedom to a smaller volume does not necessarily mean improved shimming, since despite being the smallest volume, ROI 1 is also the one presenting the largest field excursion in the depicted sagittal slices. Fig.4.9c compares the inhomogeneity inside ROI 4 when applying global vs focused shimming: convergence to very low inhomogeneity is seen at 10^{th} degree with localized shimming, versus 50^{th} degree with global shimming.

In terms of the required RSH degree for optimally shimming some region, presented results point to the need of fewer degrees of freedom when employing localized shimming, and these can be further reduced when the shimmed ROI can be positioned inside a sphere non enclosing sources of magnetic field.

4.4.5 Optimal Global and Localized Shimming with Power Constraints

The reduced number of degrees of freedom is a first practical aspect pointing to the advantage of localized shimming. Moreover, by analyzing the inhomogeneity reduction brought by optimal, power-constrained coil designs, the reduced need for RSH degrees in localized shimming translates into improved homogeneity in the target under fixed power dissipation, as observed in fig.4.10.

Inhomogeneity after global shimming with subject-optimal coils at the initial power constraint of 3 W is equivalent to 6^{th} degree RSH shimming. Improvement as power consumption is allowed to increase, however, is mild, reaching an equivalent of a 9^{th} degree RSH shim system at 100 W. As inhomogeneous field distribution becomes more and more localized after mitigation of slower spatially varying patterns, further improvement becomes harder. To address such localized patterns when performing global shimming, small loops with high electric current are needed, thus electric power drastically increases. Such behavior is in accordance with [Roméo 1984], who demonstrates that pure higher degree spherical harmonic patterns are generated by faster spatially varying, thus shorter, winding patterns, at the cost of requiring higher currents.

Subject-optimal coil design for localized shimming, however, shows that a significant 17 % drop in inhomogeneity can be achieved for the temporal lobes under the same power dissipation constraints with a dedicated system. From the results discussed so far, this is not surprising; for a fixed RSH degree, localized shimming improves the homogeneity in the target compared to global shimming; and since power dissipation is linked to RSH content, employing the same power dissipation in a localized target rather than in global shimming is the equivalent of employing the same amount of RSH degrees in localized versus global shimming. From these results, one could also expect high performance shimming in spherical ROIs satisfying the perfect shimming conditions to be achievable with low power consumption, as the RSH content required to achieve the lowest inhomogeneity in ROI 4, for instance, is of 10^{th} degree, with still very low inhomogeneity at the 6^{th}

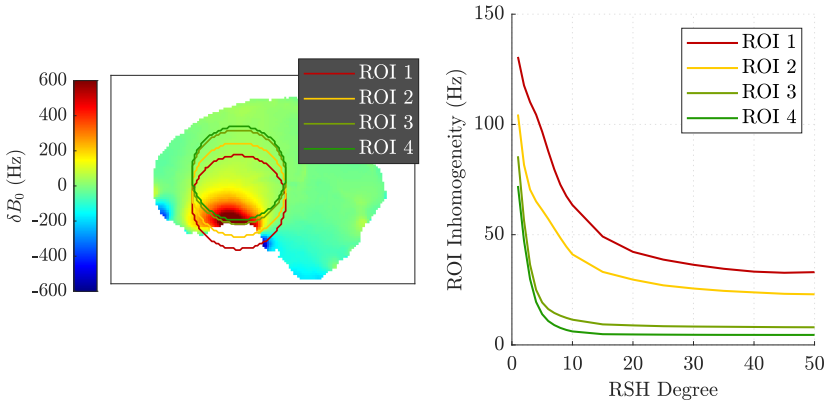

(a)

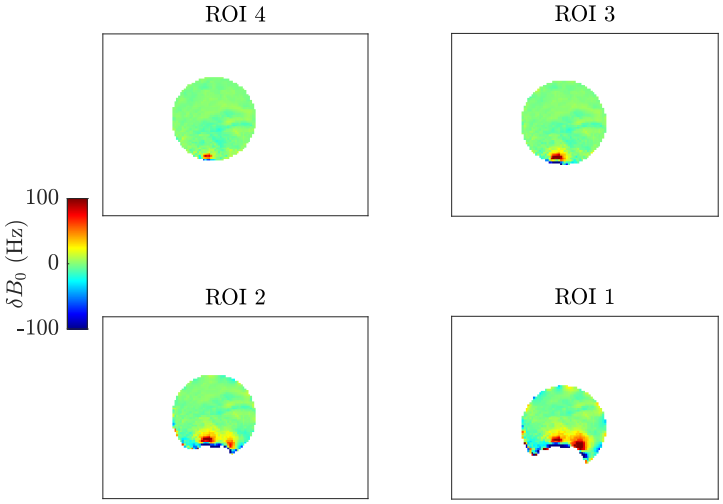

(b)

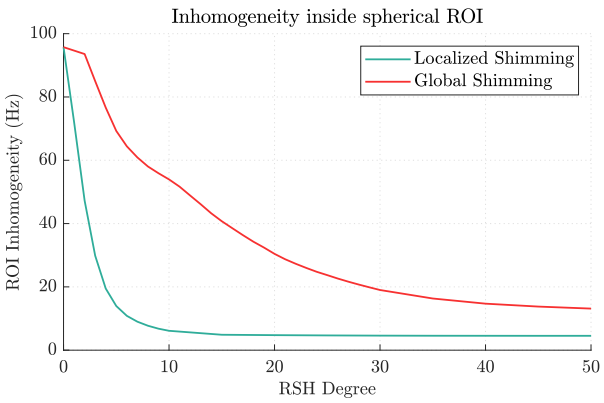

(c)

Figure 4.9 – Inhomogeneity assessment after shimming in four spherical ROIs, with ROIs 3 and 4 non-enclosing magnetic field sources, and ROIs 1 and 2 virtually enclosing such sources. Inhomogeneity as RSH degree increases (a) and fieldmap in a sagittal slice after 50^{th} degree shimming (b) are shown. Inhomogeneity evolution inside ROI 4 is also compared under localized and global shimming (c).

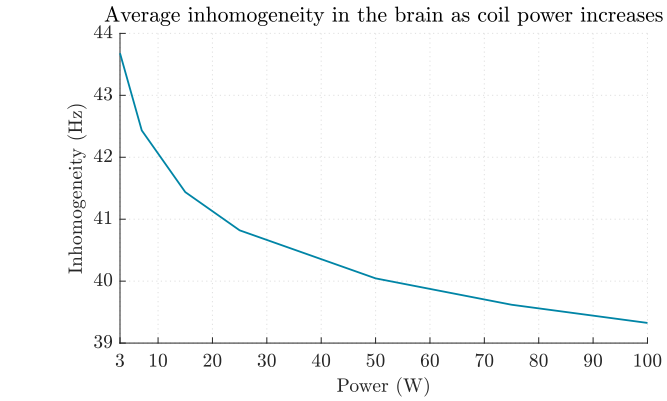

(a)

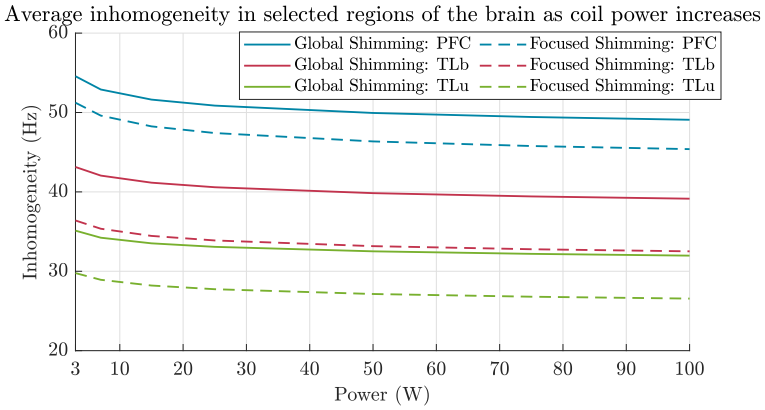

(b)

Figure 4.10 – Average inhomogeneity across fieldmaps after subject-optimal coil shimming when designed for (a) global shimming and (b) region-optimized shimming. In (b), dotted lines represent the inhomogeneity obtained with region-specific coils and the solid line represents the inhomogeneity within a specific region after whole-brain shimming optimized coils.

degree.

We emphasize that the coil design simulation and evaluation had the goal of illustrating how RSH degree content relates to power dissipation. The designed systems are not practical as they imply an optimal coil for each subject. When designing a shim system capable of addressing inter-subject variability, for a fixed power dissipation, performances tend to drop [Pinho Meneses 2020b]. Nevertheless, these simulations provided evaluation of how power capabilities can be better redirected to improve homogeneity of specific regions of interest.

We also note that, despite the low inhomogeneity theoretically achievable in global shimming, in practice such levels of inhomogeneity are probably not achievable since dedicated hardware might not be able to support current and power levels required to generate the correcting magnetic fields. At 100 W, average inhomogeneity of 39.3 Hz obtained under global shimming is only equivalent to what would be obtained with 9^{th} degree RSH shimming, thus still very far from the estimated lower bound of 12.3 Hz.

Finally, the shimming needs will mainly depend on the robustness of the acquisition

sequence to B_0 inhomogeneity. Acquisition schemes such as GRE, MP-RAGE, FSE provide high quality results at 7 T despite conditions that would be harsh for EPI; therefore for those sequences one would not need the best achievable inhomogeneity. For EPI, however, even at 90^{th} degree RSH shimming, leftover inhomogeneity hotspots would still translate into artifacts if no acceleration was used. Again for high-resolution and reduced FOV, localized shimming will facilitate greater shimming performance.

4.5 Conclusion

The mathematical fundamentals pointing to the impossibility of perfect shimming of the human brain were shown, and unconstrained RSH shimming simulations of very high degree were performed, showing reminiscent regions of high magnetic field excursion at 7 T even at the highest degree simulated, demonstrating the impossibility of perfect shimming of the human brain (12.3 Hz remaining inhomogeneity in average across a 100-subject database). Moreover, an optimized close-to-ideal cylindrical shim coil showed inhomogeneity only comparable to a 9^{th} degree RSH shim system, despite high power dissipation of 100 W. This result helps highlight the difficulty of obtaining high performance shim systems with low power consumption, and sheds light on why, despite efforts developed by many research teams, no system performing better than 6^{th} degree has been prototyped so far.

Localized shimming was shown to provide better homogeneity in a target region than global shimming for a fixed RSH degree. This property was reflected in greater performance of localized shimming under a fixed power dissipation condition.

By judiciously selecting a region to shim such that it satisfies the condition of being enclosed by a sphere not containing sources of magnetic field, very low inhomogeneity can be achieved within relatively low RSH degree, as we observed a faster convergence to the lowest achievable inhomogeneity; in this particular case, the latter is left with lower field excursion caused by less intense susceptibility gradients between tissues composing the brain. We would therefore expect rather low power requirements for shimming systems to achieve almost optimal inhomogeneity in such targets.

* * *
* *
*

Chapter 5

SCOTCH: Stream-Function SVD-Based Multi-Coil-Array Design

Chapter Outline

The methods presented in this chapter were object of the following patent:

B. Pinho Meneses and A. Amadon. *Static-magnetic-field shimming coil system for magnetic resonance imaging*, no. WO2020212463A1, October 2020.

The methods presented in this chapter were initially presented at the International Society for Magnetic Resonance in Medicine conference in 2019, 2020 and some parts of it will be presented in 2021:

B. P. Meneses, M. Luong and A. Amadon. *Optimized multi-coil array design for human brain shimming at Ultra-High Field.* In Proceedings of the 27th Annual Meeting of ISMRM, page 1477, Montreal, Canada, May 2019.

B. Pinho Meneses, J. Stockmann and A. Amadon. *First prototype of a Stream-Function-based Multi-Coil Array dedicated to human brain shimming at Ultra-High-Field.* In Proceedings of the 28th Annual Meeting of ISMRM, volume 28, page 0766, Virtual, 2020.(Awarded *Magna cum Laude*)

B. Pinho Meneses, J. Stockmann, E. Chazel, E. Giacomini, P.-F. Gapais, F. Mauconduit, M. Luong, A. Vignaud and A. Amadon. *Shim Coils Tailored for Correction of Bo Inhomogeneity in the Human Brain (SCOTCH) at Ultra High Field.* In Proceedings of the 29th Annual Meeting of the International Society for Magnetic Resonance in Medicine, Virtual Conference, 2021.

B. Pinho Meneses and A. Amadon. *The Spherical Harmonic Rating: A Metric for Bo Shim System Performance Assessment.* In Proceedings of the 29th Annual Meeting of the International Society for Magnetic Resonance in Medicine, Virtual, 2021. ISMRM.

Moving back to shimming hardware design, in this chapter we will present the Stream-Function SVD-Based Multi-Coil Array, where the winding patterns obtained from principal SF-SVD modes are decoupled into independent channels to provide greater flexibility for addressing inter-subject variability in the human brain inhomogeneity, while being positioned at strategic locations as indicated from the SF-SVD coils' wirepaths.

5.1 Methods

To design an MCA adapted to the inhomogeneous field patterns encountered in the human brain, a semi-heuristic approach for optimization of channels' geometry and position was employed. It is based on the SVD modes of a large database of SO-SFs, which provide indications of where electric current is most demanded for B_0 shimming of the human brain.

The following steps were performed for design and validation of the optimized MCA: (1) a large database of δB_0 brain fieldmaps was acquired, covering all kinds of human head morphometries; (2) SO-SFs were computed for each subject in the database and SVD was performed on the SO-SF set; (3) from the first SF-SVD modes, indication of where electric current is most demanded for human brain shimming was obtained; then an MCA is designed based on this indication; (4) shimming simulations with the obtained design are performed on an in-house database and on an open-access database for performance assessment and cross-validation; (5) a prototype was built, characterized and tested *in-vivo* in a preliminary setup.

5.1.1 Computation of Subject-Optimal Stream Function and Stream Function SVD Modes on a Coil Former

Given S subjects, $\boldsymbol{b_s} = \begin{bmatrix} \delta B_0^s(\boldsymbol{x}_1) & \delta B_0^s(\boldsymbol{x}_2) & \dots & \delta B_0^s(\boldsymbol{x}_{K_s}) \end{bmatrix}^T \in \mathbb{R}^{K_s}$, for $s = 1, \dots, S$, is a target fieldmap in the human brain for a subject s containing K_s voxels located at coordinates $\boldsymbol{x}_k \in \mathbb{R}^3$, with $k = 1, \dots, K_s$. For designing a shim coil, a cylindrical surface $\mathcal{S} \in \mathbb{R}^3$, of radius a and length L, used as coil former, exterior to the target region, is also defined. Employing the Dipole Boundary Method (DBM) [Pinho Meneses 2020b], $\mathcal{S}$ is discretized into N square elements upon which an optimal stream function $\boldsymbol{\psi_s} \in \mathbb{R}^N$ can be computed, associated to the current flow required to mitigate inhomogeneity under power constraints. While we limit ourselves to a simple cylindrical geometry, well suited for DBM square elements, other coil former geometries can be envisioned, in which case it may be necessary to use other stream function calculation methods [Pissanetzky 1992, Poole 2007b, Bringout 2015].

The SO-SFs are then assembled in a matrix $\boldsymbol{\Psi}_{\mathrm{DB}} = \begin{bmatrix} \boldsymbol{\psi}_1 & \boldsymbol{\psi}_2 & \dots & \boldsymbol{\psi}_S \end{bmatrix} \in \mathbb{R}^{N \times S}$ upon which an SVD can be applied to obtain a new matrix $\boldsymbol{\Psi}_{\mathrm{SVD}} = \begin{bmatrix} \boldsymbol{\psi}_1^{\mathrm{SVD}} & \boldsymbol{\psi}_2^{\mathrm{SVD}} & \dots & \boldsymbol{\psi}_S^{\mathrm{SVD}} \end{bmatrix} \in \mathbb{R}^{N \times S}$ whose columns are principal orthogonal modes that can be linearly combined to reconstruct each of the SO-SFs. A detailed explanation of the steps presented so far is available in [Jia 2020, Pinho Meneses 2020b], but the design is nevertheless complex and non-trivial to be translated into an actual coil, as all iso-current lines (example in fig. 5.1a) need to be carefully connected in series.

5.1.2 Selection of MCA Channels

The SF-SVD coils computed in the previous step then serve to define the position and shape of independent windings to be used in a brain-optimized Multi-Coil Array. Since

the SF-SVD modes in $\mathbf{\Psi}_{\mathrm{SVD}}$ are ordered by degree of correlation with the stream functions in $\mathbf{\Psi}_{\mathrm{DB}}$, with the first mode (first column) being the most correlated and the last mode (last column) the least correlated, we expect that the decomposition of the first few modes into MCAs will provide the most important components for human brain shimming.

Assuming the M first SF-SVD modes are selected, each SF-SVD mode is discretized into windings based on a minimum inter-wire spacing δ_w, and a family $\mathcal{C}^m_{\mathrm{SVD}}$ of closed curves describing the wirepaths obtained from the discretization is obtained for each mode m.

From the wirepath configuration of the SF-SVD mode in fig.5.1a, the presence of clusters of current is distinct. They mark where electric current is most demanded for inhomogeneity mitigation. Aware of the current requirements around the cylindrical surface, independently driven loops of analogous shapes to the clusters can be positioned on the surface to form an MCA.

Our task now is to select, for each mode, the most suitable loops to generate the MCA. From fig. 5.1b, the clusters of wirepath (or current) are associated with the extrema of the stream function, with current revolving around them: indeed the current density computed from a stream function is $\boldsymbol{j}(\boldsymbol{x}) = \boldsymbol{\nabla}\psi(\boldsymbol{x}) \times \hat{\boldsymbol{n}}(\boldsymbol{x})$, therefore, the more intense the local extremum, the greater the electric current density will flow around it. Based on this principle, a channel selection criteria was devised.

Physically, channels selected from each mode will be placed on different cylindrical layers of increasing radii.

If when selecting a mode m for discretization we observe some degree of symmetry, which can arise naturally given that these stream functions target the human brain, we effectively force symmetry on the SF by making

$$\psi^{\mathrm{sym}}_m = \frac{\psi_m(-\varphi, z) + \psi_m(\varphi, z)}{2}. \tag{5.1}$$

Let $\boldsymbol{x}^m_e \in \mathcal{S}$ be the coordinates of the extrema of $\psi_m(\boldsymbol{x})$, with $e = 1, \ldots, E_m$ and E_m the total number of extrema of ψ_m. For each extremum, a subset of wirepaths $\mathcal{C}(\boldsymbol{x}^m_e) \subset \mathcal{C}^m_{\mathrm{SVD}}$ that enclose only $\boldsymbol{x}^m_e$ among the extrema coordinates can be constructed. Furthermore, a length

$$l(c) = \oint_c |d\boldsymbol{x}| \tag{5.2}$$

can be associated to any wirepath $c \in \mathcal{C}^m_{\mathrm{SVD}}$. For each subset $\mathcal{C}(\boldsymbol{x}^m_e)$, the cardinality $\#\mathcal{C}(\boldsymbol{x}^m_e)$ indicates its level of significance for shimming, as it is directly related to the amount of current flowing around the extremum. Finally, for those subsets with higher cardinality, we choose the largest loop $c \in \mathcal{C}(\boldsymbol{x}^m_e)$ to become an independent channel approximating the current requirement around that extremum. The particular choice of the largest loop is helpful to reduce electric current demand for generating some peak magnetic field strength in a region of interest.

Having laid-out the required entities for channel definition, a number of desired channels N_{ch} for the MCA is chosen. Limitations of the driving electronics related to the maximum number of channels supported must be taken into account. Therefore, selecting channels with low influence on the overall magnetic field should be avoided; this is why a

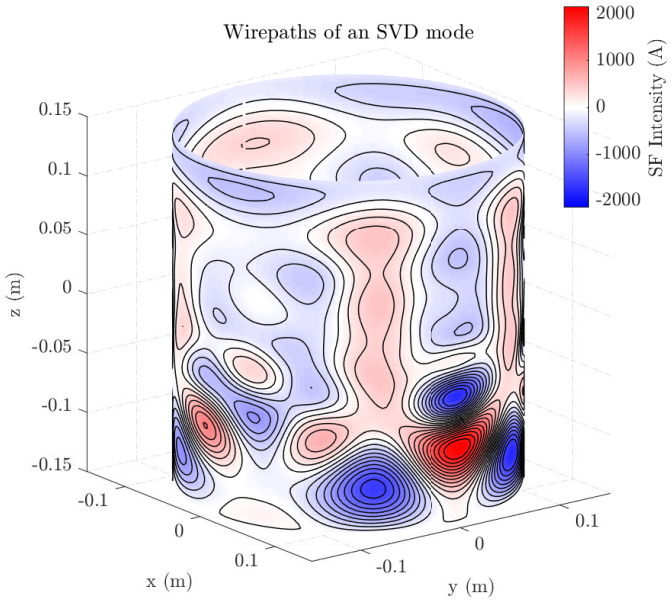

(a)

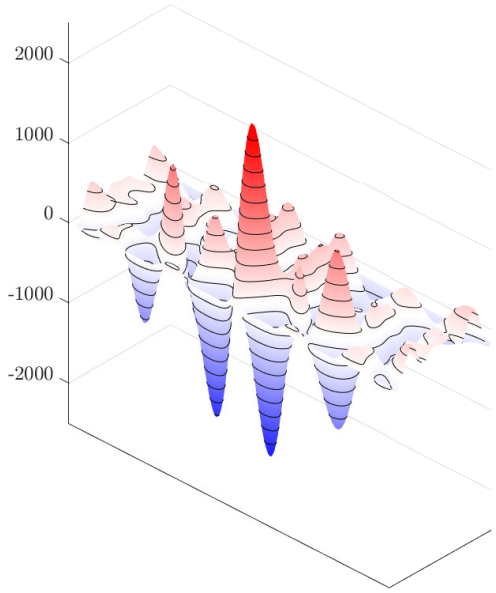

(b)

Figure 5.1 – Stream function on (a) a cylindrical surface used as coil former with current paths overlaid and (b) laid-out on a plane for easier visualization of the stream function's extrema and wire paths cluster formation around them.

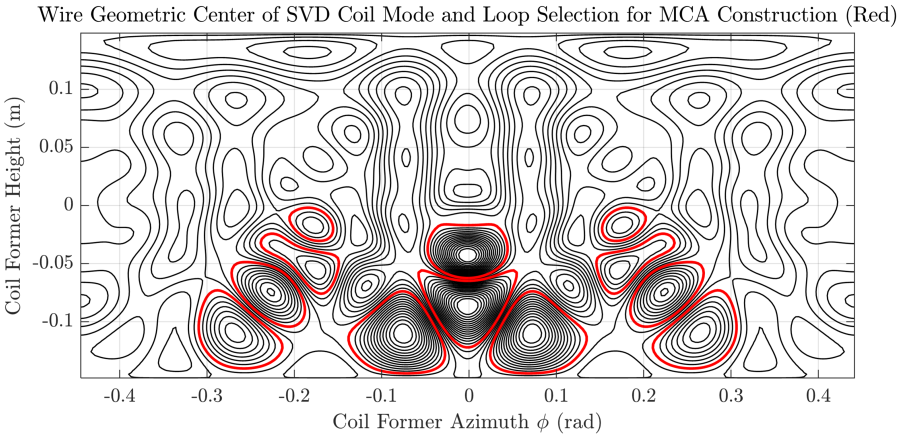

(a)

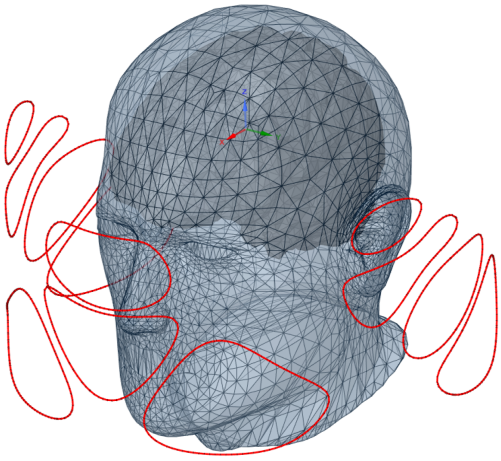

(b)

Figure 5.2 – Depiction of (a) the selection of 12 loops from a symmetrized SF-SVD mode according to the proposed criteria and (b) channels geometry and position around the human head, where an accumulation of channels is observed close to the frontal and temporal lobes.

minimum cardinality threshold τ_{card} and/or a maximum number of channels per SF-SVD mode N_m are advisable, allowing the channel selection to move to more relevant channel geometries in the subsequent SF-SVD modes without having to select all potential but eventually less performing channels from each mode.

For mode m, the first channel obtained is the largest loop from the subset of greatest cardinality among all subsets $\mathcal{C}(\boldsymbol{x}_e^m)$ associated to the mode. This subset is then discarded, and the next channel is defined as the largest loop extracted from the subset of greatest cardinality among the remaining subsets. This process is repeated until the cardinality threshold τ_{card}, or the max number of channels per mode N_m, or the total number of channels N_{ch} is reached. Once all channels within the established criteria are obtained from mode m, we move to the next mode, $m+1$, and the selection procedure is repeated.

The channel definition process must start at $m = 1$. Due to space limitations, a maximum number of modes M is also imposed to limit the number of layers and the overall thickness of the shim system. At the end of this process, the channels of the MCA are described by the set of closed loops $\mathcal{W} = \{w_1, w_2, \ldots, w_{N_{\text{ch}}}\}$.

An illustration of a few loops selected with $\tau_{\text{card}} = 3$ from a symmetrized SF-SVD mode is shown in fig. 5.2.

This "decomposition" process of SF-SVD coils into multiple independent channels is advantageous due to the multi-channel capacity of better addressing asymmetries in field distribution inside the brain. When an SF-SVD coil, driven by a single current through all the wirings, is transformed into an MCA, the degrees of freedom of the system increase, providing better adaptation to anatomy variations. Construction of the system is also simpler than having a single input current through all wires. Some complex wiring patterns present in the SF-SVD can be discarded with practically no loss of performance.

Notice that the windings defined so far were all considered to be over the same cylindrical surface. Although channel-loops from a same mode do not overlap, this is not guaranteed among distinct modes, which could make the system as defined so far impractical. The second, third and further modes must be projected onto cylindrical surfaces of higher radii, but the definition of these radii will depend on constructive aspects. Each channel is described so far by a single loop, but the real system will consist of multiple turns for each channel-winding to allow the generation of higher fields with relatively low currents. This will imply a radial wire bundle thickness, which will impose the radii of the subsequent layers of channels. The wire bundle thickness depends on the number of turns per channel and on the diameter of the wire employed.

To start defining constructive aspects of the system, an initial Single Loop Model (SLM) must be simulated.

5.1.3 Ideal System Characteristics and Simulation

To characterize and simulate the shimming performance of an optimized MCA composed of channels defined by $\mathcal{W}$, magnetic field, resistance and inductance should be estimated for each channel.

In the SLM, for field assessment, it will be considered that each channel is composed of N turns of wire of infinitesimal thickness.

From the Biot-Savart law, the magnetic field along z per unit current for the j-th channel in $\mathcal{W}$ can be computed as

$$\mathcal{B}_z^j(\boldsymbol{x}) = N\hat{\boldsymbol{z}} \cdot \frac{\mu_0}{4\pi} \oint_{w_j} d\boldsymbol{x}' \times \frac{\boldsymbol{x} - \boldsymbol{x}'}{|\boldsymbol{x} - \boldsymbol{x}'|^3}. \tag{5.3}$$

Given the wire section A_w and material conductivity κ, the resistance is

$$r_j = N\frac{l(w_j)}{\kappa A_w}. \tag{5.4}$$

And the inductance can be calculated with the Neumann-like formula [Dengler 2016]

$$L_j = N^2 \frac{\mu_0}{4\pi} \left[\left(\oiint_{w_j} \frac{d\boldsymbol{x} \cdot d\boldsymbol{x}'}{|\boldsymbol{x} - \boldsymbol{x}'|} \right)_{|s(\boldsymbol{x}) - s(\boldsymbol{x}')| > A_w/2} + \frac{l(w_j)}{2} \right], \tag{5.5}$$

with $s(\boldsymbol{x})$ being the curvilinear coordinate along the wire axis.

The optimized MCA shimming performance can then be simulated on the fieldmap database. For a fieldmap $\boldsymbol{b}_s$ to be shimmed, the contribution per unit current of each channel on the magnetic field can be calculated from 5.3 and the inverse problem of obtaining optimal currents to minimize the inhomogeneity in the brain is posed as:

$$\begin{aligned} \boldsymbol{i} &= \underset{\boldsymbol{i} \in \mathbb{R}^{N_{\text{ch}}}}{\operatorname{argmin}} \, \sigma \left(\boldsymbol{b}_s + \mathbf{B}_s \boldsymbol{i} \right), \\ &\text{s.t. } |i_j| \leq I_{\max}, \quad 1 \leq j \leq N_{\text{ch}}, \end{aligned} \tag{5.6}$$

with σ the standard deviation, $\mathbf{B}_s \in \mathbb{R}^{K_s \times N_{\text{ch}}}$ the magnetic-field matrix of elements $b_s^{k,j} = B_z^j(\boldsymbol{x}_k)$ and $I_{\max}$ a maximum current constraint. This problem was solved with MATLAB's *fmincon* function. Power dissipation resulting from the optimal currents is

$$\mathcal{P}_s = \sum_{j=1}^{N_{ch}} r_j i_j^2. \tag{5.7}$$

From these expressions, the final inhomogeneity achieved by the shim system under particular constraints can be obtained and compared, for instance, with SH-based systems for benchmark.

To find an adequate number of turns, we first set $N = 1$, simulate system performance and power dissipation for different values of $I_{\max}$. Then, assuming a non-zero number of turns N for the channels, the new current constraint for performance to be kept the same would be $I_{\max}/N$ and the power dissipation would drop to $\mathcal{P}_s/N$. On the other hand, inductance increases, as well as mutual inductance with gradient coils, which would make the shim channels more sensitive to gradient-induced eddy currents. In addition, now assuming a fill factor f for the actual winding, the cross-section occupied by the wire bundle becomes $NA_w f^{-1}$. The width and thickness of the bundle can be adjusted according to space limitations, noticing that the greater the bundle section, the more it will deviate from ideal single loop simulations, implying loss of performance of the shim array.

5.1.4 Shim Coils Tailored for Correcting B0 Inhomogeneity in the Human Brain (SCOTCH): Shim System Design and Prototype [3]

The system has been denominated SCOTCH for **S**him **Co**ils **T**ailored for **C**orrecting B_0 Inhomogeneity in the **H**uman Brain, and will be referred as such from now on.

[3] The author wishes to highlight that a considerable amount of his time was devoted to the entirely manual process of winding coils, resin coating the coils, assembling electronics and mechanical parts. He also wishes to thank other people that contributed to the assembly of this shim system: notably Jason Stockmann (from the Massachusetts General Hospital) for providing us with most of the electronics, and Edouard Chazel (from NeuroSpin) for his tremendous work in assembling the AVANTI2 RF Coil.

Human Brain Bo-map Collection

To design an SF-SVD-based MCA, an in-house database of 3D δB_0 fieldmaps composed of 100 subjects was assembled.

Fieldmaps were acquired on a MAGNETOM Prisma 3 T imager (Siemens Healthcare GmbH, Erlangen, Germany) with 1.7 mm isotropic resolution, after 2nd degree SH shimming. FSL's brain extraction tool [Smith 2002] was used for masking and restricting our analysis to the human brain. Fieldmap acquisitions were performed with two consecutive 3D gradient echo sequences, one with 2 distant echoes $TE_1 = 1.88$ ms and $TE_3 = 4.9$ ms, and one with a single echo at $TE_2 = TE_1 + 0.7$ ms. We assume TE_1 and TE_2 are close enough so that no phase excursion occurs in the brain beyond $\pm\pi$ during that 0.7 ms interval (underlying assumption: δB_0 does not exceed ± 714 Hz in the brain at 3 T). Then for each voxel, a double-point linear fit of the phase evolution between TE_1 and TE_2 is first performed to potentially incur temporal phase unwrapping of the TE_3 echo; then a triple-point linear fit of the phase evolution is performed for δB_0 estimation. The resulting δB_0 maps were cleaned with an outlier filter to avoid singularities, especially at the edge of the brain. It was then scaled up by 7/3 for investigation at 7 T. Baseline inhomogeneity of the 2nd degree SH shimmed database at 7 T is 65.7 Hz (SD: 11.4 Hz).

Dimensions of the Prototype and its Parts

Choice of geometrical parameters will vary and mainly depend on the RF coil dimensions. As a rule of thumb, the radius of the coil former should be as low as possible to produce higher intensity fields in the region of interest with lower currents. In addition, placement of the shim system outside our shielded RF coil allows decoupling between the shim and RF arrays due to the built-in RF shielding. On the other hand, if the RF coil radius is too large, it could be envisioned that the shim system is placed on the inside of the RF array, provided enough space is available, but at this point care must be taken to minimize RF-MCA interactions, which could be done with the use of RF-chokes [Stockmann 2013]. Finally, if the MCA has to be placed outside a large diameter RF array, power dissipation will most likely increase in order for performances to be maintained, but this effect has not been studied in this work.

The shim system needs to be positioned outside our in-house 8Tx/32Rx channel RF coil, named AVANTI2, of 270 mm external diameter.

For the combined system to be centered at the scanner's isocenter, the 21 mm space available between AVANTI2's external diameter and table top should be respected.

To benefit from several SF-SVD modes' characteristics and greater degrees of freedom, a three-layer system was designed. From previous experience and simulations [Pinho Meneses 2020d], 20 turns per channel was considered a good compromise to provide high performance with relatively low electric currents; further discussion on this aspect will be provided in section 5.3. Copper wire of 1 mm diameter was chosen for the design providing a good compromise between rigidity and malleability for winding the coils while also having a section large enough to keep power dissipation down. Considering the number of

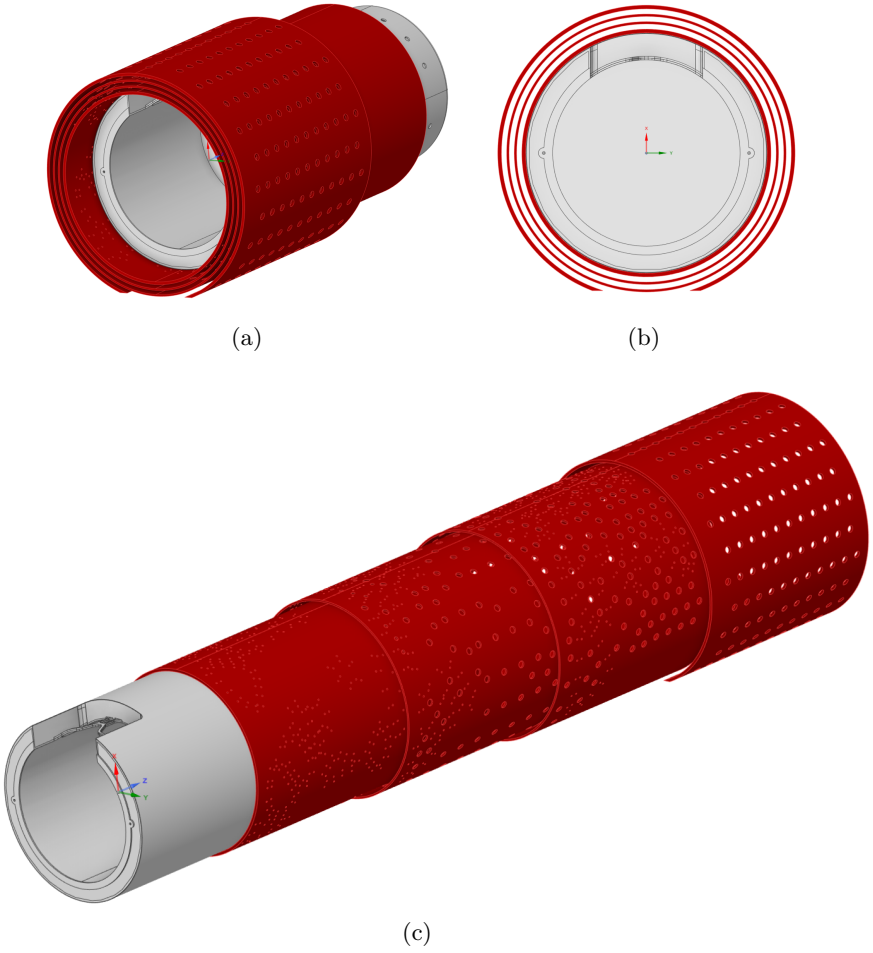

(a) (b)

(c)

Figure 5.3 – 3D model depicting the expected configuration of the optimized MCA. Three different viewing angles are shown in (a), (b) and (c), which shows and exploded view.

turns, wire section and fill factor of 0.45 for manual winding (estimated from preliminary prototypes), one wire bundle is expected to occupy approximately 36 mm^2. Once mounted and held on top of the cylindrical surface, the bundle section shape can be approximated by that of a half-ellipse. The bundle fixation structure was defined such that axial spread of the bundle would be around 9 mm and thickness normal to the coil former surface would be approximately 5 mm. The desired distance between the external diameter of a layer and the internal diameter of the next layer was then set to 6 mm.

Thickness of the supporting hollow cylinders were chosen to be 4 mm for the most interior cylinder holding the channels of the first layer and for the most external cylinder, acting only as cover for the shim system. Intermediate cylinders' thickness was set at 2.5 mm. The internal radius of the first layer was set to 271 mm to be able to slide over the AVANTI2 coil. A 3D model of the shim system layers on top of the AVANTI2 is shown in fig. 5.3.

Under the described configuration, SF-SVD modes calculation was performed using as baseline 2^{nd}-degree-shimmed database. The first three SF-SVD modes were retained and

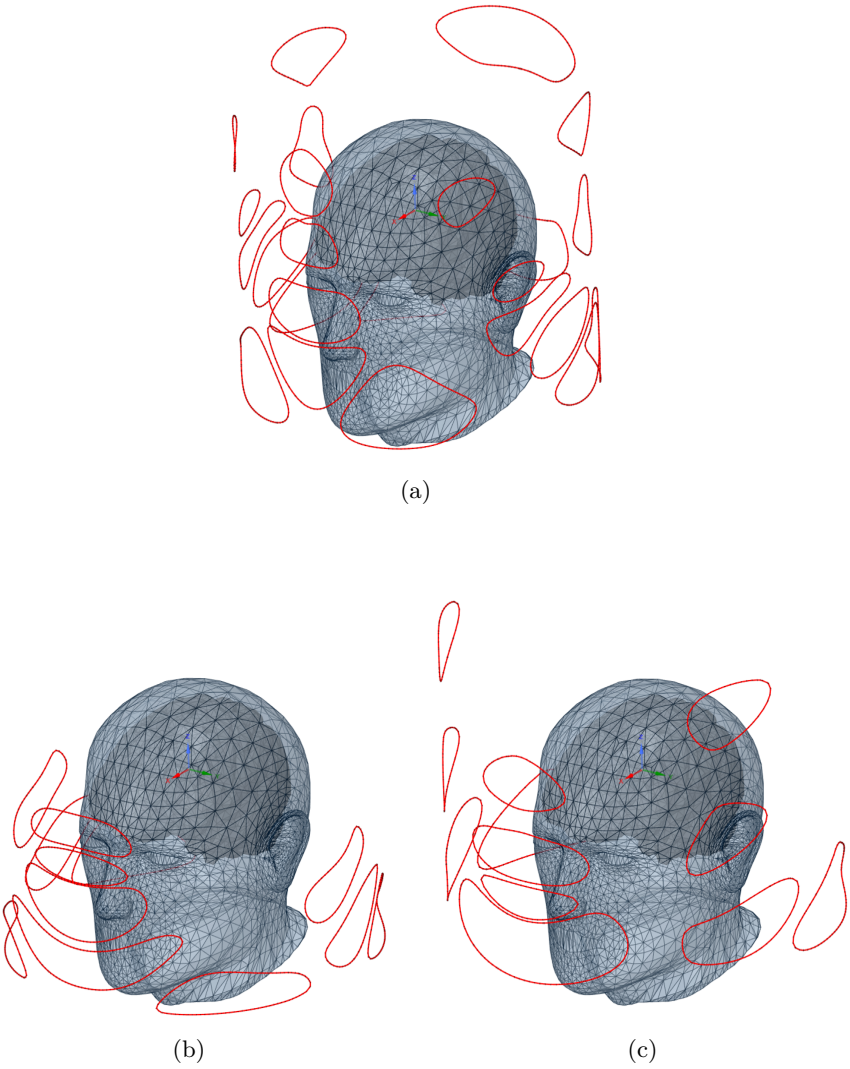

(a)

(b) (c)

Figure 5.4 – Ideal loop geometries selected for constituting the optimized MCA. The first (a), second (b) and third (c) layers of 24, 12 and 12 channels, respectively, are depicted.

calculated on coil formers of radii $a_1 = 141\,\text{mm}$, $a_2 = 149.5\,\text{mm}$ and $a_3 = 158\,\text{mm}$. Length of the cylindrical surfaces for SF calculation was $L = 300\,\text{mm}$. Cylinders were assumed to be centered at the MRI isocenter. Noticing a tendency for SF symmetry with respect to the central sagittal plane on the first three SVD-modes, they were forced to symmetry before channel extraction, by taking the average of the SF found on either side. A total of 48 channels were defined from the symmetrized modes, with 24 channels obtained from the first SF-SVD mode, placed on the first layer of radius a_1; 12 channels from the second SF-SVD mode, placed on the second layer of radius a_2; and 12 channels from the third SF-SVD mode, placed on the thrid layer of radius a_3. Channels disposition for each layer are shown in fig. 5.4.

Computational Design Method

Magnetic field, resistance and inductance of the SLM of the optimized MCA were obtained from simulations in Ansys® Electronics Desktop. Shimming simulations on the 2nd degree shimmed database are performed for different electric current constraints: 1 A, 3 A, 5 A, 10 A and unconstrained. Final inhomogeneity in the database after shimming with the ideal model is compared to unconstrained SH shimming systems of increasing degree. A balance between performance and power dissipation is studied to define the ideal operation point of the optimized MCA.

Building Process

For construction of a prototype, cylinders with the previously defined dimensions were fabricated using grade 5 Flame Retardant (FR-5) Fiberglass Epoxy. Circular holes of 2 mm diameter were punched through for cable-ties passage for holding the wire bundles of each channel; 10 mm diameter circular holes were punched throughout the surface to facilitate convection, avoiding overheating of the shim system. Winding molds for each channel were modeled in Ansys® and 3D printed with a Formlabs Form 2 printer. They were wound to 20 turns, attached to the cylindrical supports via cable-ties and finally coated with a high temperature epoxy resin (Duralco 4461) for rigidity (cf. fig 5.5).

The two first layers of the proposed design were built and the third layer is under construction. The shim system as assembled so far is depicted in fig. 5.6.

Current-Driving Source and System Calibration

Once the partial prototype assembled, the shim system is driven using an open-source multi-channel feedback-controlled current driver [Arango 2016] theoretically capable of delivering up to 8 A per channel. For fieldmap estimation per 1-A unit current in each channel, a triple-echo GRE acquisition with TR = 10 ms, TE_1 = 1.6 ms, TE_2 = 4.3 ms and TE_3 = 7 ms, 2 mm isotropic resolution and pixel bandwidth of 1860 Hz in a 180 mm diameter spherical oil phantom was performed on a MAGNETOM 7 T (Siemens Healthcare GmbH, Erlangen, Germany). For each channel, three acquisitions were performed: at −1 A, 0 A and 1 A. The acquired phase images are then unwrapped using SEGUE [Karsa 2019] and a triple point linear fit of the phase evolution in each voxel is performed to estimate the fieldmap in the characterization volume. The threes fieldmaps for each channel are finally used in a least-squares fit to obtain the field per unit current produced by the channel.

An important step in the calibration phase was to precisely record the position of the shim insert to ensure it will always be identically positioned when performing in-vivo measurements. To do so, once aligned with the MRI scanner laser used for patient positioning, reference points along SCOTCH surface coinciding with the laser were marked with a permanent marker pen.

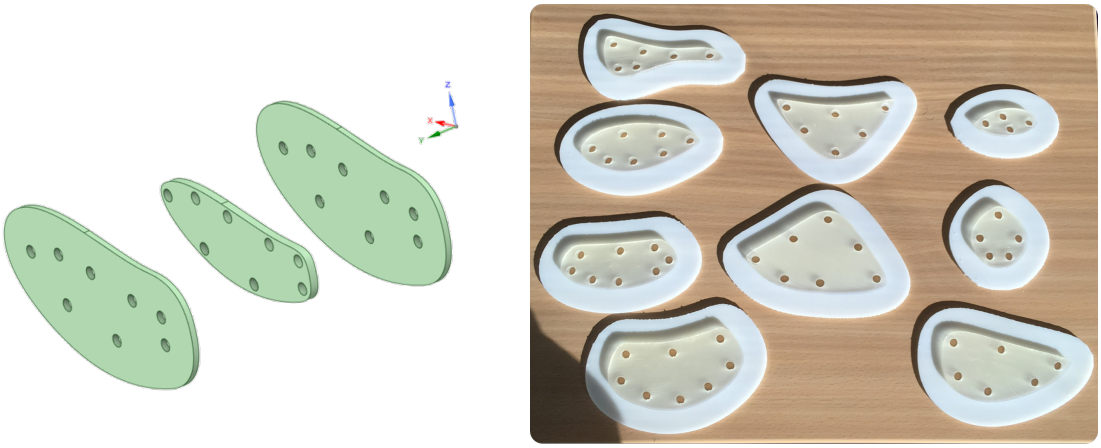

(a) (b)

(c)

Figure 5.5 – CAD model of a particular winding mold (a), 3D printed winding molds (b) and the resulting windings (c) after epoxy coating.

After characterization, shimming performance was assessed on the 2nd degree shimmed database by inputting the measured fields per unit current as shimming basis for the inverse problem in eq. 5.6. It is then compared to expected performance obtained from SLM simulations.

Safety Checking

Temperature rise measurements were performed with all channels driven by maximum current of 3 A at the same time to verify that heating was within safe levels.

5.1.5 Cross-Validation with Open-Access Fieldmap Database

Hold-out cross-validation of this method has been presented in a preliminary study [Meneses 2019c]. So in the current work, it was decided to employ the entire database of 100 subjects for SCOTCH design. Nonetheless, an open-access (OA) database composed of 126 brain fieldmaps [Elshatlawy 2019] at 7 T with 4 mm isotropic resolution has been recently

(a) (b)

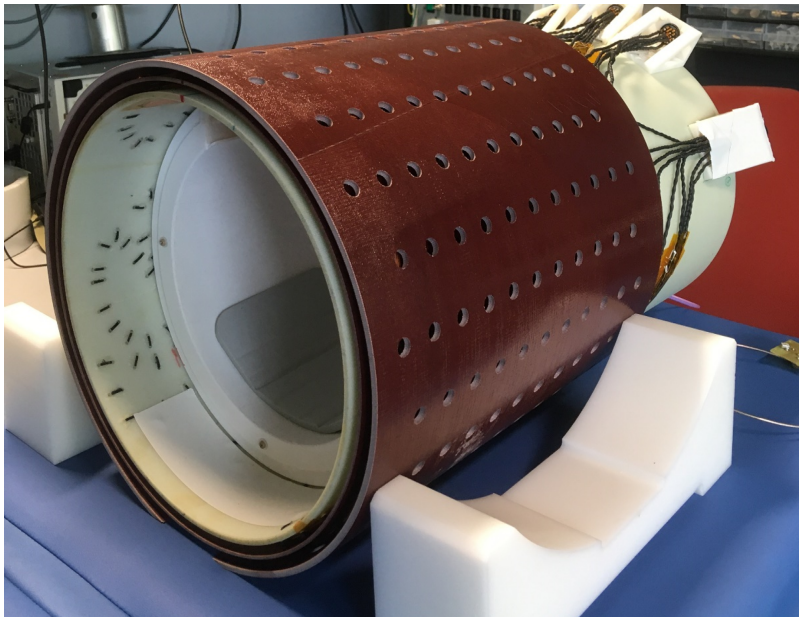

(c)

Figure 5.6 – 2-Layer 36-Channel SCOTCH prototype. First and second layers are shown in (a) and (b), and the complete setup combined with the AVANTI2 RF coil is shown in (c).

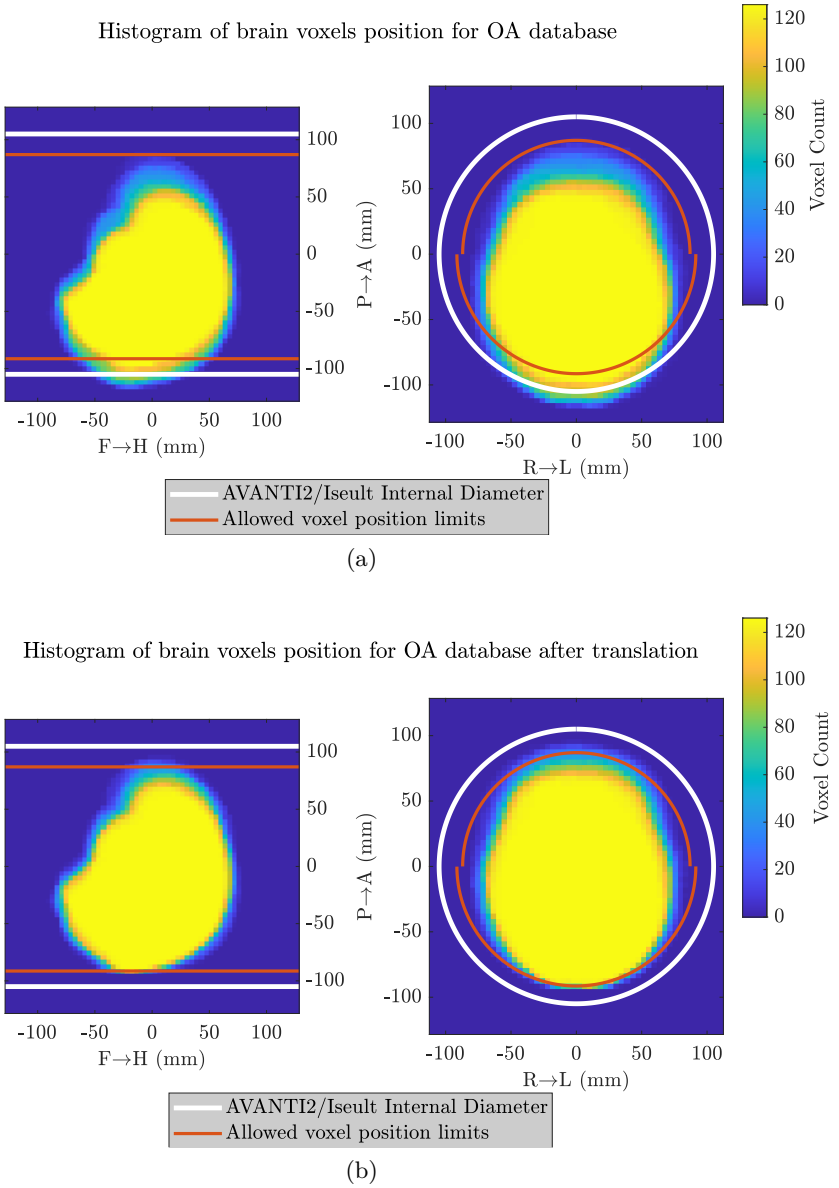

Figure 5.7 – Histogram of brain voxels position for the OA database relatively to the AVANTI2 RF coil (a) before and (b) after adjustment.

made available, and the possibility of cross-validation employing a database acquired at a different research site would increase confidence in the proposed design.

No information concerning the coordinates of the FOV center for each map was made available in the OA database. Therefore, a preliminary verification is performed to determine if the fieldmaps in the OA database would fit our RF coil of 210 mm internal diameter.

In order for the brains to fit inside the RF setup, each one must lie within a range defined by the RF coil radius and the distances between front of the brain to front of the head and back of the brain to back of the head – this accounts for thickness of bone, fat and skin surrounding the brain – resulting in the interval $[-a_{\mathrm{RF}} + d_{\mathrm{back}}, a_{\mathrm{RF}} - d_{\mathrm{front}}]$. While brain dimensions from each volunteer are readily available in the OA database, the distances between brain extremities and head extremities in the posterior-anterior (PA) direction are not. An average for those distances was then estimated by measurements performed on 10 subjects in the in-house database (where DICOM images are available). Average thicknesses are $d_{\mathrm{back}} = 13.6\,\mathrm{mm}$ and $d_{\mathrm{front}} = 18.0\,\mathrm{mm}$.

It is initially assumed that the center of the 3D matrices containing the fieldmaps data is coincident with the MRI isocenter. Under this assumption, the spread of voxels in space is shown in Figure 5.7a, with RF coil limits and allowed brain voxel limits displayed for reference.

We observe that fieldmaps in the OA database need to be translated in the PA direction in order to fit within our AVANTI2/SCOTCH setup and respect the estimated allowed region for the brain. This translation is performed on the entire database such that the back of each brain is located at the lower limit, providing a voxel position distribution as depicted in 5.7b.

The adjusted OA database will be the one employed in all further simulations and analysis.

As it will be observed in the results and subsequently discussed, despite baseline inhomogeneity of the OA database being very close to that of the in-house database, shimming simulations on the OA database will lead to much superior relative inhomogeneity improvement than what is achieved by the shim systems on the in-house database. Therefore, direct assessment of shimming system performance through inhomogeneity or relative improvement values could lead to an incorrect evaluation.

The Spherical Harmonic Rating

A new metric, the Spherical Harmonic Rating (SHR), is proposed to overcome this issue.

For a given fieldmap, if the resulting inhomogeneity σ_{shim} after shimming by some arbitrary system is between that obtained by unconstrained SH shimming of degrees n and $n+1$ ($\sigma_{\mathrm{SH}_n} \geq \sigma_{\mathrm{shim}} > \sigma_{\mathrm{SH}_{n+1}}$), the SHR of such system for this particular fieldmap is given by:

$$SHR = n + \frac{\sigma_{\mathrm{SH}_n} - \sigma_{\mathrm{shim}}}{\sigma_{\mathrm{SH}_n} - \sigma_{\mathrm{SH}_{n+1}}} \tag{5.8}$$

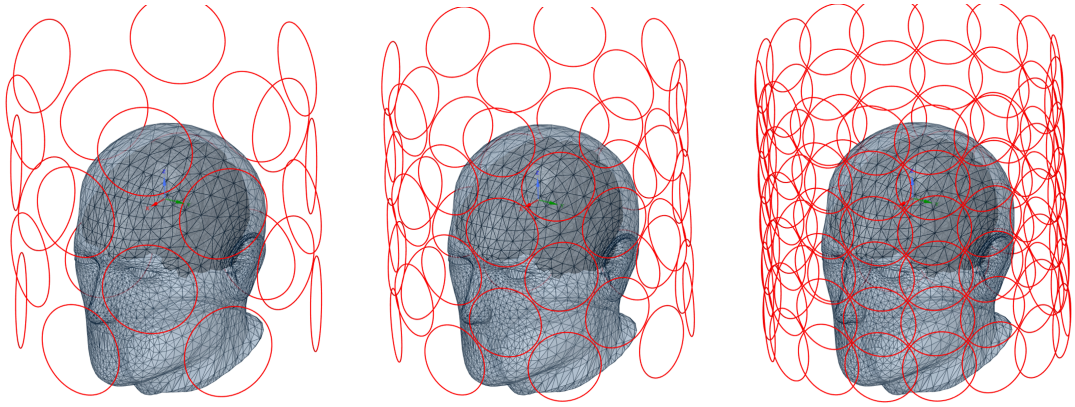

(a) (b) (c)

Figure 5.8 – Matrix MCAs of 24, 48 and 96 channels simulated for comparison with the optimized MCA.

The SHR obtained by SCOTCH shimming simulation on the in-house database is then compared to the SHR obtained from simulation on the OA database.

5.1.6 Performance Comparison with SH and Matrix MCA

To assess how the optimized MCA obtained from the proposed method improves homogeneity relatively to conventional matrix designs, simulations of three matrix MCAs of increasing channel count are performed.

Circular loops are considered as channel elements of the arrays, and are regularly distributed on top of a cylindrical coil former of a =140 mm radius and 300 mm length.

The magnetic field generated by circular loops can be calculated analytically. For a circular loop of radius a_ℓ, centered at cylindrical coordinates $(a, \varphi_\ell, z_\ell)$ over the cylinder, the magnetic field in the z direction produced by the loop per unit current is (after some algebra):

$$\mathcal{B}_z(\boldsymbol{x}) = \frac{\mu_0}{8\pi\sqrt{a_\ell}} \frac{(a - x\cos\varphi_\ell - y\sin\varphi_\ell)(z - z_\ell)}{{\rho'}^{5/2}} k \left(\frac{2-k^2}{1-k^2} E(k^2) - 2K(k^2) \right) \tag{5.9}$$

with

$$k^2 = \frac{4a\rho'}{(a+\rho')^2 + (a - x\cos\varphi_\ell - y\sin\varphi_\ell)},$$

$$\rho' = \sqrt{(x\sin\varphi_\ell - y\cos\varphi_\ell)^2 + (z - z_\ell)^2}$$

and K and E complete elliptical integrals of first and second kinds, respectively.

Three matrix MCAs of 24, 48 and 96 channels are designed for comparison, with channels' dimension and position defined so that there is full coverage of the cylindrical surface. The corresponding arrays are shown in fig. 5.8, with loop radius of 45 mm for the 24-channel array, and 35 mm for the 48 and 96-channel arrays .

Figure 5.9 – Control interface for SCOTCH to simplify shimming workflow.

5.1.7 *In-Vivo* Experiments

For experimental validation, an *in-vivo* acquisition was performed with SCOTCH shimming in a MAGNETOM 7 T scanner on one healthy volunteer. The in-house 8Tx/32Rx AVANTI2 RF coil was employed.

A control interface (cf. Fig. 5.9) was designed in MATLAB to communicate with an Arduino board and transfer ideal current setpoints to the current driver.

Restricted SAR Mode

To accelerate Internal Regulation Board (IRB) authorization for the experiments, sequences were played in the restricted SAR (rS) mode [Vignaud 2018]. Under this mode, idealized to provide unconditionally safe SAR levels, all transmitted RF power is assumed to be deposited into 10 g of biological tissue. Then TR must be adjusted such that local SAR constraints would be respected even under this conservative premise. Assuming the pulse sequence contains only a single RF pulse per TR (such as the conventional SPGR sequence), given the RF excitation pulse waveform $v_{RF}(t)$, to respect the $10\,\mathrm{W\,kg^{-1}}$ local SAR constraint:

$$\mathrm{TR} \geq \frac{1}{100\,\mathrm{mW}} \frac{\int_\tau v_{RF}^2(t)dt}{R_{\mathrm{Load}}} \tag{5.10}$$

with R_{Load} assumed equal to $50\,\Omega$ for a matched load.

Quantitative Analysis

The 3D non-selective rS-GRE was then employed for fieldmap estimation by means of a triple-echo acquisition with $TE_1 = 2\,ms$, $TE_2 = 3.6\,ms$, $TE_3 = 6\,ms$ and $TR = 100\,ms$. Isotropic resolution of 2.0 mm was employed, which was within recommendations from [Juchem 2020a]. Bandwidth per pixel was 1313 Hz. Amplitude and phase images are reconstructed using Sum of Squares technique, and the resulting DICOM data is employed for fieldmap estimation. The amplitude image is used as input in FSL's BET [Smith 2002] to create a brain mask, thus limiting the ROI to brain voxels. Then, phase images are used to performed spatial unwrapping of the phase difference between the two first echoes within the masked regions using SEGUE [Karsa 2019]. The phase of the third echo is then temporally unwrapped. The field excursion is finally estimated in each voxel as the slope of a linear fit of the phase evolution across the three echo-times. In total, 2 rS-GRE acquisitions were performed throughout the experiment. An initial acquisition was used for baseline field estimation. The baseline fieldmap was then employed for optimal 2-layer 36-channel SCOTCH's current calculation in a joint optimization with scanner's SH coefficients. The resulting currents and SH coefficients were applied for static whole-brain shimming. Then a second rs-GRE acquisition was performed for quantitative assessment of the residual magnetic field, to be compared with the expected field from simulations.

Qualitative Analysis

For qualitative assessment of B_0 related artifact mitigation, particularly geometric distortion and signal-loss, a 3D non-selective rS-EPI sequence was employed. After each fieldmap acquisition step (baseline and SCOTCH shimming), rs-EPI images with phase-encoding GRAPPA acceleration factor of 4 were acquired at 1.5 mm isotropic resolution and echo time $TE = 25\,ms$. Phase-encoding direction was set to Anterior-Posterior (AP). Repetition time was $TR = 150\,ms$. Gradient intensity was adjusted until reaching a minimum inter-echo spacing of 0.68 ms. Current amplitude was constrained to 3 A per channel in shimming experiments.

We emphasize that due to the rS constraint, employed sequences were relatively long, with approximately 7 min required for each GRE fieldmap acquisition, and around 1 min for each EPI sequence. This makes the experiment prone to errors cause by patient movement, Therefore, the volunteer is likely to move, and this was indeed observed in the experiment. In order to ensure comparisons between identical anatomic regions, image registration was employed using 3D Slicer to compensate for subject movement.

5.1.8 Expected Performance at 11.7 T

The ultimate goal of this work was to design a shim system for an 11.7 T MRI scanner [Quettier 2020], currently being installed in our facilities. This scanner will be equipped with up to partial 3^{rd} degree SH shim coils (4 coils). Therefore, the acquired δB_0 database

was re-shimmed to account for the SH shim system available in the 11.7 T scanner. After partial 3$^{\text{rd}}$ degree SH, the baseline inhomogeneity is 95.6 Hz (SD: 14.9 Hz) at 11.7 T.

SCOTCH shimming simulations were performed using ideal and measured field bases in degree to estimate the resulting inhomogeneity at 11.7 T.

To estimate expected geometric distortion in EPI acquisitions, we consider a $FOV_{PE} = 240$ mm phase-encoding FOV in the PA direction, $\tau_{ES} = 0.5$ ms echo spacing and phase-encoding acceleration factor of $R = 4$ (an adequate acceleration at 7 T as reported in [Moeller 2010]). From these parameters, geometric distortion δ_{PE} of a voxel in the phase-encoding direction can be estimated from [Wald 2012]

$$\delta_{PE} = \frac{\delta B_0 FOV_{PE} \tau_{ES}}{R_{PE}}. \tag{5.11}$$

Fieldmaps and geometric distortion maps at 11.7 T are shown in section 5.2.

Power-Minimizing Optimization of Shim Currents

As expected and observed in simulation results, the maximum electric current per channel needs to increase for the shim system to maintain high performance at a stronger magnetic field. This will come at the cost of increased power dissipation, which must be dealt with carefully for the shimming system to not overheat.

We have verified that power dissipation can be drastically reduced under the same maximum electric current constraint by changing the formulation of the optimization problem initially defined as eq.5.12.

Let $\boldsymbol{i}_0$ be the optimal currents resulting from 5.12. By relaxing the resulting SHR to a slightly reduced value while minimizing the power dissipation of the system, a small rise in global inhomogeneity will lead to considerable power dissipation drop. The problem is then formulated as follows:

$$\begin{aligned} \boldsymbol{i}_{\text{opt}} = \underset{\boldsymbol{i}\in\mathbb{R}^{N_{\text{ch}}}}{\text{argmin}}\ & \boldsymbol{i}^T \mathbf{R} \boldsymbol{i}, \\ \text{s.t. } & |i_j| \leq I_{\max}, \quad 1 \leq j \leq N_{\text{ch}}, \\ & SHR\,(\boldsymbol{b}_s + \mathbf{B}_s \boldsymbol{i}) \geq SHR(\boldsymbol{b}_s + \mathbf{B}_s \boldsymbol{i}_0) - \delta_{SHR}. \end{aligned} \tag{5.12}$$

where $\mathbf{R} \in \mathbb{R}^{N_{\text{Ch}} \times N_{\text{Ch}}}$ is a diagonal matrix composed of the resistances of each channel, and δ_{SHR} is the SHR decrease absolute tolerance.

This formulation was tested at 11.7 T with $I_{\max} = 5$ A and $\delta_{SHR} = 0.1$.

5.2 Results

Throughout this section, mentions of *simulated fields* or *ideal SCOTCH* on one hand, and *measured fields* or *realistic SCOTCH* on the other hand, refer to the $\mathbf{B}_s$ matrix of basis fields input for shimming simulation, either simulated with Ansys® or measured from GRE characterization acquisitions.

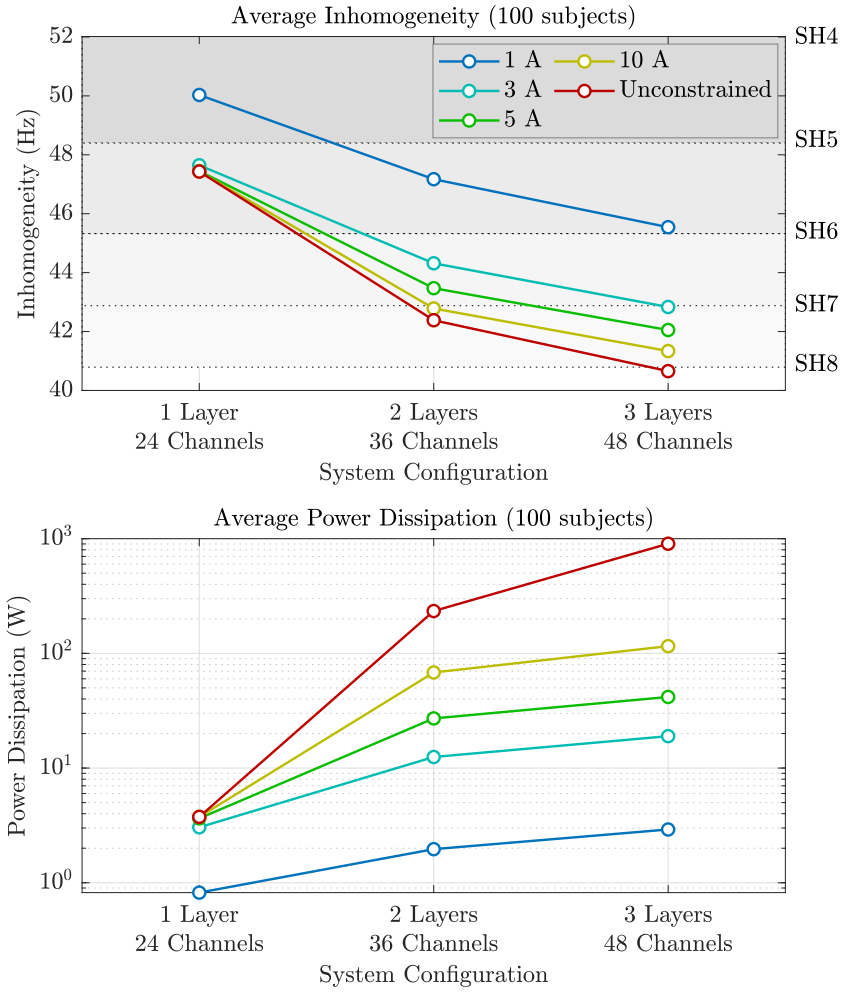

Figure 5.10 – Top plot: In-house database inhomogeneity after SCOTCH shimming at 7 T with simulated fields. Different maximum currents and numbers of layers/channels are considered for exploration of the performance evolution. Dotted lines crossing the inhomogeneity plot indicate the average inhomogeneity achieved by unconstrained SH shimming of different degrees, as indicated on the right. Bottom plot: Average power dissipation for the different parameters considered is also estimated.

The notation $L.CH$ indicating L layers and CH channels will also be employed throughout the text for brevity, i.e. 1.24, 2.36, 3.48 designate the SCOTCH configurations spawned from one, two and three SVD-modes.

5.2.1 Expected SCOTCH Performances from Simulated Field Basis

SCOTCH shimming simulation results on the 100-subject database at 7 T with simulated fields are shown in fig. 5.10. Different electric current constraints were assessed for performance, evaluated in terms of the resulting inhomogeneity across the database. Average power requirement was also estimated. The results are shown for different shim system configurations as the number of channels and layers increase.

In all simulations, improvement of the resulting homogeneity is observed as the number of optimized channels increases. At 3 A, for instance, inhomogeneity drops from a baseline of 65.7 Hz (SD: 11.4 Hz) to 47.6 Hz (SD: 8.2 Hz), 44.3 Hz (SD: 7.4 Hz) and 42.8 Hz (SD: 7.2 Hz) as the number of channels is increased from 24 to 36 and 48. Better performance is accompanied by increased power dissipation for all current constraints. At 3 A rating, power dissipation values as the number of channels increases are 3.0 W (SD: 1.5 W), 12.5 W (SD: 2.5 W) and 19.0 W (SD: 2.9 W) for 24, 36 and 48 channels, respectively. Compared to SH-based shimming, the 3.48-SCOTCH performance at 3 A would be comparable to a 7^{th} degree SH shimming (42.9 Hz (SD: 6.9 Hz)). When unconstrained, resulting 3.48-SCOTCH shimming inhomogeneity of 40.7 Hz (SD: 6.5 Hz) is comparable to unconstrained 8^{th} degree SH shimming, which results in 40.8 Hz (SD: 6.5 Hz). However, significant increase in power ratings is observed. The change from 3 A-constrained to unconstrained for 3.48-SCOTCH causes power dissipation to rise from 19.0 W (SD: 2.9 W) to 903.8 W (SD: 989.2 W).

It was also observed that significant improvement is obtained when moving from 1 A rating to 3 A rating, as we see performance increase (for 3.48 SCOTCH) from a 6^{th} degree SH equivalent to a 7^{th} degree equivalent, but as current is further increased, reduction in inhomogeneity is smaller and brings significant power dissipation increase. Considering the low-cost prototype envisioned, it was decided to restrict current rating to 3 A in the *in-vivo* experiments at 7 T.

5.2.2 Expected SCOTCH Performances from Measured Fields Basis and Cross-Validation

The SCOTCH prototype was built up to 2 layers and 36 channels. The third layer is still under construction. The 2.36-system was characterized, and measured fieldmaps were used as basis for shimming simulation. Comparison of inhomogeneity values obtained with simulated and measured fields serves as preliminary validation of the prototype. Results are shown in fig. 5.11a for electric current constrained to 3 A. Inhomogeneity values resulting from simulated matrix MCA shimming are also provided for comparison.

From the 100-subject database, a small drop in performance of the prototype is observed relatively to ideal SCOTCH performance. Resulting inhomogeneity with the 2.36 SCOTCH prototype, as evaluated with the measured fields, is 45.4 Hz (SD: 7.6 Hz), a 2.5 % (SD: 1.6 %) relative increase from to 44.3 Hz (SD: 7.4 Hz), expected from simulated fields. When compared to SH systems, inhomogeneity, initially expected to be better than the 45.3 Hz (SD: 7.3 Hz) that would be achieved by an unconstrained 6^{th} degree SH system, becomes practically equivalent to it. Compared to matrix MCAs, the realistic 1.24 SCOTCH shimming is expected to provide 48.6 Hz (SD: 8.3 Hz) inhomogeneity, 7.6 % (SD: 4.0 %) lower than the 24-channel MCA resulting inhomogeneity of 52.6 Hz (SD: 8.8 Hz). This is a first evidence of amelioration provided by the improved channel location and geometry obtained from the design method. The realistic 1.24 SCOTCH provides inhomogeneity almost equivalent to that of an unconstrained 5^{th} degree SH system, while the matrix MCA with the same number of channels provides slightly inferior performance to what

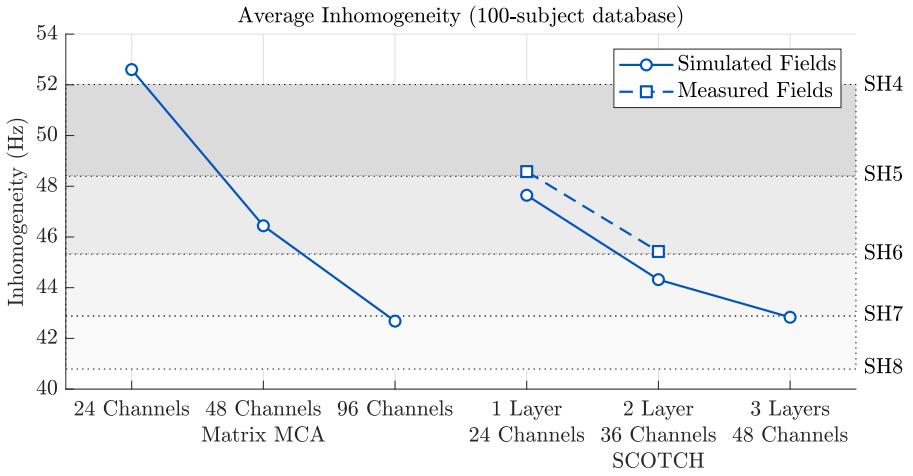

(a)

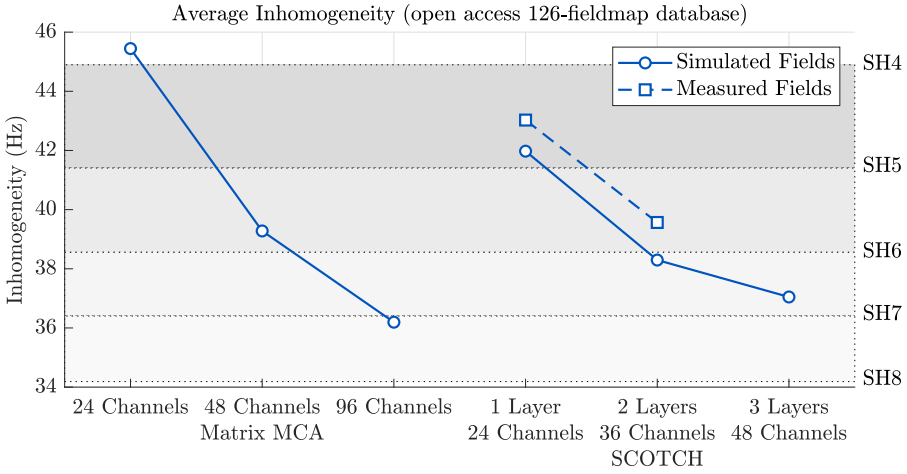

(b)

Figure 5.11 – SCOTCH shimming simulations performed on the (a) in-house and (b) open-access databases. Measured and simulated field bases are used. Matrix MCAs are also simulated on both databases for comparison with the optimized MCA designs. Electric current is constrained to 3 A in all MCA shimming simulations. Average inhomogeneity values obtained by unconstrained SH shimming simulations are indicated by dotted lines with the SH degree indicated on the right of the plots. Simulations on the open-access database serve the purpose of cross-validation analysis.

would be achieved by a 4^{th} degree SH shim system. Increasing the number of matrix MCA channels to 48 provides 46.4 Hz (SD: 7.7 Hz) inhomogeneity after shimming, closer to the inhomogeneity achievable by a 6^{th} degree SH based shimming, but still worse than the realistic 2.36 SCOTCH, despite possessing 12 extra channels.

Increasing the matrix MCA channel count to 96, resulting inhomogeneity is 42.7 Hz (SD: 7.1 Hz), close to the 42.9 Hz (SD: 6.9 Hz) obtained with 7^{th} degree SH shimming. From simulated fields, 3.48 SCOTCH would be capable of reaching approximately the same inhomogeneity (42.8 Hz (SD: 7.2 Hz)), but with half the amount of channels.

Fig. 5.11b shows shimming simulation results on the 126-fieldmap OA database. The 2.36-SCOTCH shimming simulated with measured fields shows resulting inhomogeneity

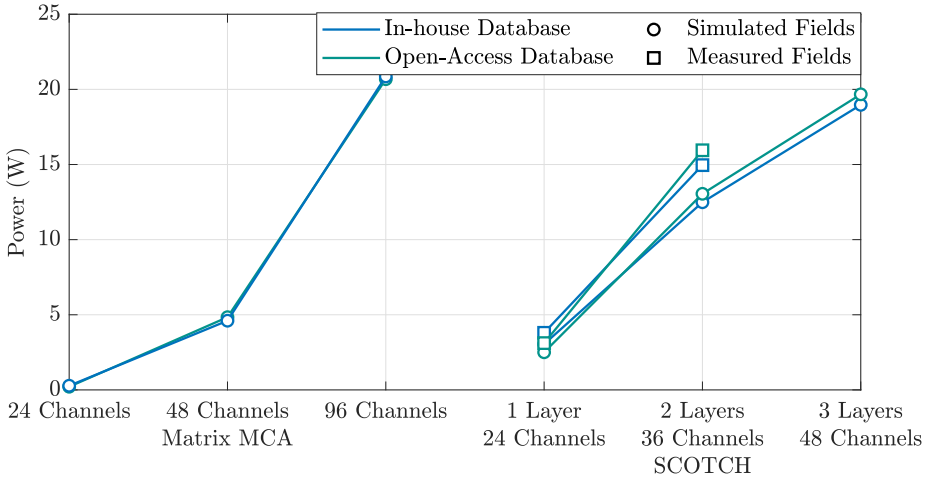

Figure 5.12 – Power dissipation for different shimming system configurations as estimated from simulations on the in-house and OA databases at 3 A maximum current per channel. Simulated and measured field bases are also considered for comparison.

of 39.6 Hz (SD: 6.7 Hz), close to the 39.3 Hz (SD: 6.9 Hz) inhomogeneity resulting from 48-channel matrix MCA shimming, but obtained with 12 channels less. SCOTCH's performance in the 2.36 configuration is still close to the 38.6 Hz (SD: 6.4 Hz) inhomogeneity obtained by a 6^{th} degree SH shimming system. For the ideal 3.48 SCOTCH shimming simulations, resulting inhomogeneity is 37.0 Hz (SD: 6.2 Hz), while 36.2 Hz (SD: 6.1 Hz) results from 96-channel matrix MCA shimming. Those are both close to the 36.4 Hz (SD: 5.9 Hz) average inhomogeneity achieved with unconstrained 7^{th} degree SH shimming, with the 96-channel MCA outperforming the 3.48 SCOTCH on this particular database.

We notice that the resulting average inhomogeneities on the OA database vary considerably from those obtained when shimming the in-house database. The realistic 2.36-SCOTCH shimming presents approximately 6 Hz difference when shimming the OA versus the in-house database. Analyzing the relative inhomogeneity reduction from baseline, 41.1 % (SD: 5.6 %) and 30.4 % (SD: 7.1 %) are obtained for the OA and in-house database, respectively. For matrix MCAs, considerable differences in resulting inhomogeneity are observed, also.

Now we can evaluate SCOTCH's robustness from the SHR: the realistic 2.36-SCOTCH leads to an SHR of 5.7 (SD: 0.6) on the OA database and 6.0 (SD: 0.6) on the in-house, a metric ratio of 0.95. If performance is measured by such a metric, we can conclude that SCOTCH is robust to new fieldmaps. The SHR was also calculated for the resulting inhomogeneity after 48-channel matrix MCA shimming, leading to 5.7 (SD: 0.5) and 5.8 Hz (SD: 0.4 Hz) on the in-house and OA databases, respectively, resulting in a 1.02 ratio. Since the matrix MCA performs similarly on both databases, the SHR is confirmed to be a universal indicator of system performance, regardless of the B0-map database.

Average power dissipation of matrix MCAs and SCOTCH constrained to 3 A per channel and estimated from simulated and measured field bases are shown in fig. 5.12. Power dissipation is observed to increase as the number of channels and shimming performance

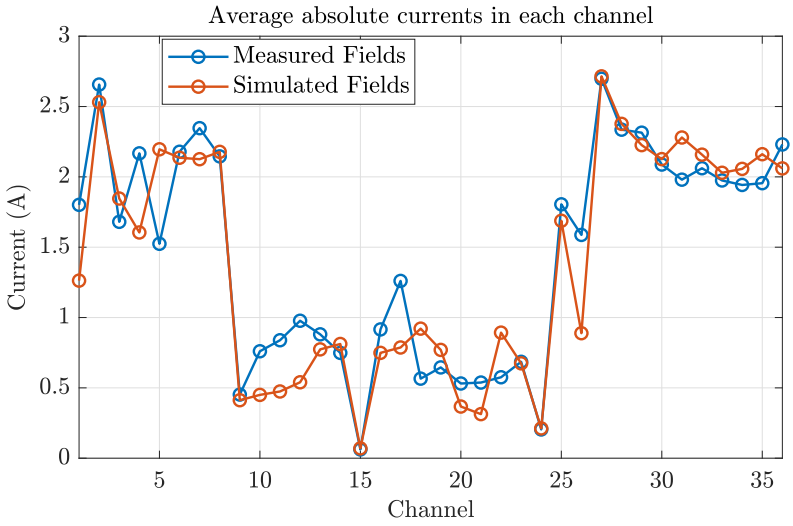

Figure 5.13 – Average of absolute currents for each of the 2.36-SCOTCH channels after shimming simulation on the 100-subject database with simulated and measured fields.

increases. For a given system design, power dissipation is practically the same on both databases. For 2.36-SCOTCH, power dissipation estimated from simulations with measured fields and resistances were 15.0 W (SD: 2.7 W) and 15.9 W (SD: 2.6 W) in the in-house and OA databases, respectively. These are superior to the 12.5 W (SD: 2.5 W) and 13.1 W (SD: 2.3 W) obtained from ideal SCOTCH simulations on the in-house and OA databases, respectively. As inhomogeneity reduces and attains similar levels to that achieved by unconstrained 7^{th} degree SH shim systems, power dissipation rises. When shimmed by the 96-channel matrix MCA, power dissipation values are 20.9 W (SD: 4.6 W) and 20.7 W (SD: 3.9 W) for the in-house and OA databases, respectively. With 3.48 SCOTCH shimming, power dissipation reaches 19.0 W (SD: 2.9 W) and 19.7 W (SD: 2.9 W) for the in-house and OA databases. Power dissipation is multiplied by six from the 1.24 configuration to the 3.48 configuration, with the former presenting 3.0 W (SD: 1.5 W) and 2.5 W (SD: 1.1 W) power dissipation, for in-house and OA databases, respectively, with ideal SCOTCH simulations.

In fig. 5.13, the average of the absolute electric current on each 2.36-SCOTCH channel when shimming the 100-subject database is shown with the measured and simulated fields. It shows a close correlation of the currents, with some differences in intensity.

Under the 3 A maximum current constraint, SCOTCH heating was assessed through thermal camera measurements with all 36 channels driven at full current for 1 h. Power dissipation estimated using measured channels' resistances was 37.5 W. Maximum temperature observed was 37 °C, with initial temperature of the setup at 21 °C. This was deemed safe for operation, with pain threshold of 65 °C as estimated from [Ungar 2010] far from being attained. This estimation considered thermal conductivity, specific heat and density of $0.343\,\mathrm{W\,m^{-1}\,K^{-1}}$, $1.1\,\mathrm{J\,g^{-1}\,K^{-1}}$ and $1.85\,\mathrm{g\,cm^{-3}}$, respectively.

As could be observed from results in fig. 5.11, the realistic SCOTCH performance is inferior to that estimated from simulated field basis. To recover the lost performance, electric

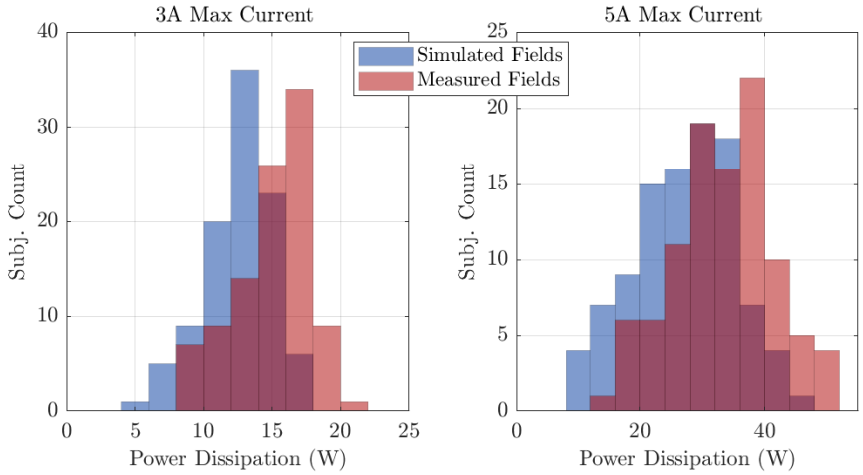

Figure 5.14 – Power dissipation histogram for shimming simulations at 7 T for different current constraints. Simulated and measured fields are used for shimming simulation. The histograms provide detailed information on the increased power dissipation already observed in fig. 5.12 as we move to the realistic SCOTCH.

current increase might be an option as long as safe temperature rise can still be guaranteed. With electric currents constrained to 5 A, 2.36 SCOTCH shimming simulations on the 100-subject database using the measured fieldmaps leads to 44.5 Hz (SD: 7.4 Hz) inhomogeneity, thus improving performance relative to the 3 A-constrained operation, as it surpasses that of a 6^{th} degree SH system.

Naturally, power dissipation will increase as maximum current is allowed to increase. This is observed in the histograms in fig. 5.14. For the 100-subject database, at 5 A, maximum power dissipation as estimated from simulations with measured fields and resistances is 49 W. This is superior to the power dissipation obtained at full current in the thermal tests, and safety cannot yet be guaranteed for this level of power dissipation. It is a significant increase from the maximum power dissipation of 21 W expected at 3 A.

5.2.3 *In-Vivo* Results

Quantitative Assessment

Fieldmaps estimated from the rS-GRE acquisitions for the volunteer are shown in Fig.5.15. Scanner-set baseline inhomogeneity was 59.2 Hz. Usual inhomogeneity hotspots are observed around and above ear canals and above the nasal sinus.

The expected fieldmap from SCOTCH's optimal shim currents provided 36.3 Hz inhomogeneity, which is a 38.7 % relative improvement from scanner baseline. Slight movement of the patient's head was observed in the experiment. Image registration was therefore employed and a new brain mask was generated for data analysis. Inhomogeneity after SCOTCH shimming was 37.9 Hz, confirming the significant improvement relatively to baseline (36.0 %). Selected slices are shown in Fig. 5.15. Amelioration in the homogeneity can be observed across all slices, with considerable reduction of inhomogeneity hotspots.

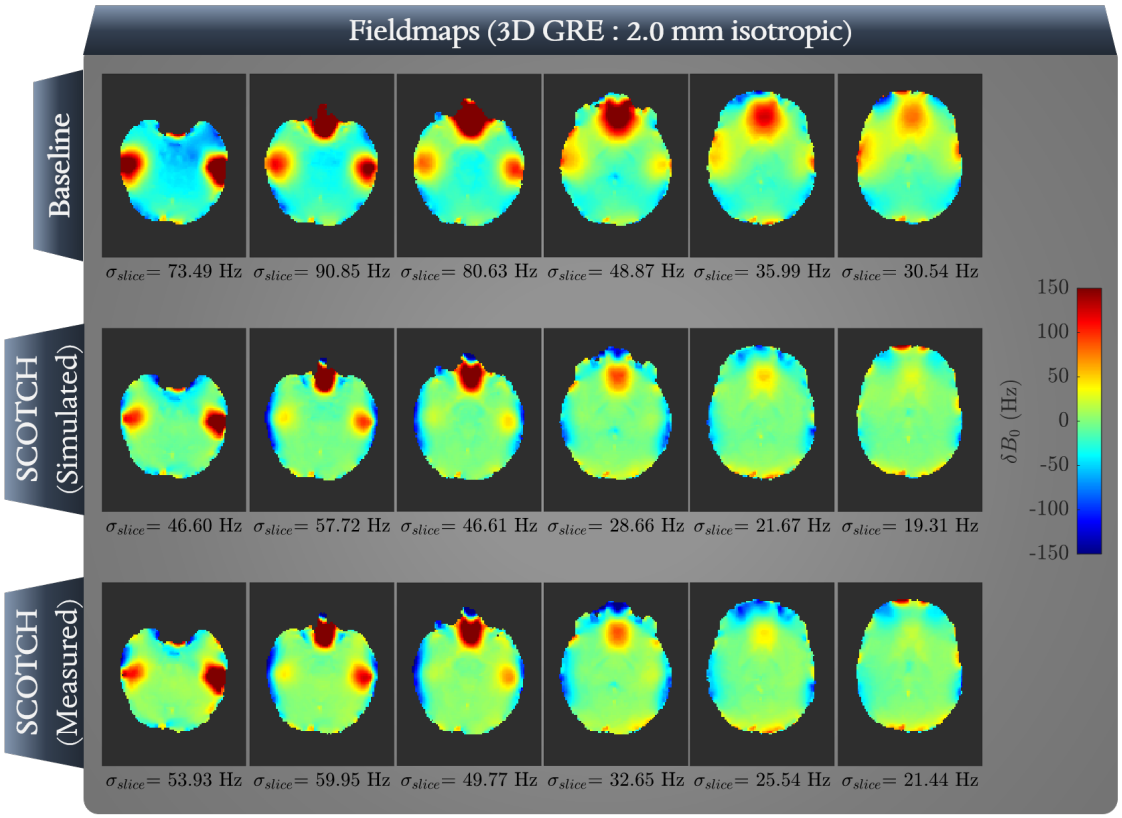

Figure 5.15 – Acquired and simulated fieldmaps after in-vivo SCOTCH shimming. Slices passing through dorsal to ventral parts of the brain are depicted from left to right. Inhomogeneity in each slice is also shown for assessment of shimming quality and comparison with expectations.

The expected SHR from the application of SCOTCH was 6.38, and the actual SHR from the measured fieldmap was 5.84.

Qualitative Assessment

Selected slices for baseline and SCOTCH-shimmed rs-EPI acquisitions are shown in Fig. 5.16. They are located in challenging regions to shim. Improved regions after shimming are indicated by arrows 1 through 9.

To ease visualization, the arrows displayed in Fig. 5.16 point to poor image quality zones in the baseline that were improved with the application of SCOTCH. Arrow 1 shows enhanced contrast in the right temporal lobe, while some modest signal recovery above the right ear canal can also be observed (arrow 2). In 3, correction of geometric distortion leading to signal recovery is noticeable above the right ear canal, with some mild recovery also above the left ear canal, although it remains mostly non-exploitable. In the following slice there is timid signal recovery in the ventral part of the pre-frontal cortex (arrow 5), while almost complete artifact mitigation is observed above the right ear canal (arrow 6). Moving to slices above the maxillary and sphenoid sinuses, perhaps the most striking signal recovery is marked by arrow 7, where SCOTCH managed to recover signal in an

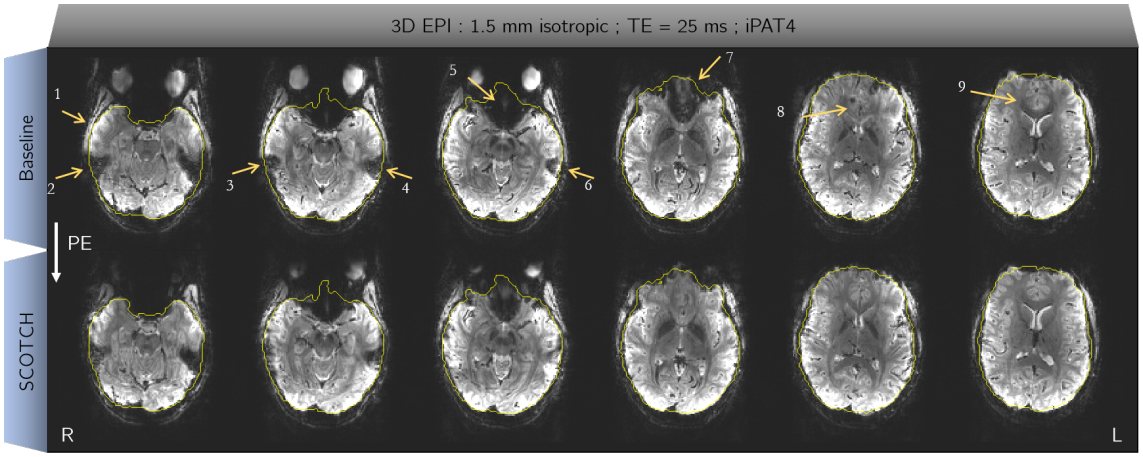

Figure 5.16 – Restricted SAR EPI acquisitions after 2nd degree SH and 2.36 SCOTCH shimming. Sequence parameters were: iPAT= 4 acceleration, TE = 25 ms, 1.5 mm isotropic resolution.

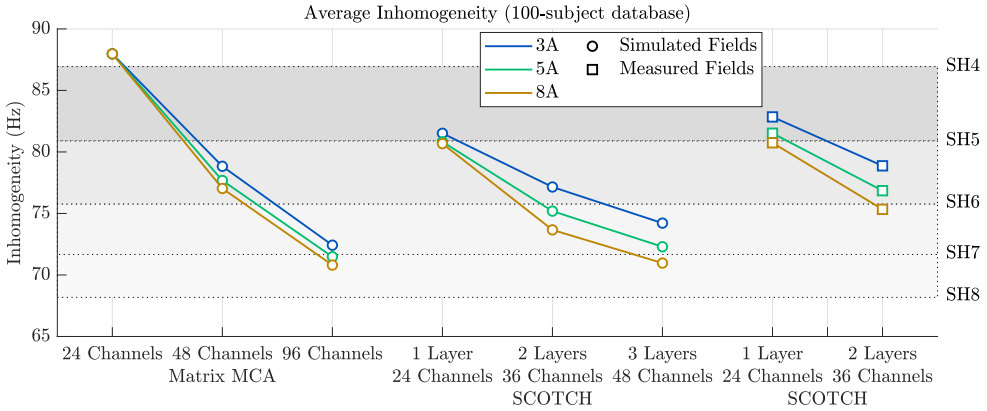

Figure 5.17 – Expected inhomogeneity resulting from SCOTCH shimming simulations at 11.7 T under different electric current constraints and using measured and simulated field basis. Inhomogeneity after matrix MCA shimming was also simulated for comparison. Equivalence to unconstrained SH shimming is also indicated by the dotted lines and SH degree is indicated on the right.

initially large void region. Moving further in the Feet-Head direction, more signal recovery and contrast enhancement in the pre-frontal cortex are observed (arrows 8 and 9).

The EPI acquisitions ultimately corroborate the homogeneity improvements expected to be brought by 2.36 SCOTCH from the rS-GRE acquisitions.

5.2.4 Expected Results at 11.7T

Shimming simulations were performed on the partial 3rd degree shimmed 100-subject database at 11.7 T (of 95.6 Hz (SD: 14.9 Hz) inhomogeneity) using SCOTCH and matrix MCAs, for different current constraints.

As the magnetic field increases, maintaining equivalent performances in terms of relative inhomogeneity reduction requires electric current to increase. At 3 A, expected inhomogeneity of SCOTCH 3.48 when considering simulated fields is 74.2 Hz (SD: 12.5 Hz),

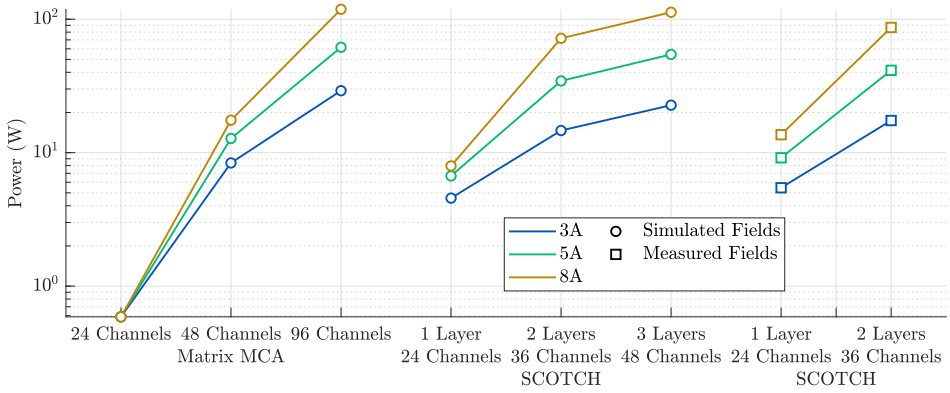

Figure 5.18 – Power dissipation estimation at 11.7 T for different shimming systems.

performing slightly better than a 6$^{\text{th}}$ degree SH system, which would provide 75.8 Hz (SD: 12.1 Hz). As current is increased to 5 A, resulting inhomogeneity is 72.3 Hz (SD: 12.2 Hz), closer to a 7$^{\text{th}}$ degree SH system, which provides 71.7 Hz (SD: 11.5 Hz) inhomogeneity. Further improvement would be expected at 8 A, with final inhomogeneity at 71.0 Hz (SD: 11.8 Hz), but power dissipation increases from 54.5 W (SD: 8.9 W) to 112.8 W (SD: 23.3 W).

However simulations with the measured field basis show a reduced performance, and 5 A is necessary for 2.36 to provide similar inhomogeneity (76.9 Hz (SD: 12.9 Hz)) to what was expected from the ideal SCOTCH simulations at 3 A (77.2 Hz (SD: 13.2 Hz)). Power dissipation at 5 A estimated from the measured fields and resistances is expected to be 41.4 W (SD: 7.6 W) , which is higher than the 34.5 W (SD: 6.9 W) initially estimated from the ideal SCOTCH model. If a similar gap in shimming performance between simulated and measured fields persists after the addition of the third layer in the prototype, 3.48 SCOTCH driven by 5 A max current would likely provide shimming performances superior to a 6$^{\text{th}}$ degree SH system, but not so near the performance of a 7$^{\text{th}}$ degree SH system.

Despite reduction in performance relatively to the ideal SCOTCH model, measured fields show that 2.36 still provides inhomogeneity of 78.9 Hz (SD: 13.3 Hz), comparable to ideal 48-channel Matrix MCA (78.8 Hz (SD: 13.2 Hz)) at 3 A, and performs better than the 48-channel matrix MCA when both are driven at 5 A max current.

We notice that at the minimum expected inhomogeneity of 71.0 Hz (SD: 11.8 Hz) provided by 3.48 SCOTCH at 8 A, despite being equivalent to what would be achieved by a 7$^{\text{th}}$ degree SH system, inhomogeneity is still superior to the 2$^{\text{nd}}$ degree shimmed baseline at 7 T.

Fieldmaps and EPI geometric distortion maps for a particular subject at partial 3$^{\text{rd}}$ degree baseline and shimmed with 3.48-SCOTCH limited to 5 A per channel are shown in fig. 5.19. Improvement in the fieldmap is observed for all slices displayed, with significant reduction of the high magnetic field zones. The geometric distortion map is proportional to the δB_0 inhomogeneity, and is shown in fig. 5.19b, with the colormap saturated at $\pm$10 mm. While distortion clusters remain, they have been considerably reduced for this particular subject, relative to baseline. Voxels with absolute geometric distortion superior to 10 mm were reduced by 33.0 %, leading to a remaining 1.1 % of voxels shifted by more

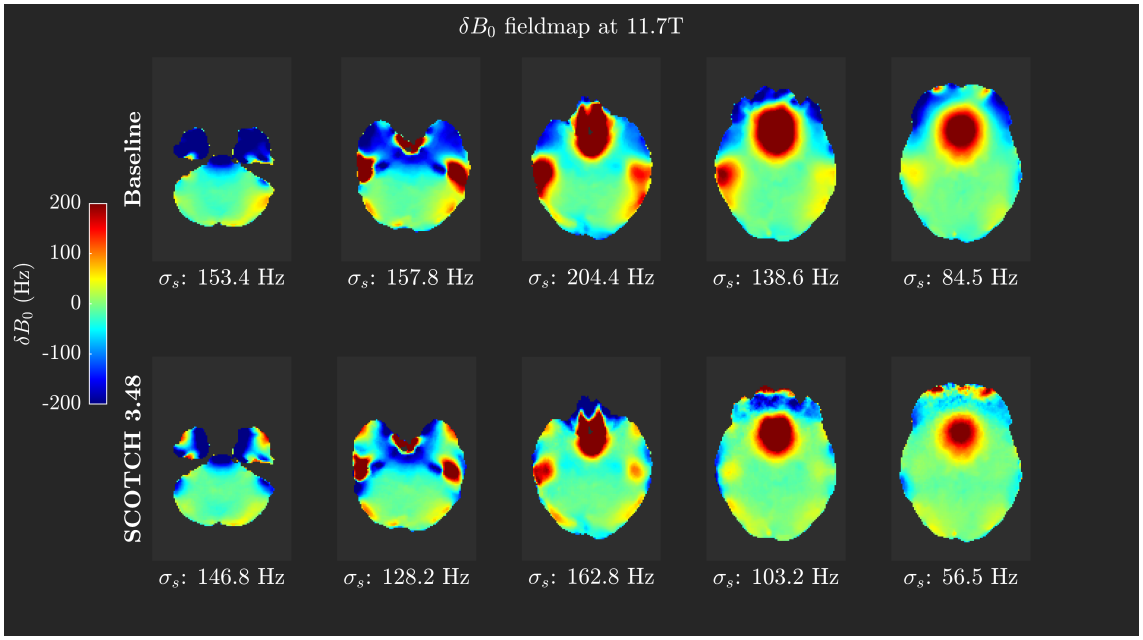

(a)

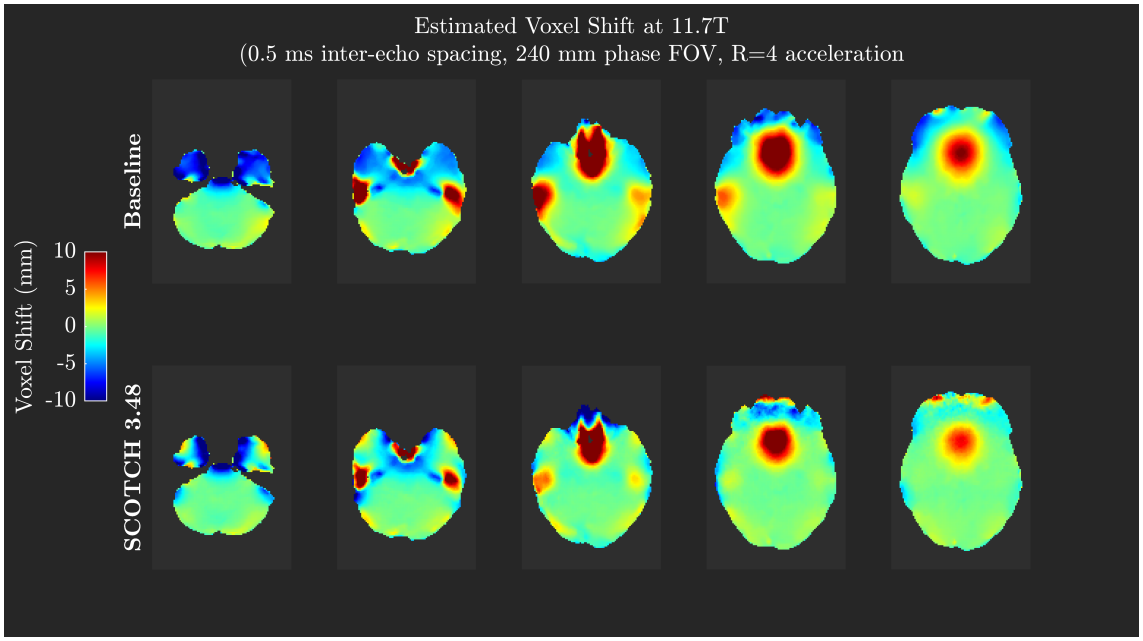

(b)

Figure 5.19 – Fieldmap (a) and voxel shift map (b) for a subject at 11.7 T after 3.48 SCOTCH shimming simulation at 5 A.

than 10 mm, and voxels with absolute geometric distortion superior to 5 mm were reduced by 38.5 %, resulting in only 3.5 % of voxels shifted by more than 5 mm.

Finally, at 5 A, as observed in the previous results, power will considerably increase relatively to what is demanded for shimming at 7 T. To try and address this issue, shimming simulation of SCOTCH 3.48 using the power minimization approach in eq.5.7 was performed with currents constrained to 5 A, and a 0.1 tolerated reduction in the SHR. Resulting inhomogeneity of 72.7 Hz (SD: 12.2 Hz) was obtained, only 0.6 % (SD: 0.2 %) su-

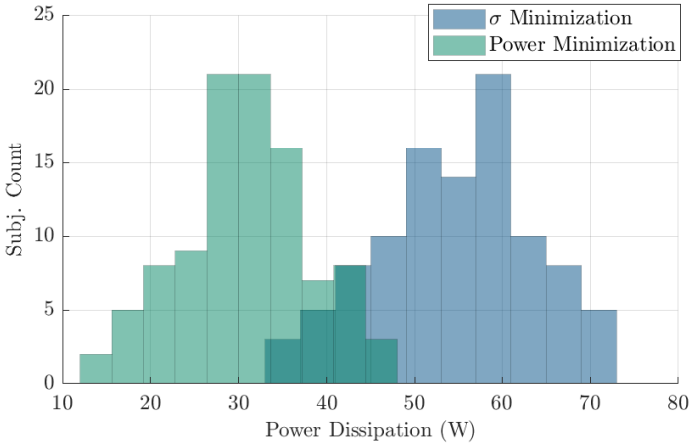

(a)

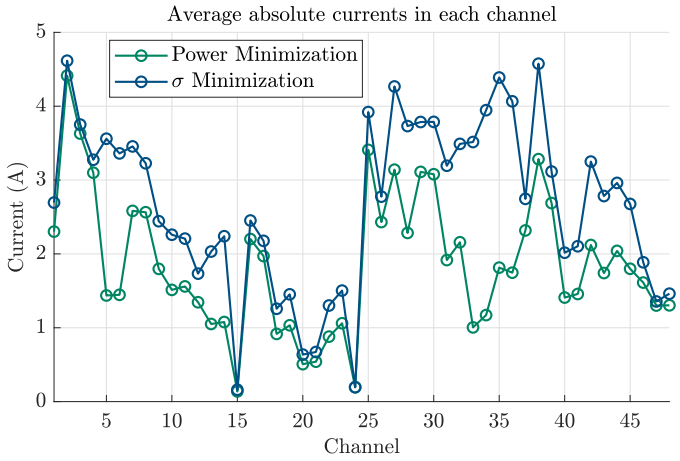

(b)

Figure 5.20 – Electric ratings for simulated 3.48 SCOTCH shimming employing different optimization formulations at 5 A. For the two different optimization formulations, (a) power dissipation histograms and (b) electric currents are shown.

perior to the minimized inhomogeneity. Power dissipation, on the other hand, dropped to 30.8 W (SD: 7.2 W), with max power in the database at 47.3 W. This corresponds to a 43.7 % (SD: 8.3 %) drop in power dissipation, while maintaining inhomogeneity almost at the same level. The max power dissipation becomes inferior to the average power dissipation that was estimated when using the original minimization approach. Histograms with the relative shift in power distribution across the database are shown in fig.5.20. The average of the absolute current in each channel is also shown.

5.3 Discussion and Conclusion

5.3.1 SCOTCH Added-Value with Respect to Prior Art

A novel method for optimized MCA design for human brain shimming was proposed in this work. Contrarily to other proposed MCA optimization methods [Aghaeifar 2020,

Oh 2020], no *a priori* assumption is made relative to the coil geometries, other than the cylindrical support. As such, SCOTCH coil geometries were observed to be very different from circular or rectangular loops employed in other MCA optimization works. A common feature between resulting designs from the different methodologies is the accumulation of channels in front and on the sides of the subject's head, where frontal sinus and ear canals are located and are known to generate strong magnetic field excursions.

Once optimal channel geometries were defined, the effects of increasing the allowed electric current in each channel were explored, as well as the expected power dissipation accompanied by the relaxation of these constraints. This exploration is useful to find an adequate operation point for the system by finding a balance between performance and power dissipation; the latter needs to be limited to avoid overheating and the need for thermal dissipation structures, which would increase complexity. In our case, 3 A was considered a good compromise as, for the 3-layer design, it provided a 7^{th} degree SH equivalent performance against a 6^{th} degree equivalent when at 1 A. But further increase in current to 5 A would provide marginal improvement, while average power dissipation would be more than double (19.0 W to 41.7 W). While considerations to heating and safety are made and experimental verification is carried out in several MCA related works [Juchem 2010c, Aghaeifar 2018, Aghaeifar 2020], little attention has been given to the power dissipation itself and how it evolves as shimming performance increases. Despite being somewhat overlooked in most MCA related works, power dissipation was extensively analyzed in this work, and was verified to be a bottleneck for performance. To improve this analysis, further thermal simulations could be envisioned in the future to have a better assessment of what is indeed acceptable.

Despite having the potential to present shimming performances equivalent to that of an 8^{th} degree SH system, the 3-layer ideal design is limited by the very high power consumption of almost 1 kW required to achieve this potential, which is evidently impractical for a system that is going to be near the patient, unless forced cooling is employed. Gradient systems, for instance, can indeed reach much higher power consumption (more than 30 kw), but are actively cooled, and completely isolated from the patient. Our choice in this work was to avoid this supplementary burden for our system. We do not discard, however, the possibility that this could be necessary if shimming performances must be increased. Although power dissipation values alone don't provide a clear picture of the max temperatures achieved by the system, a rough estimation of max temperature evolution as a function of power dissipation can be made from the thermal measurements performed for safety assessment of the shim system. A 0.5 °C temperature rise per Watt is estimated, and a limit of 80 W max power could be established resulting in 60 °C max temperature, inferior to the pain threshold temperature of 65 °C.

As the ideal SCOTCH simulations showed shimming performance in the in-house database superior to that of 6^{th} degree SH for the 2-layer 36-channel design and equivalent to 7^{th} degree SH for the 3-layer 48-channel design, construction of the prototype was carried out. To our knowledge, when compared to unconstrained SH shimming systems, no MCA shimming system presented in the literature so far has shown expected whole

brain shimming performances as high as those. The 32-channel optimized array presented in [Aghaeifar 2020] showed superior performance to a 4^{th} degree SH system when constrained to 2 A at 9.4 T, and slightly better than a 5^{th} degree SH system when unconstrained. In [Zhou 2020], the judicious placement of a set of coils in front of the frontal lobe provided a 3 A-constrained 39-channel MCA with simulated performances comparable to a 6^{th} degree SH system at 3 T.

5.3.2 Performance Loss from Ideal Single-Loop Model to Realistic Multi-Turn Bundles

With the prototype built and characterized, shimming simulations constrained to 3 A (the chosen operation current) could be performed for comparison of realistic versus ideal SCOTCH performances. Resulting inhomogeneity from realistic SCOTCH shimming simulation was greater than expected, on both the in-house and OA databases. The loss in performance is not surprising since ideal SCOTCH simulations were performed considering the basis field for each channel as the field of a single loop multiplied by the number of turns (twenty); however, realistic wire bundles composing each channel deviate from the ideal SLM. This deviation also causes an increase in power dissipation, as electric currents also become higher. Due to the proximity of some ideal loops to one-another, the wire bundles could not always be wound having their geometric center coincident with the ideal loop coordinates, causing the winding to have its thickness towards the center of the loop; this in turn reduces the effective magnetic moment of the channel, therefore the magnetic field generated, finally leading to the rise in currents and power dissipation. Nevertheless, the power dissipation deviation as seen from the histograms in fig. 5.14 is not drastic.

5.3.3 Cross-validation and Spherical Harmonic Rating

One of the most important aspects of the design was cross-validation, required to guarantee robustness to new fieldmaps and inter-subject variability. However, resulting inhomogeneity after shimming simulations on the in-house and OA databases, independently of the shim system employed (optimized or matrix), was very different from one database to the other, despite baseline inhomogeneity being numerically close. Shimmed inhomogeneity was lower on the OA database. This suggested that the inhomogeneity metric might not be the ideal for the cross-validation study. Looking at the SH equivalent performance indicated by the dotted lines in fig. 5.11, a more stable behavior is observed. The matrix MCAs, which should deliver the same performance independently of the database, provide practically the same performance with the SH equivalence, despite showing numerical differences in the final inhomogeneity. From this observation, the SHR was envisioned, and indeed seems to be a robust metric for assessing shim system performance (more results related to this metric are shown in appendix D). Despite a lower realistic SCOTCH performance on the OA database compared to the in-house database, SHR is still 5.8, thus almost equivalent to a 6^{th} degree SH system. The loss of performance on the OA database could be explained by a biased SF-SVD-based design. Alternatively, the re-positioning

of the OA fieldmaps to match the AVANTI2 coil dimensions was performed such that subjects were lifted in the PA direction only enough to respect the estimated position limits. This caused the fieldmaps to be located further away from the frontal channels, compared to imaging routine where cushions can be positioned under the subject head, lifting it even more. As such, performance could be smaller in the OA database. This was nevertheless a conscious choice to avoid biasing the shifted database in our favour, but might have biased it to provide lower performances.

The issue of the variability of inhomogeneity values observed across different research sites has been mentioned in some works [Stockmann 2016, Zhou 2020]. This variability might be caused by different factors ranging from fieldmap acquisition and post-processing to brain mask topology differences.

Translating inhomogeneity values into the SH equivalents can provide a sense of engineering effort required to achieve a certain homogeneity level. Considering the in-house database, the difference in average inhomogeneity when shimmed by unconstrained 6^{th} and 7^{th} degree SH systems is 2.4 Hz. While it could be considered a low improvement, a total of 15 SH-based coils would need to be added to a 6^{th} degree SH system in order to attain this seemingly low improvement. The small numeric improvement in inhomogeneity as SH degrees are increased is likely due to remaining higher-degree localized magnetic field patterns; this incremental improvement ends up being diluted by the global inhomogeneity metric, but is nonetheless required to recover good image quality in δB_0 critical regions.

5.3.4 SCOTCH vs Matrix-MCAs for Whole-Brain Shimming

The shimming simulations and comparison of ideal SCOTCH to ideal matrix MCAs showed that the optimized channels' positions and geometry provided improved homogeneity with less channels. From simulations on the in-house database, the 1.24 SCOTCH shows vastly superior performance to that of a 24-channel m-MCA. With the former presenting SHR superior to 5 and the latter inferior to 4. With the 2.36 configuration, SHR is superior to 6, whilst the SHR for the 48-channel m-MCA inferior to 6, despite presenting higher channel count. As the number of SCOTCH channels are increased to 48, further improvement in performance is observed, and a 7^{th} degree SH equivalent is reached. This is similar performance to that achieved by a 96-channel m-MCA, but with half the amount of channels, which vastly decrease electronics hardware costs.

5.3.5 What About Dynamic Shimming ?

The proposed method is aimed at whole brain shimming, and performances of the shimming system under this condition was thoroughly explored. Other shimming techniques such as dynamic slice-by-slice or region-specific shimming were not assessed in this work, but have been explored in one of our previous studies [Pinho Meneses 2020c] (appendix E), where it was shown that SF-SVD based MCAs could still provide high dynamic shimming performance, although not as high as matrix MCAs. Although dynamic shimming

has been shown in the literature to provide high inhomogeneity reduction and significantly reduce artifacts in EPI [Juchem 2015], as submillimeter resolution is targeted, SNR when acquiring a single slice will drop, and either 3D or Multi-Band EPI will be required to compensate this signal loss. If 3D acquisition is employed, whole brain shimming is required *a priori*. In the case of Multi-Band (MB), it has recently been demonstrated that 2-slice MB with an SH-based shim insert of up to full 4^{th} degree and 2 extra 5^{th} degree coils is actually capable of providing the same performance as slice-by-slice shimming [Hetherington 2021]. Moreover in [Stockmann 2016], it was shown in simulations that dynamic shimming with $MB = 3$ still presented better performance than global shimming for matrix MCAs. Nevertheless, as the MB factor increases to provide higher acceleration beneficial to fMRI at UHF, dynamic MB shimming and global shimming performances will likely converge. Therefore, global shimming would be preferred, as the burden of rapid current switching can be avoided.

5.3.6 In-Vivo Measurements

An adequate match between measured and simulated fieldmaps was observed, with a difference of only 1.6 Hz between expected and measured inhomogeneity (with measured inhomogeneity higher than simulated). It provided performances close to what would be achieved by a 6^{th} degree unconstrained SH system, as indicated by the SHR of 5.84. Assessment was performed only in a single subject so far, and we intend to perform further in-vivo experiments to have a more statistically significant outcome. Our match was slightly better than what was observed in [Juchem 2011] (average 2 Hz difference in global inhomogeneity across 6 subjects in dynamic shimming) and significantly better than in [Aghaeifar 2020], where the difference was 4.8 Hz (when re-scaled to 7 T) averaged across 5 subjects. We believe our improved accuracy to be the result of the careful positioning of the shimming system relatively to the characterization positioning, which resulted in an improvement also when compared to previous results with SCOTCH in a preliminary setup (cf. appendix C).

In-vivo EPI acquisitions with SCOTCH showed significant image quality enhancement in the frontal lobe relative to baseline, with some improvements also observed in the temporal lobes. Geometric distortion correction and strong signal recovery were observed, with the resulting shimmed brain image closely resembling the actual brain outline, particularly for slices closer to the dorsal part of the brain. Several artifacts were completely or partially mitigated, with an expressive amelioration in the pre-frontal cortex, where signal was improved and contrast enhanced. Considerable improvement was also observed above the ear canals. Nevertheless, despite the high shimming performance (similar to that of an unconstrained 6^{th} degree SH system), improvement is still required in the lower parts of the pre-frontal cortex and of temporal lobes. Overall, application of SCOTCH shimming brought impressive signal recovery, with contrast between gray and white matter enhanced in the frontal and temporal lobes, regions notoriously hard to shim.

5.3.7 Perspectives at 11.7T

Although experiments were performed with 3 A max current, the employed current driver is theoretically capable of driving up to 8 A as stated in the operational amplifier datasheet [TI 2005], as long as temperature rise in the OPA is limited to 125 °C. Nonetheless, as configured, static gain limits maximum current to 4 A. At 11.7 T, performance with the 3.48 SCOTCH system could be maintained equivalent to that of a 7^{th} degree SH system if electric current is allowed to increase to 5 A.

From simulations with measured fields, however, there might be a need to further increase electric current, but power dissipation might become too high. An improved inverse problem formulation was verified to provide significantly lower power dissipation at the same current constraint while marginally reducing the SHR. This method, however, requires an initial step of estimating the maximum SHR achievable under the current constraint, to subsequently compute the new currents, increasing the required time in the shimming pipeline.

Estimation of the voxel distortion map showed promising artifact mitigation at 11.7 T with 48-channel SCOTCH at 5 A, but strong geometric distortion clusters will still remain. For these ideal SCOTCH simulations, further increasing the max current to 8 A provides small improvement in homogeneity and SHR, whilst average power dissipation would rise to 161.8 W. Therefore, further improving global homogeneity might not be possible without a high performance cooling system for the shimming insert. Alternatively, if only a specific region within the brain is being targeted, optimized MCA designs to address such regions could be obtained using the presented methodology. As has been shown in chapter 4, focused shimming could improve local homogeneity under the same power dissipation level.

* * *
* *
*

General Conclusions and Perspectives

THROUGHOUT this work, we explored and proposed new methodologies for the design of shimming systems targeting B_0 homogeneity in the human brain under static whole-brain shimming.

Our exploration started with the development of the Stream-Function SVD coils, leveraging the similarity of inhomogeneous field patterns across different subjects to obtain a very small set of independently driven shim coils theoretically capable of providing high inhomogeneity reduction. Under the chosen cylindrical geometry to be placed around the human head, a simple power-regularized stream-function computation method was developed and applied on a large database of brain B_0-fieldmaps. It provided a set of Subject-Optimal Stream Functions upon which Singular Value Decomposition was applied. By selecting the first few SF-SVD modes, a limited-power (15 W average) 3-channel SF-SVD shim system was shown to provide equivalent performance to what would be achieved by an unconstrained 4^{th} degree SH shim system, which on the other hand would require 16 extra coils. Performance could be further improved as long as power dissipation or the number of SVD modes selected for composing the shim system were allowed to increase. In both cases, the shim system would become more complex: more expensive power supplies and forced cooling could become necessary in the first case, and a less compact assembly would result in the second case. We would nevertheless recommend increasing the amount of channels if performance were to be increased, since it would add extra degrees of freedom in the system, making it more robust to inter-subject variability.

The SF-SVD coils can present quite complex winding, which makes fabrication not straightforward. On the other hand, those winding patterns were shown to carry valuable information of where electric current was most demanded for shimming of the human brain. As such, we segmented the SF-SVD coils obtained from our database of brain fieldmaps into multiple independently-driven loop-like channels, thus defining a Multi-Coil Array optimized for correction of B_0 inhomogeneity in the human brain, so-called SCOTCH. A 3-Ampere constrained, 2-layer 36-channel SCOTCH is expected to achieve equivalent performance to that of unconstrained 6^{th} degree SH shim systems; further increasing the amount of channels to 48 channels over 3 layers is expected to provide comparable performance to that of 7^{th} degree SH shim systems. When compared to matrix MCAs, the

improvement in performance is also remarkable, with 3-layer 48-channel SCOTCH being comparable to a 2-layer 96-channel matrix MCA.

For cross validation, performances of SCOTCH designs were also assessed on a different fieldmap database. To cope with inter-site differences in fieldmap acquisitions, a novel evaluation metric was proposed in this work, the Spherical Harmonic Rating SHR. Although some expected loss in performance is obtained with this new unbiased database, the shimming performance of the 2-layer 36-channel SCOTCH is still maintained comparable to that of unconstrained 6^{th} degree SH shim systems, and the performance of a 3-layer 48-channel SCOTCH is in between that of a 6^{th} and 7^{th} degree SH-based shim system.

We also noticed that there is still margin for improvement of performance as long as the maximum electric current in each SCOTCH channel is allowed to increase. Also, for reported SHR performances to be maintained when moving from 7 T systems to the 11.7 T Iseult scanner, current will have to increase proportionally. The increase of currents, however, will cause large power dissipation increase, a feature that was considered throughout our analysis, and identified to be a bottleneck for shimming performance increase if no forced cooling is employed.

Given the promising shimming performance, a SCOTCH prototype was built, characterized and tested in-vivo. The characterized magnetic fields of the prototype were used in shimming simulations to assess how the real system was expected to perform relatively to its ideal model. There was, at this step, some loss of performance, as a result of deviations of the actual wire bundles from the thin single wire model considered in simulations, but realistic shimming performances were still expected to be almost as high as 6^{th} degree unconstrained SH shimming.

The few in-vivo experiments performed in this work confirmed the expected inhomogeneity reduction brought by SCOTCH. Fieldmaps showed field excursion mitigation in the pre-frontal cortex and over the ear canals. Its translation into image artifact mitigation was appreciable signal recovery in highly accelerated EPI in the pre-frontal cortex, with some apparent contrast enhancement between gray and white matter. At lower acceleration factors, considerable reduction of geometric distortion was noticed. These preliminary results were promising, and a very good match between expected and measured fieldmaps was observed. We expect SCOTCH to be particularly beneficial at 11.7 T, if not absolutely required for EPI.

Finally, we observed that there are physical limits to the mitigation of inhomogeneous magnetic field, due to the incompatibility between the location of magnetic field perturbation sources and that of correcting structures outside the human head. We showed, nevertheless, that perfect inhomogeneity mitigation could be achieved provided that the region to be shimmed can be enclosed by a sphere that does not contain any field perturbation sources. This points us towards shimming systems tailored to target specific regions of interest inside the brain. The design of such systems, in particular targeting the temporal lobes where inner ears cause strong B_0 gradients, could very well be performed with the methods exposed herein. Some preliminary work has actually been started to

this end.

* * *
* *
*

Appendices

Appendix A

In-Vivo EPI Acquisitions with SCOTCH Shimming

A collection of slices for 3D EPI (with parameters as indicated in chapter 5) acquired after SCOTCH shimming is shown in this appendix for appreciation of image quality improvement throughout a large number of slices.

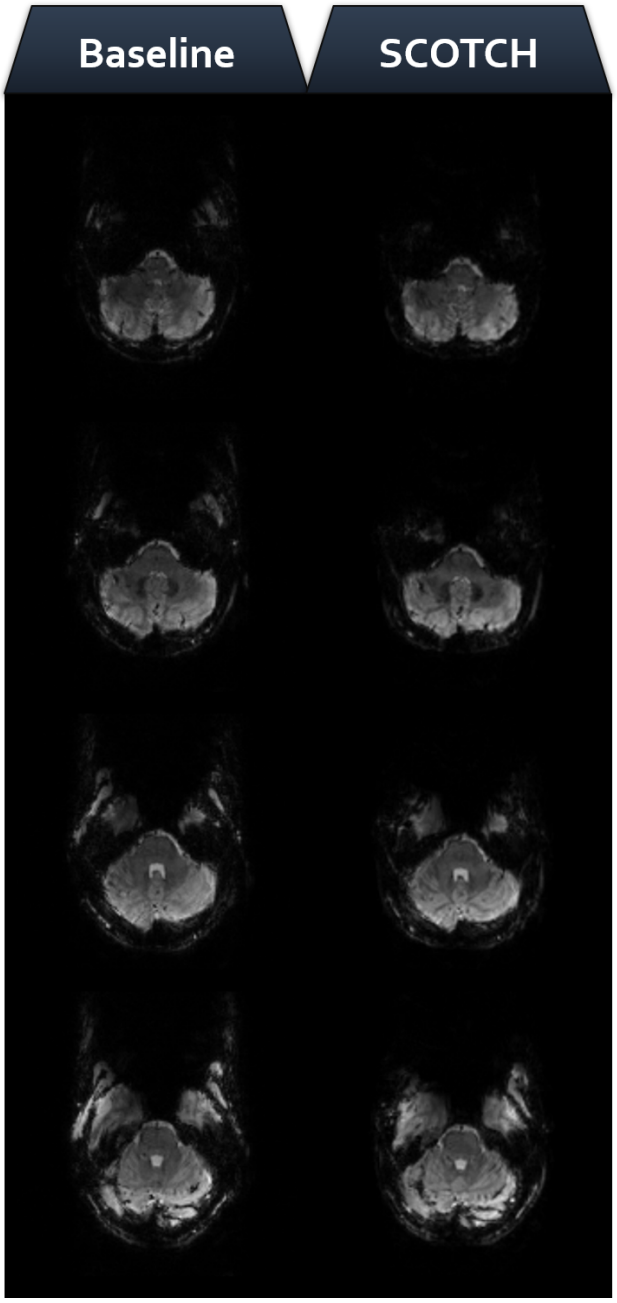

Figure A.1 – Restricted SAR EPI acquisitions after 2nd degree SH and 2.36 SCOTCH shimming. Sequence parameters were: iPAT= 4 acceleration, TE = 25 ms, 1.5 mm isotropic resolution. Part 1 of 6.

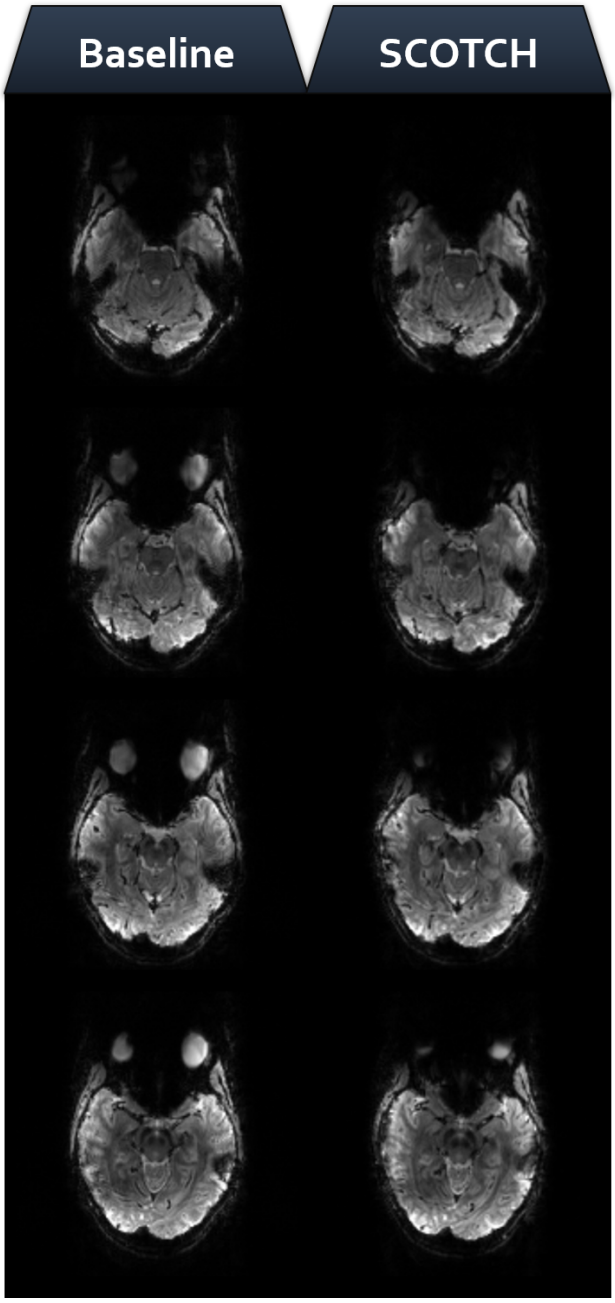

Figure A.2 – Restricted SAR EPI acquisitions after 2nd degree SH and 2.36 SCOTCH shimming. Sequence parameters were: iPAT= 4 acceleration, TE = 25 ms, 1.5 mm isotropic resolution. Part 2 of 6.

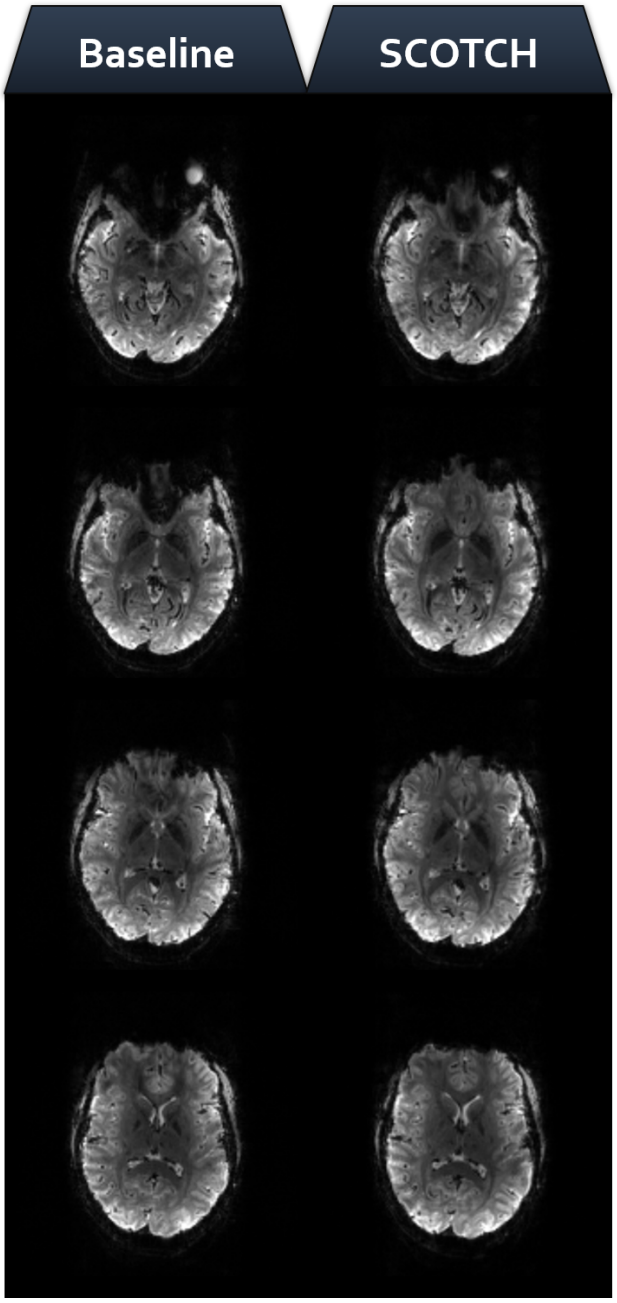

Figure A.3 – Restricted SAR EPI acquisitions after 2nd degree SH and 2.36 SCOTCH shimming. Sequence parameters were: iPAT= 4 acceleration, TE = 25 ms, 1.5 mm isotropic resolution. Part 3 of 6.

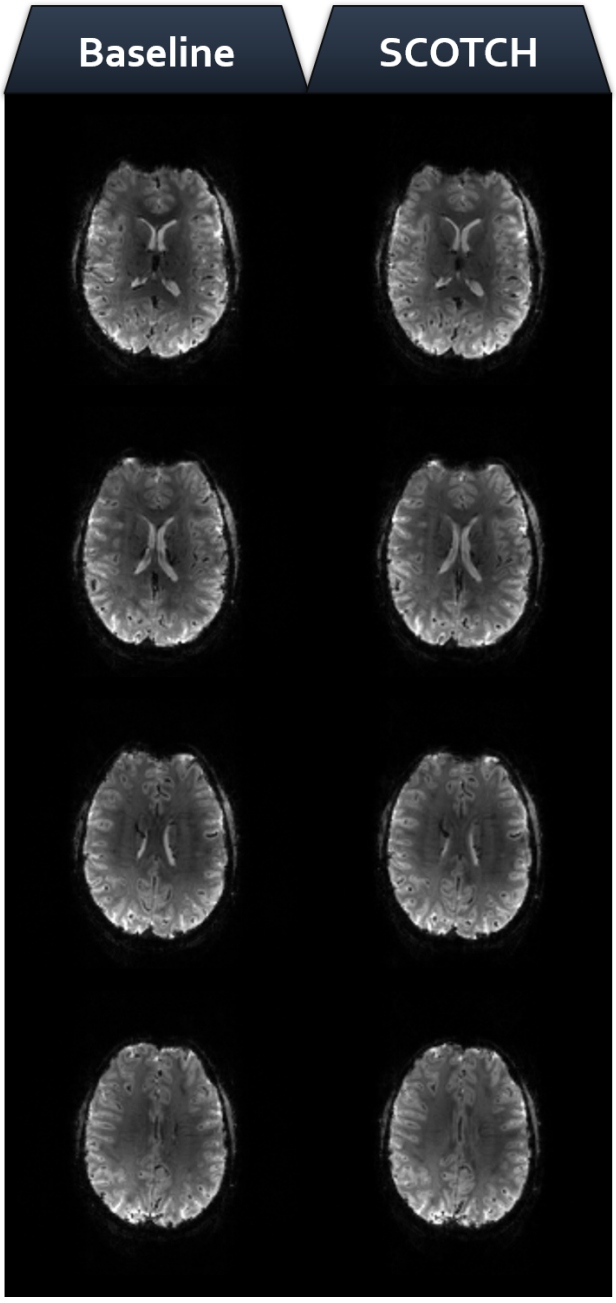

Figure A.4 – Restricted SAR EPI acquisitions after 2nd degree SH and 2.36 SCOTCH shimming. Sequence parameters were: iPAT= 4 acceleration, TE = 25 ms, 1.5 mm isotropic resolution. Part 4 of 6.

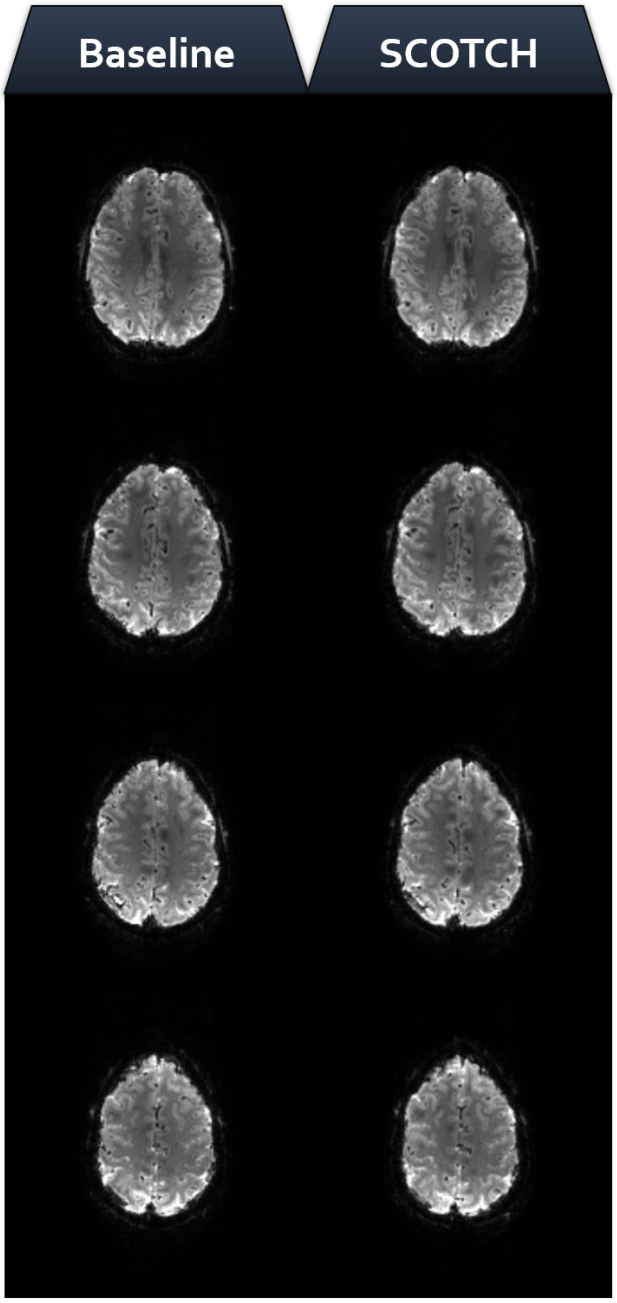

Figure A.5 – Restricted SAR EPI acquisitions after 2nd degree SH and 2.36 SCOTCH shimming. Sequence parameters were: iPAT= 4 acceleration, TE = 25 ms, 1.5 mm isotropic resolution. Part 5 of 6.

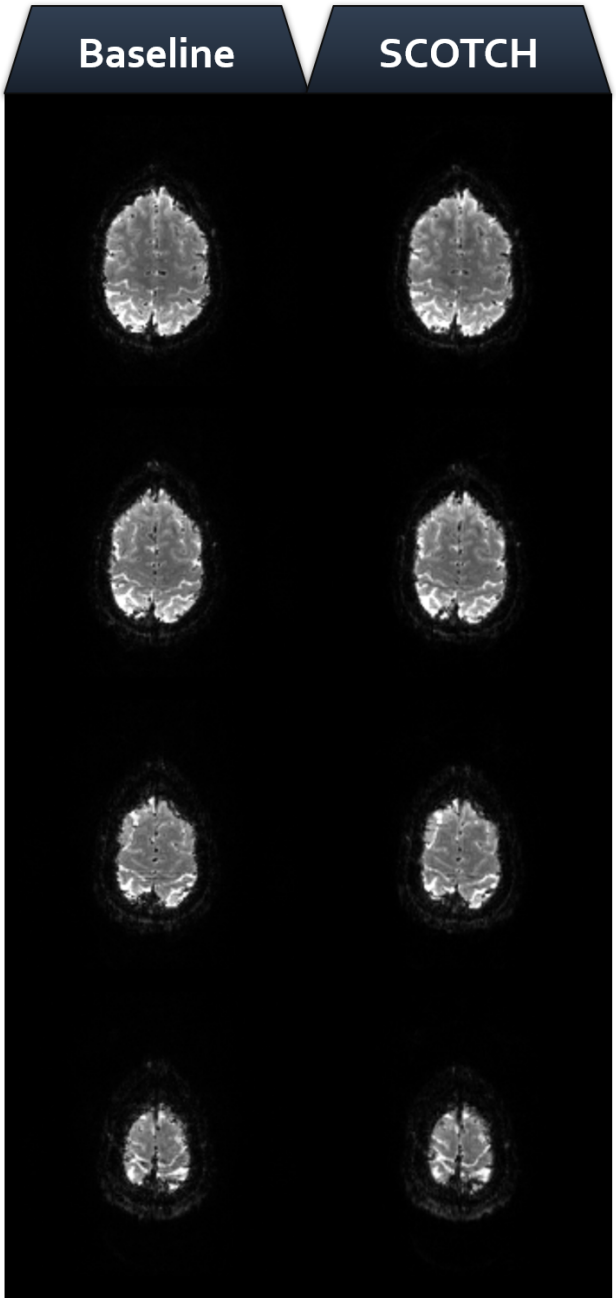

Figure A.6 – Restricted SAR EPI acquisitions after 2nd degree SH and 2.36 SCOTCH shimming. Sequence parameters were: iPAT= 4 acceleration, TE = 25 ms, 1.5 mm isotropic resolution. Part 6 of 6.

Appendix **B**

Brief Description of the Electronics and Control Aspects of the Shim Current Driver

This appendix describes the operation of the open-source shim current driver (SCD) [Arango 2016] employed in this work, also outlining a method for assessing gradient induced eddy-currents in an electronics simulation model. It assumes basic knowledge of modern control theory [Ogata 2010]. Electronics simulation are performed and adaptations of the SCD for operation at 11.7 T are proposed.

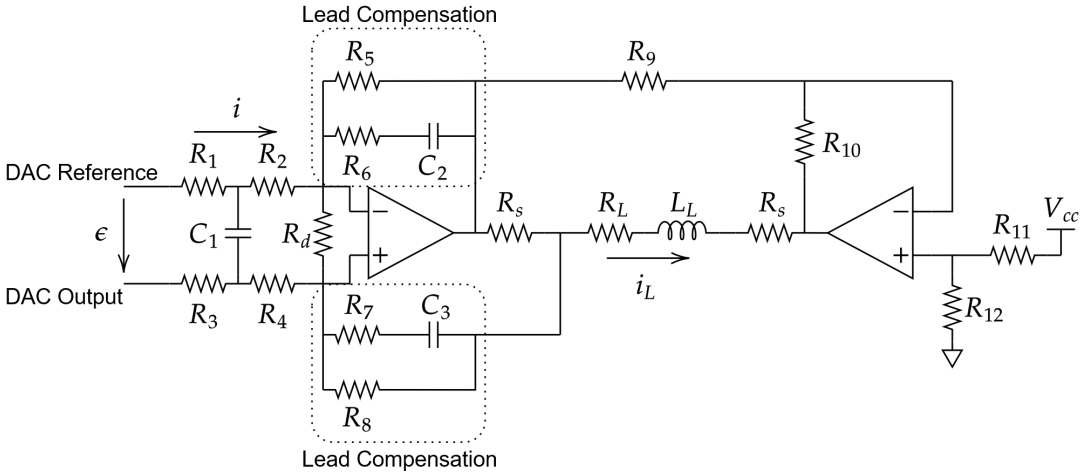

Figure B.1 – Push-pull topology of the SCD. Current setpoint depends on the input differential voltage ε, and it is kept stable due to the Lead Compensation structures whose action depends on the current across the sense resistor R_s.

Table B.1 – Components dimensioning as employed at 7 T.

Components	Value
R_1 and R_3	10 kΩ
Rd	22 kΩ
R_2 and R_4	68.1 kΩ
C_1	1 nF
C_2 and C_3	100 pF
R_5 and R_8	51.1 kΩ
R_6 and R_7	5.1 kΩ
R_9 and R_{10}	2 kΩ
R_{11} and R_{12}	2 kΩ
R_s	0.2 Ω
Amplifier	OPA549

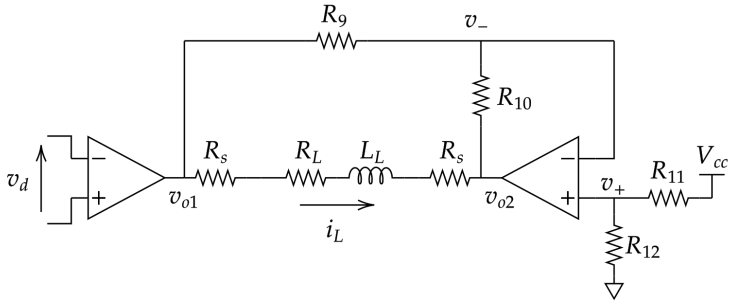

Figure B.2 – Push-pull topology without feedback control.

B.1 Theoretical Model

Electric current driving and stabilization for the shim coils is achieved using an open-source feedback-controlled push-pull topology [Arango 2016], as shown in Fig. B.1. It achieves load current stabilization and disturbance rejection, counteracting on gradient induced eddy-currents, due to a Lead Compensation structure, providing load current feedback for actuation of the operational amplifiers, implemented using an OPA549 [TI 2005] linear amplifier.

The dimensioning of the circuit as employed at 7 T, where current was constrained to 3 A, is as shown in table B.1.

We can start understanding its behavior by looking at the actuator block (cf. Fig. B.2).

By controlling v_d, the output current of the system can be controlled. Resistors R_{11} and R_{12} being of same value will make $v_+ = V_{cc}/2$, which in turn implies $v_- = V_{cc}/2$. Resistors R_9 and R_{10} are also of equal value, leading to a same voltage drop Δv across each of them. Therefore

$$v_{o1} = \frac{V_{cc}}{2} + \Delta v, \tag{B.1}$$

$$v_{o2} = \frac{V_{cc}}{2} - \Delta v \tag{B.2}$$

and

$$v_{o1} - v_{o2} = 2\Delta v. \tag{B.3}$$

If v_d is set such that $v_{o1} < V_{cc}/2$, then $\Delta v < 0$ and the current will flow from v_{o2} to v_{o1}. It will flow on the opposite direction if $v_{o1} > V_{cc}/2$. This provides a bi-directional current flow without the need for a bipolar voltage supply.

However, operational amplifiers have very high gain, and the actuator will be unstable without a negative feedback-loop.

The feedback loop is accomplished by connecting the compensating structure as shown in Fig. B.1. In this new structure, the voltage v_d will be influenced by the voltage $R_s i_L$ across the sense resistor, and if the resistors and capacitors are adequately dimensioned the system will be stable.

B.1.1 Load Impedance Measurement

Stability and the ideal dimensioning will depend on the load characteristics. Therefore, resistance and inductance of each channel of the two first SCOTCH layers were measured. Resistances are mainly dominated by cable resistances, resulting in a 509.9 mΩ average and within the interval $[438.6, 614.6]$ mΩ. Measured inductances showed 47.3 µH in average, within the interval $[23.2, 75.6]$ µH.

B.1.2 Frequency Analysis

We can evaluate the behavior of the system in the frequency domain, which is performed considering signal variations around the bias point. As such, system stability can be evaluated from the frequency response of the open-loop transfer function of the compensated system.

The Laplace transform variable is denoted $s \in \mathbb{C}$ in the following expressions.

Usual stability criteria require a phase margin (the difference between the phase at crossover frequency and 180°) within 30° to 60°. For the SCOTCH loads, without compensation, the transfer function $H_{OP}(s)H_{os}(s)$ shows average phase margin of $-1.3°$ across all channels, with $H_{OP}(s)$ the OPA549 operational amplifier transfer function, and

$$H_{os}(s) = \frac{2}{2R_s + Z_L}, \tag{B.4}$$

and $Z_L = R_L + sL_L$. This is clearly unstable, and the lead compensator makes itself necessary.

We now need to obtain the transfer function of the SCD. Around a bias point, $v_{o1} = \Delta v$ and $v_{o2} = -\Delta v$. Therefore, the load current is

$$i_L = H_{os}(s)\Delta v, \tag{B.5}$$

with

$$\Delta v = -H_{OP}(s)v_d. \tag{B.6}$$

Let the voltage difference between DAC Output and DAC Reference be ε and, neglecting the effect of C_1, the following equations can be assembled

$$-\varepsilon = 2R_{in}i + v_d \tag{B.7}$$

$$v_d = 2Z_c\left(i - \frac{v_d}{R_d}\right) + R_s i_L \tag{B.8}$$

where $R_{in} = R_1 + R_2$ (with $R_3 = R_1$ and $R_2 = R_4$) and

$$Z_c = \frac{R_5(sR_6C_2 + 1)}{s(R_5 + R_6)C_2 + 1}. \tag{B.9}$$

Expressions B.7 and B.8 lead to

$$v_d = \left(-\varepsilon + \frac{R_{in}R_s}{Z_c}i_L\right)\left(\frac{R_dZ_c}{R_dZ_c + R_{in}(R_d + 2Z_c)}\right). \tag{B.10}$$

Define

$$\beta(s) = \frac{R_{in}R_s}{Z_c} \tag{B.11}$$

and

$$\mu(s) = \frac{R_dZ_c}{R_dZ_c + Z_{in}(R_d + 2Z_c)}, \tag{B.12}$$

then

$$\mu(s)\beta(s) = K\frac{sT + 1}{s\alpha T + 1}, \tag{B.13}$$

which is the characteristic transfer function of a lead compensator, with

$$T = (R_5 + R_6)C_2 \tag{B.14}$$

$$\alpha T = \frac{R_5R_6(R_d + R_{in}) + R_{in}R_d(R_5 + R_6)}{R_5(R_d + 2R_{in}) + R_{in}R_d}C_2 \tag{B.15}$$

and

$$K = \frac{R_{in}R_5R_d}{R_5(R_d + R_{in}) + R_{in}R_d}. \tag{B.16}$$

The resistances in the circuit should then be adjusted to provide a desired crossover frequency for defining speed, and a phase-margin for reduced overshooting. Its transfer function is shown in Fig. B.3, and we observe that it should be able to increase the phase-margin from the $-1.3°$ average, stabilizing the SCD.

Combining equations B.6 and B.10, the transfer function of the system is given by

$$\frac{i_L(s)}{\varepsilon(s)} = \frac{\mu(s)H_{OP}(s)H_{os}(s)}{1 + \beta(s)\mu(s)H_{OP}(s)H_{os}(s)}, \tag{B.17}$$

and is represented by the block diagram in Fig. B.4.

In the steady-state, since $|H_{OP}(0)| \to \infty$, the static voltage to current gain is

$$\frac{i_L}{\varepsilon} = \frac{1}{\beta(0)} = \frac{1}{R_s}\frac{R_5}{R_1 + R_2}. \tag{B.18}$$

The static gain requirement depends on the target max current and limitations of the input differential voltage (DAC Output to DAC Reference). The Digital to Analog

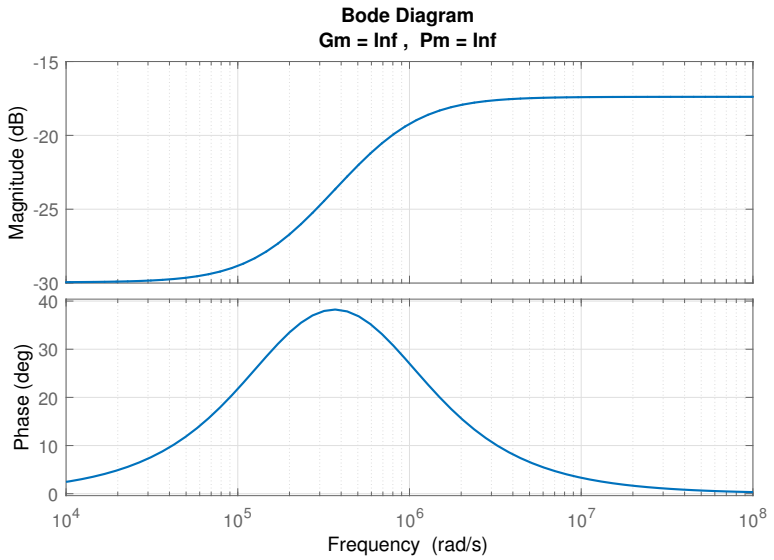

Figure B.3 – Bode diagram of the Lead Compensator dimensioned according to table B.1.

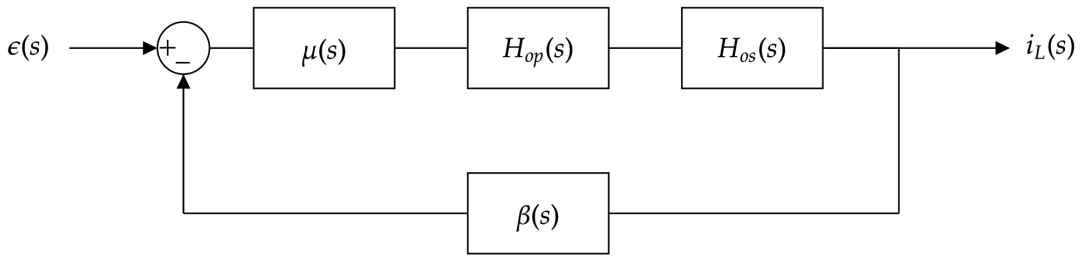

Figure B.4 – Block-diagram of the shim current driver.

Converter used to provide the DAC Reference and DAC Output signals, the LTC2656-L [LT 2009], can provide output voltages up to 2.5 V, while its reference voltage is 1.25 V. This bounds ε to $[-1.25, 1.25]$. Under the current configuration, the static gain is equal to 3.27, providing max current of approximately 4.1 A.

Stability analysis of the system can be performed by evaluation of the Bode plot of the open loop transfer function

$$H_{\text{open}}(s) = \beta(s)\mu(s)H_{OP}(s)H_{os}(s). \tag{B.19}$$

The Bode diagrams of H_{open} for all SCOTCH channels were plotted, as well as the closed-loop step response, leading to the curves shown in Figs. B.5 and B.6.

Simulations showed phase-margin to be within 27.4° and 41.9°, with an average 33.1°. The effect of these relatively low phase-margins can be seen in Fig. B.6. There is considerable overshoot and ringing, which could contribute to vibration due to Lorentz forces and should preferably be avoided, specially at 11.7 T. A different dimensioning will be proposed in section B.2.3.

System speed depends on the crossover frequency of $H_{\text{open}}(s)$. Which was verified to be within $0.83 \times 10^5\,\text{rads}^{-1}$ and $1.63 \times 10^5\,\text{rads}^{-1}$, with $1.11 \times 10^5\,\text{rads}^{-1}$ average. Step

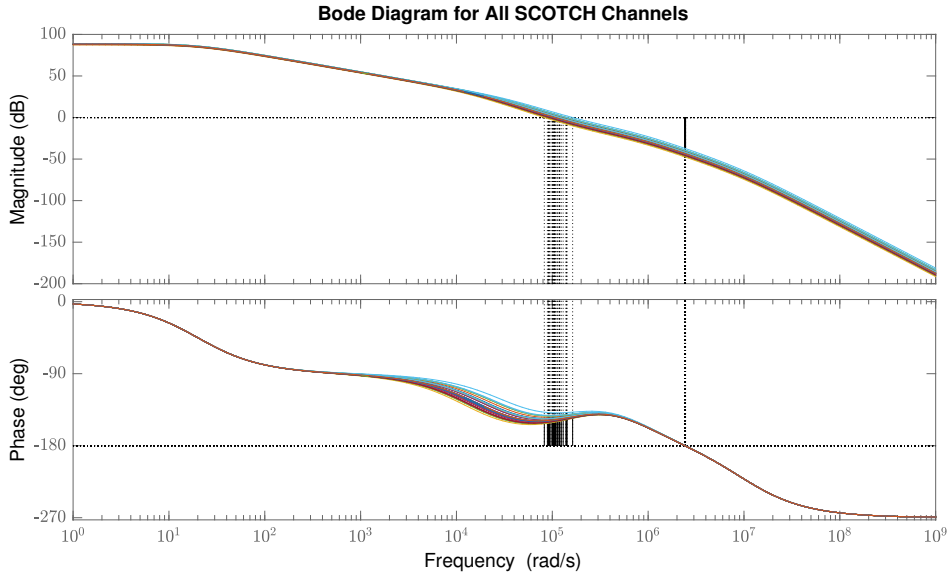

(a)

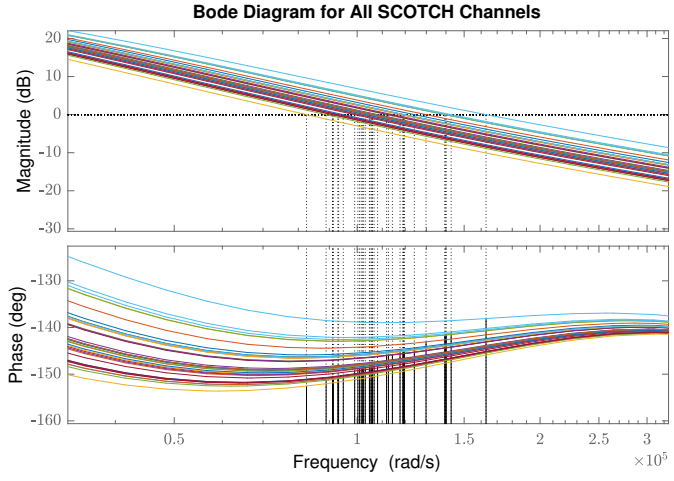

(b)

Figure B.5 – Superimposed bode diagrams for the open-loop transfer function H_{open} for the different SCOTCH channels, with a zoomed view in (b).

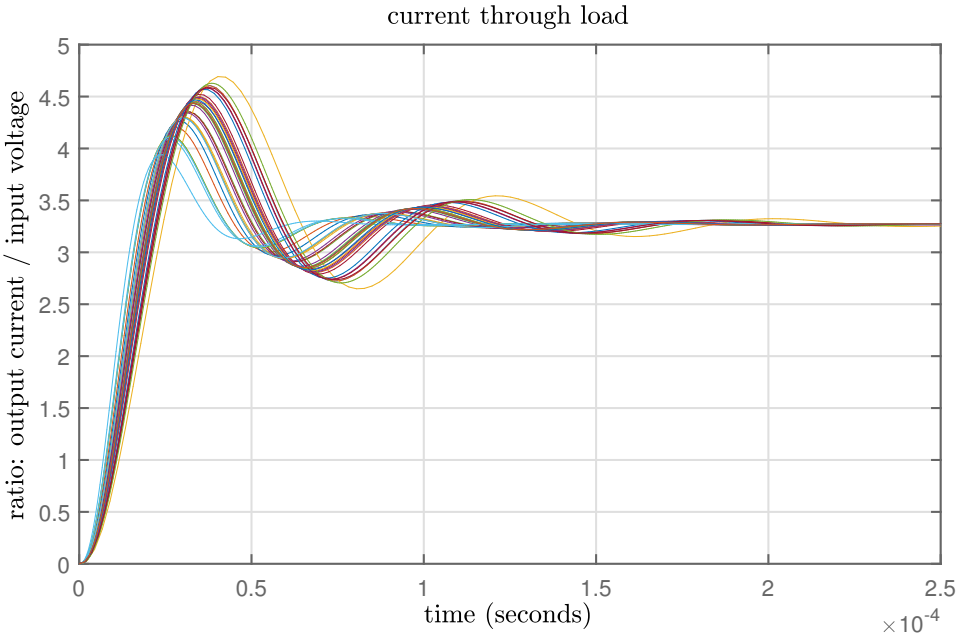

Figure B.6 – Ideal step response of the shim current driver for the different SCOTCH channels.

response simulation showed 40.3 µs and 23.4 µs for max and min times to reach the overshoot peak. Therefore, the currents can rise quickly, but we can see that, due to ringing, they are settled only after 200 µs (when the currents are within ±2 % of their setpoint). This is nonetheless a fast settling time, which is not a crucial factor for static shimming, but is important to be kept at low values for fast switching in dynamic shimming in order to not compromise acquisition time.

B.2 Electronics Simulations

To verify the behavior of the current driver under more realistic conditions, an electronics simulation software, LTSpice, was employed. A high-level model of the OPA549 can be used for precise assessment, and non-linear effects such as voltage saturation due to limited power supply voltage can be observed.

B.2.1 Modeling Gradient Interactions

It is straightforward to evaluate gradient induced eddy-currents in the SCOTCH coils within an electronics simulation environment.

Circuit Model

For modeling the gradient coil, a series RL circuit is employed with 135 mΩ and 820 µH. A z-gradient coil is assumed, as it simplifies the estimation of the magnetic field in the ρ-direction, which is the field component generating a magnetic induction flux in the

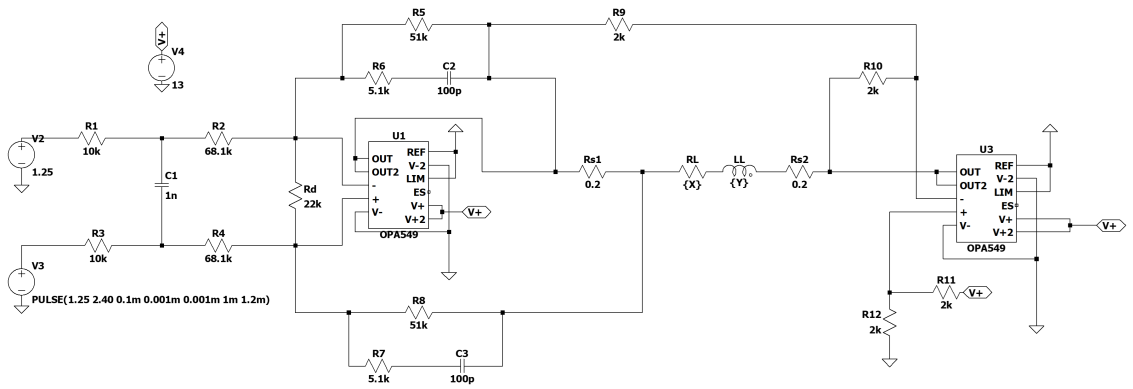

Figure B.7 – Electronics model employed in LTSpice simulations.

SCOTCH coils. Gradient sensitivity S_g is $0.112\,\mathrm{mTm^{-1}A^{-1}}$, and max slew-rate $SR_{\max}$ is $200\,\mathrm{Tm^{-1}s^{-1}}$. Disregarding the voltage drop in the gradient resistance, the required voltage from the Gradient Power Amplifier (GPA) to achieve some slew-rate is

$$V_{GPA} = \frac{L_g \mathrm{SR}}{S_g}. \tag{B.20}$$

The gradient inductance and MCA channel inductance are then coupled through an LTSpice directive taking into account their inductance values and a coupling factor, which needs to be estimated. Then, applying the required voltage, interactions between the coils can be assessed for different slew-rate values.

Coupling Factor

The coupling factor is defined as

$$k = \frac{M}{\sqrt{L_L L_g}} \tag{B.21}$$

with M the mutual inductance and L_L and L_g the self-inductance values for an MCA coil and the gradient coil, respectively.

The magnetic flux in a SCOTCH winding generated by the gradient is

$$\Phi_{Lg} = M i_g. \tag{B.22}$$

Also,

$$\Phi_{Lg} = N \int_{\mathcal{S}_c} \boldsymbol{B}_g(\boldsymbol{x}) d\boldsymbol{a}, \tag{B.23}$$

with N the number of turns of the shim coil. With the coil laid on a cylindrical surface, we have

$$k = \frac{N \int_{\mathcal{S}_c} B_\rho(\boldsymbol{x}) a d\varphi dz}{i_g \sqrt{L_L L_g}}, \tag{B.24}$$

where a is the radius of the cylindrical coil former. We will assume it is fixed at $a = 140.5\,\mathrm{mm}$ for simplicity. The magnetic field in the ρ-direction is therefore necessary for the coupling factor estimation.

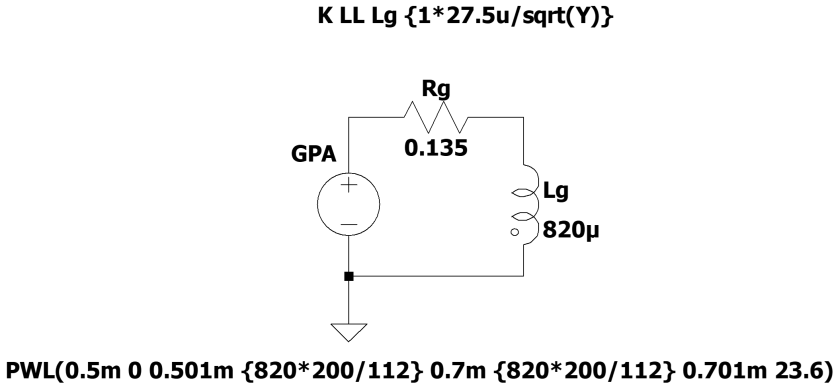

Figure B.8 – Series RL gradient model and directive for inductance coupling in LTSpice.

Since $\boldsymbol{\nabla} \cdot \boldsymbol{B} = 0$, we obtain

$$B_\rho(\boldsymbol{x}) = -\frac{G_z}{2}\rho \tag{B.25}$$

for some gradient intensity G_z in the z-direction.

Back to equation B.24, we obtain

$$k = -\frac{NA_cS_ga}{2\sqrt{L_LL_g}} \tag{B.26}$$

with A_c the area enclosed by the channel winding on the cylindrical surface which will be approximated by that of a 4 cm radius circle for simplicity. With $N = 20$ we obtain

$$k = -\frac{27.5 \times 10^{-6}}{\sqrt{L_L}}. \tag{B.27}$$

This expression is used in the LTSpice simulation, therefore being computed for each different inductance.

The resulting electronic simulation model is shown in Fig. B.8.

B.2.2 Simulations at 7 T

The circuit is initially simulated with the OPA549 outputs short-circuited to assess the gradient induced current intensities in the load. Resulting voltage and current waveforms for all loads with the gradient at max slew-rate ($200\,\mathrm{Tm^{-1}s^{-1}}$) during a 200 µs duration (enough to reach $40\,\mathrm{mTm^{-1}}$) are shown in Fig. B.9. Voltage was measured across the shim coil inductance terminals.

The gradient is switched-on at 0.5 ms, an induced voltage close to 1.4 V is observed. The eddy currents are seen to reach values as high as 1.6 A. After gradient current stabilization, induced currents and voltages start dropping to zero, but they are relatively long lived, dropping to zero only after a 200 µs interval. This is equivalent to one third of the inter-echo spacing in a common EPI sequence, and could produce ghosting artifacts, as well as degrade the B_0 shimming quality.

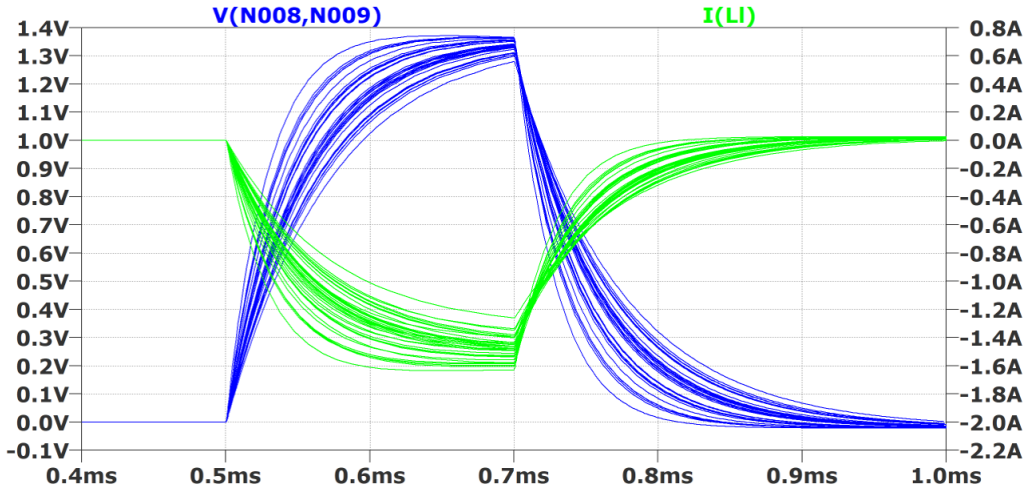

Figure B.9 – Simulation of gradient induced voltage and currents in the SCOTCH channels without active compensation.

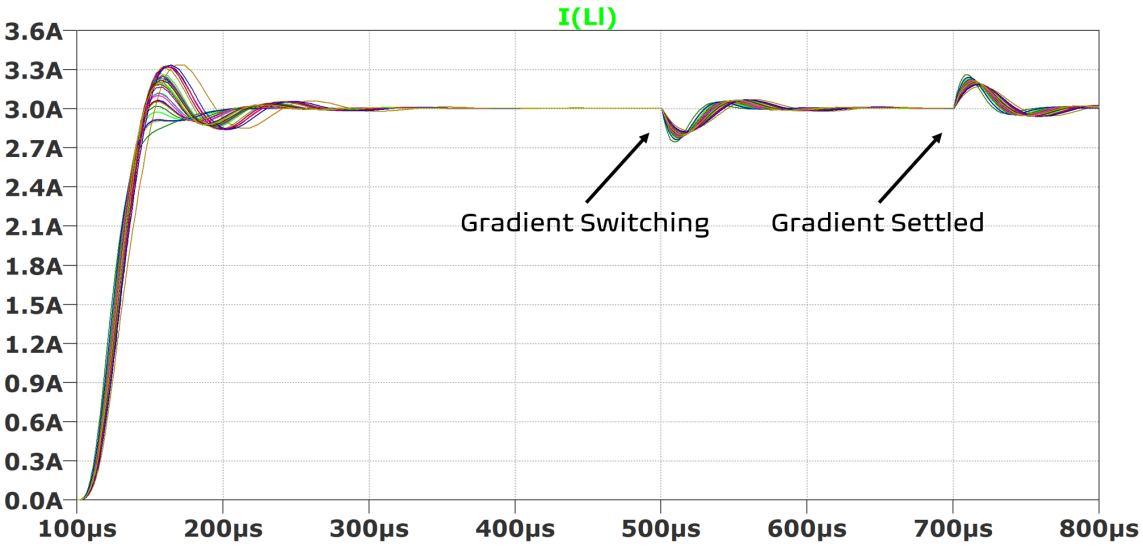

Figure B.10 – Electronics simulation of the SCD showing transient behavior and eddy-current compensation.

We see that active compensation of the eddy-currents is required. Simulation of the active current driver targeting 3 A is then performed, providing the current waveforms shown in B.10. Power supply voltage for the operational amplifiers was 13 V. We observe a fast rise time and ringing of the currents as expected from ideal simulations step-response analysis. After 200 µs there is less than 1 % deviation from the setpoint, and we can safely say the current is stabilized.

As the gradient is switched-on at maximum slew-rate we can see an the electric current disturbance of maximum intensity close to 250 mA, thus a 82.1 % reduction compared to when no active compensation is present. The currents return to stability within 100 µs.

We can verify that the current settling time is adequate for dynamic shimming applications. Assuming a 2D acquisition of 160 axial slices with 1 mm thickness providing full brain coverage, for EPI acquisitions, an extra 32 ms would be added to the sequence dur-

ation, which is a short increase. Even considering slower acquisition sequences, for a GRE with 240 phase-encoding lines being acquired, total extra duration would be 7.7 s, a very short addition compared to usual duration of a few minutes for most common sequences.

B.2.3 Adapted Dimensioning for the Iseult Scanner

Although we verified fast rise times and eddy current compensation at 7 T with the electric current constrained to 3 A, the present static gain of the circuit does not allow the current to rise to 5 A. And, as pointed out in section 5.3.7, if shimming performances, when compared to SH systems, are to be kept the same when employing SCOTCH for shimming at 11.7 T, the max electric current supply should be able to reach this value. Moreover, considerable ringing was observed, and a smoother curve could be envisioned, which should be attainable by changing the values of capacitors C_2 and C_3. This smoother current rise would help reduce mechanical vibration and noise caused by electric current switching.

Static Gain

Under the max differential input voltage of 1.25 V, a static gain of at least 4.16 A/V is required. Therefore

$$\frac{R_5}{R_1 + R_2} = 0.832, \tag{B.28}$$

leading to two simple options to obtain this ratio:

- R_5 is kept fixed, leading to $R_1 + R_2 = 61.4\,\text{k}\Omega$, which cannot be achieved by changing R_1, but will be obtained if $R_2 = 51.4\,\text{k}\Omega$, or, to provide some margin and considering a commercial resistance value, $R_2 = 46\,\Omega$;
- R_1 and R_2 are kept fixed, and R_5 needs to be increased to 65.0 kΩ, or, to account for a commercial value, $R_5 = 68.1\,\text{k}\Omega$.

In the subsequent simulations, we will change R_5 to 68 kΩ, resulting in a static-gain of $4.36\,\text{AV}^{-1}$.

Smoother Current Rise

As mentioned, it might be prudent to change the C_2 capacitor value in order to slow down current switching. Although fast switching is important for performing dynamic shimming and to reject gradient induced perturbations, a slower rise-time might be beneficial at 11.7 T to limit mechanical vibrations in the stronger magnetic field. Indeed, the ratio of Lorentz forces at 11.7 T to that at 7 T will be 2.8, the square of the magnetic field ratio ($(11.7/7)^2$), due to increase of the field itself and of the max current. At 7 T, volunteers in preliminary dynamic shimming experiments didn't report any extra discomfort or noise related to the current switching. Similar experiments will need to be carried out at 11.7 T in order to assess the need for changing this capacitance.

We observed that by changing C_2 and C_3 to 390 pF, the phase margin increased to 41.5° in average, and is within a 34.2° to 46.8° range. This is expected to provide more

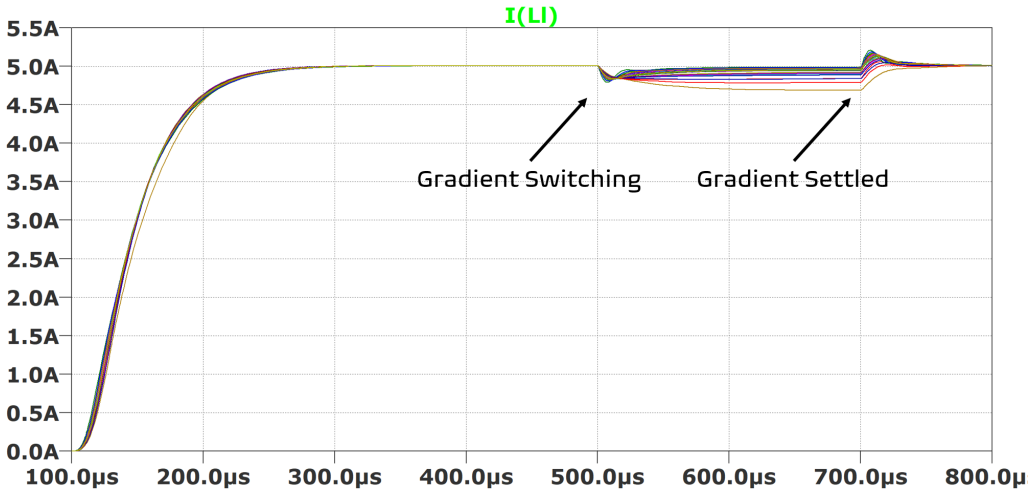

(a)

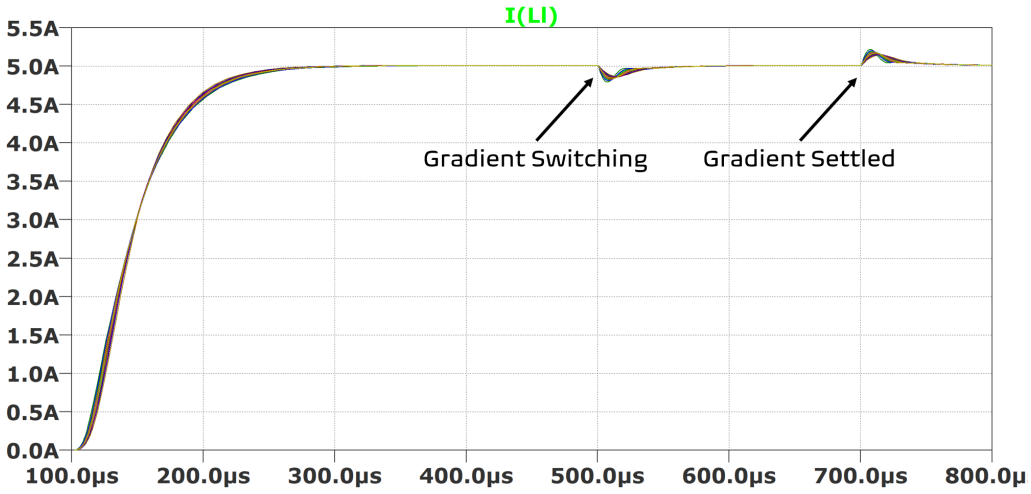

(b)

Figure B.11 – Electronics simulation of the SCD showing transient behavior and eddy-current compensation with optimized dimensioning for use at 11.7 T. Simulations were performed with (a) 13 V power supply and (b) 24 V power supply.

stability, and as we will see in the electronics simulations, it provides robustness to the range of loads employed.

Electronics simulations with the new dimensioning were performed. As shown in Fig. B.11a, a smoother rise time was obtained and the electric current reaches the desired setpoint of 5 A. However, gradient induced eddy-currents could not be compensated.

Increasing the Power Supply Voltage

It was observed that the gradient induced eddy-currents were not properly compensated at 5 A due to not enough voltage provided by the power supply. Therefore, power supply voltage had to be raised to 24 V (to consider common commercial values), and gradient induced perturbations were effectively compensated, as shown in Fig. 5.19b.

Under this new condition, the new component dimensioning not only provide the

desired smoother current rise, but robustness to the different channel loads is apparent. An interval of 200 µs is observed to be enough for the currents to reach their setpoints, therefore maintaining the fast switching when compared to the current dimensioning.

B.3 Final Remarks

The fast current switching and disturbance rejection provided by the current driver were observed in the simulations when considering the system dimensioning that has been employed for the experiments described in this thesis. The step response of the SCD drive was not optimal for our loads, as inferred from the overshot and ringing observed. This sub-optimallity, however, did not prevent us from performing the experiments described throughout the thesis, and the absence of artifacts in the acquired images and adequate quantitative match in the fieldmaps is a somewhat indirect proof of the expected stable behavior of the SCD.

For use at 11.7 T, where electric current should be allowed to increase to 5 A, a new dimensioning was proposed. Current rise will be smoother, while still fast. To ensure disturbance rejection, it was observed that power supply voltage should be increased. Under these modifications, the shim system should provide adequate performances for use at 11.7 T.

Appendix C

Shim Coils Tailored for Correction of B0 Inhomogeneity in the Human Brain (SCOTCH) at Ultra High Field

The methods and principles contained in this appendix were accepted for presentation at an international conferences as:

B. Pinho Meneses, J. Stockmann, E. Chazel, E. Giacomini, P.-F. Gapais, F. Mauconduit, M. Luong, A. Vignaud and A. Amadon. *Shim Coils Tailored for Correction of B0 Inhomogeneity in the Human Brain (SCOTCH) at Ultra High Field.* In Proceedings of the 29th Annual Meeting of the International Society for Magnetic Resonance in Medicine, Virtual Conference, 2021.

C.1 Introduction

Susceptibility-induced static-field inhomogeneity in the human brain becomes stronger with the main B0 field. As MRI scanners move to Ultra-High Fields (UHF) of 10.5T, 11.7T [Quettier 2020] and more, 2nd/3rd order Spherical Harmonic (SH) shim systems commonly available in commercial scanner are insufficient to provide artifact-less high-resolution acquisitions, especially in Echo Planar Imaging (EPI).

To push the boundaries of B0 shimming at UHF, we have proposed a new method for Multi-Coil Array optimization based on Singular Value Decomposition (SVD) of Stream Functions (SF) [Meneses 2019c, Pinho Meneses 2020d, Pinho Meneses 2020e]. Optimized channel geometry and placement over a cylindrical surface are obtained, delivering higher performance than conventional matrix MCAs (M-MCAs) with reduced channel count.

A 13-channel prototype was recently presented [Pinho Meneses 2020e] and expected system performance was assessed from measured fields, providing satisfying match to estimations from ideal, simulated fields. In this work, we present an improved optimized

MCA prototype, denominated SCOTCH, consisting on 2 layers and 36 channels. The prototype was characterized, shimming simulations using measured fields were performed on two different fieldmap databases for cross validation, and finally, in-vivo acquisition was performed for quantitative and qualitative assessment.

C.2 Methods

An in-house 100-subject δB_0 brain fieldmap database4, scaled to 7T, was employed for the SVD-based MCA design, optimized for global (whole-brain) shimming. Cylinders of 140.5-mm and 149.0-mm radii, and 300-mm length, were used as coil formers in the optimization, centered at the MRI isocenter. A 2-layer 36-channel design is obtained (Fig. C.1). Expected inhomogeneity mitigation of the designed system was simulated on the in-house database and on an open-access database [Elshatlawy 2019] for cross-validation. Coils are assumed to have 20 turns.

For construction of the prototype, 3D printed molds were used to wind each coil to 20 turns. These are placed onto the corresponding fiberglass cylindrical surface (Fig. C.1b) and coated with epoxy resin. An open-source multi-channel current driver [Arango 2016] is used for electric current control of individual channels.

System characterization was performed with fieldmap measurement of each channel/coil at 1A in a large oil phantom. After characterization, expected shimming performance was assessed by inputting the measured fields per unit current as shimming basis for computational global shimming of both design and cross-validation database.

Two M-MCAs of 24 and 48 twenty-turn circular loop channels over cylindrical formers of identical dimensions to SCOTCH's first layer are also simulated for comparison (Fig. C.1c).

Finally, an in-vivo acquisition with SCOTCH shimming was performed in a 7T Siemens MAGNETOM using a simplified single-loop Tx/Rx RF setup (Fig. C.2), as the in-house 8Tx/32Rx RF coil to be used with SCOTCH is still in fabrication. To accelerate Internal Review Board authorization for the experiment, Restricted SAR [Vignaud 2018] (rS) sequences were employed. A triple-echo 3D rS-GRE was used for field mapping and brain masking, required for optimal channel current calculation; and a 2D rS-EPI was employed for qualitative assessment of artifact mitigation. EPIs under global (static) and slice-wise (dynamic) shimming were acquired, with optimal currents for the 36 channels computed from a 2nd-order SH-shimmed baseline fieldmap (obtained after brain masking and re-shimming). Due to the simplified RF setup, no acceleration was possible in the EPI acquisitions, rendering it very sensitive to B0 field inhomogeneity.

Current amplitude is constrained to 3A per channel in all shimming simulations and in-vivo experiment.

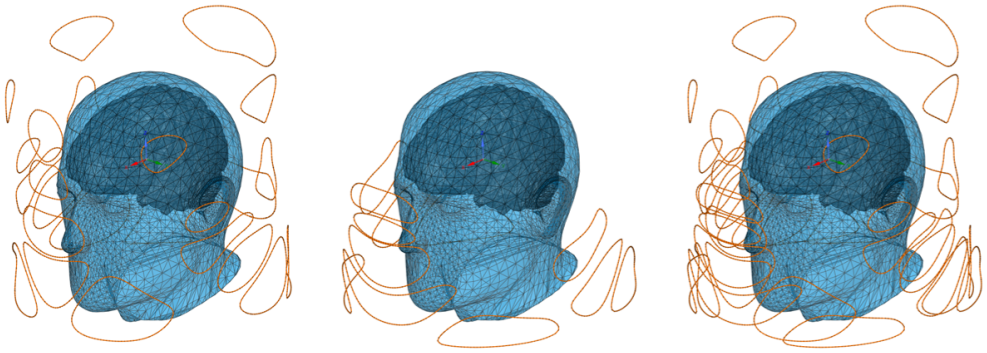

(a)

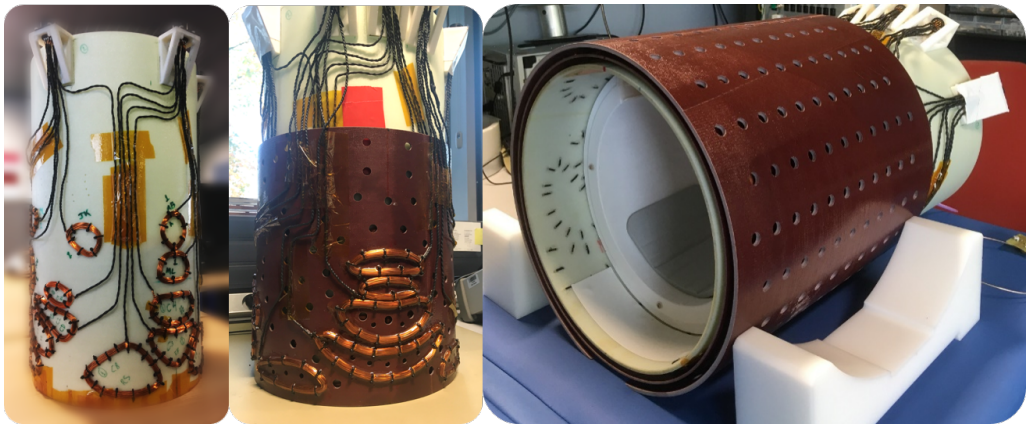

(b)

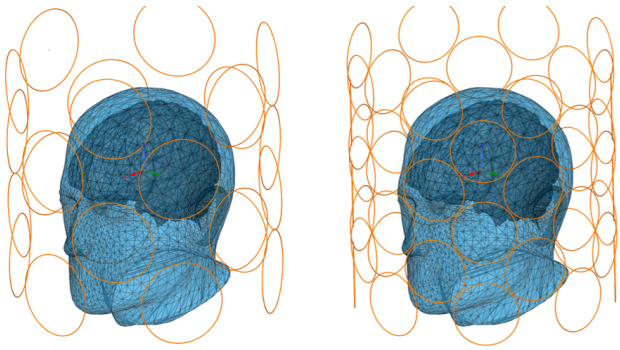

(c)

Figure C.1 – (a) Ideal channel disposition for first and second layers, both layers resulting from the SVD-based MCA optimization; and ideal 2-layer 36-channel system. (b) The two prototype layers and the assembled shimming system with RF housing at the interior of the shim layers. (c) Simulation models of generic 24-ch and 48-ch M-MCA used for comparison. Circular coil radii are 4.5-cm and 3.5-cm, respectively.

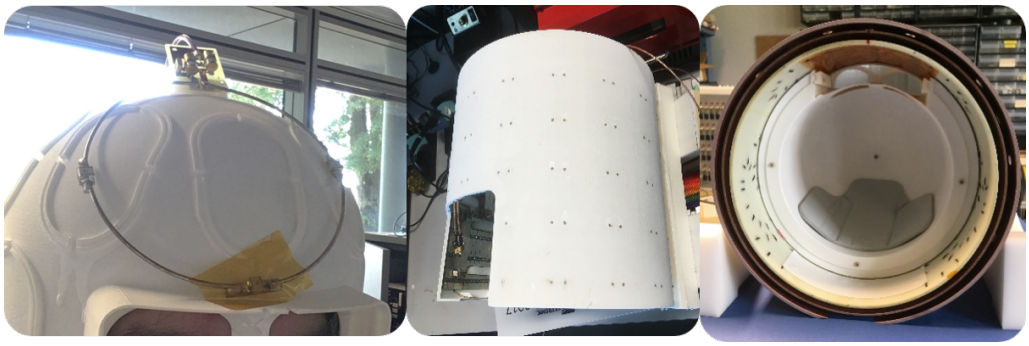

Figure C.2 – Single-loop transmit/receive simplified RF setup used for acquisitions. This loop was used in-vivo in restricted SAR mode, i.e. time-averaged transmit power was limited to 0.1 W, lengthening all MRI sequences.

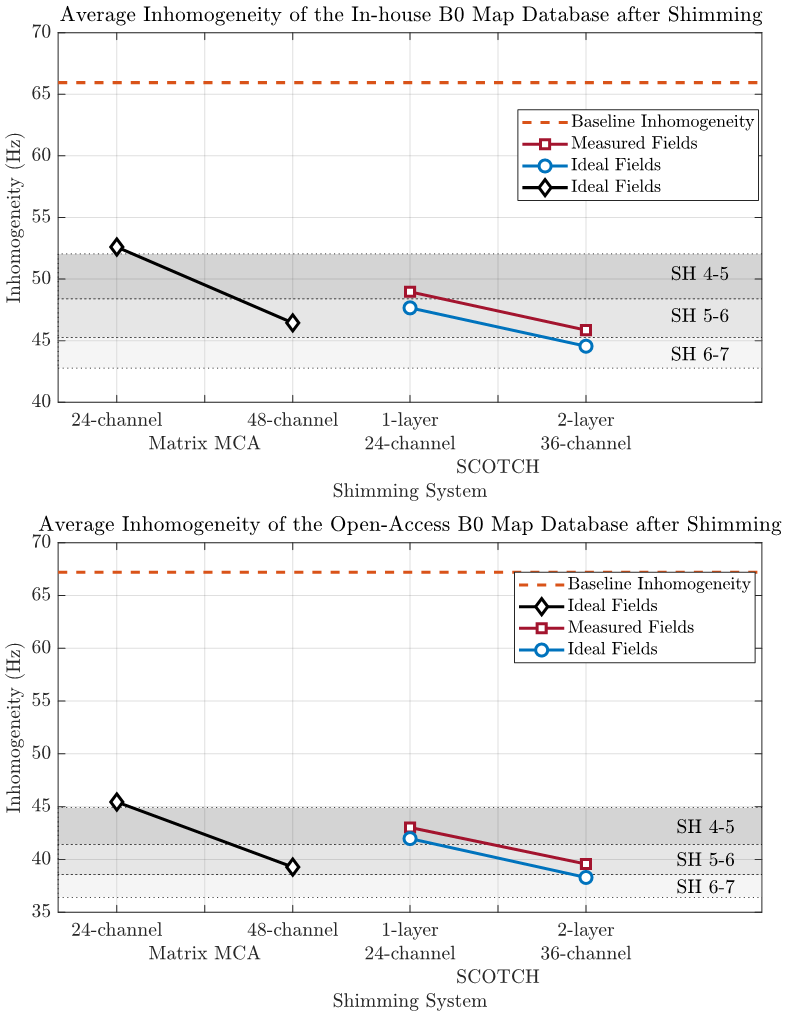

Figure C.3 – Global shimming simulation results for different shim systems over the 100-brain in-house database and 126-fieldmap open-access database, used for cross-validation. Baseline composed of 2nd-order SH shimmed fieldmaps (65.7 Hz and 67.2 Hz average inhomogeneity for in-house and open-access, respectively). Global inhomogeneity is the B0 standard deviation across brain voxels. The calibration SCOTCH fieldmaps measured on a phantom are used to computationally shim the brain databases, and results are compared to the expected SCOTCH performance evaluated a priori using simulated fieldmaps, as well as to simulated M-MCAs.

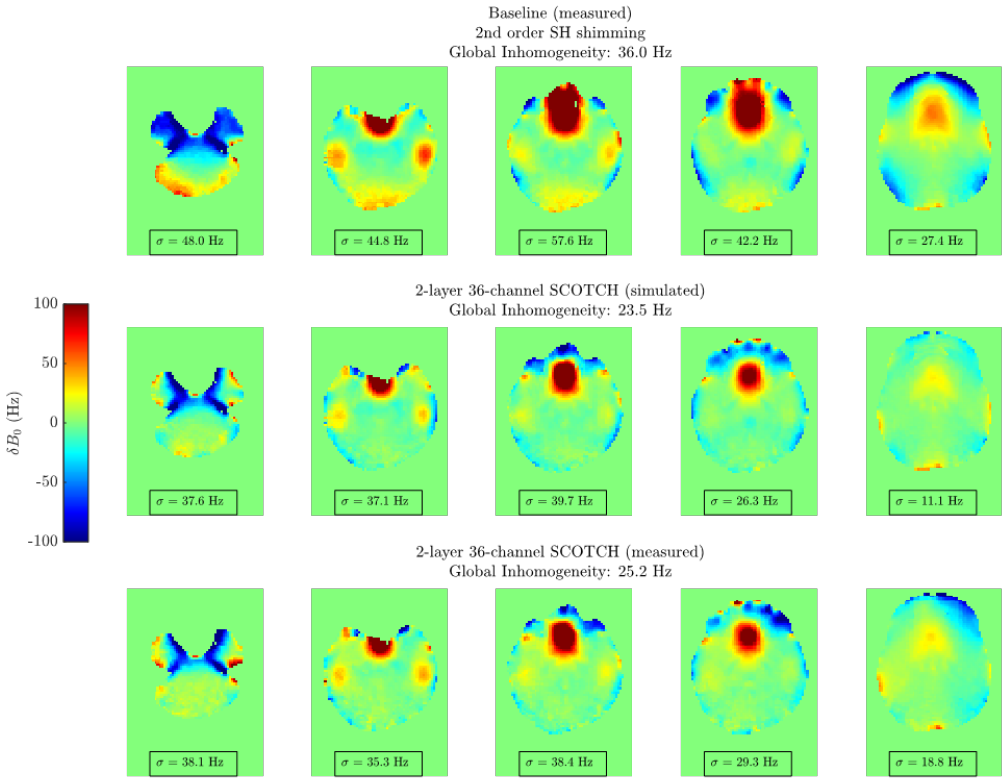

Figure C.4 – Simulated and measured fieldmaps after 2-layer 36-channel SCOTCH global shimming on top of 2nd order SH shimmed baseline. Inhomogeneities are given for each axial slice. Field mapping rS-GRE sequence parameters were 2.5-mm isotropic resolution, TE1/TE2/TE3/TR=1/2.6/4.5/125ms.

C.3 Results and Discussion

Simulations with SCOTCH's ideal and measured fields over both databases show good agreement between performances (Fig. C.3). A small drop is seen for the prototype, with slightly higher average final inhomogeneity on both in-house and open-access databases (44.5 Hz to 45.9 Hz, and 38.3 Hz to 39.6 Hz, respectively, with 36 channels). This drop is not surprising, as realistic wire bundles deviate in geometry relatively to ideal single-loop models used in preliminary simulations. Compared to SH, SCOTCH's performance is expected to be within that achieved by 5th and 6th order SH systems. Compared to M-MCAs, 24-channel SCOTCH shows vastly superior performance than a 24-channel M-MCA, while 36-channel SCOTCH is expected to provide slightly superior performance to that of 48-channel M-MCA.

Fieldmaps from in-vivo acquisition are shown in Fig. C.4. Significant inhomogeneity reduction is obtained in the frontal lobe (3rd and 4th columns). Amelioration in the temporal lobes and right above the ear canals, regions notoriously hard to shim, are also observed. Measured global inhomogeneity (25.3 Hz) is close to expectations (23.5 Hz), despite deviations on upper slices (4th and 5th columns), which might be caused by

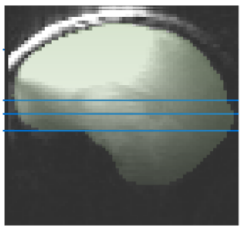

(a)

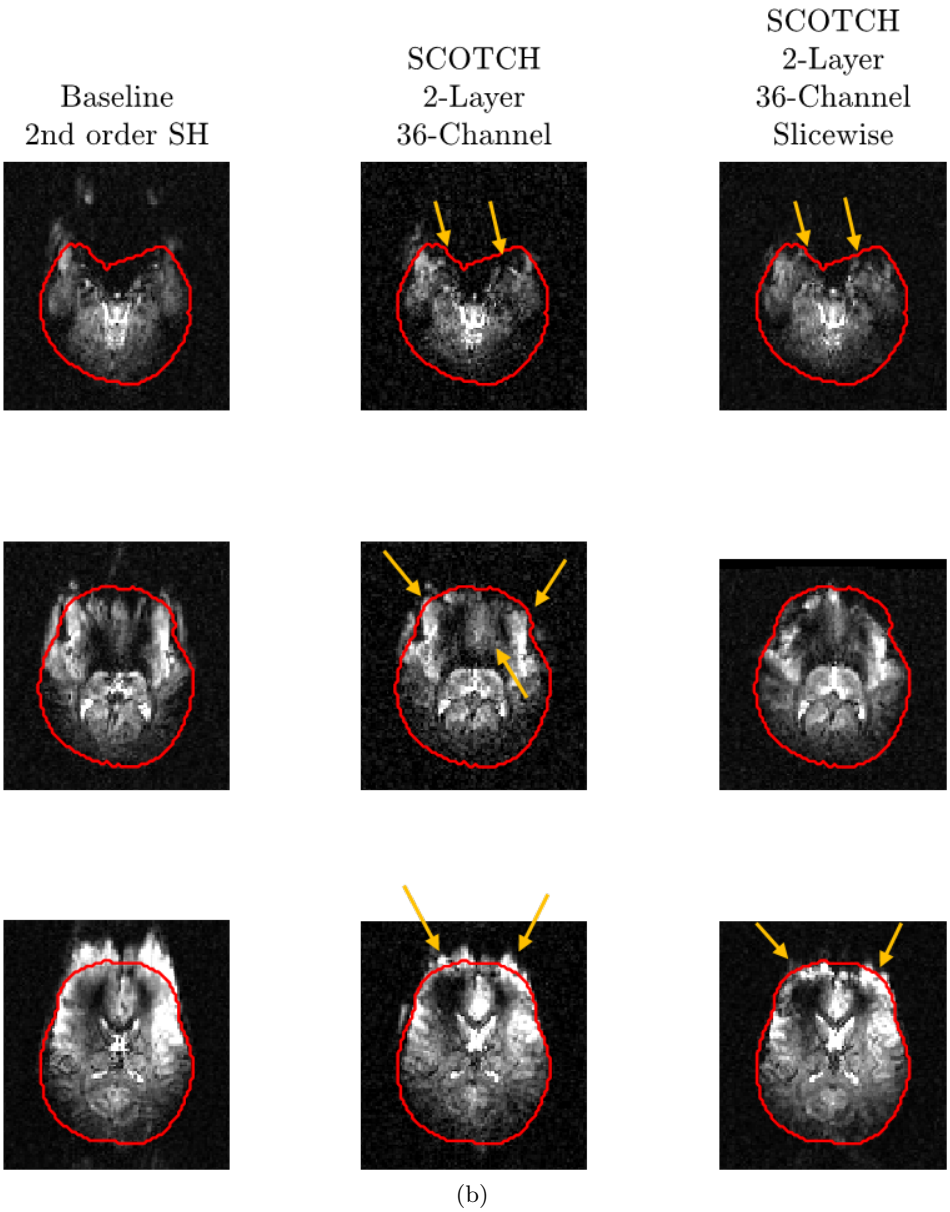

(b)

Figure C.5 – a) Brain mask overlay (green) considered for optimal current calculations for global shimming and selected slices (blue) presented in b) rs-EPI acquisitions. Baseline, global and slicewise (dynamic) 2-layer 36-channel SCOTCH shimming are shown. rS-EPI sequence parameters were 2-mm in-plane resolution, fifteen 3-mm-thick slices, TE/TR=44/84000ms. Yellow arrows highlighting zones with significant improvement.

differences in SCOTCH positioning relatively to characterization setup.

Fieldmap results are corroborated by EPI acquisitions (Fig. C.5), where geometric distortion is greatly reduced in the frontal lobe, with marked signal recovery as well. Despite being optimized for global shimming, SCOTCH provides further improvement when in slice-wise shimming, with ameliorations on the first and last slices. Yet, some degradation is seen in the middle slice compared to global shimming, again, possibly caused by imperfect positioning of the shim system relative to characterization.

C.4 Conclusion

SCOTCH simulations from ideal and measured fields over different databases showed adequate agreement in performance, providing confidence in the design, which outperforms more conventional matrix arrays. In-vivo acquisitions confirmed the system efficiency in artifact mitigation. Improvements are still expected after better characterization and more accurate positioning of the system for future experiments with the 8Tx/32Rx RF coil.

* * *
* *
*

Appendix D

The Spherical Harmonic Rating: A Metric for B0 Shim System Performance Assessment

The methods and principles contained in this appendix were accepted for presentation at an international conferences as:

B. Pinho Meneses and A. Amadon. *The Spherical Harmonic Rating: A Metric for B0 Shim System Performance Assessment.* In Proceedings of the 29th Annual Meeting of the International Society for Magnetic Resonance in Medicine, Virtual, 2021. ISMRM.

D.1 Introduction

As MRI scanners move to Ultra-High Field (UHF), B0 inhomogeneity in the human brain increases proportionally, notably exacerbating geometric distortion and signal loss in Echo Planar Imaging (EPI). To reduce such artifacts, a significant amount of work has been done by several research groups to design B0 shim systems capable of pushing the boundaries of inhomogeneity mitigation [Juchem 2011, Pan 2012, Juchem 2015, Stockmann 2013, Kim 2017, Stockmann 2018, Aghaeifar 2018, Meneses 2019b, Meneses 2019c, Pinho Meneses 2020d, Zhou 2020, Can 2019, Pinho Meneses 2020b, Pinho Meneses 2020e, Aghaeifar 2020, Hetherington 2021, Oh 2020] relatively to conventional 2nd/3rd order Spherical Harmonics (SH) shimming, integrated in commercial scanners. The widespread metric for evaluating B0 inhomogeneity is the standard deviation of the magnetic field excursion ($\sigma(\delta B_0)$) across voxels in the region of interest. However, significant variability of this metric across different sites even at the same B0 field strength has been observed [Stockmann 2018, Zhou 2011], making it insufficient for assessment and comparison of performance of different shim systems across research sites. Examples of baseline inhomogeneity reported by different sites at different field strengths are shown in Table D.1, with cases

Table D.1 – Average global (whole-brain) inhomogeneity reported across different works. All values have been scaled to represent the inhomogeneity at 7T.

Reference	Number of Fieldmaps	Original Field Strenght	Average Global Inhomogeneity at 7T
Zhou et al	7	3 T	65.1 Hz
Mustafa et al	31	3 T	96.9 Hz
Juchem et al	5	7 T	40.6 Hz
Kim et al	8	7 T	29.7 Hz
Stockmann et al	7	7 T	48.7 Hz
Pinho-Meneses et al	100	7 T	65.7 Hz
Hetherington et al	8	7 T	32.4 Hz
Elshatlaway et al	126	7 T	67.2 Hz
Aghaeifar et al	10	9.4 T	70.0 Hz
Aghaeifar et al	14	9.4 T	53.5 Hz

of strong variability even at a same site at the same field strength. Noise, different brain mask topology and fieldmap estimation method, for instance, have been hypothesized as potential sources of noticed variability [Zhou 2020], but the question remains open. To overcome this difficulty, we propose a simple and robust metric denominated Spherical Harmonic Rating (SHR), which is based on a quantitative comparison of the proposed shim system to SH based systems.

D.2 Methods

For a given fieldmap, if the resulting inhomogeneity σ_{shim} after shimming by some arbitrary system is between that obtained by unconstrained SH shimming of degrees n and $n+1$ ($\sigma_{\text{SH}_n} \geq \sigma_{\text{shim}} > \sigma_{\text{SH}_{n+1}}$), the SHR of such system for this particular fieldmap is given by:

$$SHR = n + \frac{\sigma_{\text{SH}_n} - \sigma_{\text{shim}}}{\sigma_{\text{SH}_n} - \sigma_{\text{SH}_{n+1}}} \tag{D.1}$$

To verify consistency of this metric across different sites, an in-house database14 composed of 100 fieldmaps, acquired at 3T and re-scaled to 7T, and an open-access (OA) database19 with 126 fieldmaps, acquired at 7T, are used in shimming simulations, first with two different matrix Multi-Coil Arrays (M-MCAs) (cf. Fig. D.1a), of 24 and 48 channels. The M-MCAs are composed of regularly distributed circular loops around a cylindrical surface of 300-mm length and 280-mm diameter. The uniform coverage of the cylindrical surface by these generic designs should provide an unbiased system, delivering similar performance across different databases. In addition, two 2-layer 36-channel optimized MCAs designed using a SVD-based methodology [Meneses 2019c, Pinho Meneses 2020e] are simulated and evaluated using the SHR (Figs. D.1b and D.1c). A low-bias and a high-bias SVD-based MCA system (S-MCA) with respect to the in-house database were designed based on 50 and 100 fieldmaps, respectively. Besides using only 50 subjects, relaxed field-error tolerance was allowed in the low-bias S-MCA design. All shim systems are simulated over both databases considering coils with 20 wire turns and

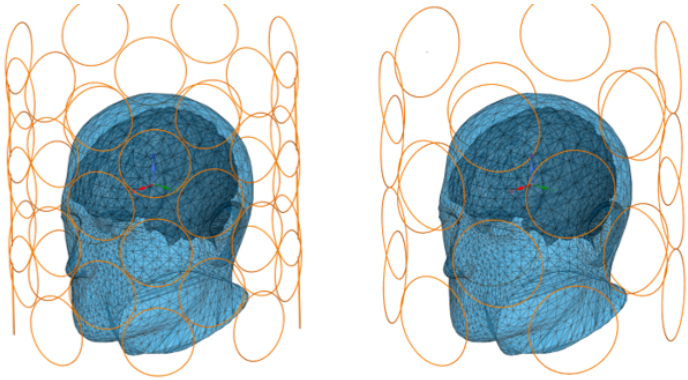

(a)

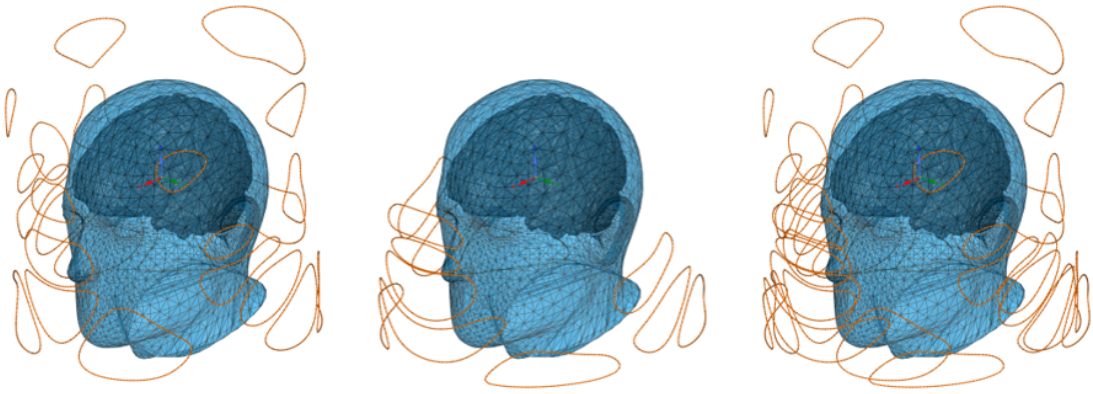

(b)

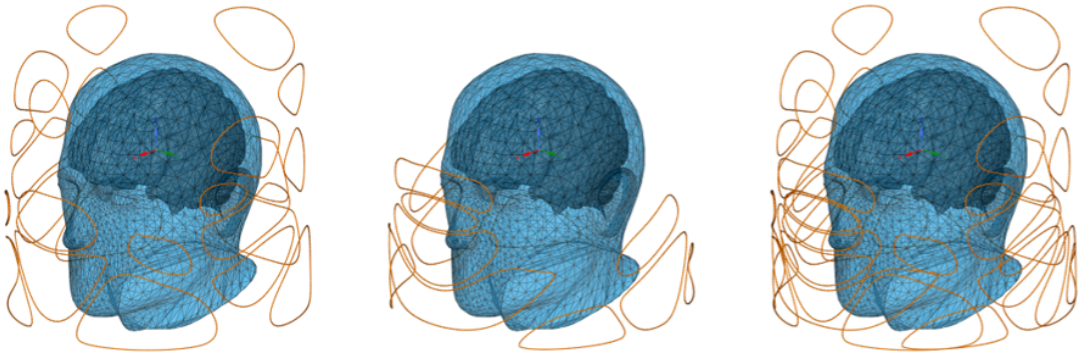

(c)

Figure D.1 – MCAs designed over a 300-mm length, 280-mm diameter cylindrical coil former. a) Matrix MCAs of 24 and 48 channels; b) and c) SVD-based MCA design. From left to right: first layer with 24 channels, second layer with 12 channels and full 2-layer 36-channel shim system; b) Low bias and c) High bias.

maximum 3A per channel. Average baseline inhomogeneity across fieldmaps of the in-house and OA database are 65.7-Hz and 67.2-Hz, respectively. The SHR is compared to the inhomogeneity metric and to relative improvement over baseline inhomogeneity.

D.3 Results and Discussion

From results in Figs. D.2b and D.2c, assessment of the MCAs' robustness across sites from inhomogeneity and inhomogeneity reduction metrics is not evident. Considerable metric differences across databases for each MCA are observed. An exact same M-MCA would appear to present over 10% absolute difference in inhomogeneity reduction when used on different sites at the same magnetic field and electric current constraints, despite the different databases presenting similar values of baseline inhomogeneity. The differences considering the inhomogeneity metric are also large, circa 7Hz. However, although the variability in this metric makes it unsuitable for performance comparison, it is the standard metric for inhomogeneity assessment and it presents valuable information regarding the magnetic field in the ROI. The average SHR for the different systems is shown in Figure D.2a. From this metric, M-MCAs seem to provide practically the same performances across different databases, which is expected for these generic designs. This evidences the invariant characteristic of the proposed metric. The 24 and 48-channel M-MCAs present a SHR difference between databases of 0.01 and 0.09, respectively. For S-MCAs, we see that the low-bias system behaves similarly to a 48-channel M-MCA in terms of robustness to inter-subject variability, with difference in SHR across databases of 0.09. For the high-bias S-MCA, the difference is 0.33, clearly indicating its reduced robustness, as the difference is 3.7 times greater than for the low-bias design. Therefore, the SHR easily highlights drop in performance of the high-bias S-MCA on the OA database relatively to the in-house database.

D.4 Conclusion

The SHR provides numerical values consistent with the expected behavior of the different shim systems. Certainly, although providing consistent values across different databases for a same shim system, the SHR alone does not provide all the information needed for assessing the expected image quality from some acquisition, and observing the field excursion values across different slices and the global inhomogeneity is necessary. Nevertheless, to aid clinicians and researchers to pick their shim system from the many designs available in the literature, this metric is extremely helpful and we encourage its use; or that comparisons between the inhomogeneity obtained by the shim system design and what would be achieved with unconstrained SH shim systems are provided. Therefore, using a common basis for analysis, consistent across sites.

* * *
* *
*

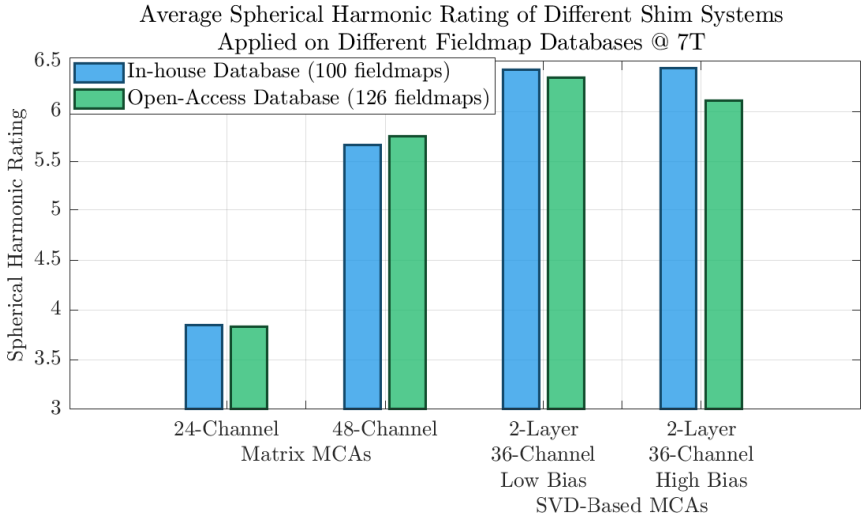

(a)

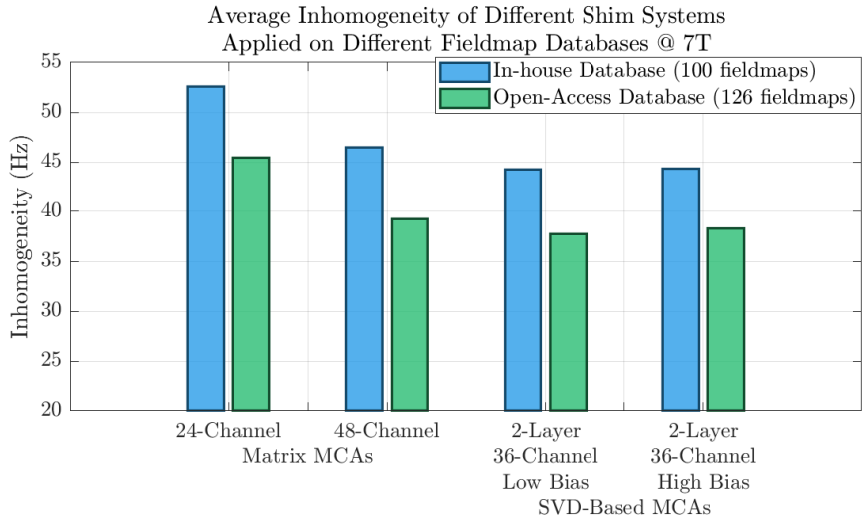

(b)

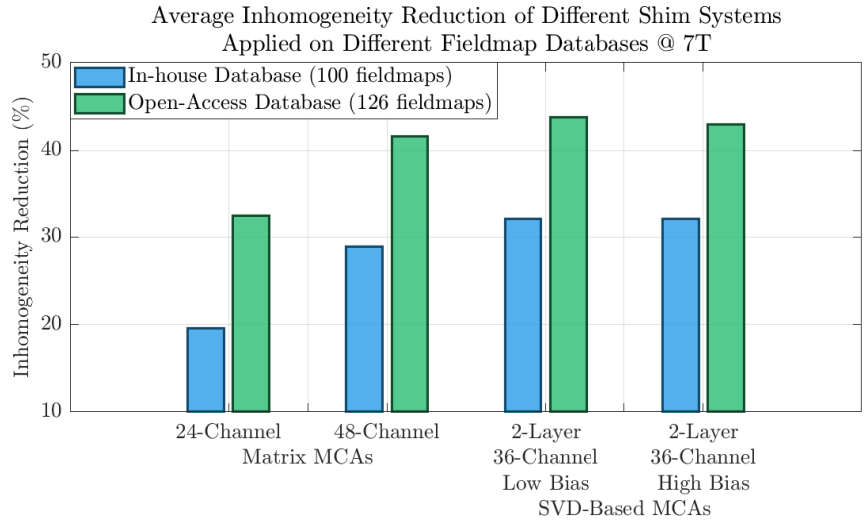

(c)

Figure D.2 – Shimming simulation results, presented with different metrics, on both fieldmap databases for different shim systems.

Appendix **E**

Human brain shimming performance comparison between matrix-like and stream-function SVD-based multi-coil arrays

The methods and principles contained in this appendix were presented at an international conferences as:

B. Pinho Meneses and A. Amadon. *Human brain shimming performance comparison between matrix-like and stream-function SVD-based multi-coil arrays.* In Proceedings of the 28th Annual Meeting of ISMRM, volume 28, page 4222, Virtual Conference, 2020.

E.1 Synopsis

Last year we presented a novel whole-brain B0-shimming Multi-Coil Array design based on Stream Function Singular Value Decomposition on a cylindrical surface. Here this design is compared to more conventional single-layer matrix arrays in simulations based on a 100-subject B_0-map database. While whole-brain shimming performance is naturally improved by our method, the effects of such optimization on slice-by-slice and region-specific shimming are not evident and are therefore explored in this work.

E.2 Summary

Optimization of Multi-Coil Arrays by Stream Function Singular Value Decomposition successfully improved whole brain B_0 shimming performances with low or no degradation of slice-by-slice and region-specific shimming compared to Matrix MCAs.

E.3 Introduction

Multi-Coil Arrays (MCA) [Juchem 2011,Stockmann 2016,Aghaeifar 2018] for B_0 shimming in the human brain have become a popular alternative to Spherical Harmonics (SH) shim coils in the past few years due to their relative easiness to build, better performance on whole-brain shimming and their ability to perform dynamic slice-by-slice [Juchem 2015] shimming . These arrays are usually built so that circular coil windings are regularly distributed over a cylindrical surface, creating a matrix of channels, yet not strictly optimized for the human brain anatomy. We proposed a new method [Meneses 2019c] for designing optimized MCAs based on Singular Value Decomposition (SVD) of optimal Stream Functions [Pinho Meneses 2020d] (SF), providing loops of arbitrary geometry and optimally positioned to mitigate whole-brain inhomogeneity, showing, in simulations, superior performance to that of usual matrix MCAs (M-MCA) in whole-brain shimming while presenting a reduced channel count. Nevertheless, assessment of slice-by-slice and region-specific shimming performances, of particular interest in high-resolution fMRI or spectroscopy, is also relevant to establish SF-SVD-based designs capable of satisfying several applications. Therefore, three brain Optimized MCA (O-MCA) designs are simulated in this work and compared to M-MCAs with increasing channel count.

E.4 Methods

A 100-subject database of three-dimensional δB_0 brain fieldmaps was built from 3 T acquisitions in a Siemens Magnetom Prisma imager equipped with second-order SH shim coils at 1.7 mm isotropic resolution. The δB_0 field intensities were rescaled to 7 T, since a shim system for UHF is intended. FSL's brain extraction tool was used to exclude non-brain voxels.

All fieldmaps are used as target fields, providing 100 SFs [Meneses 2019a] upon which SVD is applied [Meneses 2019b]; then the optimized loops are extracted from the three first principal modes, each loop being associated with a shimming channel [Pinho Meneses 2020d]. Three concentric cylindrical coil formers of equal length $L = 300$ mm and radii $a_1 = 140.5$ mm, $a_2 = 149.5$ mm and $a_3 = 158.5$ mm accommodate the optimized loops extracted from first, second and third modes respectively, as shown in Fig. E.1c. Single-turn models of each loop are exported to ANSYS®-Maxwell for the calculation of their magnetic field distribution (in a region enclosing all brains) and of their complex impedance. The loops are assumed to be 20-turn windings of copper wire with 1 mm diameter to improve shimming efficiency with limited power supply. Loop current is constrained to 5 A. Each winding is assumed to yield the same normalized magnetic field profile as a single turn. For comparison purposes, four different M-MCAs of 16, 24, 32 and 48 circular loop channels over cylindrical formers of 140.5 mm radius are designed with similar windings and current constraints (cf. Fig. E.2a).

For every subject, the shimming performance of each MCA is simulated by computing the electric currents minimizing the L_2 norm of the residual magnetic field in the region

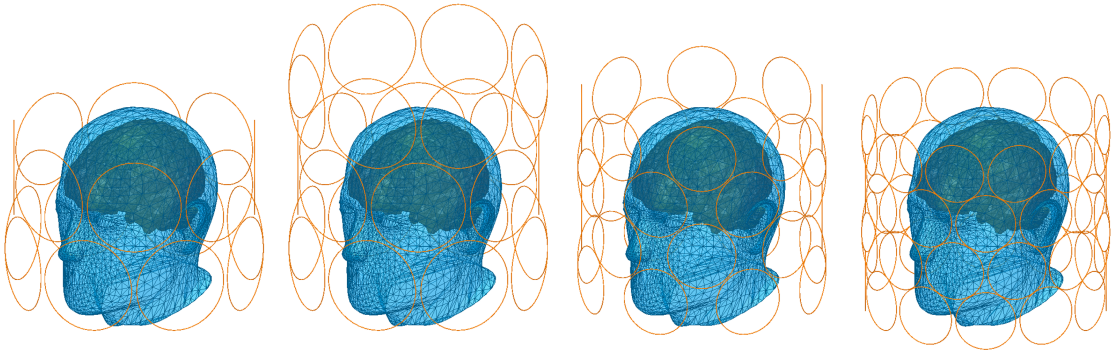

(a)

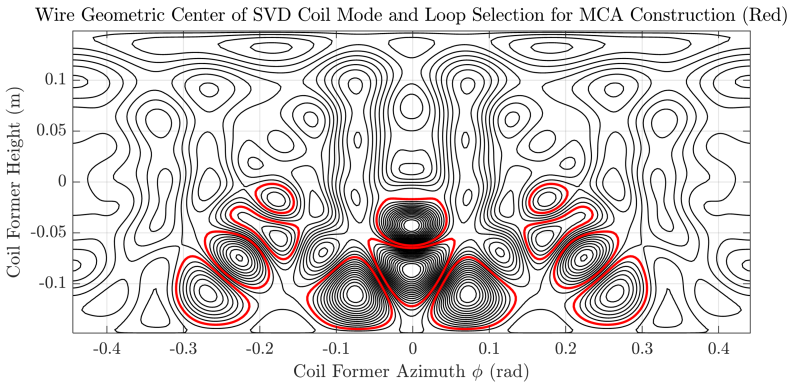

(b)

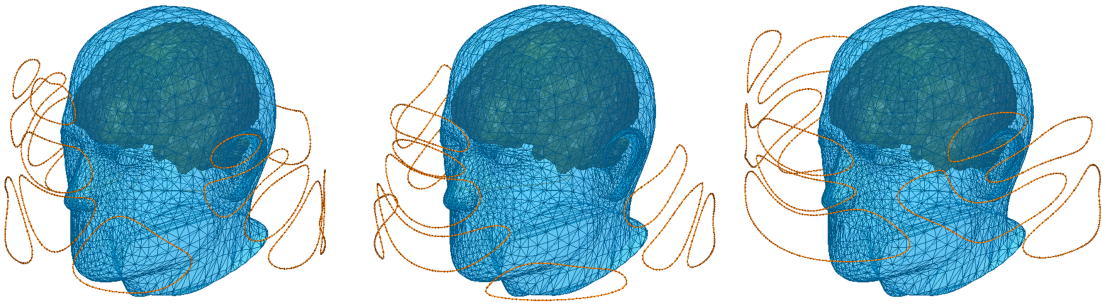

(c)

Figure E.1 – a) Matrix MCA designs composed of 16, 24, 32 and 48 channels, with circular loop radii of 5.5 cm, 5.5 cm, 4.5 cm and 3.5 cm, respectively. b) Illustration of independent loop channels selection from first SVD coil mode for composing one layer of an SVD-based Optimized MCA. c) Optimized MCA layers formed from loop selections out of first, second and third SVD modes of tailored Stream Functions. The layers are composed of 16, 12 and 11 channels, respectively.

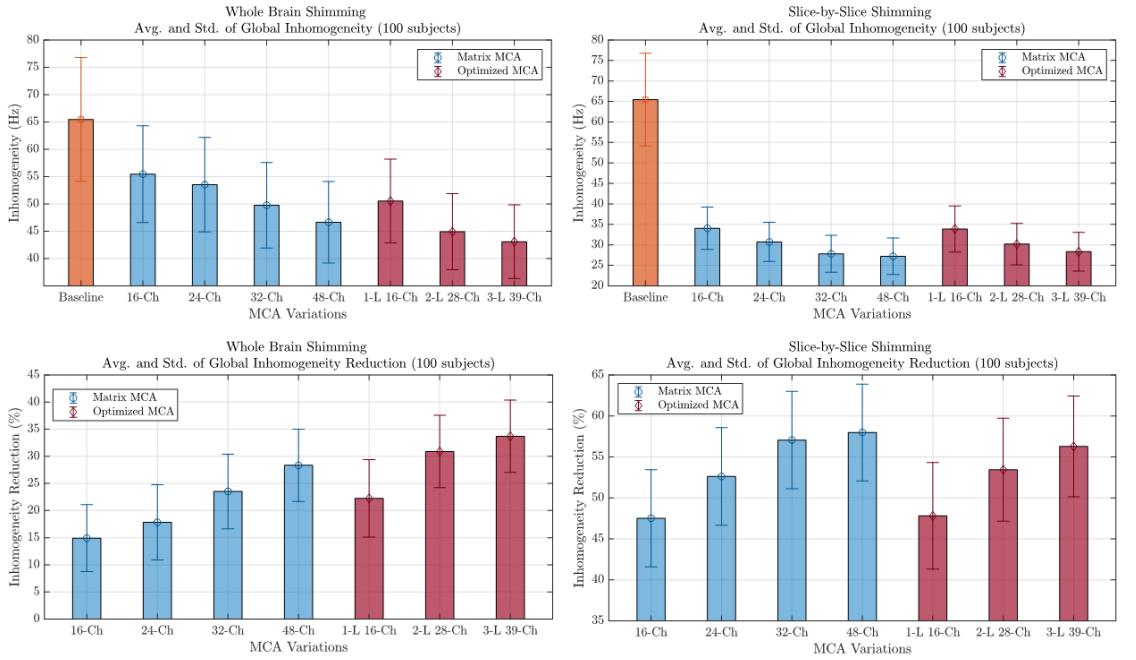

(a)

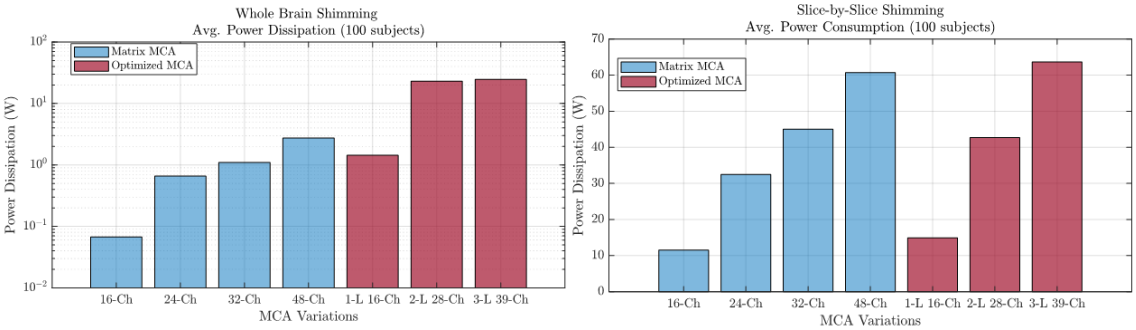

(b)

Figure E.2 – a) Comparison of B_0 inhomogeneity (Hz) and inhomogeneity reduction (%) from our 100-subject database at 7T shimmed by different MCA technologies performing whole-brain or slice-by-slice shimming. The average 65-Hz baseline value results from 2nd-order shimming by the scanner. b) Average power dissipation for the above conditions.

of interest, which can be the whole-brain, a thin transverse slice or a slab covering some cerebral lobe depending on the application. Here the frontal and temporal lobes, known to be strongly affected by susceptibility gradients, are addressed with slabs located by hand on 20 randomly-chosen brains of our database. Finally, resulting inhomogeneity (=standard deviation of the δB_0 residual across all voxels of interest), inhomogeneity reduction and power dissipation are assessed.

E.5 Results and Discussion

From Figures E.2a and E.4, O-MCAs outperform M-MCAs in whole-brain shimming while having much smaller channel count. The 2-layer, 28-channel O-MCA shows slightly better inhomogeneity reduction, 30.9 % (SD: 6.7 %), on the database than the 48-channel M-MCA,

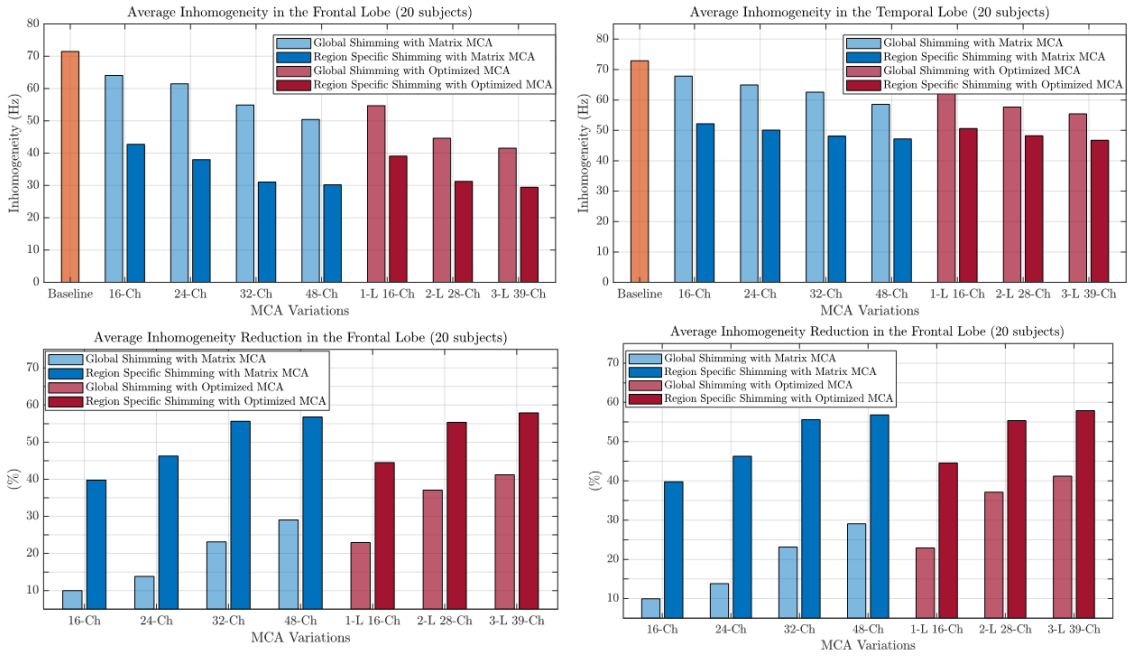

(a)

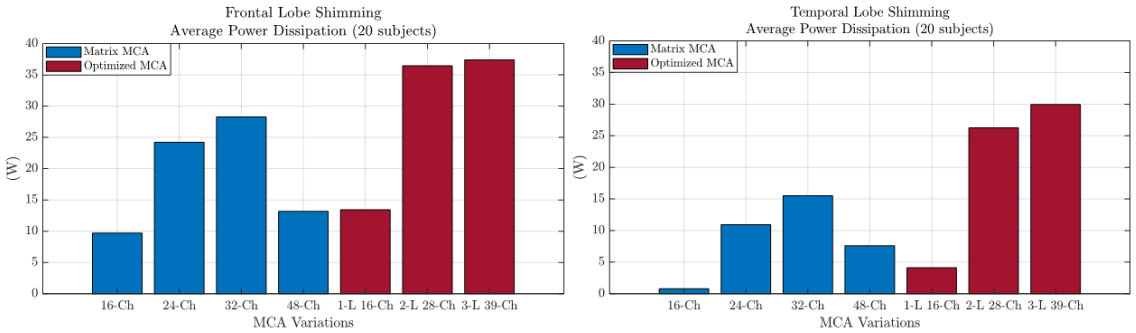

(b)

Figure E.3 – a) Comparison of B_0 inhomogeneity (Hz) and inhomogeneity reduction (%) in the frontal lobe and temporal lobes of a 20-subject database at 7T, shimmed by different MCA technologies performing whole-brain or region- (slab-) specific shimming. b) Average power dissipation for slab-specific shimming.

28.3 % (SD: 6.7 %), and much superior performance than the 23.5 % (SD: 6.9 %) achieved by 32-channel M-MCA, a relative improvement of 31.5 %. From Figures E.3a and E.5, still in whole-brain shimming, O-MCAs show improvement in the frontal and temporal lobes compared to M-MCAs, not surprising in view of the channel concentration in front of these regions. In slice-by-slice shimming, however, the regular distribution of channels in M-MCA is more advantageous, as the 32-channel MCA outperforms the 3-layer, 39-channel O-MCA. Nevertheless, inhomogeneity reduction achieved by 2-layer and 3-layer O-MCAs, at 53.4 % (SD: 6.3 %) and 56.3 % (SD: 6.2 %), respectively, are satisfactory compared to the 57.1 % (SD: 5.9 %) and 58.0 % (SD: 5.9 %) for 32-ch. and 48-ch. M-MCA. For region specific shimming, Figures 3a and 5, the 28-channel O-MCA inhomogeneity reduction for frontal and temporal lobes (55.4 % and 32.8 %) are very close to that achieved by 32-ch (55.6 % and 32.8 %) and 48-ch. M-MCA (56.8 % and 34.3 %), while the 39-channel O-MCA

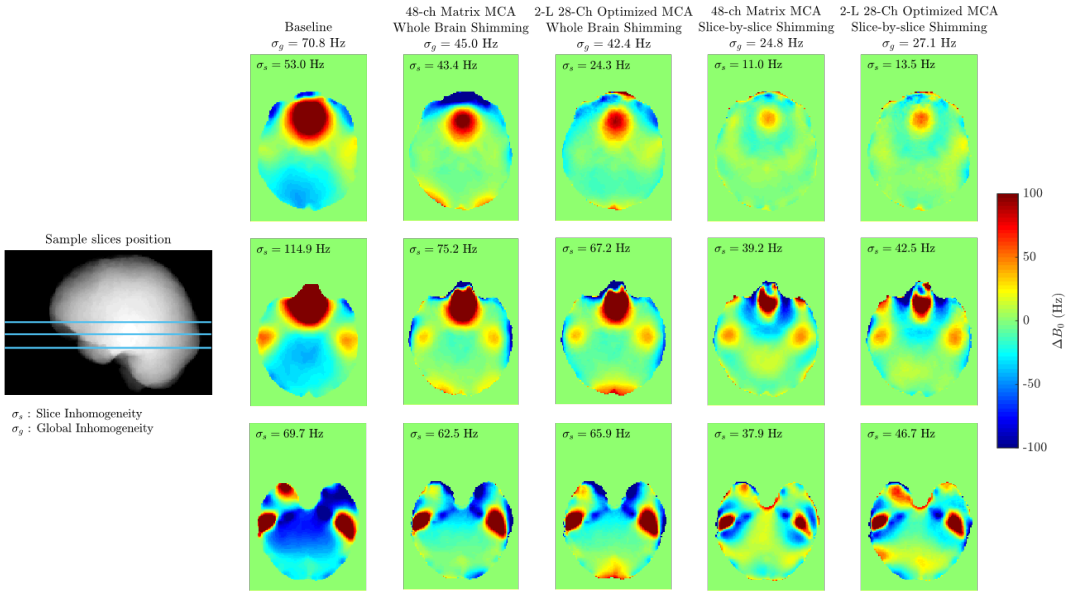

Figure E.4 – Comparison of δB_0 fieldmaps in selected slices shimmed by a 48-Channel Matrix MCA or a 2-Layer 28-Channel driven for whole-brain and slice-by-slice shimming.

outperforms them both by a small margin. Within a design methodology, from Figure 2b, it is observed that power dissipation of the systems tends to increase with the homogeneity improvement, whether in slice-by-slice or whole-brain shimming. The 28-channel O-MCA produces 23.1 W average dissipation for global shimming, much superior to the 2.8 W dissipation of the 48-ch. M-MCA. However, in slice-by-slice shimming, dissipation of the latter surpasses the 42.7 W of the former by 18 W.

E.6 Conclusion and Perspectives

The SF-SVD-based optimization of MCAs is a powerful method for designing shimming systems with lower channel count, higher whole-brain shimming performance, while maintaining satisfactory results when used for slice-by-slice or focused shimming, in particular in the frontal lobe. The 2-layer, 28-channel system presents a good compromise between performance and channel count. The present simulations resulted from an SF-SVD design targeting the whole brain. Further improvement of the optimized MCA performance could be attained if application-specific systems are envisioned, designed for addressing specific brain regions.

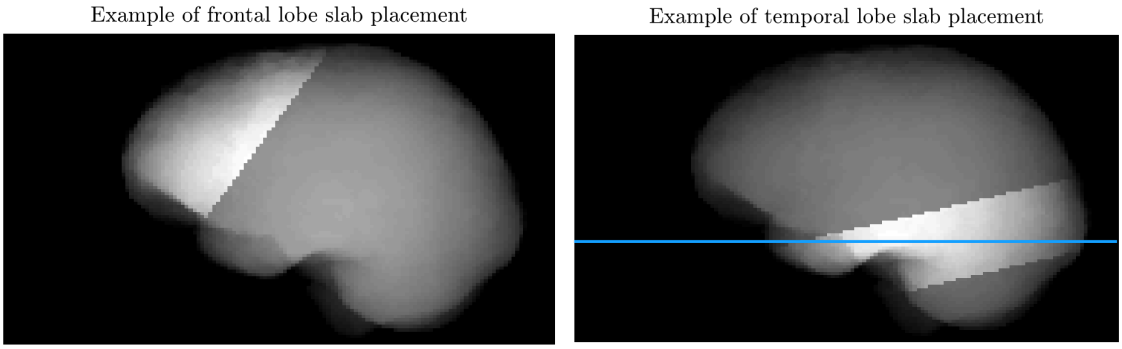

(a)

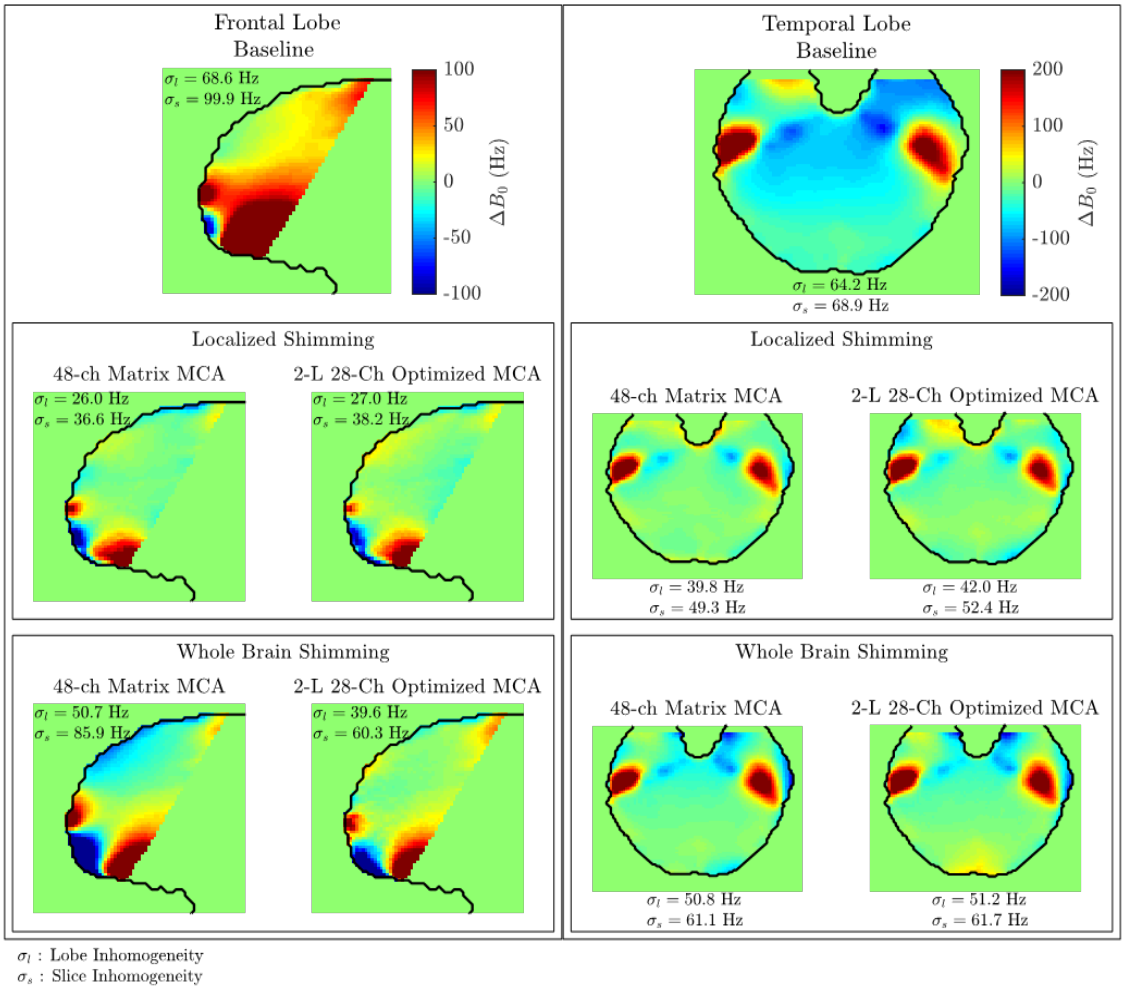

(b)

Figure E.5 – a) Example of brain mask outline (actually the addition of all sagittal slices) and highlighted slab placement for frontal and temporal lobe focused shimming. b) δB_0 fieldmaps of the frontal and temporal lobes after localized shimming and whole-brain shimming performed by 48-channel Matrix MCA and 2-layer 28-channel optimized MCA. The depicted slices are in the central sagittal plane (left) and inferior axial plane (right). $\sigma_l = B_0$ std in entire slab; $\sigma_s = B_0$ std in depicted slice.

Appendix F

Résumé en français

Abstract in French

Sujet : Homogénéisation du Champs Magnétique Statique dans le Cerveau Humain pour l'IRM à Ultra-Haut Champs : Limites Conceptuelles et Développement d'un Nouveau Prototype.

Les différents aspects abordés dans cette thèse sont résumés ici. On commence par introduire les contexte et état de l'art, pour ensuite décrire les nouvelles méthodologies et instrumentation développés dans ce travail pour s'attaquer au défis de l'homogénéisation du champs statique pour l'IRM à Ultra Haut Champs.

F.1 Contexte et état de l'art

L'imagerie par résonance magnétique (IRM) est devenue l'étalon-or de l'imagerie médicale grâce à sa polyvalence, assurée non seulement par sa multitude de contrastes naturels (T_1, T_2, densité de protons), mais aussi par l'ingénieux et riche ensemble de séquences d'impulsions qui permettent d'observer l'anatomie, les flux, l'activité métabolique, etc.

L'IRM s'appuie sur un champ magnétique principal puissant, le B_0, pour générer une aimantation d'origine nucléaire dans les tissus du corps. Cette aimantation est ensuite manipulée pour générer une image. Le rapport signal/bruit (SNR) de l'image augmente de façon supra-linéaire avec le champ magnétique principal. C'est pourquoi des efforts importants ont été faits pour augmenter le champ principal de l'IRM de 0.35 T dans sa première démonstration in-vivo à 7 T disponible aujourd'hui dans les scanners cliniques. Des scanners encore plus puissants à 9.4, 10.5 et 11.7 T, actuellement dédiés à la recherche, pourraient aussi trouver un jour leur place dans la routine clinique. En effet, ils peuvent atteindre des résolutions submillimétriques avec un temps d'acquisition acceptable.

Pour bénéficier des gains SNR apportés par les UHF, le projet Iseult a été lancé en 2007 avec l'Institut de Recherche sur les Lois Fondamentales de l'Univers (IRFU) au CEA pour concevoir un scanner IRM 11.7 T corps entier qui est en cours d'installation à NeuroSpin.

Avec un champs aussi intense, nous espérons améliorer considérablement le rapport contraste/bruit (CNR) en IRM fonctionnelle (IRMf), une fenêtre sur les rouages complexes du cerveau humain. Le SNR intrinsèquement plus élevé sera également bénéfique pour l'imagerie et la spectroscopie des noyaux X (Sodium, Phosphore, Lithium). Et, naturellement, pour la plupart des séquences anatomiques. L'augmentation du SNR, du CNR et de la résolution dans une large gamme de séquences d'imagerie devrait également permettre d'éclairer les défis cliniques tels que le diagnostic précoce des maladies neurodégénératives.

F.1.1 Inhomogénéité de B0 Induite par Gradients de Susceptibilité, et Artefacts Liés.

L'exploitation d'un aimant aussi puissant s'accompagne toutefois de plusieurs défis techniques et méthodologiques. L'un de ces défis est lié à l'inhomogénéité du champ magnétique principal. L'IRM nécessite d'un champ magnétique très homogène dans la région d'intérêt. Cependant, même si l'aimant principal est conçu pour offrir un niveau d'homogénéité exceptionnel dans l'air, lorsqu'un patient est inséré dans le champ magnétique, les gradients de susceptibilité magnétique entre les différents tissus, et surtout entre les tissus et l'air, produiront des champs magnétiques inhomogènes à proximité de ces frontières (cf. Fig. F.1).

A partir des équations fondamentales décrivant le phénomène IRM, nous pouvons observer comment les excursions du champ magnétique produisent des artefacts d'image. Les artefacts sont effectivement plus importants lorsque les excursions du champ magnétique augmentent. En plus, l'inhomogénéité induite par les gradients de susceptibilité croît linéairement avec le champ magnétique principal, ce qui est particulièrement problématique pour l'imagerie à UHF. On constate que la réduction de l'excursion du champ magnétique n'est qu'un des moyens possibles de réduire les artefacts liés à l'inhomogénéité, mais si chaque solution entraîne une pénalité, la réduction de l'excursion du champ magnétique lui même semble être celle qui a le moins d'effets négatifs.

Une séquence notoirement sensible au B_0 est celle de l'imagerie écho planaire (EPI), la séquence la plus couramment utilisée dans les études d'IRMf. Elle présente une forte distorsion géométrique et perte de signal autour des sinus et des canaux auditifs, régions qui présentent un intérêt significatif dans de nombreuses études de neurosciences réalisées en IRMf. Ces artefacts sont déjà intenses à 7 T, et on s'attend donc à ce qu'ils soient aggravés à 11.7 T.

L'atténuation des artefacts liés au B_0 en UHF est donc essentielle, et c'est l'objectif de ce projet de thèse.

F.1.2 B0 Shimming dans le Cerveau Humain : Méthodologie et Instrumentation

L'atténuation de ces artefacts par la réduction des excursions du champ magnétique est réalisée par la génération de champs magnétiques antagonistes. Ce processus, connu sous

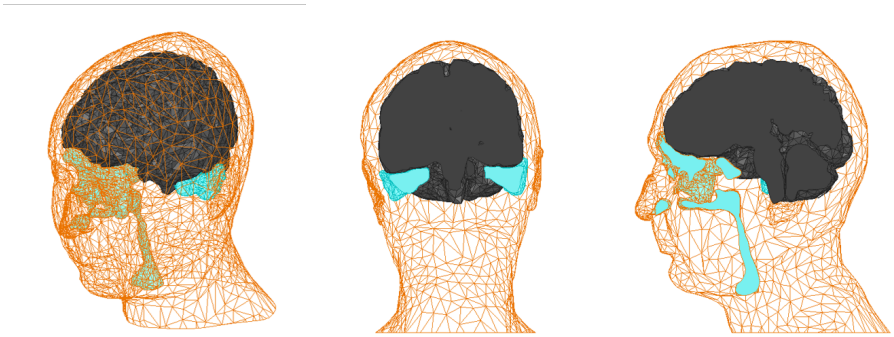

(a)

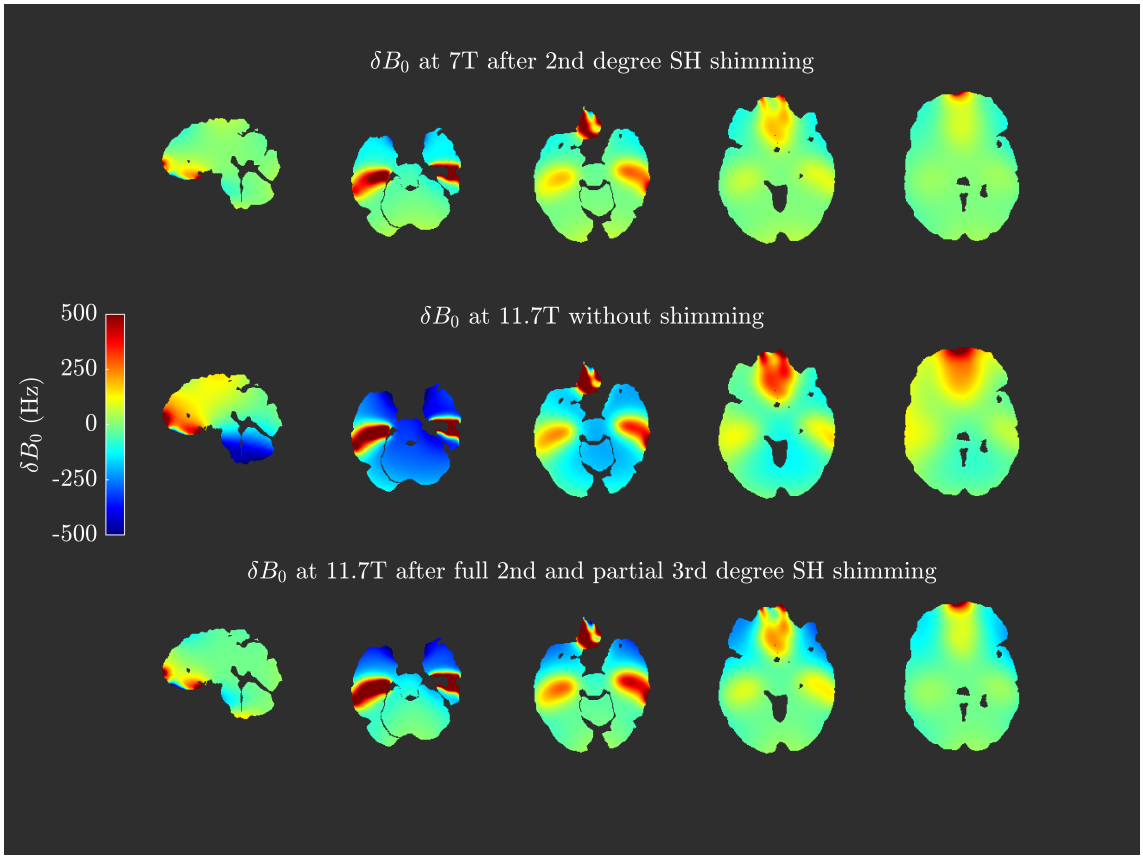

(b)

FIGURE F.1 – Disposition de cavités d'air dans une tête humaine (a) et inhomogeneité de B_0 résultant des champs induits par les gradients de susceptibilité entre air et tissu à 7 T et 11.7 T (b).

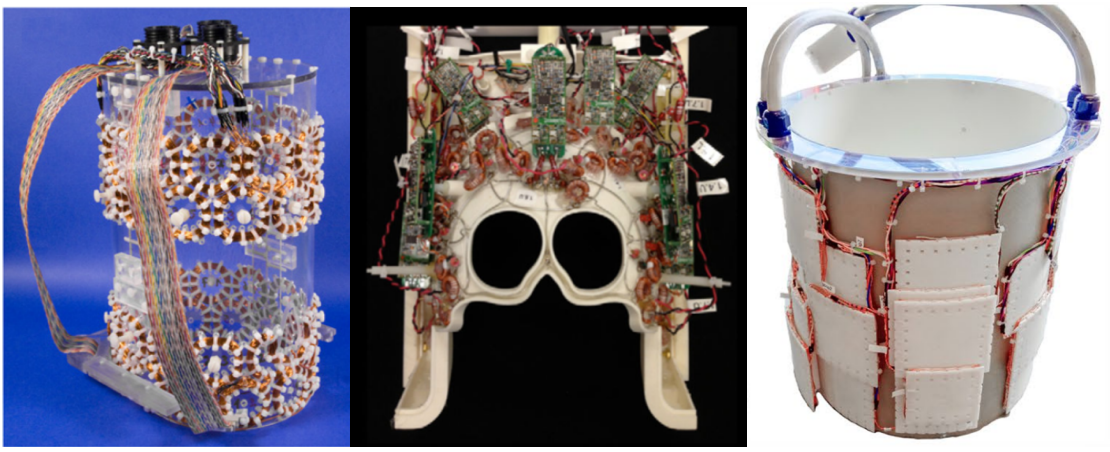

(a) (b) (c)

FIGURE F.2 – Exemples de MCAs utilisé pour l'homogénéisation du champs B_0 dans le cerveau humain, dont : le premier MCA proposé dans la littérature (a), avec 48 canaux ; un MCA dont les bobines de réception RF sont aussi utilisé pour générer des champs de shimming (b) ; et un design MCA avec boucles rectangulaires de dimensions optimisés pour le shimming du cerveau humain (c).

le nom de shimming, est généralement réalisé avec des bobines corrigeant les harmoniques sphériques (SH) du champ jusqu'au troisième degré dans les scanners IRM modernes, mais la correction fournie par le shimming basé sur les SH avec ce degré devrait être insuffisante à 11.7 T. Il est possible d'améliorer le shimming basé sur les SH en augmentant le degré de l'ensemble de bobines SH, mais cela implique l'ajout de plusieurs bobines de dimensions et poids non-négligeable aboutissant à un système lourd et finalement peu pratique.

En tant que solution compacte et flexible, les systèmes de shimming composés de petites bobines circulaires placées régulièrement sur une surface cylindrique entourant la tête du patient, appelés matrix Multi-Coil Arrays (MCA) (cf. Fig. F.2), ont présenté des performances comparables à celles des systèmes basés sur le SH de haut degré, tout en étant alimentés par des courants relativement faibles. Cependant, jusqu'au moment où ce projet de thèse a commencé, il y avait peu de tentatives d'optimisation de la géométrie et de la position de ces bobines pour cibler une anatomie particulière telle que le cerveau humain.

F.2 Développements Méthodologiques

Dans ce travail, inspiré des MCA, on attaque la racine du problème, en essayant de réduire les excursions du champ magnétique à l'intérieur du cerveau humain par l'application de champs magnétiques antagonistes.

Étant donné que la distribution du champ magnétique à l'intérieur du cerveau humain présente des similitudes d'un sujet à l'autre, nous avons supposé que les solutions de shimming actuelles pourraient être optimisées pour présenter des performances plus élevées si leur conception prenait pour cible l'excursion réelle du champ magnétique à l'intérieur

du cerveau humain.

Nous avons donc développé une méthodologie pour la conception de systèmes de shim optimisés pour le cerveau.

F.2.1 Le *Dipole Boundary Method* et le Design de Bobines de Shim Basé sur la Décomposition en Valeurs Singuliers

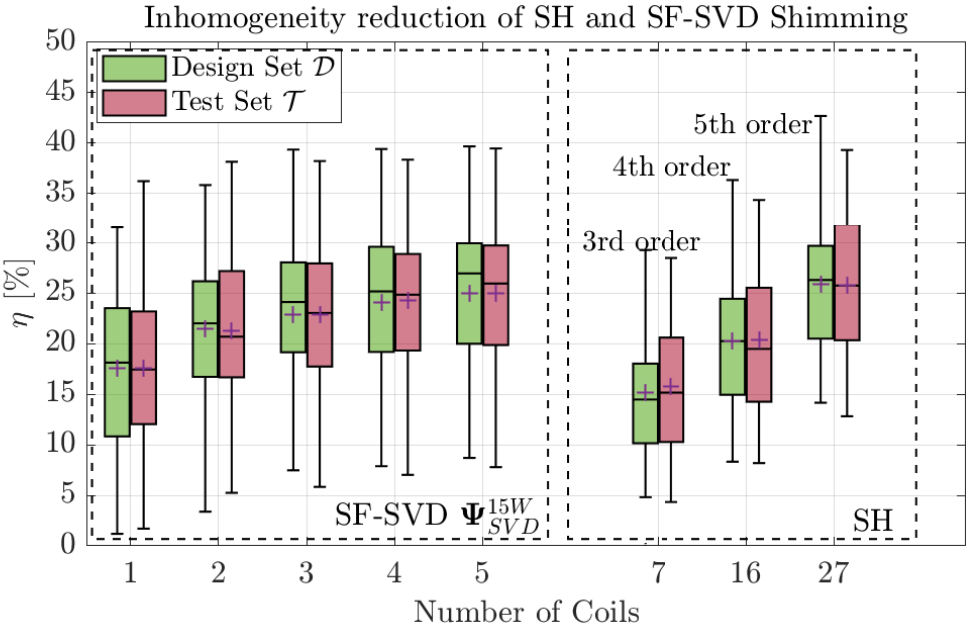

FIGURE F.3 – Performances d'un système de shimming basé sur bobines SF-SVD comparé contre un système basé sur les harmoniques sphérique sans contraintes.

Pour prendre en compte la variabilité inter-sujet dans le design de notre système de shimming, l'acquisition et traitement d'une grande base de données de cartes de champ B_0 dans le cerveau humain a été réalisé.

Ensuite, une méthode simple de conception des bobines, le Dipole Boundary Method, a été développée et utilisée pour le calcul, sur une surface cylindrique, des fonctions de flux (SF) optimisé pour réduire l'excursion du champs magnétique dans le cerveau de chaque sujet dans la base de données.

Pour bénéficier de la similitude entre les distributions de champ inhomogène des différents sujets, et par conséquence entre les fonctions de flux optimisé pour chaque sujet, on applique une Décomposition en Valeurs Singuliers (SVD) sur l'ensemble des fonctions de flux. En sélectionnant les premiers modes SF-SVD, on obtient un très petit ensemble de bobines de shimming entraînées indépendamment et théoriquement capables de fournir une réduction conséquente de l'inhomogénéité. On observe qu'un système de shim SF-SVD à 3 canaux avec puissance limitée (15 W en moyenne) offrait des performances équivalentes à celles qui seraient obtenues par un système de shim SH sans contraintes de 4-eme degré, qui nécessiterait en revanche de 16 bobines (cf. Fig. F.3). Les performances pourraient être encore améliorées si la dissipation de puissance ou le nombre de modes SVD sélectionnés

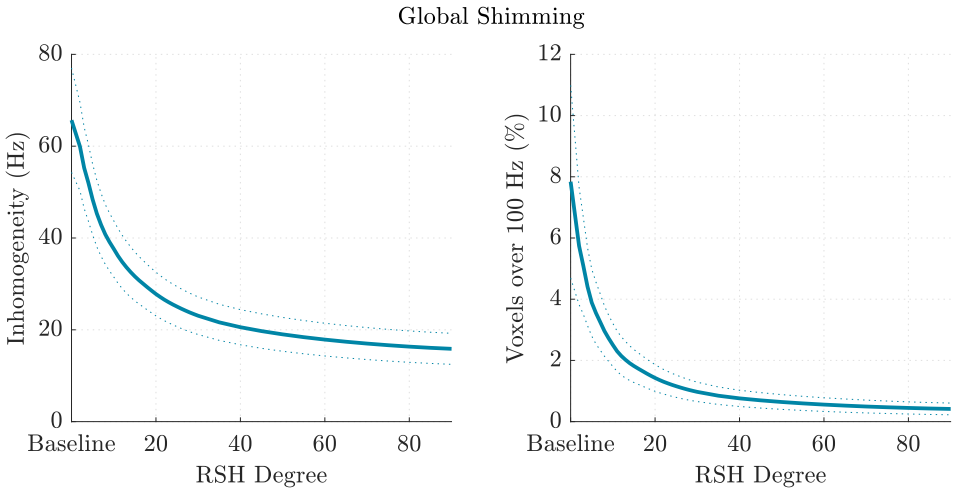

(a)

FIGURE F.4 – Comportement asymptotique de l'inhomogénéité moyenne sur une base de données de 100 sujets après shimming Harmonique Sphérique avec différents dégrées, ce qui indique une impossibilité d'aboutir à une inhomogéneité nulle. Le minimum d'inhomogéneité a été estimé à 12.3 Hz.

pour composer le système de shimming pouvaient augmenter. Dans les deux cas, le système deviendrait plus complexe : des alimentations plus coûteuses et un refroidissement forcé pourraient devenir nécessaires dans le premier cas, et un assemblage moins compact en résulterait dans le second cas. Nous recommandons néanmoins d'augmenter le nombre de canaux si les performances devaient être accrues, car cela ajouterait des degrés de liberté supplémentaires au système, le rendant plus robuste à la variabilité inter-sujet.

F.2.2 Limites Physiques pour l'Homogénéisation du Champs Statique dans le Cerveau Humain

Nous avons observé qu'il existe une limite physique à l'atténuation du champ magnétique inhomogène (cf. Fig. F.4), en raison de l'incompatibilité entre l'emplacement des sources de perturbation du champ magnétique et celui des structures de correction situées en dehors de la tête humaine. Nous avons néanmoins montré qu'il était possible d'obtenir une atténuation parfaite de l'inhomogénéité à condition que la région à homogénéiser puisse être entourée par une sphère qui ne contient aucune source de perturbation du champ (interfaces air/tissu). Cela nous oriente vers des systèmes de shimming conçus pour cibler des régions d'intérêt spécifiques à l'intérieur du cerveau. La conception de tels systèmes, visant en particulier les lobes temporaux où les oreilles internes provoquent de fortes excursions de B_0, pourrait très bien être réalisée avec les méthodes exposées dans cette thèse. Des travaux préliminaires ont d'ailleurs été entrepris à cette fin.

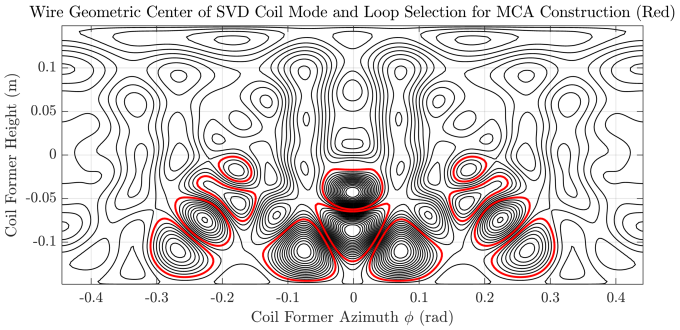

(a)

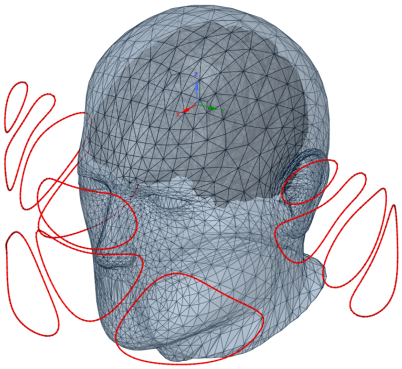

(b)

(c)

(d)

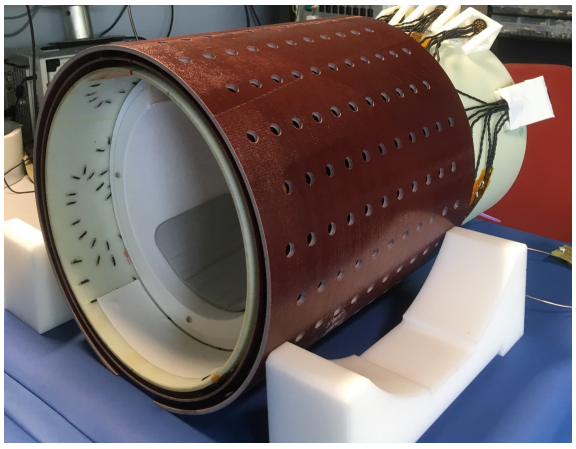

(e)

FIGURE F.5 – Exemple de sélection des boucles pour définition des canaux du MCA optimisé (a,b) ; et prototype résultant de deux modes SF-SVD (c,d,e).

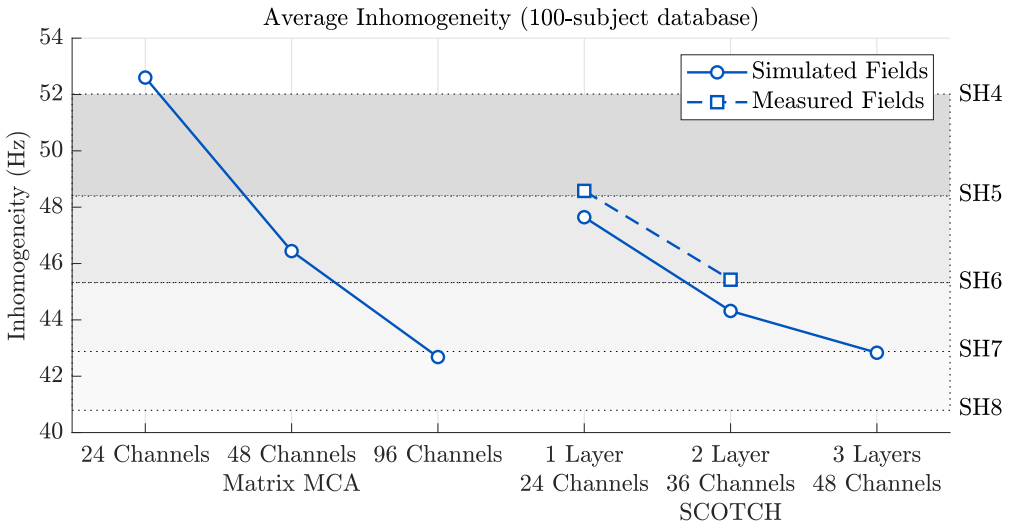

FIGURE F.6 – Comparaison de performance entre MCA de type matriciel et le MCA optimisé (SCOTCH) proposé avec différentes configurations de canaux. Simulations à 7 T avec courant max sous contrainte de 3 A

F.2.3 SCOTCH : Design d'un MCA Basé sur la Décomposition en Valeurs Singulières de Fonctions de Flux

Les bobines SF-SVD peuvent présenter une disposition des fils assez complexe (cf. Fig. F.5a), ce qui rend leur fabrication difficile. D'autre part, ces dispositions d'enroulement contiennent des informations précieuses sur les endroits où le courant électrique était le plus demandé pour le shimming du cerveau humain. Elles servent donc de guide pour placer des bobines indépendantes plus petites afin d'obtenir un MCA optimisée pour le cerveau. Ainsi, on conçoit une méthodologie de sélection de la géométrie et de la position des bobines pour concevoir un MCA basé sur la SF-SVD.

Nous avons donc segmenté les bobines SF-SVD obtenues à partir de notre base de données de cartes de champ du cerveau en de multiples canaux en forme de boucle, entraînés indépendamment, définissant ainsi un MCA optimisé pour la correction de l'inhomogénéité de B_0 dans le cerveau humain. Le design du MCA optimisé est nommé SCOTCH, acronyme pour **S**him **Co**ils **T**ailored for **C**orrecting B_0 Inhomogeneity in the **H**uman Brain. Sous contrainte de 3 A par canal, simulations avec un design composé par 36 canaux disposé sur 2 couche ont montré l'obtention de performances équivalentes à celles des systèmes de shimming SH sans contraintes du 6ème degré. En augmentant encore le nombre de canaux à 48 canaux disposés sur 3 couches, on espère atteindre des performances comparables à celles des systèmes de shimming SH du 7ème degré. Par rapport aux MCA matriciels, l'amélioration des performances est également remarquable, avec SCOTCH à 3 couches et 48 canaux étant comparable à un MCA matriciel à 2 couches et 96 canaux.

Pour une validation croisée, les performances des modèles SCOTCH ont également été évaluées sur une base de données de cartes de champs B_0 différente. Pour faire face aux différences inter-sites dans les acquisitions de cartes de champs magnétique, une nouvelle métrique d'évaluation a été proposée dans ce travail, le SHR (Spherical Harmonic Ra-

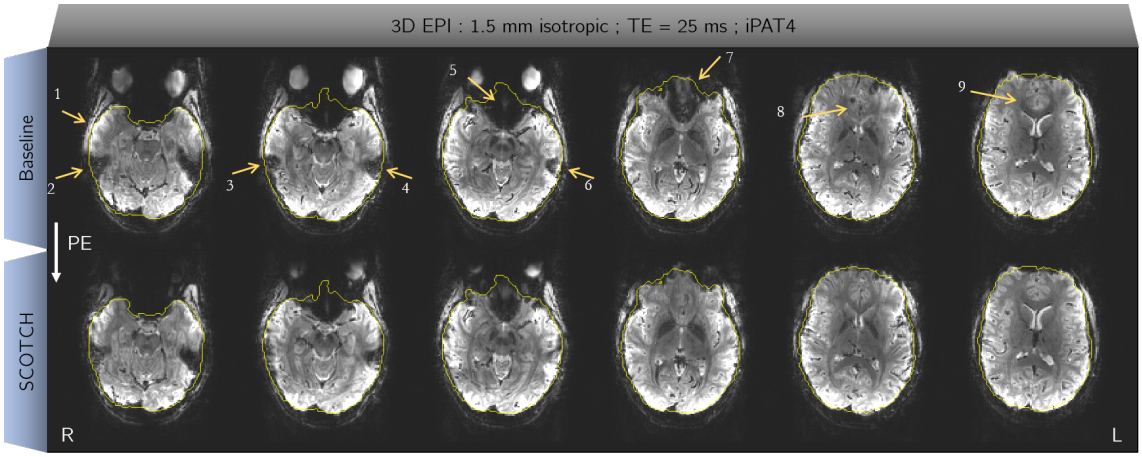

FIGURE F.7 – Acquisitions EPI à DAS Restreint après SH shimming du 2ème dégrée et shimming avec SCOTCH avec 36 canaux. Le paramètres de l'acquisition sont accélération iPAT= 4, TE = 25 ms, 1.5 mm de résolution isotropique. Des améliorations dans la qualité de l'image sont indiqué par les flèches jaunes.

ting). Bien qu'une certaine perte de performance soit attendue avec cette nouvelle base de données, la performance du shimming avec SCOTCH à 2 couches et 36 canaux reste comparable à celle des systèmes de shimming SH du 6ème degré sans contraintes, et la performance de SCOTCH à 3 couches et 48 canaux se situe entre celle des systèmes de shimming SH du 6ème et 7ème degré.

Nous avons également remarqué qu'il existe encore une marge d'amélioration des performances tant que le courant électrique maximal dans chaque canal SCOTCH est autorisé à augmenter. De plus, pour que les performances rapportées du SHR soient maintenues lors du passage de l'IRM à 7 T au scanner Iseult à 11.7 T, le courant devra augmenter proportionnellement. Cependant, l'augmentation des courants entraînera une forte augmentation de la dissipation de puissance, une caractéristique qui a été prise en compte tout au long de notre analyse et qui a été identifiée comme un goulot d'étranglement pour l'augmentation des performances du shimming si aucun refroidissement forcé n'est utilisé.

Compte tenu des performances prometteuses du shimming avec le système simulé, un prototype composé par 36 canaux disposés sur 2 couches a été construit (cf. Fig. F.5), caractérisé et testé *in-vivo* à 7 T. Les champs magnétiques caractérisés du prototype ont été utilisés dans des simulations de shimming pour évaluer comment le système réel devait se comporter par rapport à son modèle idéal (cf. Fig. F.6). Il y a eu, à cette étape, une certaine perte de performance, en raison des déviations des enroulements de fils réels par rapport au modèle de fil unique considéré dans les simulations, mais les performances réalistes du shimming devaient encore être presque aussi élevées que le shimming SH sans contraintes du 6ème degré.

Les expériences in-vivo réalisées dans ce travail ont confirmé la réduction attendue de l'inhomogénéité apportée par SCOTCH. Les cartes de champ ont montré une atténuation de l'excursion de champ dans le cortex préfrontal et au-dessus des canaux auditifs. Sa traduction en atténuation des artefacts d'image a été une récupération appréciable du signal

en EPI hautement accélérée dans le cortex préfrontal, avec une amélioration apparente du contraste entre la matière grise et la matière blanche (cf. Fig. F.7). Quantitativement, on constate une amélioration proche de ce que serait apporté par un système de shimming SH du 6ème degré, donc cohérent avec les simulations.

F.3 Conclusion

Dans ce travail, nous avons proposé une nouvelle méthodologies pour la conception des systèmes de shimming visant l'atténuation de l'inhomogénéité B_0 dans le cerveau humain sous shimming statique du cerveau entier. Les résultats préliminaires du prototype d'un design MCA optimisé sont prometteurs, et une très bonne correspondance entre les cartes de champ attendues et mesurées a été observée. Nous croyons que SCOTCH sera particulièrement bénéfique à 11.7 T, voire absolument nécessaire pour l'EPI.

* * *
* *
*

Publications

Articles in Peer-Reviewed Journals

Bruno Pinho Meneses and Alexis Amadon. *A fieldmap-driven few-channel shim coil design for MRI of the human brain.* Physics in Medicine & Biology, vol. 66, no. 1, pp. 5001, Jan. 2021.

Abstracts at International Conferences with Reading Committee and Proceedings

Bruno Pinho Meneses, Jason P. Stockmann, Edouard Chazel, Eric Giacomini, Paul François Gapais, Franck Mauconduit, Michel Luong, Alexandre Vignaud and Alexis Amadon. *Shim Coils Tailored for Correction of B0 Inhomogeneity in the Human Brain (SCOTCH) at Ultra-High Field.* Proceedings of the 29th Annual Meeting of the International Society for Magnetic Resonance in Medicine, Virtual, 2021. Digital Poster. (Accepted).

Bruno Pinho Meneses and Alexis Amadon. *The Spherical Harmonic Rating: A Metric for B0 Shim System Performance Assessment.* Proceedings of the 29th Annual Meeting of the International Society for Magnetic Resonance in Medicine, Virtual, 2021. Digital Poster. (Accepted).

Bruno Pinho Meneses, Jason P. Stockmann and Alexis Amadon. *First prototype of a Stream-Function-based Multi-Coil Array dedicated to human brain shimming at Ultra-High-Field.* Proceedings of the 28th Annual Meeting of the International Society for Magnetic Resonance in Medicine, Virtual, 2020. Oral Presentation. Awarded *Magna cum Laude.*

Bruno Pinho Meneses and Alexis Amadon. *Human brain shimming performance comparison between matrix-like and stream-function SVD-based multi-coil arrays.* Proceedings of the 28th Annual Meeting of the International Society for Magnetic Resonance in Medicine, Virtual, 2020. Digital Poster.

Bruno Pinho Meneses and Alexis Amadon. *Analysis of Bo Field Shimming Limitations in the Human Brain at Ultra-High-Field.* Proceedings of the 28th Annual Meeting of the International Society for Magnetic Resonance in Medicine, Virtual, 2020. Digital Poster.

Bruno Pinho Meneses, Michel Luong and Alexis Amadon. *Optimized multi-coil array design for human brain shimming at Ultra-High Field.* Proceedings of the 27th Annual Meeting of the International Society for Magnetic Resonance in Medicine, Montreal, Canada, 2019. Digital Poster.

Bruno Pinho Meneses and Alexis Amadon. *A novel few-channel coil design for human brain shimming based on stream function Singular Value Decomposition.* Proceedings of the 27th Annual Meeting of the International Society for Magnetic Resonance in Medicine, Montreal, Canada, 2019. Digital Poster.

Bruno Pinho Meneses and Alexis Amadon. *The Dipole Boundary Method : a simple approach to compute stream functions for shim coil design.* Proceedings of the 27th Annual Meeting of the International Society for Magnetic Resonance in Medicine, Montreal, Canada, 2020. Digital Poster.

Patent

Bruno Pinho Meneses and Alexis Amadon. *Static-magnetic-field shimming coil system for magnetic resonance imaging*, no. WO2020/212463A1, October 2020.

Bibliography

[Abragam 2007] A. Abragam. The principles of nuclear magnetism. Number 32 de The international series of monographs on physics. Oxford Univ. Press, Oxford, reprinted édition, 2007. (Cited on page 27.)

[Abramowitz 2013] M. Abramowitz and I. A. Stegun, editors. Handbook of mathematical functions: with formulas, graphs, and mathematical tables. Dover books on mathematics. Dover Publ, New York, NY, 9. dover print.; [nachdr. der ausg. von 1972] édition, 2013. OCLC: 935935300. (Cited on page 15.)

[Adalsteinsson 1999] E. Adalsteinsson, S. Conolly, H. Xu and D. M. Spielman. *Design of Dedicated Shim Fields*. Proc. Int. Soc. Magn. Reson. Med, 1999. (Cited on page 64.)

[Adamiak 1981] K. Adamiak. *On fredholm integral equations of the first kind occurring in synthesis of electromagnetic fields*. International Journal for Numerical Methods in Engineering, vol. 17, no. 8, pages 1187–1200, 1981. (Cited on page 44.)

[Aghaeifar 2018] A. Aghaeifar, C. Mirkes, J. Bause, T. Steffen, N. Avdievitch, A. Henning and K. Scheffler. *Dynamic B0 shimming of the human brain at 9.4 T with a 16-channel multi-coil shim setup*. Magnetic Resonance in Medicine, vol. 80, no. 4, pages 1714–1725, October 2018. (Cited on pages 56, 64, 93, 104, 142, 183, and 190.)

[Aghaeifar 2020] A. Aghaeifar, J. Zhou, R. Heule, B. Tabibian, B. Schölkopf, F. Jia, M. Zaitsev and K. Scheffler. *A 32-channel multi-coil setup optimized for human brain shimming at 9.4T*. Magnetic Resonance in Medicine, vol. 83, no. 2, pages 749–764, February 2020. (Cited on pages 56, 57, 64, 87, 93, 102, 104, 141, 142, 143, 145, and 183.)

[Arango 2016] N. Arango, J. P. Stockmann, T. Witzel, L. L. Wald and J. White. *Open-source, low-cost, flexible, current feedback-controlled driver circuit for local B0 shim coils and other applications*. Proc. Int. Soc. Magn. Reson. Med, 2016. (Cited on pages 56, 122, 161, 162, and 176.)

[Arango 2019] N. Arango, J. P. Stockmann, E. Adalsteinsson and J. White. *Ultimate Bo Shim and the Design of Optimal Shim Bases.* Proc. Int. Soc. Magn. Reson. Med, May 2019. (Cited on pages 65 and 88.)

[Arango 2020] N. Arango, J. Stockmann, E. Adalsteinsson and J. White. *Computational Shim Coil Design Applied to Augmenting a Shim Array with a Non-Eye-Occluding Face Plate.* In Proceedings of the 28th Annual Meeting of the International Society for Magnetic Resonance in Medicine, volume 28, page 4224, Virtual, 2020. ISMRM. (Cited on pages 56 and 57.)

[Bandettini 2012] P. A. Bandettini. *Twenty years of functional MRI: The science and the stories.* NeuroImage, vol. 62, no. 2, pages 575–588, August 2012. (Cited on page 92.)

[Bayin 2006] S. Bayin. Mathematical Methods in Science and Engineering. John Wiley & Sons, New York, NY, 2006. OCLC: 897540176. (Cited on page 14.)

[Bernstein 2010] M. A. Bernstein, K. F. King and Z. J. Zhou. Handbook of MRI pulse sequences. MyiLibrary, La Vergne (Tenn.), 2010. OCLC: 758321601. (Cited on page 8.)

[Bieri 2013] O. Bieri and K. Scheffler. *Fundamentals of balanced steady state free precession MRI.* Journal of Magnetic Resonance Imaging, vol. 38, no. 1, pages 2–11, 2013. (Cited on page 39.)

[Blamire 1996] A. M. Blamire, D. L. Rothman and T. Nixon. *Dynamic shim updating: A new approach towards optimized whole brain shimming.* Magnetic Resonance in Medicine, vol. 36, no. 1, pages 159–165, 1996. (Cited on page 48.)

[Bloch 1946] F. Bloch. *Nuclear Induction.* Physical Review, vol. 70, no. 7-8, pages 460–474, October 1946. (Cited on page 28.)

[Boulant 2012] N. Boulant and D. I. Hoult. *High tip angle approximation based on a modified Bloch–Riccati equation.* Magnetic Resonance in Medicine, vol. 67, no. 2, pages 339–343, 2012. (Cited on page 29.)

[Brideson 2002] M. A. Brideson, L. K. Forbes and S. Crozier. *Determining complicated winding patterns for shim coils using stream functions and the target-field method.* Concepts in Magnetic Resonance, vol. 14, no. 1, pages 9–18, 2002. (Cited on pages 45 and 46.)

[Bringout 2015] G. Bringout and T. M. Buzug. *Coil Design for Magnetic Particle Imaging: Application for a Preclinical Scanner.* IEEE Transactions on Magnetics, vol. 51, no. 2, pages 1–8, February 2015. (Cited on pages 65, 71, and 113.)

[Brown 2014] R. W. Brown, Y.-C. N. Cheng, E. M. Haacke, M. R. Thompson and R. Venkatesan. Magnetic resonance imaging: physical principles and sequence design.

John Wiley & Sons, Inc, Hoboken, New Jersey, second edition édition, 2014. (Cited on page 8.)

[Cai 2020] Y. Cai, H.-J. Yang, X. Li, T. Hu, Y. Huang, Y. Shan, M. Lu, W. S. Liu, D. Li and H. Han. *Optimization of Multi-Coil Array Design for Efficient Human Brain Shimming at 3T.* In Proceedings of the 28th Annual Meeting of the International Society for Magnetic Resonance in Medicine, volume 28, page 4229, Virtual, 2020. ISMRM. (Cited on page 57.)

[Can 2019] M. K. Can, P.-Y. Li, J. Zhou, P.-Y. Wu, Y.-T. Li, R. Ilmoniemi and F.-H. Lin. *Designs of shim coils with distributed currents for 3T human brain magnetic resonance imaging.* Proc. Int. Soc. Magn. Reson. Med, May 2019. (Cited on pages 65 and 183.)

[Chang 2018] P. Chang, S. Nassirpour and A. Henning. *Modeling real shim fields for very high degree (and order) B0 shimming of the human brain at 9.4 T.* Magnetic Resonance in Medicine, vol. 79, no. 1, pages 529–540, 2018. (Cited on pages 47, 48, and 50.)

[Chmurny 1990] G. N. Chmurny and D. I. Hoult. *The Ancient and Honourable Art of Shimming.* Concepts in Magnetic Resonance, vol. 2, no. 3, pages 131–149, 1990. (Cited on pages 21, 44, and 63.)

[Collins 2002] C. M. Collins, B. Yang, Q. X. Yang and M. B. Smith. *Numerical calculations of the static magnetic field in three-dimensional multi-tissue models of the human head.* Magnetic Resonance Imaging, vol. 20, no. 5, pages 413–424, June 2002. (Cited on page 100.)

[Damme 2021] L. V. Damme, F. Mauconduit, T. Chambrion, N. Boulant and V. Gras. *Universal nonselective excitation and refocusing pulses with improved robustness to off-resonance for Magnetic Resonance Imaging at 7 Tesla with parallel transmission.* Magnetic Resonance in Medicine, vol. 85, no. 2, pages 678–693, 2021. (Cited on page 29.)

[Darnell 2017] D. Darnell, T.-K. Truong and A. W. Song. *Integrated parallel reception, excitation, and shimming (iPRES) with multiple shim loops per radio-frequency coil element for improved B0 shimming.* Magnetic Resonance in Medicine, vol. 77, no. 5, pages 2077–2086, 2017. (Cited on page 56.)

[Darnell 2018] D. Darnell, Y. Ma, H. Wang, F. Robb, A. W. Song and T.-K. Truong. *Adaptive integrated parallel reception, excitation, and shimming (iPRES-A) with microelectromechanical systems switches.* Magnetic Resonance in Medicine, vol. 80, no. 1, pages 371–379, 2018. (Cited on page 56.)

[Davids 2021] M. Davids, B. Guérin, V. Klein and L. L. Wald. *Optimization of MRI Gradient Coils With Explicit Peripheral Nerve Stimulation Constraints.* IEEE

Transactions on Medical Imaging, vol. 40, no. 1, pages 129–142, January 2021. (Cited on page 37.)

[Dengler 2016] R. Dengler. *Self inductance of a wire loop as a curve integral.* Advanced Electromagnetics, vol. 5, no. 1, pages 1–8, January 2016. (Cited on page 118.)

[Durand 1968] E. Durand. Magnetostatique. Masson et Cie, Paris, France, 1968. (Cited on page 18.)

[Durrant 2003] C. Durrant, M. Hertzberg and P. Kuchel. *Magnetic susceptibility: Further insights into macroscopic and microscopic fields and the sphere of Lorentz.* Concepts in Magnetic Resonance, vol. 18A, no. 1, pages 72–95, 2003. (Cited on page 22.)

[Duyn 2012] J. H. Duyn. *The future of ultra-high field MRI and fMRI for study of the human brain.* NeuroImage, vol. 62, no. 2, pages 1241 – 1248, 2012. (Cited on page 63.)

[Elshatlawy 2019] H. Elshatlawy, F. Jia, A. Aghaeifar, X. Gao, K. Scheffler and M. Zaitsev. *18X7 Human brain field maps for shim coil designs*, November 2019. type: dataset. (Cited on pages 123 and 176.)

[Engelsberg 1992] M. Engelsberg. *Target-field approach for the design of power-efficient solenoidal magnets.* Measurement Science and Technology, vol. 3, no. 11, pages 1063–1067, November 1992. (Cited on page 46.)

[Ernst 1966] R. R. Ernst and W. A. Anderson. *Application of Fourier Transform Spectroscopy to Magnetic Resonance.* Review of Scientific Instruments, vol. 37, no. 1, pages 93–102, January 1966. (Cited on page 33.)

[Esmaeili 2020] M. Esmaeili, J. Stockmann, B. Strasser, N. Arango, B. Thapa, Z. Wang, A. van der Kouwe, J. Dietrich, D. P. Cahill, T. T. Batchelor, J. White, E. Adalsteinsson, L. Wald and O. C. Andronesi. *An integrated RF-receive/B 0 -shim array coil boosts performance of whole-brain MR spectroscopic imaging at 7 T.* Scientific Reports, vol. 10, no. 1, page 15029, September 2020. (Cited on page 56.)

[Fillmer 2016] A. Fillmer, S. J. Vannesjo, M. Pavan, M. Scheidegger, K. P. Pruessmann and A. Henning. *Fast iterative pre-emphasis calibration method enabling third-order dynamic shim updated fMRI.* Magnetic Resonance in Medicine, vol. 75, no. 3, pages 1119–1131, 2016. (Cited on pages 48 and 49.)

[Forbes 2001] L. K. Forbes and S. Crozier. *A novel target-field method for finite-length magnetic resonance shim coils: I. Zonal shims.* Journal of Physics D: Applied Physics, vol. 34, no. 24, pages 3447–3455, December 2001. (Cited on page 46.)

[Forbes 2002] L. K. Forbes and S. Crozier. *A novel target-field method for finite-length magnetic resonance shim coils: II. Tesseral shims.* Journal of Physics D: Applied Physics, vol. 35, no. 9, pages 839–849, May 2002. (Cited on page 46.)

[Forbes 2003] L. K. Forbes and S. Crozier. *A novel target-field method for magnetic resonance shim coils: III. Shielded zonal and tesseral coils.* Journal of Physics D: Applied Physics, vol. 36, no. 2, pages 68–80, January 2003. (Cited on page 46.)

[Golay 1958] M. J. E. Golay. *Field Homogenizing Coils for Nuclear Spin Resonance Instrumentation.* Review of Scientific Instruments, vol. 29, no. 4, page 313, 1958. (Cited on page 44.)

[Graaf 2003] R. A. d. Graaf, P. B. Brown, S. McIntyre, D. L. Rothman and T. W. Nixon. *Dynamic shim updating (DSU) for multislice signal acquisition.* Magnetic Resonance in Medicine, vol. 49, no. 3, pages 409–416, 2003. (Cited on page 48.)

[Gray 1978] C. G. Gray. *Simplified derivation of the magnetostatic multipole expansion using the scalar potential.* American Journal of Physics, vol. 46, no. 5, pages 582–583, May 1978. (Cited on page 13.)

[Griffiths 2017] D. J. Griffiths. Introduction to quantum mechanics. Cambridge University Press, Cambridge, second edition [2017 edition] édition, 2017. (Cited on page 27.)

[Griswold 2002] M. A. Griswold, P. M. Jakob, R. M. Heidemann, M. Nittka, V. Jellus, J. Wang, B. Kiefer and A. Haase. *Generalized autocalibrating partially parallel acquisitions (GRAPPA).* Magnetic Resonance in Medicine, vol. 47, no. 6, pages 1202–1210, 2002. (Cited on page 36.)

[Guerin 2020] B. Guerin, E. Milshteyn, L. L. Wald and J. Stockmann. *Improvements in flip-angle uniformization at 7 Tesla using an integrated RF/Bo shim array coil and composite pulses.* In Proceedings of the 28th Annual Meeting of the International Society for Magnetic Resonance in Medicine, volume 28, page 613, Virtual, 2020. ISMRM. (Cited on page 57.)

[Haacke 1999] E. M. Haacke, R. W. Brown, M. R. Thompson and R. Venkatesan. Magnetic Resonance Imaging - Physical Principles And Sequence Design. Wiley-Liss, 1999. (Cited on page 34.)

[Hahn 1950] E. L. Hahn. *Nuclear Induction Due to Free Larmor Precession.* Physical Review, vol. 77, no. 2, pages 297–298, January 1950. (Cited on page 31.)

[Han 2013] H. Han, A. W. Song and T.-K. Truong. *Integrated parallel reception, excitation, and shimming (iPRES): Integrated Parallel Reception, Excitation, and Shimming.* Magnetic Resonance in Medicine, vol. 70, no. 1, pages 241–247, July 2013. (Cited on pages 56, 64, and 93.)

[Hetherington 2021] H. P. Hetherington, C. H. Moon, M. Schwerter, N. J. Shah and J. W. Pan. *Dynamic B_o shimming for multiband imaging using high order spherical harmonic shims.* Magnetic Resonance in Medicine, vol. 85, no. 1, pages 531–543, January 2021. (Cited on pages 48, 50, 145, and 183.)

[Hillenbrand 2005] D. F. Hillenbrand, K. M. Lo, W. F. B. Punchard, T. G. Reese and P. M. Starewicz. *High-order MR shimming: a simulation study of the effectiveness of competing methods, using an established susceptibility model of the human head.* Applied Magnetic Resonance, vol. 29, no. 1, pages 39–64, March 2005. (Cited on pages 44, 93, and 100.)

[Hoult 1976] D. I. Hoult and R. E. Richards. *The signal-to-noise ratio of the nuclear magnetic resonance experiment.* Journal of Magnetic Resonance (1969), vol. 24, no. 1, pages 71–85, October 1976. (Cited on page 30.)

[Hoult 1998] D. I. Hoult and D. Lee. *Shimming a superconducting nuclear-magnetic-resonance imaging magnet with steel.* Review of Scientific Instruments, vol. 56, no. 1, page 131, June 1998. (Cited on page 21.)

[Hsu 2005] J.-J. Hsu and G. H. Glover. *Mitigation of susceptibility-induced signal loss in neuroimaging using localized shim coils.* Magnetic Resonance in Medicine, vol. 53, no. 2, pages 243–248, 2005. (Cited on pages 52 and 53.)

[Iwasa 2009] Y. Iwasa. Case studies in superconducting magnets: design and operational issues. Springer, New York, second edition édition, 2009. (Cited on page 20.)

[Jackson 2007] J. Jackson. CLASSICAL ELECTRODYNAMICS, 3RD ED. Wiley India Pvt. Limited, 2007. (Cited on pages 7, 13, 18, 66, and 94.)

[Jesmanowicz 2001a] A. Jesmanowicz, V. Roopchansingh, R. W. Cox, P. Starewicz, W. F. B. Punchard and J. S. Hyde. *Local Ferroshims Using Office Copier Toner.* In Proceedings of the International Society for Magnetic Resonance in Medicine, volume 9, page 617, 2001. (Cited on pages 51 and 93.)

[Jesmanowicz 2001b] A. Jesmanowicz, J. S. Hyde, W. F. Punchard and P. M. Starewicz. *Method for Shimming a Static Magnetic Field in a Local MRI Coil*, no. US 6294972 B1, September 2001. (Cited on pages 51 and 52.)

[Jezzard 1995] P. Jezzard and R. S. Balaban. *Correction for geometric distortion in echo planar images from Bo field variations.* Magnetic Resonance in Medicine, vol. 34, no. 1, pages 65–73, 1995. (Cited on pages 63 and 92.)

[Jia 2020] F. Jia, H. Elshatlawy, A. Aghaeifar, Y. Chu, Y. Hsu, S. Littin, S. Kroboth, H. Yu, P. Amrein, X. Gao, W. Yang, P. LeVan, K. Scheffler and M. Zaitsev. *Design of a shim coil array matched to the human brain anatomy.* Magnetic Resonance in Medicine, vol. 83, no. 4, pages 1442–1457, April 2020. (Cited on pages 65 and 113.)

[Juchem 2006] C. Juchem, B. Muller-Bierl, F. Schick, N. K. Logothetis and J. Pfeuffer. *Combined passive and active shimming for in vivo MR spectroscopy at high magnetic fields.* Journal of Magnetic Resonance, vol. 183, no. 2, pages 278–289, December 2006. (Cited on page 93.)

[Juchem 2010a] C. Juchem, T. W. Nixon, P. Diduch, D. L. Rothman, P. Starewicz and R. A. D. Graaf. *Dynamic shimming of the human brain at 7 T.* Concepts in Magnetic Resonance Part B: Magnetic Resonance Engineering, vol. 37B, no. 3, pages 116–128, 2010. (Cited on page 48.)

[Juchem 2010b] C. Juchem, T. W. Nixon, S. McIntyre, D. L. Rothman and R. A. d. Graaf. *Magnetic field homogenization of the human prefrontal cortex with a set of localized electrical coils.* Magnetic Resonance in Medicine, vol. 63, no. 1, pages 171–180, 2010. (Cited on pages 52 and 53.)

[Juchem 2010c] C. Juchem, T. W. Nixon, S. McIntyre, D. L. Rothman and R. A. d. Graaf. *Magnetic field modeling with a set of individual localized coils.* Journal of Magnetic Resonance, vol. 204, no. 2, pages 281–289, June 2010. (Cited on pages 47 and 142.)

[Juchem 2011] C. Juchem, T. W. Nixon, S. McIntyre, V. O. Boer, D. L. Rothman and R. A. d. Graaf. *Dynamic multi-coil shimming of the human brain at 7T.* Journal of Magnetic Resonance, vol. 212, no. 2, pages 280 – 288, 2011. (Cited on pages 26, 54, 56, 64, 93, 102, 145, 183, and 190.)

[Juchem 2013] C. Juchem, D. Green and R. A. de Graaf. *Multi-coil magnetic field modeling.* Journal of Magnetic Resonance, vol. 236, pages 95–104, November 2013. (Cited on page 54.)

[Juchem 2015] C. Juchem, S. Umesh Rudrapatna, T. W. Nixon and R. A. de Graaf. *Dynamic multi-coil technique (DYNAMITE) shimming for echo-planar imaging of the human brain at 7 Tesla.* NeuroImage, vol. 105, pages 462–472, January 2015. (Cited on pages 49, 54, 56, 145, 183, and 190.)

[Juchem 2017a] C. Juchem and R. A. de Graaf. *B 0 magnetic field homogeneity and shimming for in vivo magnetic resonance spectroscopy.* Analytical Biochemistry, vol. 529, pages 17–29, July 2017. (Cited on page 63.)

[Juchem 2017b] C. Juchem and R. A. d. Graaf. *Bo magnetic field homogeneity and shimming for in vivo magnetic resonance spectroscopy.* Analytical Biochemistry, vol. 529, pages 17 – 29, 2017. (Cited on page 56.)

[Juchem 2020a] C. Juchem, C. Cudalbu, R. A. d. Graaf, R. Gruetter, A. Henning, H. P. Hetherington and V. O. Boer. *Bo shimming for in vivo magnetic resonance spectroscopy: Experts' consensus recommendations.* NMR in Biomedicine, vol. n/a, no. n/a, page e4350, 2020. (Cited on pages 39, 47, and 129.)

[Juchem 2020b] C. Juchem, S. Theilenberg, C. Kumaragamage, M. Mullen, L. DelaBarre, G. Adriany, P. B. Brown, S. McIntyre, T. W. Nixon, M. Garwood and R. A. d. Graaf. *Dynamic multicoil technique (DYNAMITE) MRI on human brain.* Magnetic Resonance in Medicine, vol. 84, no. 6, pages 2953–2963, 2020. (Cited on page 57.)

[Karsa 2019] A. Karsa and K. Shmueli. *SEGUE: A Speedy rEgion-Growing Algorithm for Unwrapping Estimated Phase.* IEEE Transactions on Medical Imaging, vol. 38, no. 6, pages 1347–1357, June 2019. (Cited on pages 43, 122, and 129.)

[Kikinis 2014] R. Kikinis, S. D. Pieper and K. G. Vosburgh. *3D Slicer: A Platform for Subject-Specific Image Analysis, Visualization, and Clinical Support.* In F. A. Jolesz, editor, Intraoperative Imaging and Image-Guided Therapy, pages 277–289. Springer, New York, NY, 2014. (Cited on page 48.)

[Kim 2017] T. Kim, Y. Lee, T. Zhao, H. P. Hetherington and J. W. Pan. *Gradient-echo EPI using a high-degree shim insert coil at 7 T: Implications for BOLD fMRI: GE BOLD fMRI With a Shim Insert Coil at 7 T.* Magnetic Resonance in Medicine, vol. 78, no. 5, pages 1734–1745, November 2017. (Cited on pages 64 and 183.)

[Koch 2006a] K. M. Koch, P. B. Brown, D. L. Rothman and R. A. de Graaf. *Sample-specific diamagnetic and paramagnetic passive shimming.* Journal of Magnetic Resonance, vol. 182, no. 1, pages 66–74, September 2006. (Cited on page 51.)

[Koch 2006b] K. M. Koch, S. McIntyre, T. W. Nixon, D. L. Rothman and R. A. de Graaf. *Dynamic shim updating on the human brain.* Journal of Magnetic Resonance, vol. 180, no. 2, pages 286–296, June 2006. (Cited on pages 48, 49, and 102.)

[Koch 2006c] K. M. Koch, X. Papademetris, D. L. Rothman and R. A. d. Graaf. *Rapid calculations of susceptibility-induced magnetostatic field perturbations for in vivo magnetic resonance.* Physics in Medicine and Biology, vol. 51, no. 24, pages 6381–6402, December 2006. (Cited on page 22.)

[Koch 2009] K. M. Koch, D. L. Rothman and R. A. de Graaf. *Optimization of static magnetic field homogeneity in the human and animal brain in vivo.* Progress in Nuclear Magnetic Resonance Spectroscopy, vol. 54, no. 2, pages 69–96, February 2009. (Cited on page 35.)

[Kochan 2015] M. Kochan, P. Daga, N. Burgos, M. White, M. J. Cardoso, L. Mancini, G. P. Winston, A. W. McEvoy, J. Thornton, T. Yousry, J. S. Duncan, D. Stoyanov and S. Ourselin. *Simulated field maps for susceptibility artefact correction in interventional MRI.* International Journal of Computer Assisted Radiology and Surgery, vol. 10, no. 9, pages 1405–1416, September 2015. (Cited on page 100.)

[Kreis 2020] R. Kreis, V. Boer, I. Choi, C. Cudalbu, R. A. Graaf, C. Gasparovic, A. Heerschap, M. Krššák, B. Lanz, A. A. Maudsley, M. Meyerspeer, J. Near, G. Öz, S. Posse, J. Slotboom, M. Terpstra, I. Tkáč, M. Wilson, W. Bogner and Experts' Working Group on Terminology for MR Spectroscopy. *Terminology and concepts for the characterization of in vivo MR spectroscopy methods and MR spectra: Background and experts' consensus recommendations.* NMR in Biomedicine, August 2020. (Cited on page 25.)

[Ladd 2018] M. E. Ladd, P. Bachert, M. Meyerspeer, E. Moser, A. M. Nagel, D. G. Norris, S. Schmitter, O. Speck, S. Straub and M. Zaiss. *Pros and cons of ultra-high-field MRI/MRS for human application.* Progress in Nuclear Magnetic Resonance Spectroscopy, vol. 109, pages 1 – 50, 2018. (Cited on page 63.)

[Lagrange 1869] J. L. Lagrange. Mémoire Sur la Théorie du Mouvement des Fluides. Gauthier-Villars, Paris, 1869. (Cited on page 18.)

[Larsson 2003] E. G. Larsson, D. Erdogmus, R. Yan, J. C. Principe and J. R. Fitzsimmons. *SNR-optimality of sum-of-squares reconstruction for phased-array magnetic resonance imaging.* Journal of Magnetic Resonance, vol. 163, no. 1, pages 121–123, July 2003. (Cited on page 43.)

[Lauterbur 1973] P. C. Lauterbur. *Image Formation by Induced Local Interactions: Examples Employing Nuclear Magnetic Resonance.* Nature, vol. 242, no. 5394, pages 190–191, March 1973. (Cited on page 32.)

[Lazarus 2019] C. Lazarus, P. Weiss, N. Chauffert, F. Mauconduit, L. E. Gueddari, C. Destrieux, I. Zemmoura, A. Vignaud and P. Ciuciu. *SPARKLING: variable-density k-space filling curves for accelerated T2*-weighted MRI.* Magnetic Resonance in Medicine, vol. 81, no. 6, pages 3643–3661, 2019. (Cited on page 39.)

[Lee 2018] S. Lee, S. Hwang, J. Barg and S. Yeo. *Rapid, theoretically artifact-free calculation of static magnetic field induced by voxelated susceptibility distribution in an arbitrary volume of interest.* Magnetic Resonance in Medicine, vol. 80, no. 5, pages 2109–2121, November 2018. (Cited on page 23.)

[Lemdiasov 2005] R. A. Lemdiasov and R. Ludwig. *A stream function method for gradient coil design.* Concepts in Magnetic Resonance Part B: Magnetic Resonance Engineering, vol. 26B, no. 1, pages 67–80, 2005. (Cited on page 46.)

[Li 1995] S. Li, G. D. Williams, T. A. Frisk, B. W. Arnold and M. B. Smith. *A computer simulation of the static magnetic field distribution in the human head.* Magnetic Resonance in Medicine, vol. 34, no. 2, pages 268–275, 1995. (Cited on page 100.)

[Li 1996] S. Li, B. J. Dardzinski, C. M. Collins, Q. X. Yang and M. B. Smith. *Three-dimensional mapping of the static magnetic field inside the human head.* Magnetic Resonance in Medicine, vol. 36, no. 5, pages 705–714, 1996. (Cited on page 100.)

[Lopez 2009a] H. S. Lopez, F. Liu, M. Poole and S. Crozier. *Equivalent Magnetization Current Method Applied to the Design of Gradient Coils for Magnetic Resonance Imaging.* IEEE Transactions on Magnetics, vol. 45, no. 2, pages 767–775, February 2009. (Cited on page 46.)

[Lopez 2009b] H. S. Lopez, M. Poole and S. Crozier. *An improved equivalent magnetization current method applied to the design of local breast gradient coils.* Journal of Magnetic Resonance, vol. 199, no. 1, pages 48–55, July 2009. (Cited on page 46.)

[LT 2009] LT. *Octal 16-/12-Bit Rail-to-Rail DACs with 10ppm/°C Max Reference*, 2009. (Cited on page 165.)

[Lustig 2007] M. Lustig, D. Donoho and J. M. Pauly. *Sparse MRI: The application of compressed sensing for rapid MR imaging.* Magnetic Resonance in Medicine, vol. 58, no. 6, pages 1182–1195, 2007. (Cited on page 39.)

[Lüdeke 1985] K. M. Lüdeke, P. Röschmann and R. Tischler. *Susceptibility artefacts in NMR imaging.* Magnetic Resonance Imaging, vol. 3, no. 4, pages 329–343, January 1985. (Cited on page 92.)

[MacRobert 1948] T. MacRobert. Spherical Harmonics: An Elementary Treatise on Harmonic Functions, with Applications. Chronic illness in the United States. Dover Publications, 1948. (Cited on page 15.)

[Makris 2008] N. Makris, L. Angelone, S. Tulloch, S. Sorg, J. Kaiser, D. Kennedy and G. Bonmassar. *MRI-based anatomical model of the human head for specific absorption rate mapping.* Medical & Biological Engineering & Computing, vol. 46, no. 12, pages 1239–1251, December 2008. (Cited on pages 23 and 97.)

[Mansfield 1977a] P. Mansfield. *Multi-planar image formation using NMR spin echoes.* Journal of Physics C: Solid State Physics, vol. 10, no. 3, pages L55–L58, February 1977. (Cited on pages 33 and 34.)

[Mansfield 1977b] P. Mansfield and A. A. Maudsley. *Medical imaging by NMR.* The British Journal of Radiology, vol. 50, no. 591, pages 188–194, March 1977. (Cited on page 32.)

[Markl 2012] M. Markl and J. Leupold. *Gradient echo imaging.* Journal of Magnetic Resonance Imaging, vol. 35, no. 6, pages 1274–1289, 2012. (Cited on page 33.)

[Marques 2005] J. Marques and R. Bowtell. *Application of a Fourier-based method for rapid calculation of field inhomogeneity due to spatial variation of magnetic susceptibility.* Concepts in Magnetic Resonance Part B: Magnetic Resonance Engineering, vol. 25B, no. 1, pages 65–78, April 2005. (Cited on page 22.)

[Meneses 2019a] B. P. Meneses and A. Amadon. *The Dipole Boundary Method : a simple approach to compute stream functions for shim coil design.* In Proceedings of the 27th Annual Meeting of ISMRM, page 1476, Montreal, Canada, 2019. (Cited on pages 62, 66, 190, and 208.)

[Meneses 2019b] B. P. Meneses and A. Amadon. *A novel few-channel coil design for human brain shimming based on stream function Singular Value Decomposition.* In Proceedings of the 27th Annual Meeting of ISMRM, page 1483, Montreal, Canada, 2019. (Cited on pages 62, 64, 183, 190, and 208.)

[Meneses 2019c] B. P. Meneses, M. Luong and A. Amadon. *Optimized multi-coil array design for human brain shimming at Ultra-High Field.* In Proceedings of the 27th Annual Meeting of ISMRM, page 1477, Montreal, Canada, May 2019. (Cited on pages 64, 93, 112, 123, 175, 183, 184, 190, and 208.)

[Moeller 2010] S. Moeller, E. Yacoub, C. A. Olman, E. Auerbach, J. Strupp, N. Harel and K. Uğurbil. *Multiband multislice GE-EPI at 7 tesla, with 16-fold acceleration using partial parallel imaging with application to high spatial and temporal whole-brain fMRI.* Magnetic Resonance in Medicine, vol. 63, no. 5, pages 1144–1153, 2010. (Cited on page 130.)

[Morrell 1997] G. Morrell and D. Spielman. *Dynamic shimming for multi-slice magnetic resonance imaging.* Magnetic Resonance in Medicine, vol. 38, no. 3, pages 477–483, 1997. (Cited on page 48.)

[Mullen 2020] M. Mullen and M. Garwood. *Contemporary approaches to high-field magnetic resonance imaging with large field inhomogeneity.* Progress in Nuclear Magnetic Resonance Spectroscopy, vol. 120-121, pages 95–108, October 2020. (Cited on pages 35 and 92.)

[Ogata 2010] K. Ogata. Modern control engineering. Prentice-Hall electrical engineering series. Instrumentation and controls series. Prentice-Hall, Boston, 5th ed édition, 2010. (Cited on page 161.)

[Ogawa 1990] S. Ogawa, T. M. Lee, A. R. Kay and D. W. Tank. *Brain magnetic resonance imaging with contrast dependent on blood oxygenation.* Proceedings of the National Academy of Sciences, vol. 87, no. 24, pages 9868–9872, 1990. (Cited on page 34.)

[Oh 2020] C. Oh, E. Choi, W. Jung, H.-g. Shin and J. Lee. *Machine designing: a multi-coil local shim design using Bayesian optimization.* In Proceedings of the 28th Annual Meeting of the International Society for Magnetic Resonance in Medicine, volume 28, page 4227, July 2020. (Cited on pages 57, 141, and 183.)

[Pan 2012] J. W. Pan, K.-M. Lo and H. P. Hetherington. *Role of very high order and degree B0 shimming for spectroscopic imaging of the human brain at 7 tesla.* Magnetic resonance in medicine, vol. 68, no. 4, pages 1007–1017, October 2012. (Cited on pages 44, 48, 64, 93, and 183.)

[Peeren 2003] G. N. Peeren. *Stream function approach for determining optimal surface currents.* PhD Thesis, Technische Universiteit Eindhoven, 2003. (Cited on pages 18, 19, 46, 65, 66, 69, 71, and 72.)

[Pinho Meneses 2020a] B. Pinho Meneses and A. Amadon. *Analysis of B0 Field Shimming Limitations in the Human Brain at Ultra-High-Field.* In Proceedings of the 28th Annual Meeting of ISMRM, volume 28, page 4223, Virtual, 2020. (Cited on pages 92 and 208.)

[Pinho Meneses 2020b] B. Pinho Meneses and A. Amadon. *A fieldmap-driven few-channel shim coil design for MRI of the human brain.* Physics in Medicine & Biology, vol. 66, no. 1, 2020. (Cited on pages 62, 99, 109, 113, 183, and 207.)

[Pinho Meneses 2020c] B. Pinho Meneses and A. Amadon. *Human brain shimming performance comparison between matrix-like and stream-function SVD-based multi-coil arrays.* In Proceedings of the 28th Annual Meeting of ISMRM, volume 28, page 4222, Virtual Conference, 2020. (Cited on pages 144, 189, and 207.)

[Pinho Meneses 2020d] B. Pinho Meneses and A. Amadon. *Static-magnetic-field shimming coil system for magnetic resonance imaging*, no. WO2020212463A1, October 2020. (Cited on pages 62, 64, 112, 119, 175, 183, and 190.)

[Pinho Meneses 2020e] B. Pinho Meneses, J. Stockmann and A. Amadon. *First prototype of a Stream-Function-based Multi-Coil Array dedicated to human brain shimming at Ultra-High-Field.* In Proceedings of the 28th Annual Meeting of ISMRM, volume 28, page 0766, Virtual, 2020. (Cited on pages 93, 102, 112, 175, 183, 184, and 207.)

[Pinho Meneses 2021a] B. Pinho Meneses and A. Amadon. *The Spherical Harmonic Rating: A Metric for B0 Shim System Performance Assessment.* In Proceedings of the 29th Annual Meeting of the International Society for Magnetic Resonance in Medicine, Virtual, 2021. ISMRM. (Cited on pages 112, 183, and 207.)

[Pinho Meneses 2021b] B. Pinho Meneses, J. Stockmann, E. Chazel, E. Giacomini, P.-F. Gapais, F. Mauconduit, M. Luong, A. Vignaud and A. Amadon. *Shim Coils Tailored for Correction of B0 Inhomogeneity in the Human Brain (SCOTCH) at Ultra High Field.* In Proceedings of the 29th Annual Meeting of the International Society for Magnetic Resonance in Medicine, Virtual Conference, 2021. (Cited on pages 112, 175, and 207.)

[Pissanetzky 1992] S. Pissanetzky. *Minimum energy MRI gradient coils of general geometry.* Measurement Science and Technology, vol. 3, no. 7, pages 667–673, July 1992. (Cited on pages 44, 65, 71, and 113.)

[Pohmann 2016] R. Pohmann, O. Speck and K. Scheffler. *Signal-to-noise ratio and MR tissue parameters in human brain imaging at 3, 7, and 9.4 tesla using current receive coil arrays.* Magnetic Resonance in Medicine, vol. 75, no. 2, pages 801–809, 2016. (Cited on page 31.)

[Poole 2007a] M. Poole. *Improved Equipment and Techniques for Dynamic Shimming in High Field MRI.* PhD, University of Nottingham, 2007. (Cited on pages 41, 45, and 46.)

[Poole 2007b] M. Poole and R. Bowtell. *Novel gradient coils designed using a boundary element method.* Concepts in Magnetic Resonance Part B: Magnetic Resonance

Engineering, vol. 31B, no. 3, pages 162–175, August 2007. (Cited on pages 65, 71, and 113.)

[Poole 2010] M. Poole, P. Weiss, H. S. Lopez, M. Ng and S. Crozier. *Minimax current density coil design.* Journal of Physics D: Applied Physics, vol. 43, no. 9, page 095001, March 2010. (Cited on pages 44 and 46.)

[Poole 2014] M. S. Poole and N. Jon Shah. *Convex optimisation of gradient and shim coil winding patterns.* Journal of Magnetic Resonance, vol. 244, pages 36–45, July 2014. (Cited on page 46.)

[Punchard 2013] W. F. Punchard. *Shim Insert for High-Field MRI Magnets*, no. US 8536870 B2, September 2013. (Cited on pages 64 and 89.)

[Quettier 2020] L. Quettier, G. Aubert, J. Belorgey, C. Berriaud, P. Bredy, G. Dilasser, O. Dubois, G. Gilgrass, Q. Guihard, V. Jannot, F.-P. Juster, H. Lannou, F. Molinie, F. Nunio, A. Roger, T. Schild, L. Scola, A. Sinanna, V. Stepanov and P. Vedrine. *Commissioning Completion of the Iseult Whole Body 11.7 T MRI System.* IEEE Transactions on Applied Superconductivity, vol. 30, no. 4, pages 1–5, June 2020. (Cited on pages 57, 92, 129, and 175.)

[Robinson 2014] S. Robinson, H. Schödl and S. Trattnig. *A method for unwrapping highly wrapped multi-echo phase images at very high field: UMPIRE.* Magnetic Resonance in Medicine, vol. 72, no. 1, pages 80–92, 2014. (Cited on page 43.)

[Roméo 1984] F. Roméo and D. I. Hoult. *Magnet field profiling: Analysis and correcting coil design.* Magnetic Resonance in Medicine, vol. 1, no. 1, pages 44–65, 1984. (Cited on pages 14, 18, 44, 45, 63, 96, and 107.)

[Rudrapatna 2016] S. U. Rudrapatna, C. Juchem, T. W. Nixon and R. A. d. Graaf. *Dynamic multi-coil tailored excitation for transmit B1 correction at 7 Tesla.* Magnetic Resonance in Medicine, vol. 76, no. 1, pages 83–93, 2016. (Cited on page 57.)

[Rudrapatna 2019] S. U. Rudrapatna, F. Fluerenbrock, T. W. Nixon, R. A. d. Graaf and C. Juchem. *Combined imaging and shimming with the dynamic multi-coil technique.* Magnetic Resonance in Medicine, vol. 81, no. 2, pages 1424–1433, 2019. (Cited on page 57.)

[Rzedzian 1983] R. Rzedzian, P. Mansfield, M. Doyle, D. Guilfoyle, B. Chapman, R. E. Coupland, A. Chrispin and P. Small. *REAL-TIME NUCLEAR MAGNETIC RESONANCE CLINICAL IMAGING IN PAEDIATRICS.* The Lancet, vol. 322, no. 8362, pages 1281–1282, December 1983. (Cited on page 34.)

[Sadeghi-Tarakameh 2020] A. Sadeghi-Tarakameh, L. DelaBarre, R. L. Lagore, A. Torrado-Carvajal, X. Wu, A. Grant, G. Adriany, G. J. Metzger, P.-F. V. d. Moortele, K. Ugurbil, E. Atalar and Y. Eryaman. *In vivo human head MRI at*

10.5T: A radiofrequency safety study and preliminary imaging results. Magnetic Resonance in Medicine, vol. 84, no. 1, pages 484–496, 2020. (Cited on page 92.)

[Salomir 2003] R. Salomir, B. D. de Senneville and C. T. Moonen. *A fast calculation method for magnetic field inhomogeneity due to an arbitrary distribution of bulk susceptibility.* Concepts in Magnetic Resonance Part B: Magnetic Resonance Engineering, vol. 19B, no. 1, pages 26–34, 2003. (Cited on pages 22, 63, and 92.)

[Schwerter 2019] M. Schwerter, H. Hetherington, C. H. Moon, J. Pan, J. Felder, L. Tellmann and N. J. Shah. *Interslice current change constrained B $_o$ shim optimization for accurate high-order dynamic shim updating with strongly reduced eddy currents.* Magnetic Resonance in Medicine, vol. 82, no. 1, pages 263–275, July 2019. (Cited on page 48.)

[Smith 2002] S. M. Smith. *Fast robust automated brain extraction.* Human Brain Mapping, vol. 17, no. 3, pages 143–155, November 2002. (Cited on pages 97, 119, and 129.)

[Smith 2009] S. M. Smith, P. T. Fox, K. L. Miller, D. C. Glahn, P. M. Fox, C. E. Mackay, N. Filippini, K. E. Watkins, R. Toro, A. R. Laird and C. F. Beckmann. *Correspondence of the brain's functional architecture during activation and rest.* Proceedings of the National Academy of Sciences of the United States of America, vol. 106, no. 31, pages 13040–13045, 2009. (Cited on page 48.)

[Smith 2010] T. B. Smith and K. S. Nayak. *MRI artifacts and correction strategies.* Imaging in Medicine, vol. 2, no. 4, pages 445–457, August 2010. (Cited on page 92.)

[Stockmann 2013] J. Stockmann, T. Witzel, J. Blau, J. Polimeni, Z. Wei, B. Keil and L. Wald. *Combined shim-rf array for highly efficient shimming of the brain at 7 tesla.* Proc. Int. Soc. Magn. Reson. Med, vol. 21, January 2013. (Cited on pages 56, 64, 93, 119, and 183.)

[Stockmann 2016] J. P. Stockmann, T. Witzel, B. Keil, J. R. Polimeni, A. Mareyam, C. LaPierre, K. Setsompop and L. L. Wald. *A 32-channel combined RF and Bo shim array for 3T brain imaging.* Magnetic resonance in medicine, vol. 75, no. 1, pages 441–451, January 2016. (Cited on pages 55, 56, 64, 144, 145, and 190.)

[Stockmann 2018] J. P. Stockmann and L. L. Wald. *In vivo B 0 field shimming methods for MRI at 7 T.* NeuroImage, vol. 168, pages 71–87, March 2018. (Cited on pages 26, 41, 64, 104, and 183.)

[TI 2005] TI. *High-Voltage, High-Current Op Amp, Excellent Output Swing, OPA549*, October 2005. (Cited on pages 146 and 162.)

[Topfer 2016] R. Topfer, P. Starewicz, K.-M. Lo, K. Metzemaekers, D. Jette, H. P. Hetherington, N. Stikov and J. Cohen-Adad. *A 24-channel shim array for the human*

spinal cord: Design, evaluation, and application. Magnetic Resonance in Medicine, vol. 76, no. 5, pages 1604–1611, 2016. (Cited on page 56.)

[Truong 2014] T.-K. Truong, D. Darnell and A. W. Song. *Integrated RF/shim coil array for parallel reception and localized Bo shimming in the human brain.* NeuroImage, vol. 103, pages 235–240, December 2014. (Cited on pages 55 and 56.)

[Turner 1986] R. Turner. *A target field approach to optimal coil design.* Journal of Physics D: Applied Physics, vol. 19, no. 8, pages L147–L151, August 1986. (Cited on page 44.)

[Turner 1988] R. Turner. *Minimum inductance coils.* Journal of Physics E: Scientific Instruments, vol. 21, no. 10, pages 948–952, October 1988. (Cited on page 44.)

[Turner 1993] R. Turner. *Gradient coil design: A review of methods.* Magnetic Resonance Imaging, vol. 11, no. 7, pages 903–920, January 1993. (Cited on page 44.)

[Ungar 2010] E. Ungar and K. Stroud. *A New Approach to Defining Human Touch Temperature Standards.* In 40th International Conference on Environmental Systems, International Conference on Environmental Systems (ICES). American Institute of Aeronautics and Astronautics, July 2010. (Cited on page 135.)

[Van Vaals 1990] J. J. Van Vaals and A. H. Bergman. *Optimization of eddy-current compensation.* Journal of Magnetic Resonance (1969), vol. 90, no. 1, pages 52–70, October 1990. (Cited on page 48.)

[Vignaud 2018] A. Vignaud, F. Mauconduit, V. Gras, N. Boulant, O. Girard, A. Raaijmakers, F. Kober, D. Le Bihan and R. Abdeddaim. *Fast and unconditionally safe in vivo MR head protocol for home-made coil prototype assessment at 7T.* Journal of Physics: Conference Series, vol. 1092, page 012159, September 2018. (Cited on pages 128 and 176.)

[Wald 2012] L. L. Wald. *The future of acquisition speed, coverage, sensitivity, and resolution.* NeuroImage, vol. 62, no. 2, pages 1221–1229, August 2012. (Cited on pages 37, 63, 92, and 130.)

[Walsh 2000] D. O. Walsh, A. F. Gmitro and M. W. Marcellin. *Adaptive reconstruction of phased array MR imagery.* Magnetic Resonance in Medicine, vol. 43, no. 5, pages 682–690, 2000. (Cited on page 43.)

[Wang 2013] Q. Wang. Practical design of magnetostatic structure using numerical simulation. John Wiley & Sons Inc, Hoboken, NJ, 2013. (Cited on page 20.)

[Webb 2016] A. Webb, editor. Magnetic resonance technology: hardware and system component design. Number 7 de New developments in NMR. Royal Society of Chemistry, Cambridge, UK, 2016. OCLC: 933438677. (Cited on pages 21, 36, and 44.)

[Wilson 2002] J. L. Wilson, M. Jenkinson and P. Jezzard. *Optimization of static field homogeneity in human brain using diamagnetic passive shims.* Magnetic Resonance in Medicine, vol. 48, no. 5, pages 906–914, 2002. (Cited on pages 51 and 52.)

[Wilson 2003] J. L. Wilson, M. Jenkinson and P. Jezzard. *Protocol to determine the optimal intraoral passive shim for minimisation of susceptibility artifact in human inferior frontal cortex.* NeuroImage, vol. 19, no. 4, pages 1802–1811, August 2003. (Cited on page 51.)

[Winkler 2018] S. A. Winkler, F. Schmitt, H. Landes, J. de Bever, T. Wade, A. Alejski and B. K. Rutt. *Gradient and shim technologies for ultra high field MRI.* NeuroImage, vol. 168, pages 59–70, March 2018. (Cited on page 36.)

[Yang 2011] S. Yang, H. Kim, M.-O. Ghim, B.-U. Lee and D.-H. Kim. *Local in vivo shimming using adaptive passive shim positioning.* Magnetic Resonance Imaging, vol. 29, no. 3, pages 401–407, April 2011. (Cited on page 51.)

[Zhao 2005] Y. Zhao, A. W. Anderson and J. C. Gore. *Computer simulation studies of the effects of dynamic shimming on susceptibility artifacts in EPI at high field.* Journal of Magnetic Resonance, vol. 173, no. 1, pages 10–22, March 2005. (Cited on pages 35 and 92.)

[Zhou 2011] A. Zhou, H. Murillo and Q. Peng. *Novel segmentation method for abdominal fat quantification by MRI.* Journal of Magnetic Resonance Imaging, vol. 34, no. 4, pages 852–860, October 2011. (Cited on page 183.)

[Zhou 2020] J. Zhou, J. P. Stockmann, N. Arango, T. Witzel, K. Scheffler, L. L. Wald and F. Lin. *An orthogonal shim coil for 3T brain imaging.* Magnetic Resonance in Medicine, vol. 83, no. 4, pages 1499–1511, April 2020. (Cited on pages 56, 102, 143, 144, 183, and 184.)

* * *
* *
*

Abbreviations and Acronyms

2D	two-dimensional
3D	three-dimensional
BOLD	blood-oxygenation-level dependent
bSSFP	balanced steady-state free precession
CNR	contrast-to-noise ratio
COR	coronal plane
DFT	discrete fourier transform
DSU	dynamic shim updating
DWI	diffusion-weighted imaging
EPI	echo planar imaging
ETL	echo train length
FA	flip angle
FFT	fast fourier transform
FID	free induction decay
fMRI	functional MRI
FOV	field of view
FS	fat saturation
FT	fourier transform
FWHM	full width at half-maximum
GRAPPA	generalised autocalibrating partially parallel acquisition
GRE	gradient-recalled echo

HASTE	half-fourier acquisition single-shot turbo spin echo imaging
IBEM	inverse boundary element method
iFFT	inverse fast fourier transform
ISH	irregular solid harmonic
MB	multi band
MCA	multi-coil array
MP-RAGE	magnetisation-prepared rapid gradient echo
MRI	magnetic resonance imaging
NMR	nuclear magnetic resonance
NRMSE	normalised root-mean-square error
PDw	proton-density-weighted
PF	partial Fourier
ppm	parts per million
pTx	parallel transmission
RF	radiofrequency
ROI	region of interest
RSH	regular solid harmonic
SAG	sagittal plane
SAR	specific absorption rate
SD	sample standard deviation
SF	stream function
SH	spherical harmonic
SNR	signal-to-noise ratio
STA	small tip angle
sTx	single-channel transmission
T_1w	T_1-weighted
T_2w	T_2-weighted
T_2^*w	T_2^*-weighted
TA	acquisition time
TE	echo time
TFM	target field method
TI	inversion time
TL	temporal lobe

TR	repetition time
TRA	transverse plane
UHF	ultra-high field

* * *
* *
*

ÉCOLE DOCTORALE
Physique et ingénierie : Electrons, Photons, Sciences du vivant (EOBE)

Titre : Homogénéisation du Champs Magnétique Statique dans le Cerveau Humain pour l'IRM à Ultra-Haut Champs : Limites Conceptuelles et Développement d'un Nouveau Prototype

Mots clés : IRM, Bobines de Shim, Homogénéisation de B0, Multi-Coil Array, Ultra-Haut Champ, Fonctions de Flux

Résumé : Le rapport signal/bruit des images en imagerie par résonance magnétique (IRM) augmente avec l'intensité du champ magnétique principal: les ultra-hauts champs (7T et plus) peuvent atteindre des résolutions submillimétriques dans un temps d'acquisition viable. Ainsi un scanner IRM corps entier de 11,7T a été conçu pour l'imagerie du cerveau humain et est actuellement en cours d'installation à NeuroSpin.

Cependant, certaines séquences IRM comme l'Imagerie Echo-Planaire (EPI) sont très sensibles à l'inhomogénéité du champ magnétique causée par les gradients de susceptibilité entre les tissus biologiques et l'air. Cette inhomogénéité croît linéairement avec le champ magnétique principal et entraîne des pertes de signal et de fortes distorsions géométriques, exacerbées dans les régions du cerveau proches des canaux auditifs et des sinus.

L'atténuation de ces artefacts est réalisée par la génération de champs magnétiques antagonistes réduisant les excursions de champ causées par les gradients de susceptibilité. Ce processus, connu sous le nom de shimming, est généralement effectué avec des bobines corrigeant les harmoniques sphériques (SH) du champ jusqu'au troisième degré, mais la correction fournie par l'ensemble des bobines de ce degré devrait être insuffisante à 11,7T. Pour augmenter les degrés et performances des systèmes SH, il faudrait ajouter de nombreuses bobines occupant beaucoup d'espace, qui constitueraient un système lourd et peu pratique.

Comme alternative compacte et polyvalente, les systèmes de shim composés de petites bobines circulaires régulièrement placées sur des surfaces cylindriques près de la tête du patient, appelés Multi-Coil Arrays (MCA) matriciels, offrent des performances comparables à celles des systèmes SH à haut degré, tout en étant alimentés par des courants relativement faibles.

Dans cette thèse, nous avons commencé par explorer l'application de l'analyse en composantes principales des fonctions de flux adaptées à chaque sujet d'une base de données de 100 cartes de champ de leur cerveau. Nous avons montré que les quelques premiers modes principaux pouvaient être discrétisés en nappes de courant pour construire un système de shim à 3, 4 ou 5 canaux capable de fournir des performances équivalentes à celles de systèmes SH de 4e et 5e degrés.

Ensuite, pour plus de flexibilité, l'identification de clusters de flots de courant dans les modes principaux des fonctions de flux a permis de fournir la géométrie et la position de bobines pour concevoir un MCA optimisé. Le MCA résultant a montré des performances supérieures à celles des MCA matriciels avec un nombre de canaux similaire ou même réduit. Les simulations à 7T ont montré qu'un MCA optimisé à 36 canaux et 2 couches avec courants limité à 3A pouvait fournir des performances équivalentes à celles de systèmes SH du 6e degré sans contraintes, et même du 7e degré sans contraintes lorsqu'il était équipé d'une 3ème couche et de 48 canaux. Un prototype à deux couches de 36 canaux a été construit et testé in vivo à 7T pour la preuve de concept, montrant des résultats cohérents avec les simulations. Il a permis de réduire fortement l'inhomogénéité du champ et d'atténuer considérablement les artefacts en EPI, ce qui devrait être particulièrement bénéfique à 11,7T.

Dans un cadre plus théorique, les limites intrinsèques de la correction de l'inhomogénéité B0 ont été étudiées, et il a été démontré qu'aucun système de shim placé à l'extérieur de la tête humaine n'est capable de réduire à zéro les excursions de champ magnétique causées par les gradients de susceptibilité air/tissu dans l'ensemble du cerveau. Néanmoins, en sélectionnant des régions d'intérêt plus petites satisfaisant à des conditions particulières, une homogénéisation parfaite est possible.

Title: Static Field Shimming in the Human Brain for Ultra-High Field MRI: Conceptual Limits and Development of a Novel Hardware Prototype

Keywords: MRI, Shim Coil Design, B0 Shimming, Multi-Coil Array, Ultra-High Field, Stream Functions

Abstract: Image signal-to-noise ratio in Magnetic Resonance Imaging (MRI) increases with the main magnetic field intensity: Ultra-High Fields (7T and above) can achieve submillimetre resolutions within viable acquisition time. Thus, a whole-body 11.7T MRI was conceived for human brain imaging and is currently being installed at NeuroSpin.

However, some MRI sequences like Echo-Planar Imaging (EPI) are very sensitive to magnetic field inhomogeneity caused by susceptibility gradients between biological tissues and air. This inhomogeneity grows linearly with the main magnetic field and causes signal-loss and strong geometric distortions, exacerbated in brain regions close to ear canals and sinuses.

Mitigation of these artifacts is performed through the generation of counteracting magnetic fields reducing the field excursions caused by susceptibility gradients. This process, known as shimming, is usually performed with coils correcting field spherical harmonics (SH) up to third degree, but the correction provided by the set of coils with this degree is expected to be insufficient at 11.7T. Increasing the degree and performance of SH systems requires adding many space-consuming coils, building up to a heavy and impractical system.

As a compact and versatile solution, shimming systems composed of small circular coils regularly placed over cylindrical surfaces close to the patient's head, so-called matrix Multi-Coil Arrays (MCA), have been shown to provide comparable performance to that of high-degree SH systems, while being driven by relatively low currents.

In this thesis, we started with the exploration of the application of principal component analysis of subject-optimal stream functions computed from a hundred-brain field-map database. We showed that the first few principal modes could be discretized into windings to build a 3 to 5 channel-count shim system capable of providing equivalent performances to that of 4^{th} and 5^{th} degree SH systems.

Then, to provide more flexibility, identification of current flow clusters in the principal stream function modes provided geometry and position of coils to design an optimized MCA. The resulting MCA showed performance superior to that of matrix MCAs with a similar or even reduced amount of channels. Simulations at 7T showed that a 2-layer 36-channel optimized MCA with currents constrained to 3A could provide a performance equivalent to that of unconstrained 6^{th} degree SH systems and was expected to achieve unconstrained 7^{th} degree SH equivalence when equipped with a third layer and a total of 48 channels. A 2-layer 36-channel prototype was built and tested in-vivo at 7T for proof-of-concept, showing consistent results with simulations. It provided high field inhomogeneity reduction and considerable EPI artifact mitigation, expected to be particularly beneficial at 11.7T.

Within a more theoretical framework, the intrinsic limits to B0 inhomogeneity correction were studied, and it was shown that no shimming hardware placed outside the human head is capable of zeroing out the magnetic field excursions caused by air/tissue susceptibility gradients throughout the entire brain. Nevertheless, by selecting smaller regions of interest satisfying particular conditions, perfect homogenization is possible.